MODELING OF MECHANICS AND DYNAMICS OF BORING

By

Fuat Atabey

B.A.Sc. (Mechanical Engineering)

Istanbul Technical University

A THESIS SUBMITTED IN PARTIAL FULFILLMENT OF

THE REQUIREMENTS FOR THE DEGREE OF

MASTER OF APPLIED SCIENCE

in

THE FACULTY OF GRADUATE STUDIES

Department of
MECHANICAL ENGINEERING

We accept this thesis as conforming

to the required standard

THE UNIVERSITY OF BRITISH COLUMBIA

February 2001

In presenting this thesis in partial fulfilment of the requirements for an advanced degree at the University of British Columbia, I agree that the Library shall make it freely available for reference and study. I further agree that permission for extensive copying of this thesis for scholarly purposes may be granted by the head of my department or by his or her representatives. It is understood that copying or publication of this thesis for financial gain shall not be allowed without my written permission.

Department of Mechanical Engineering

The University of British Columbia
Vancouver, Canada

Date April 27, 2001

DE-6 (2/88)

Abstract

This thesis investigates the mechanics and dynamics of boring operations. The mechanics of boring operations deal with the prediction of cutting forces as a function of tool geometry, work material properties, and cutting conditions such as feed rate, radial depth of cut, and cutting speed. The dynamics of the process involve the modeling of interactions between the structural dynamics of a long, slender boring bar, with boring process mechanics. Evaluation of forces allows the prediction of static deflection errors, torque and the power required from the machine tool. Evaluation of the dynamic stability of the process leads to the prediction of the chatter vibration free feed rate, spindle speed, radial depth of cut, and tool geometry.

The thesis shows that boring forces are strongly dependent on the tool nose geometry, side cutting edge angle, radial depth of cut, feed rate and cutting speed. The chip thickness distribution along the curved edge of the tool is rather complex. The chip close to the nose is thin, and becomes thicker along the curved edge as the radial depth of cut increases. The chip thickness distribution is also affected by the feedrate.

It is proposed that cutting forces are modeled as a function of total chip area and cutting coefficients. The chip area is divided into several distinct geometric regions, and the center of each area is identified. Friction and tangential cutting forces are formed at each region. Cutting forces are modeled at each region, and summed up to find the resultant friction and tangential cutting forces. Using an equivalent friction or lead angle, the friction force is projected in the radial and feed directions. This model allows the prediction of cutting forces in all three Cartesian directions. The influence of tool setting errors for boring heads having multiple inserts are also considered in the general model. Several experimental results are compared with the predictions based

on the proposed mathematical model. The predictions are shown to have errors varying between 2% and 15%. The proposed model contributes to the improved prediction of boring mechanics.

The fundamental mechanism behind chatter vibrations in boring process is also investigated. It is shown that the cutting coefficients, i.e. process gain, and directional factors, are dependent on the feed rate, radial depth of cut, tool geometry, and cutting speed. While the tool geometry and speed may be kept constant, vibrations modulate radial depth of cut, and leads it to be a time-varying process input parameter. This is the fundamental non-linearity in the process, which differs from milling operations. The dynamic process is modeled in both frequency and time domains. However, the process non-linearity varies significantly during the process, preventing the application of classical linear chatter stability laws to the boring process. It is shown that the time domain modeling also suffers, mainly due to the digital integration of a significant number of tool deflection waves left on the boring surface.

Table of Contents

List of Tables

List of Figures

Acknowledgment

I would like to express my sincere appreciation to my research supervisor Dr. Yusuf Altintas for his guidance, support, and encouragement throughout my research at the University of British Columbia. I am also indebted to Dr. Ismail Lazoglu, who supervised me while Dr. Altintas was away. My thanks are also due to my friends and colleagues in the Manufacturing Automation Laboratory at UBC, for their assistance, patience and friendship.

I am deeply grateful to my parents for their constant support, patience, and encouragement during my graduate study. I dedicate this work to them.

Nomenclature

a	depth of cut
a_d	dynamic depth of cut
A	total uncut chip area
A_1	uncut chip area of Region 1
A_2	uncut chip area of Region 2
A_3	uncut chip area of Region 3
b	width of cut
c	feed rate
D	diameter of the hole
$F^*_{frc_1}$	vectorial friction force component for Region 1
$F^*_{frc_2}$	vectorial friction force component for Region 2
$F_{fr\,Ð\,s}$	predicted friction force for stable cutting conditions
$F_{fr\,Ð\,d}$	predicted friction force when the system has chatter vibrations
F_x	regional force in x direction
F_y	regional force in y direction
F_z	regional force in z direction
F_X	total force in x direction
F_Y	total force in Y direction
F_Z	total force in Z direction
h	the chip thickness
h_0	intended chip thickness
h_c	the cut chip thickness
i	oblique angle
K_{tc}	tangential cutting force coefficient

K_{frc}	friction cutting force coefficient
K_{frc_1}	friction cutting force coefficient for Region 1
K_{frc_2}	friction cutting force coefficient for Region 2
K_m	effective lead angle modification factor
K_{m_1}	modification factor for $a < R$
K_{m_2}	modification factor for a>R
K_{rc}	radial cutting force coefficient
K_{fc}	feed cutting force coefficient
K_{te}	tangential edge cutting force coefficient
K_{fre}	friction edge cutting force coefficient
K_{re}	radial edge cutting force coefficient
K_{fe}	feed edge cutting force coefficient
L_c	total cutting edge contact length
L_{c_1}	cutting edge contact length of Region 1
L_{c_2}	cutting edge contact length of Region 2
L_p	Distance between two depths in rotational direction when the system has chatter
L_T	length of a wave in a period
N	the number of waves counted on the surface finish
n	spindle speed
r_c	chip ratio
r, r^*	residues in transfer function of the structure
R	corner radius of the tool
T	period of the spindle speed or period of one chatter wave
V	cutting speed
ω_c	chatter frequency

y	radial vibration
α_1 , α_2	angles used to describe the route of the tool during the chatter vibrations
α_n	normal rake angle
α_0	orhogonal angle
α_f	side rake angle
α_p	back rake angle
α_r	rake angle
β_a	friction angle
β_n	normal friction angle
ε	phase shift between two successive revolutions
ϕ_n	normal shear angle
ϕ_c	shear angle
ϕ_{Lds}	predicted effective lead angle considering the system is stable for given cut conditions
ϕ_{Ldd}	predicted effective lead angle when the system has chatter vibrations
ϕ_L	effective lead angle
ϕ_L^*	predicted effective lead angle without modification
ψ	approach angle of the tool
ψ_r	side relief angle
γ_L	side cutting edge angle
γ_c	end cutting edge angle
η	chip flow angle
τ_s	shear stress
θ_i	angular increment in the uncut chip area calculation
θ_G	angle of gravity center with respect to the center of the corner radius
Δa_t	the portion of the tangential displacement in the depth of cut variation

Δx	displacement of the tool in tangential direction
Δy	displacement of the tool in radial direction

Chapter 1

Introduction

Boring is a machining operation used to enlarge internal bore diameters of holes. Typical examples can be listed as engine cylinders, bearing mounting locations, inner surfaces of bearing rings, and gears. The holes are first opened either by drilling, or during the fabrication of blanks. using forging or casting technology. Depending on the size of the workpiece and hole diameter, either turning machines or large boring centers are used to carry out boring operations. Small parts, such as bearing rings and gears, can be mounted on the spindles of regular CNC lathes. The boring operation can be carried out with a single point tool mounted on a slender boring bar. The boring bar is attached to the tool carriage or turret, and linearly fed towards the hole of the rotating part mounted on the spindle chuck (Figure 1.1). Large workpieces, such as engine blocks, are mounted on a table. The boring bar is attached to the non-rotating spindle, and the circular motion is either provided by the contouring actions of the spindle carriage or table drives. Some machines, such as vertical lathes, have rotating tables.

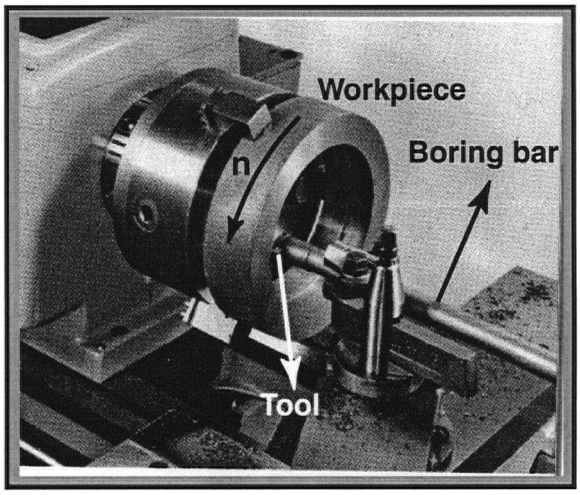

Figure 1.1 : Schematic illustration of boring process

The boring bars are usually very flexible, due to large overhang length (L) to diameter ratio (D). The boring bar can be considered as a large cantilevered beam with cutting forces applied at the free end. The cutting force magnitude depends on the work material's hardness and the area of the metal chip cut instantaneously. The direction of the cutting force depends on the tool geometry, and feed rate and radial depth of cut in boring operations. The slender boring bar elastically deflects under the excitation of the cutting force, which leads to changes in the chip area; hence the magnitude and direction of the cutting forces. In summary, the process has a closed loop dynamic system which may be stable or unstable depending on the process parameters, such as depth of cut and feed, and structural dynamics of the boring bar at its free end.

When the process is stable, the system does not experience any vibrations, and this remains a desired operation. However, the cutting forces cause static deflection of the boring bar which may be larger than the tolerance of the hole surface. If the process is modeled mathematically, it may be possible to select a suitable tool geometry, boring bar cross section, and radial depth of cut and feed-rates, which do not violate the tolerance of the part due to static deflections.

When the process is unstable, the structural modes of the boring bar are excited leading to self-excited chatter vibrations. The magnitude of the vibrations grows exponentially until the tool jumps out of the cut or breaks. Boring operations fail when chatter occurs, since this leads to poor surface finish and damage to the cutting tool. Chatter stability depends on the structural dynamics of the boring bar, the direction of dynamic cutting forces which are in turn dependent on the tool geometry, the work material hardness, radial depth of cut, feed rate and surface speed of the workpiece. If the process is modeled mathematically, it may be possible to avoid those cutting conditions that lead to unacceptable chatter vibrations before the part is machined.

Although a significant amount of research has been conducted on general cutting mechanics and dynamics, boring has been studied less than conventional operations such as orthogonal cutting and milling. Unlike the dynamics in orthogonal cutting and milling operations, the dynamics

of the boring process are quite non-linear. The process gain and directions of excitations depend on the process input parameters, such as feed when the system vibrates.

This thesis presents time domain mathematical modeling of the boring process, with or without the presence of chatter vibrations. The thesis is organized as follows:

Previous research is reviewed in Chapter 2. The modeling of cutting forces with tools having a nose radius and inclination angle is surveyed. The time and frequency domain modeling of general cutting operations, as well as boring operations that were limited, is surveyed. The fundamental difficulties in modeling the boring operations are highlighted in Chapter 2.

The chip geometry, the identification of force magnitude and directions, and process mechanics are modeled in Chapter 3. The chip area is evaluated by dividing the chip into several geometric regions. It is assumed that the force is acting at the centroid of the chip area. The friction force is identified as a function of tool geometry and chip area, and it is resolved in the feed and radial directions. The tangential force is modeled as a function of chip area. Methods for both mechanistic and oblique cutting mechanics are presented in modeling the process mechanics.

When the part is large, holes may be opened directly with a rotating boring head plunging into the hole. The boring heads usually have an even number of multiple inserts which are distributed symmetrically. The symmetrical distribution cancels the radial forces, which minimize the radial deflections. However, it is not possible to place inserts accurately on the boring head. Inserts may have radial and axial deviations, which lead to uneven chip loads for each insert. As a result, the cutting forces are not uniform and the radial forces are not canceled completely. These are called process faults, and they are modeled in Chapter 4.

The dynamics of the boring process are presented in Chapter 5. The closed loop dynamics of the boring process and the source of its fundamental non-linearity are discussed. The difficulties of solving boring chatter stability are highlighted. A time domain solution for boring chatter is presented briefly, and the difficulties involved in modeling the process physics are discussed.

The thesis is concluded with a brief summary of contributions, difficulties in modeling the boring process, and recommended future research.

Chapter 2

Literature Review

2.1. Overview

In this chapter, a literature review of the boring process is presented. Existing force prediction models are briefly discussed, followed by the recent developments of the chatter stability theory in metal cutting.

2.2. Boring Force Models

Generally, the mechanics of cutting processes are geometrically evaluated with two basic cutting process models, namely, orthogonal and oblique cutting (Figure 2.1). The difference between the two processes can be described with the orientation of the tool cutting edge with respect to the velocity vector of the process. In orthogonal cutting, the velocity vector is perpendicular to the cutting edge of the tool. This makes the cutting geometry simple due to its two-dimensional geometrical structure. Merchant [3] presented the basics of general 2-D orthogonal cutting mechanics. On the other hand, in oblique cutting, the cutting edge of the tool has an inclination angle i with the velocity vector (Figure 2.1). Oblique cutting has a three dimensional nature, thus, the relations between the cutting geometry and forces are more complicated. The most common geometrically complex cutting operations are usually defined with the aid of oblique cutting geometry.

In the past, extensive research has been devoted to the prediction of the cutting forces in machining, showing that the cutting forces could be defined as proportional to the uncut chip area A and width of cut b. The conventional formulation can be expressed as,

$$\left.\begin{aligned} F_t &= F_{tc} + F_{te} = K_{tc}A + K_{te}b \\ F_r &= F_{rc} + F_{re} = K_{rc}A + K_{re}b \\ F_f &= F_{fc} + F_{fe} = K_{fc}A + K_{fe}b \end{aligned}\right\} \tag{2.1}$$

where F_{tc}, F_{rc} and F_{fc} are cutting force components associated with shearing during the machining process. On the other hand, F_{te}, F_{re} and F_{fe} are the edge cutting force components caused by the rubbing on the cutting edge and do not have any contribution to the shear deformation in the cutting process.

The orthogonal to oblique transformation method proposed by Armarego [22-23] is one of the methods used to predict the cutting forces in the boring process. In this method, the oblique cutting forces are predicted based on an existing orthogonal cutting database. If the data base has been previously developed, there is no need to perform any further calibration test. In this method, first the orthogonal cutting tests are performed in order to determine the orthogonal cutting parameters for a specific tool and workpiece pair. These parameters are then transformed to the oblique cutting geometry under specific rules [2]. The details of this method are explained in Chapter 3. This method is practical, and saves time by not requiring the performance of tests if the database has already been developed for the workpiece-tool pair intended to be used in the boring operation. However, it requires that the cutting mechanics of the tool be exactly defined with the oblique cutting geometry along the cutting edge. In other words, the tool should have a sharp cutting edge and a flat rake face.

At present, most boring tools are manufactured with a nose radius and special chip breaking grooves along the cutting edge. Sometimes, the cutting geometry of these tools cannot be modeled with the existing oblique cutting models. For the force prediction of these tools, the mechanistic modeling approach is employed. Cutting force coefficients are empirically estimated for a

specific cutter geometry and workpiece material, relating force to the cutting parameters (i.e., depth of cut, feed rate and cutting speed) and other geometrical properties of the tool.

One of the first cutting mechanics models is the one proposed by Kronenberg [5]. In this model, the tangential force F_t is proportional to the uncut chip area A. The radial and feed forces (F_r, F_f) are proportional to the tangential force.

$$\begin{aligned} F_t &= K_1 A \\ F_r &= K_2 F_t \\ F_f &= K_3 F_t \end{aligned} \tag{2.2}$$

where K_1, K_2 and K_3 are the cutting coefficients that are functions of the tool geometry, tool and workpiece material, and cutting parameters. In this model, the corner radius of the tool is not considered.

Hallam and Allsopp [6] proposed a method in which the uncut chip area is calculated by an integration method, which considers the depth of cut, feed rate, and corner radius of the tool as inputs. In this model, the cutting coefficients are assumed to be constant. The dependency of the cutting forces on the depth of cut showed good agreement with the experimental data, however , the model did not accurately predict the cutting forces as functions of feed rate.

Sabberwal [9] later proposed that tangential and friction forces are proportional to the uncut chip area and the cutting coefficients are not constants but a function of the chip thickness.

$$\begin{aligned} K_t &= b_0 h^{b_1} \\ K_{fr} &= d_0 h^{d_1} \end{aligned} \tag{2.3}$$

where b_o, b_1, d_0 and d_1 are empirical contants. Based on this method, a force prediction model for boring process has been developed by Subramani et. al.[16]. Sutherland et al. [17] modified the model presented by Subramani, including the cutting speed and the effect of tool geometry in the prediction of the cutting coefficients (Eq. 2.4).

$$K_t = c_0 \alpha_n^{c_1} V^{c_2} h^{c_3}$$
$$K_{fr} = d_0 \alpha_n^{d_1} V^{d_2} h^{d_3} \tag{2.4}$$

where, α_n and V are the normal rake angle of the tool and cutting speed, respectively.

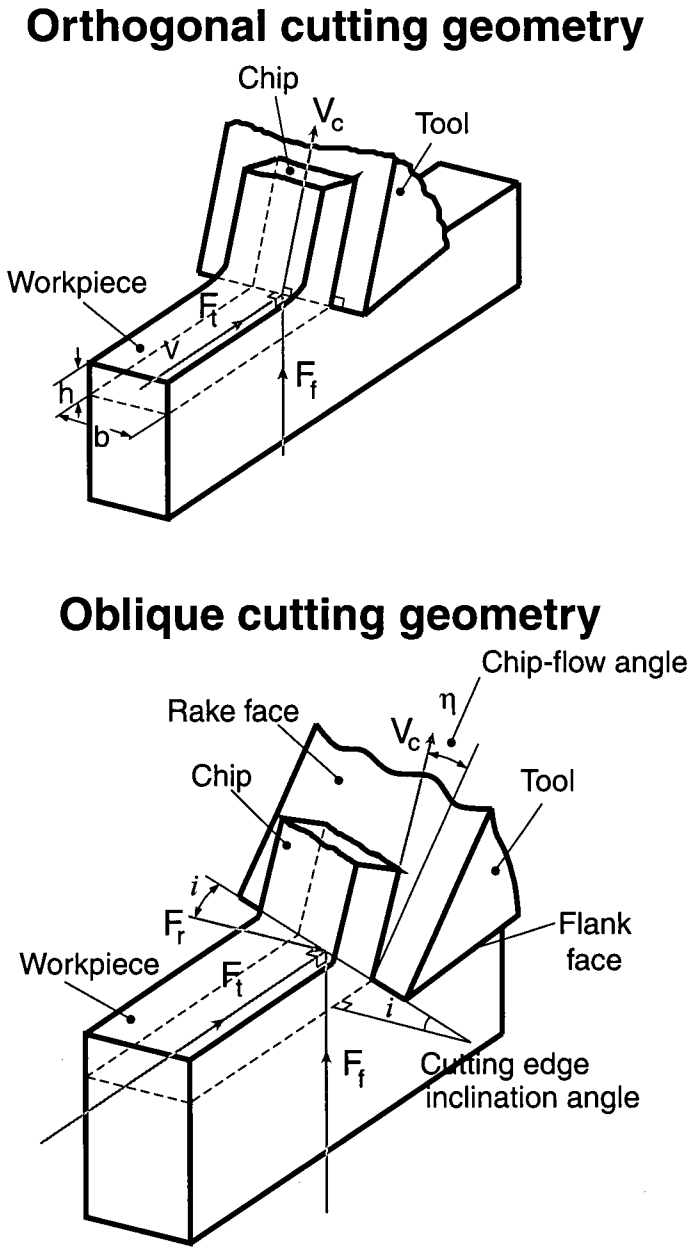

Figure 2.1 : Geometries of orthogonal and oblique cutting

2.3. Chatter Stability Analysis in Boring

This section examines the background related to chatter stability of the boring process.

In boring operations, the length to diameter ratio of the boring (L/D) bar (Figure 2.3) is usually large and any dynamic force variation can easily excite the structure due to its low dynamic stiffness. If the cutting force is in resonance with one of the natural frequencies of the boring structure, vibrations become significant in determining surface finish quality. Any change in length to diameter ratio (L/D) has a substantial effect on the dynamic stiffness and the system stability. A steel shank plain boring bar can usually be used up to the value of 4.5-5 length to diameter ratio (L/D) for chatter free machining. However, for the large (L/D), cutting conditions are limited for a stable cutting process.

Significant research efforts have been made in finding a method to increase the stability of the boring process. One of the approaches which researchers have been interested in is to increase the dynamic stability of the structure using passive vibration control techniques [36, 37]. In this technique, the vibration of the boring bar structure is absorbed using springs and dashpots. The forces generated by the passive vibration components tend to decrease the magnitude of vibration. By means of this method it is possible to increase the stable operation range up to length to diameter ratios (L/D) of 5.5-6.0. The method of using passive vibration absorbers is commonly used by boring bar manufacturers.

Passive vibration, on the other hand, has limitations in terms of system stability in large length to diameter ratios (L/D). Using an active dynamic observer makes it possible to perform a stable boring operation up to the length to diameter ratios (L/D) of 9 by supressing bar vibrations [24, 25, 26]. In these applications, a piezoelectric actuator is used as an active dynamic absorber and optimal control is applied to the system for the control of boring bar motion.

These techniques help to increase the stability of the structure for a specific application, however, due to some configuration problems and their high cost it cannot be applied to all boring operations.

This study focuses on the investigation of chatter stability due to self-excited vibrations. The main cause of self-excited chatter is the regenerative effect introduced by Tobias [29], [30], Tlusty [4] and Merrit [7]. If there is a relative vibration between the cutting tool and the workpiece, the tool leaves a wavy surface behind. In the next revolution, the tool encounters this wavy surface and removes material with a time-varying uncut chip area [29]. Periodic variation of the uncut chip area causes a variation in cutting forces. Thus, the structure is excited and chatter vibrations take place.

Regenerative effect is caused by the phase shift between the waves generated on the cut surface (Figure 2.5). This phase shift can be defined as a function of spindle period T, and chatter frequency ω_c.

$$\varepsilon = T\omega_c - 2\pi k \tag{2.5}$$

where k is the integer number of the waves on the cut surface in one full revolution. Figure 2.5 shows the variation of the chip thickness depending on the phase angle ε between the successive undulations. Zero phase angle produces constant chip thickness, hence, there is no regenerative effect, even though the system still has vibrations. When the phase angle ε becomes π [rad], an extreme case of wave regeneration occurs. The oscillation of the chip thickness causes the forces to vary with its period, leading to unstable cutting conditions. The nonlinearity of the regeneration can be recognized when the tool jumps out of the workpiece [31].

There are some factors that increase the system stability. Among these factors, process damping which is caused by the time-varying relief angle due to vibrations is important in low cutting speeds [33, 34, 35]. Figure 2.6 shows a tool moving to the right while it is oscillating. It should be noted that for low cutting speeds the lengths of the generated waves become short, causing the flank face of the tool to touch the cut surface. This creates a positive damping effect in the process due to the rubbing occuring on the flank face of the tool. In contrast, when the length of the wave is longer (as occurs at high cutting speeds) the relief angle of the tool becomes larger. In such a

case, the flank face does not come into contact with the surface and, hence, does not contribute to the damping of the system. As the modeling of process damping is rather difficult, its effect is not included in the analytical and time domain stability solution in this study.

System stability is investigated and the force variation of a machining system, torque, bending moment and surface finish can be obtained in time domain solution whose pioneering work was introduced by Tlusty [11, 32]. The other advantage of the time domain simulation of the process is that it is possible to investigate the nonlinearities of the process, such as the jumping of the tool from the workpiece and process faults.

Chatter stability has been commonly expressed with stability lobe diagrams (Figure 2.2), which show the boundary between the stable and unstable cutting conditions in the form of axial depth of cut limit versus spindle speed (Figure 2.2). Tobias [30], Tlusty and Polacek [4] predicted this borderline considering the regenerative effect in a multi-degree of freedom system.

Research dedicated to the stability analysis of the boring process is rarely found in the literature. This may be because the dynamics of the boring process are rather complex compared to other machining processes.

One of the first attempts to solve the stability problem in boring is the one by Zhang [18, 19]. His Ph.D. thesis analyzed the stability for two conditions;1- The cutting condition with no overlapping, 2- The cutting condition with overlapping. In both cases, the critical stiffness of the boring bar is investigated under spiral cutting conditions, which are not representative of the boring process. In his model, for the purpose of facilitating the solution of stability analysis, equivalent width of cut and chip thickness are considered as system parameters instead of the direct use of depth of cut and feed rate (Figure 2.7). Dynamic chip load is calculated as,

$$A = b(h_0 - h(t) + \mu h(t-T)) \tag{2.6}$$

where b, h_0, $h(t)$, $h(t-T)$ and μ are the width of cut, intended chip thickness, current chip thickness, the chip thickness at the previous tool position and overlapping factor, respectively.

Kuster et. al. [12] proposed a time domain solution model for the boring process. In the model they predicted the forces in three directions (i.e. tangential, radial and feed directions). They did not take into account the nonlinearity of the interactions between the current and previous tool positions and all possible uncut chip area configurations depending on the previous tool positions. They investigated the stability limit by considering the vibrations in three directions of the boring bar; However, the presented experimental results to support the prediction of the stability limit were poor.

S. Jayaram et al. suggested an analytical solution to the boring process [27]. In their model, the nose radius of the tool is not considered, and vibrations in the radial direction are neglected, even though they have the most significant effect in regenerative chatter in the boring process. In this model the boring bar is assumed to vibrate in the feed direction. However, it has been perceived from the transfer function measurements that the boring bar is relatively stiffer in the feed direction. In the model the boring process is analyzed in the same way as in the turning process. Good accuracy in the prediction of stability is presented; however, this validation is unrealistic since the dynamics of turning and boring processes are different.

E.W. Parker investigated boring stability with a boring bar having rectangular cross-section [28]. The tool is attached to the tip of the boring bar with a ring and arranged at different angular position on the bar (Figure 2.4). Stability of the structure for different angular tool positions was investigated considering the model as a two-degree of freedom mass, spring damper system. The stability of the boring bar system shows dependence on the angular location of the tool on the ring of the bar and the optimum angular position of the tool was found.

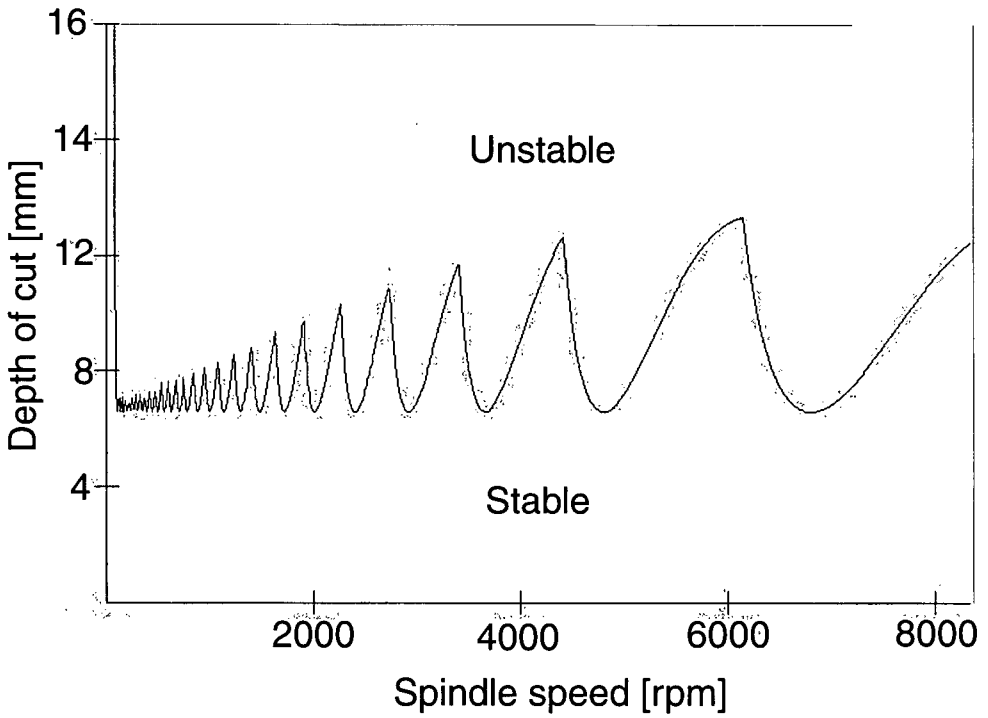

Figure 2.2 : Chatter stability lobes

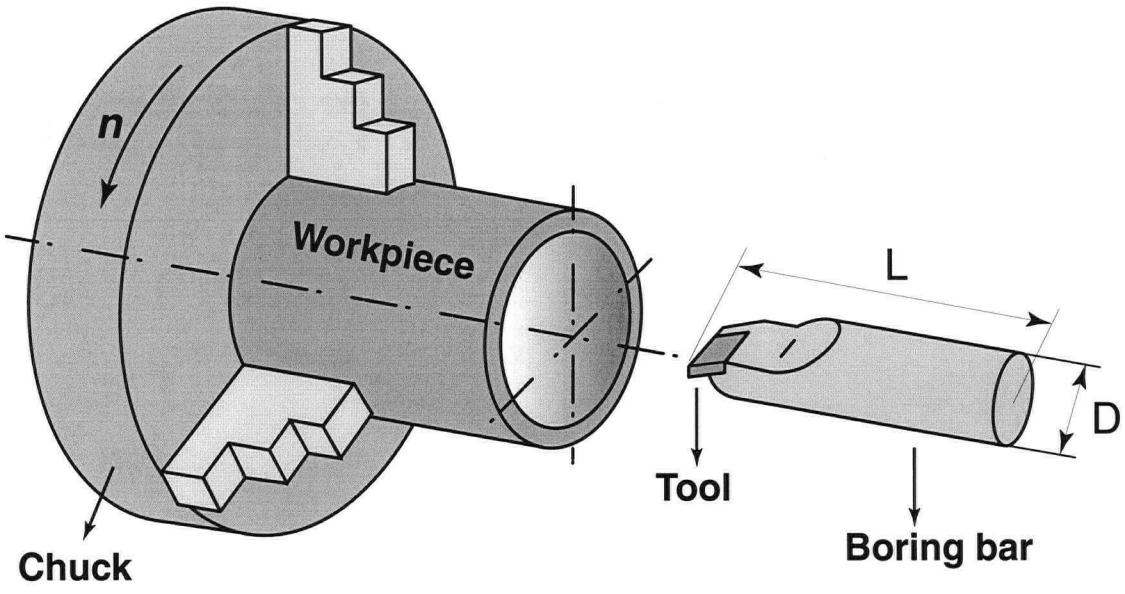

Figure 2.3 : Schematic illustration of the boring process

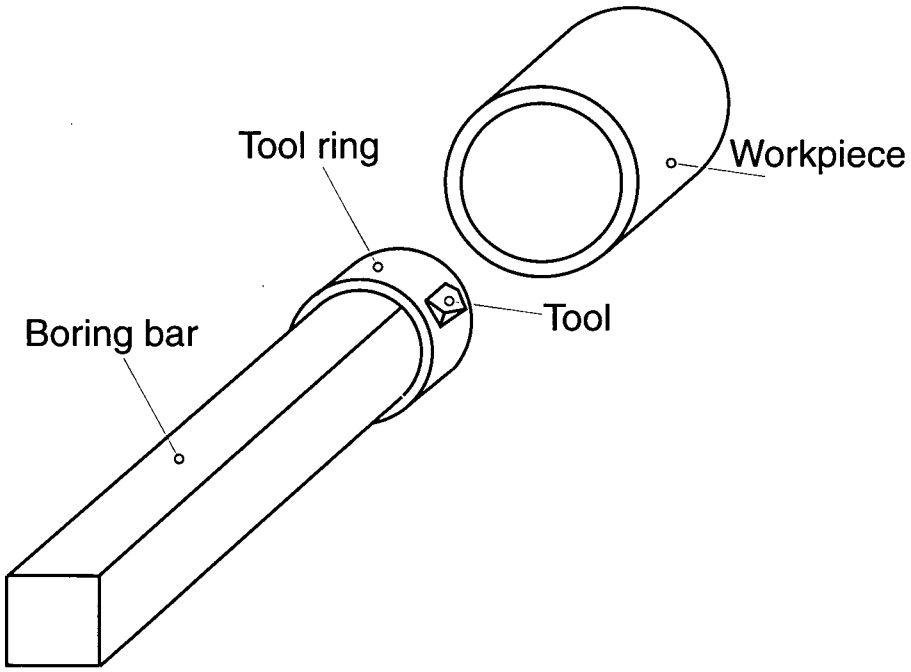

Figure 2.4 : Boring bar with flat surface

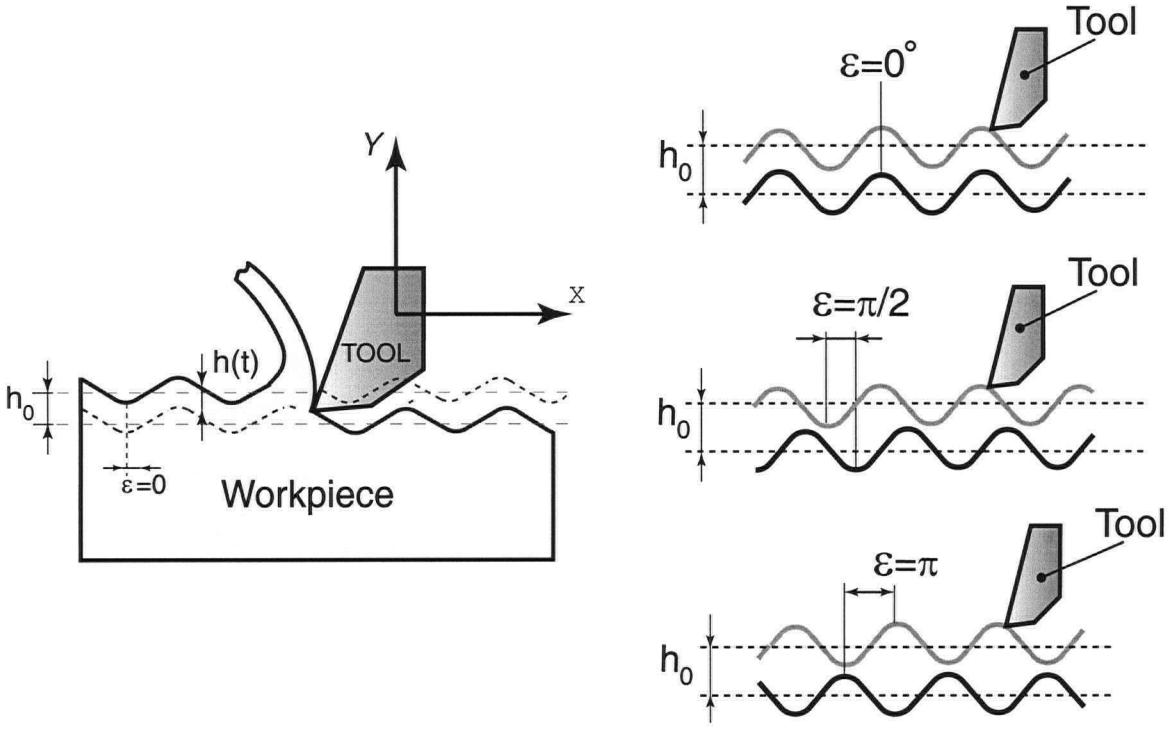

Figure 2.5 : Regeneration of waves with different phase angles

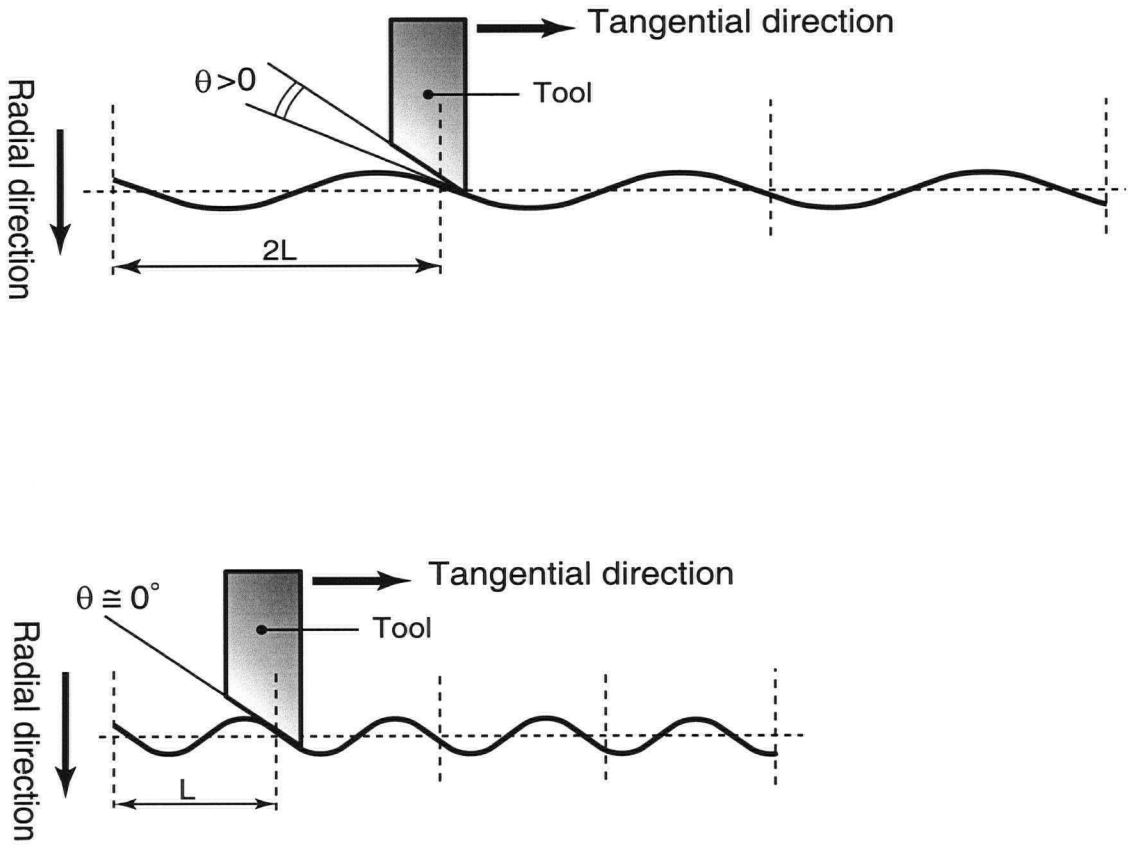

Figure 2.6 : Relationship between the process damping and relief angle

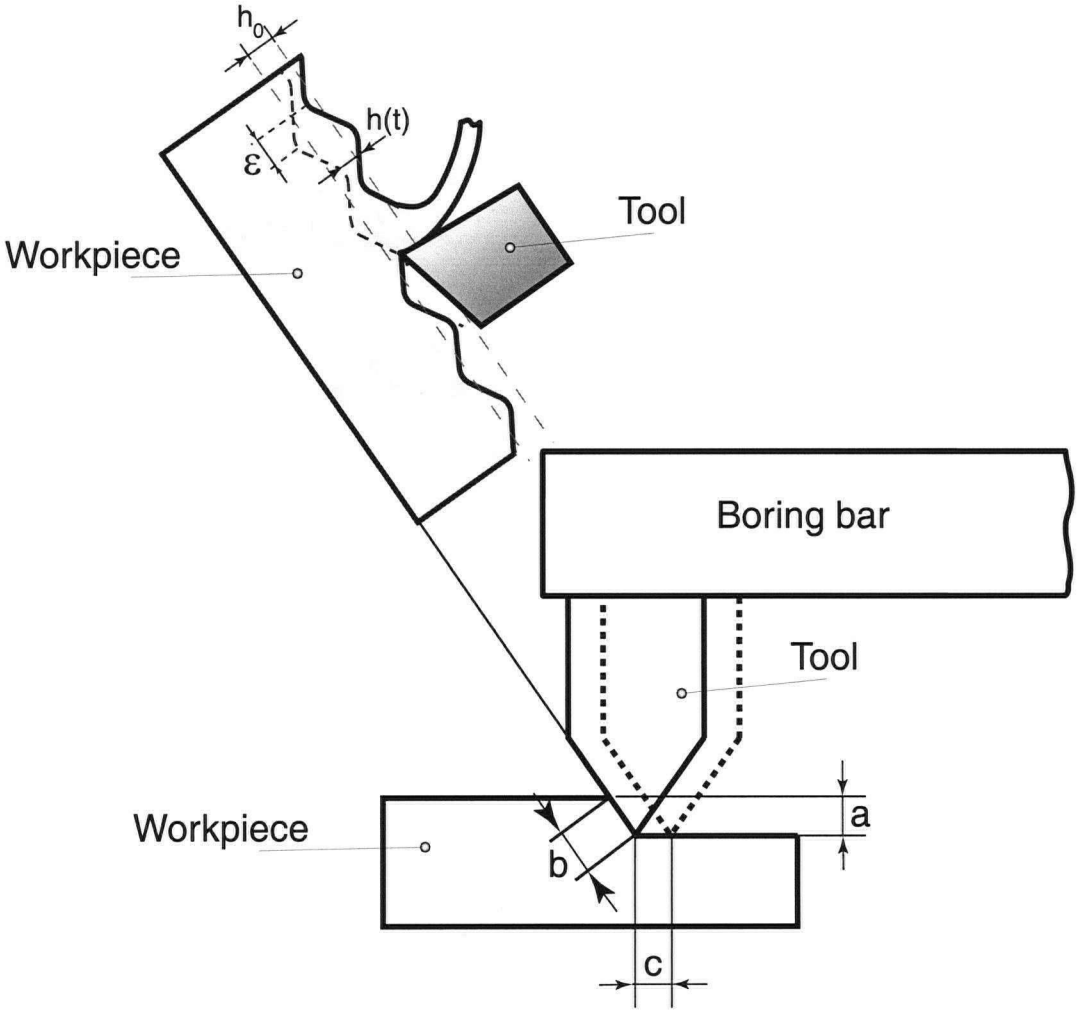

Figure 2.7 : Model of dynamic boring process presented in Zhang's thesis [18]

2.4. Summary

There has been very little research presented in the literature, which provided successful prediction of chatter stability in boring. Neither time domain nor frequency domain models were successful in even modest prediction of chatter stability in boring operations.

Chapter 3

Force Prediction in Boring

3.1. Introduction

Most boring tools used in industry are specially designed and manufactured with a nose radius, chip breaking grooves, a side cutting edge angle, side and back rake angles (Figure 3.1). The aims of these are to increase dimensional accuracy, to improve surface finish quality, and to extend the life of the tool in order to prevent failure. Prediction of the cutting forces and chatter vibrations enables the engineer to set the design parameters of the machine tool, cutting parameters, and fixture in an optimal fashion so that productivity can be increased by minimizing the machining cost per piece. Selecting inappropriate cutting parameters may cause damages on machine tool components, early tool wear and tool breakage, chipping, and poor surface finish quality, all of which are undesirable in manufacturing.

One such method is to predict the cutting forces from an orthogonal cutting database using *Orthogonal to Oblique Transformation Method* [1]. Although this method is practical, it is not applicable for tools that have a chip breaking groove on the cutting edge. This is because the transformation can only be implemented for tools with a sharp cutting edge and flat rake face. Once an orthogonal cutting data base is developed for a tool-workpiece pair, orthogonal cutting parameters can be transformed to other complex tools (whose cutting geometry can be characterized as oblique cutting). Thus, the need for calibration of each tool geometry is eliminated, and cutting forces can be predicted without performing any new experiments. This transformation is performed in a special manner that requires certain assumptions, which will be explained in detail in the following sections.

The second method for force prediction is the *Mechanistic Identification Method,* which has a simple formulation and results in accurate prediction for tools having complex cutting edge geometry. One of the drawbacks of the mechanistic approach is that more experimental data is needed to take the effect of all cutting and geometrical parameters on the cutting forces into account. Correlations between the parameters and cutting force coefficients are identified for each tool geometry.

In the first part of this chapter, a mechanistic modeling approach for the prediction of the cutting forces in the boring process is described. The majority of this study lies in the prediction of the cutting force coefficients and effective lead angle for both stable and unstable cutting conditions. The methodology behind this approach is discussed. In the model, the expressions of the cutting force coefficients are estimated based on experimental data. Then, the model is experimentally validated.

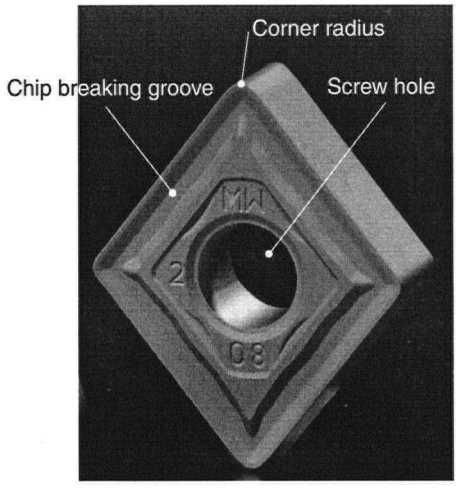

Figure 3.1 : Single point cutting tool with corner radius and chip breaking groove

The second part of this chapter deals with the force prediction by utilizing the *Orthogonal to Oblique Transformation Method.* The identification of the cutting force coefficients based on the

orthogonal cutting database and its application to tools with a nose radius are described in detail. Accuracy in the prediction of the cutting forces is experimentally investigated.

3.2. Mechanics of Boring

The boring operation is performed in two different ways, depending on the machine type: 1- the boring bar rotates and is linearly fed into the workpiece with feed rate c, while the workpiece remains stationary; 2- The workpiece rotates as the boring bar makes a linear move into the work-piece with the feed rate c. The versatility of the operation can be increased with different types of boring bar and machines. In this chapter, a boring bar with a single insert under the second cutting condition, (described above), is considered.

3.2.1. Boring Bar with one Insert

Figure 3.2 illustrates a schematic of the boring operation with a single insert. In this process, forces can be resolved into two components (Figure 3.3), namely the tangential force F_t, which acts perpendicular to the uncut chip area, and the friction force F_{fr}, which is the sum of the forces acting perpendicular to the cutting edge. The direction of the friction force for each angular differential element varies along the cutting edge contact length due to the nose radius, and is defined with effective lead angle ϕ_L, which is the angle between the directions of the friction and the feed forces.

Radial and feed forces (F_r and F_f) are obtained by projecting the total friction force F_{fr} into the radial and feed directions. The X, Y and Z directions are referred to as the tangential, radial and feed directions, respectively (Figure 3.2).

$$\left.\begin{aligned} F_x &= F_t \\ F_y &= F_r = F_{fr}\sin\phi_L \\ F_z &= F_f = F_{fr}\cos\phi_L \end{aligned}\right\} \tag{3.1}$$

In the process, the combined linear motion of the boring bar with the feed rate per revolution and rotation of the workpiece causes the insert to travel along a spiral path. It is reasonable to assume that the pitch of this spiral is equal to the feed rate c. If the workpiece hole is rolled out onto a plane, the path followed by the insert can be shown in Figure 3.4. At any point on the path traveled, the distance between the current and preceding positions of the insert is equal to the feed rate c. L is equal to the circumference of the workpiece hole.

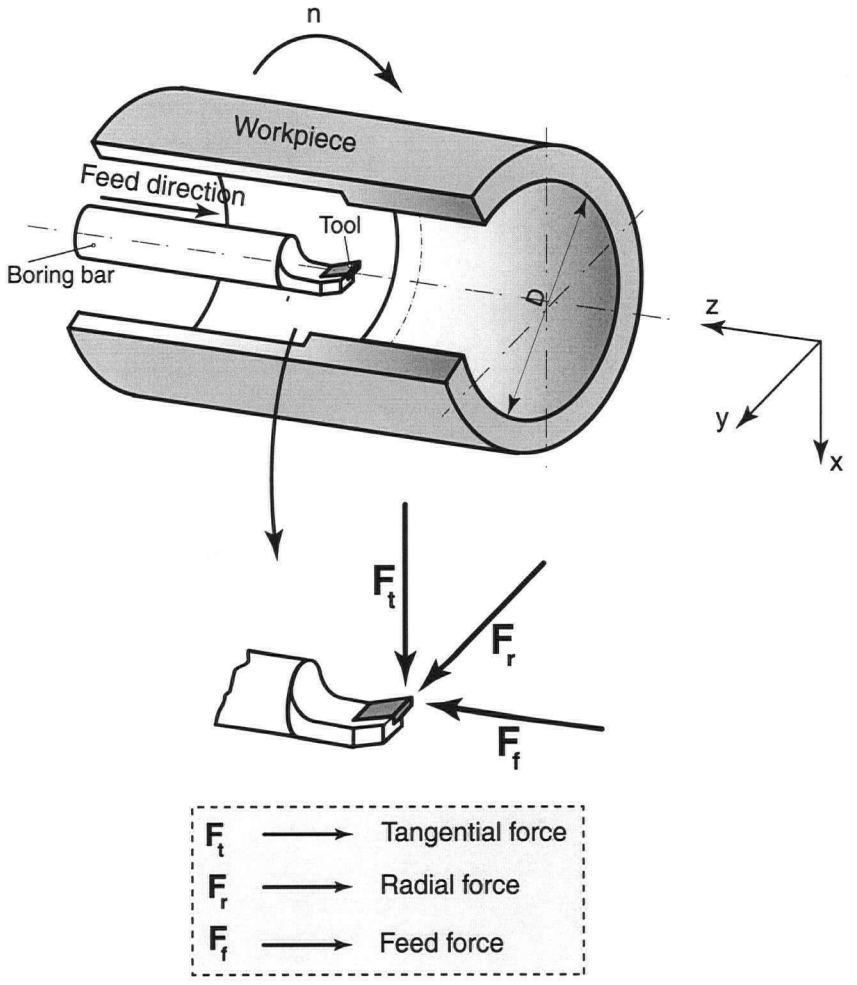

Figure 3.2 : Schematic illustration of force directions in boring process

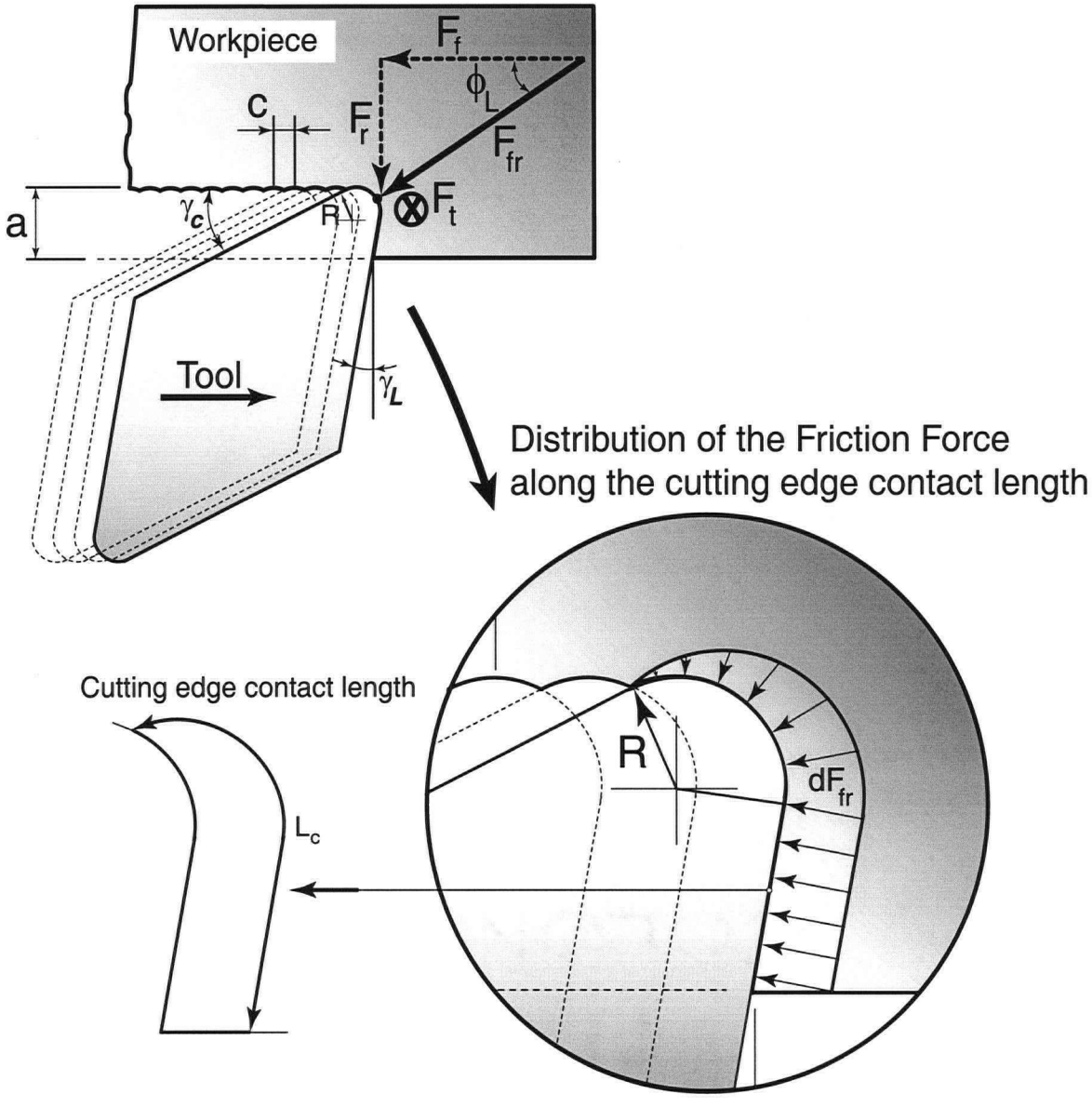

Figure 3.3 : Definition of the forces, cutting and geometrical parameters in boring process; friction force distribution along the cutting edge contact length L_c

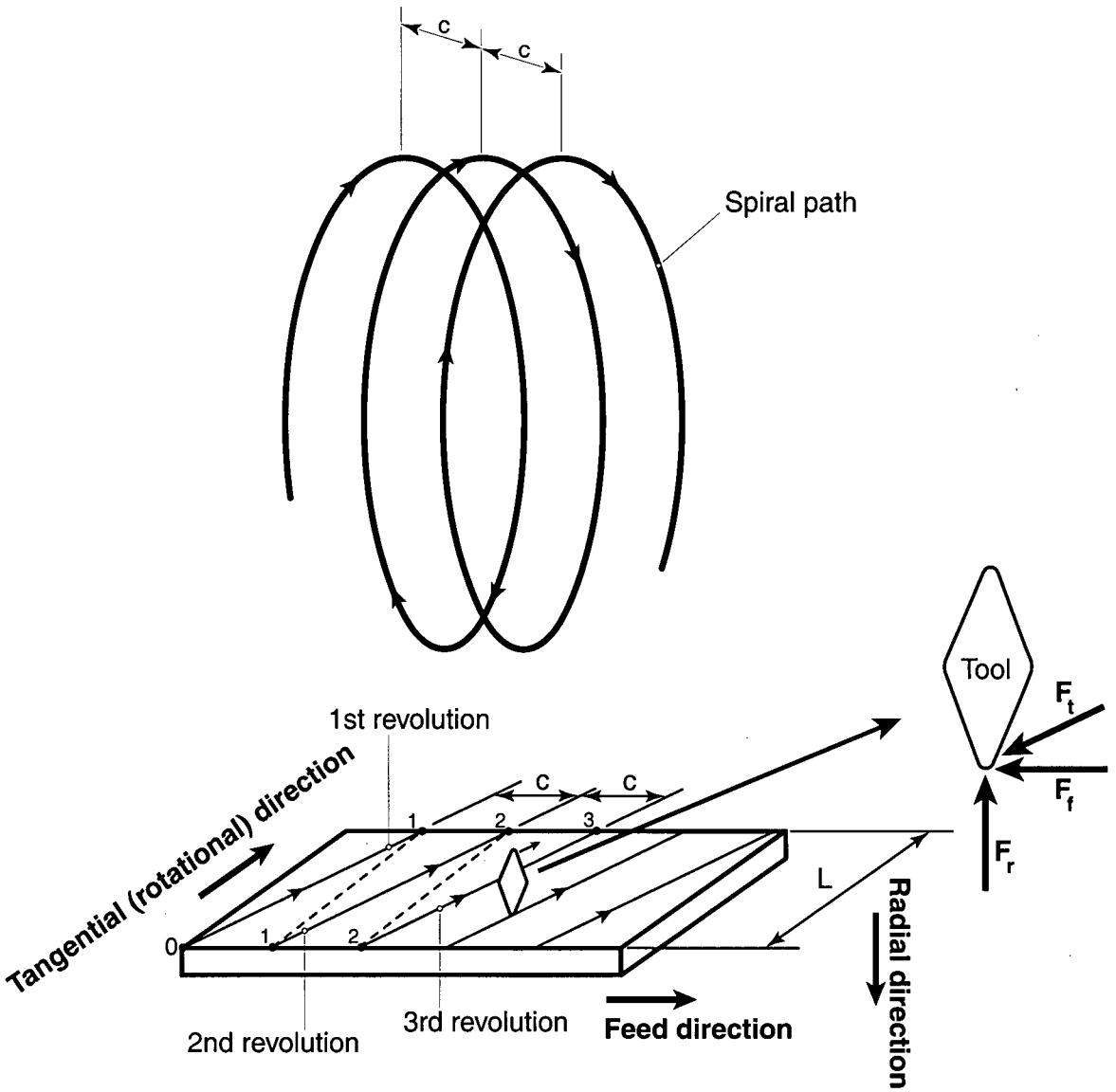

Figure 3.4 : Spiral path of boring tool, $L = \pi D$

3.3. Force Prediction in Boring

3.3.1. Mechanistic Model

The mechanistic model approach relates the cutting and geometrical parameters (i.e. depth of cut *a*, feed rate *c*, cutting speed *V*, corner radius of the tool R, side cutting edge angle γ_L, end cutting edge angle γ_c) to the cutting forces. The basic force equation can be expressed as,

$$F = KA \tag{3.2}$$

where K and A are the cutting coefficient ($[N/mm^2]$), which is also known as the proportionality constant in the literature, and the uncut chip area ($[mm^2]$), respectively. In this expression, K is not considered as a constant, but rather, as a function of cutting and geometrical parameters [9, 13, 14, 15, 16 and 17]. For the prediction of the cutting forces, the uncut chip area and the cutting coefficient need to be determined. In this study, two different inserts, with specified geometry, are employed, and cutting force coefficients have been investigated within the desired range of cutting parameters. The effect of the tool geometry is considered in the calculation of the uncut chip area. It should be noted that in the mechanistic modeling approach the cutting coefficients are predicted separately for each different workpiece-tool pair.

3.3.1.1. Uncut Chip Area and Cutting Edge Contact Length Calculation

In the boring process, the uncut chip area varies as a function of the depth of cut a, feed rate c, side cutting edge angle γ_L and end cutting edge angle γ_c. For the uncut chip area calculation, four main different configurations (Figure 3.5) and nine various tool-workpiece interferences can be defined with respect to the cutting parameters (i.e. a, c and R)[23]. However, the most common case encountered in boring applications is when the feed rate is less than the nose radius of the tool, due to the feed rate limitations for the given workpiece and cutting tool. Therefore, this study considers only five of nine interferences mentioned.

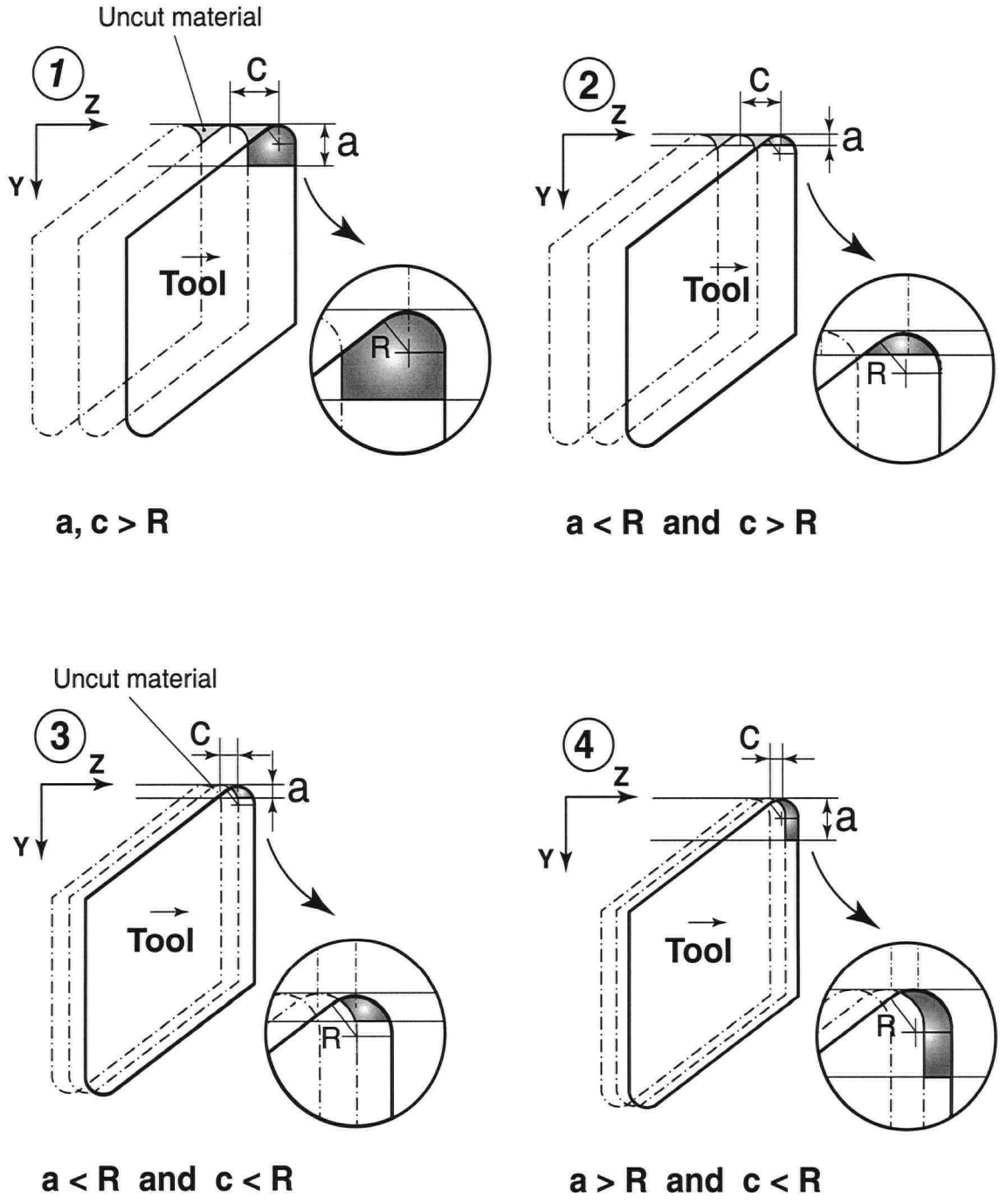

Figure 3.5 : Four different uncut chip area configurations defined with depth of cut *a,* feed rate, *c* and corner radius of the tool *R*

Figure 3.5 also illustrates the relative positions of the insert at successive revolutions of the workpiece in four different configurations. Notice that the material left behind (uncut material) depends on the feed rate c and corner radius R and is expected to be large when the feed rate c is much greater. The uncut material also determines the surface finish quality. While large corner radii R and small feed rates c create good surface, small corner radii and large feed rates c cause the cut surface to be rough.

The uncut chip area model contains five inputs, a [mm], c [mm/rev], R [mm], γ_L [Deg] and γ_c [Deg]. From these inputs, only the side cutting edge angle γ_L may have a negative value that defines the straight side edge of the tool to have an earlier contact with the workpiece rather than the corner of the tool at the begining of cutting. The uncut chip area is calculated by discretizing the uncut chip area into small differential elements (Figure 3.6). The calculation is executed separately for regions defined in the uncut chip area. In the following, the calculation of the uncut chip area A and cutting edge contact length L_c are explained for only the first configuration.

For Region 1, the uncut chip area of each differential element is approximated by subtracting the area of the triangle $A_{OBB'}$, from the area of the circular ring sector $A_{ODD'}$

$$A_{OBB',i} = 0.5|OB|_i|OB'|_i\sin\theta_i \tag{3.3}$$

$$A_{ODD',i} = 0.5\theta_i R^2 \tag{3.4}$$

$$A_{1,i} \cong A_{ODD',i} - A_{OBB',i} \tag{3.5}$$

The total area of region 1 is calculated as a subtotal of the area of each differential element as,

$$A_1 \cong \sum_{i=1}^{n} A_{1,i} \tag{3.6}$$

Region 2 is assumed to be a rectangle, although one side of it (i.e. side KE) has a slight curvature caused by the corner radius of the previous tool position. Its area can be approximated as,

$$A_2 \cong |MG||KM| \tag{3.7}$$

Region 3 is a simple triangle and its area is calculated as,

$$A_3 = 0.5|KM||LM|\sin\gamma_L \tag{3.8}$$

Finally, total uncut chip area is found by adding together these areas for each region.

$$A = A_1 + A_2 + A_3 \tag{3.9}$$

The cutting edge contact length is calculated by considering only Region 1 and 2. Region 3 does not have any contribution to the total contact length. The total cutting edge contact length is,

$$L_c = L_{c1} + L_{c2} \tag{3.10}$$

where L_{c_1} is the contact length of Region 1 and equal to $L_{c1} = \sum_{i}^{n} |DD'|_i$ (n is the number of element in Region 1). Similarly, L_{c_2} is the contact length of Region 2 and equal to the length of MG.

The uncut chip areas A and cutting edge contact lengths L_c are calculated with the same manner for other configurations shown in Figure 3.7.

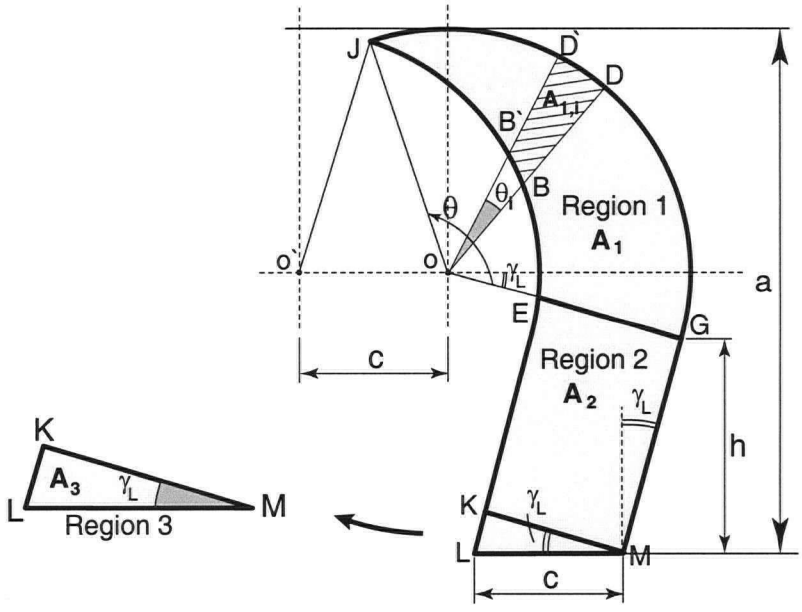

Figure 3.6 : Uncut chip area calculation for Configuration 1 and the definitions of the regions

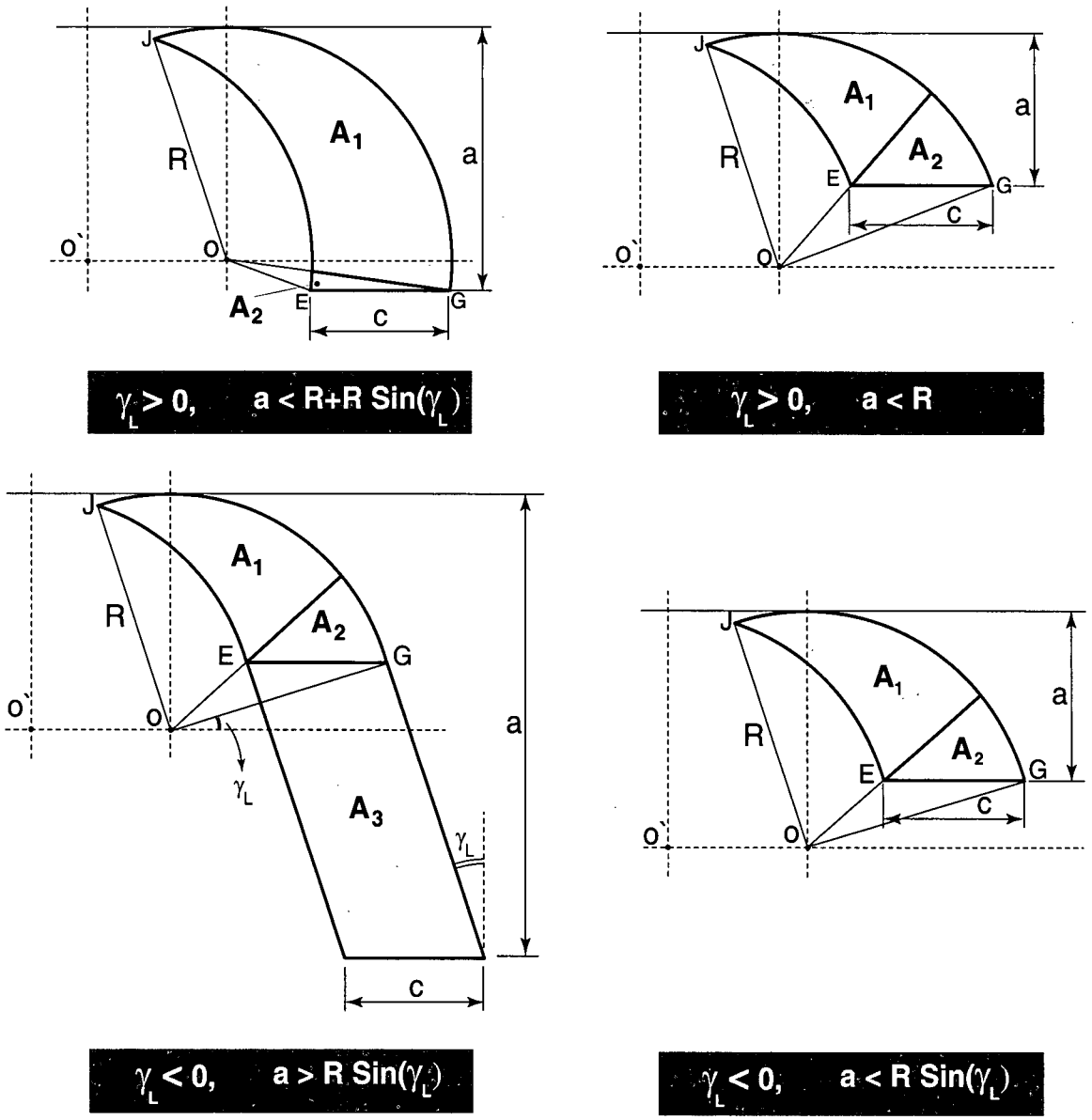

Figure 3.7 : Other uncut chip area configurations considered in the area calculation model

3.3.1.2. Experimental setup

Calibration tests have been conducted with Aluminum 6061-T6 disks (Figure 3.8) on a *Hardinge Superslant* turning center that has a high precision positioning accuracy of 0.0005 [mm]. A *Kistler 9257A three axis dynamometer*, which has a maximum *5000 [N]* measurement capacity in each direction, has been used for the force calibration. For the use of the boring bar on the machine a special tool holder had to be designed (Figure 3.9). The force signals were sampled at 1000 [Hz] and amplified by *Kistler 5010B1 Dual Mode Charge Amplifiers* prior to being digitized by data acquisition software *CutPro-MALDaq*. One thousand data points were collected in one second and the average value of this data is used in the development of the mechanistic model (Figure 3.10).

Two different inserts have been used in the experiments:

- *Kennametal CPMT-32.52 K720 coated insert* with *A12-SCFPR3 steel shank boring bar* with 0° side cutting edge angle γ_L (Figure 3.11)

- *Valenite CCGT432-FH* 80° *Carbide PVD coated diamond insert* with *A-SCLPR/L boring bar* with -5° side cutting edge angle γ_L.

In the experiments, in order to avoid chatter vibrations, the boring bar was clamped onto the tool holder with a short *length to diameter ratio* (L/D=2.5). Specifications of the inserts and boring bars are shown in Figures 3.11 and 3.12.

Two sets of experiments for each insert were conducted with different combinations of the cutting parameters within the ranges of *0.05-0.19 [mm/rev]* feed rate c, *75-275 [m/min]* cutting speed V, *0.25-3.25 [mm]* depth of cut a. The first set of experiments was used to determine the empirical constants in the equations for the estimation of the cutting force coefficients. The second series of experiments were carried out to further examine the validity of the mechanistic model.

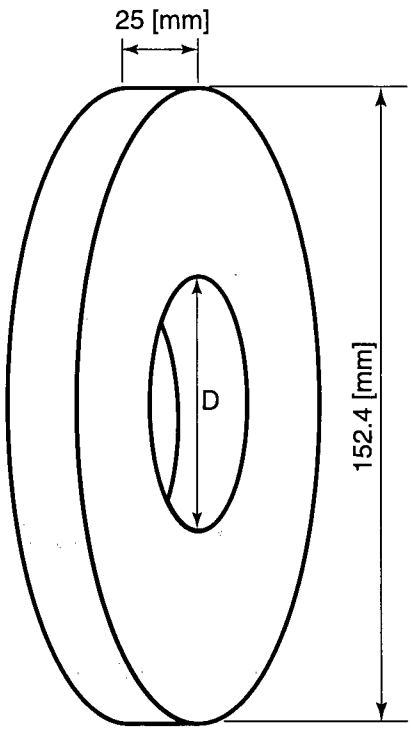

Figure 3.8 : Workpiece-Al 6061-T6 used in the experiments

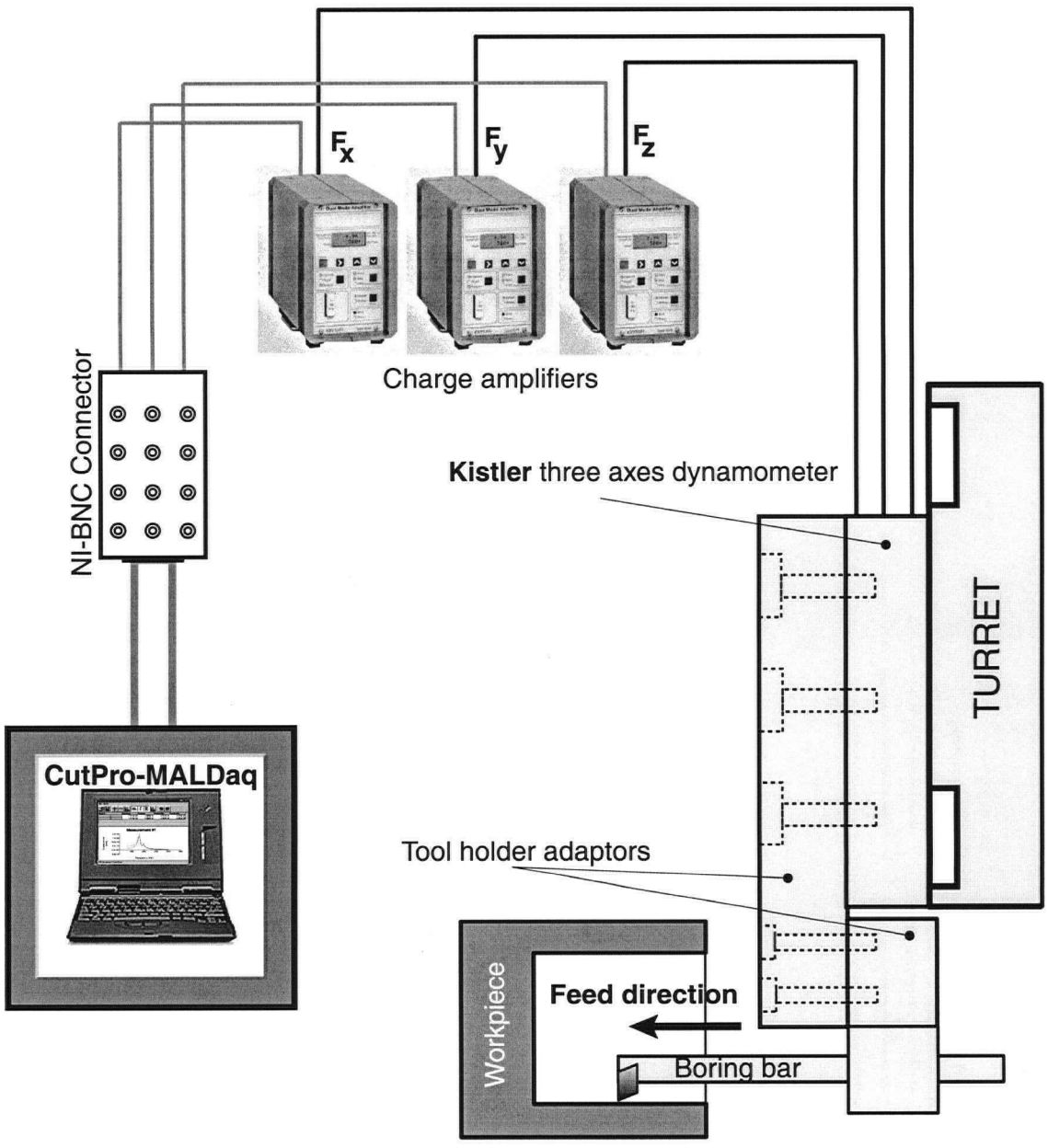

Figure 3.9 : Schematic illustration of the experimental setup for force calibration

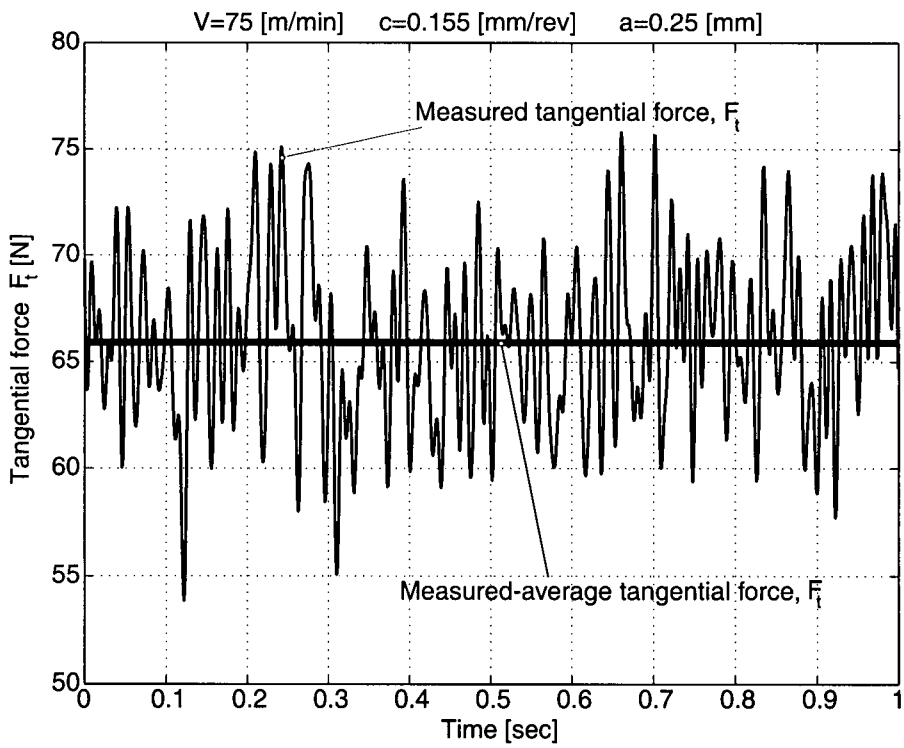

Figure 3.10 : Determination of the average tangential force value based on the collected data, V=75[m/min], c=0.155[mm/rev], a=0.25[mm]

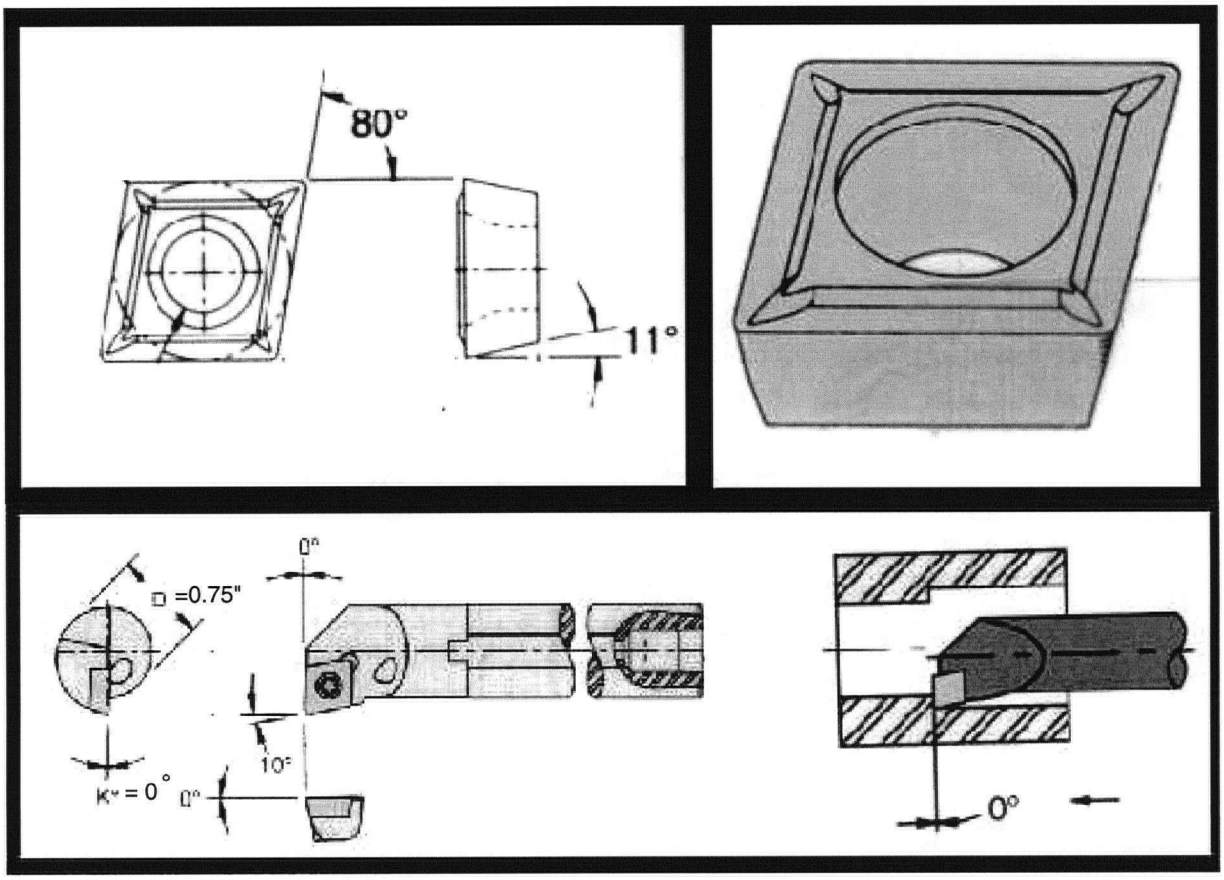

Figure 3.11 : Kennametal CPMT-32.52 K720 coated insert and A12-SCFPR3 steel shank boring bar

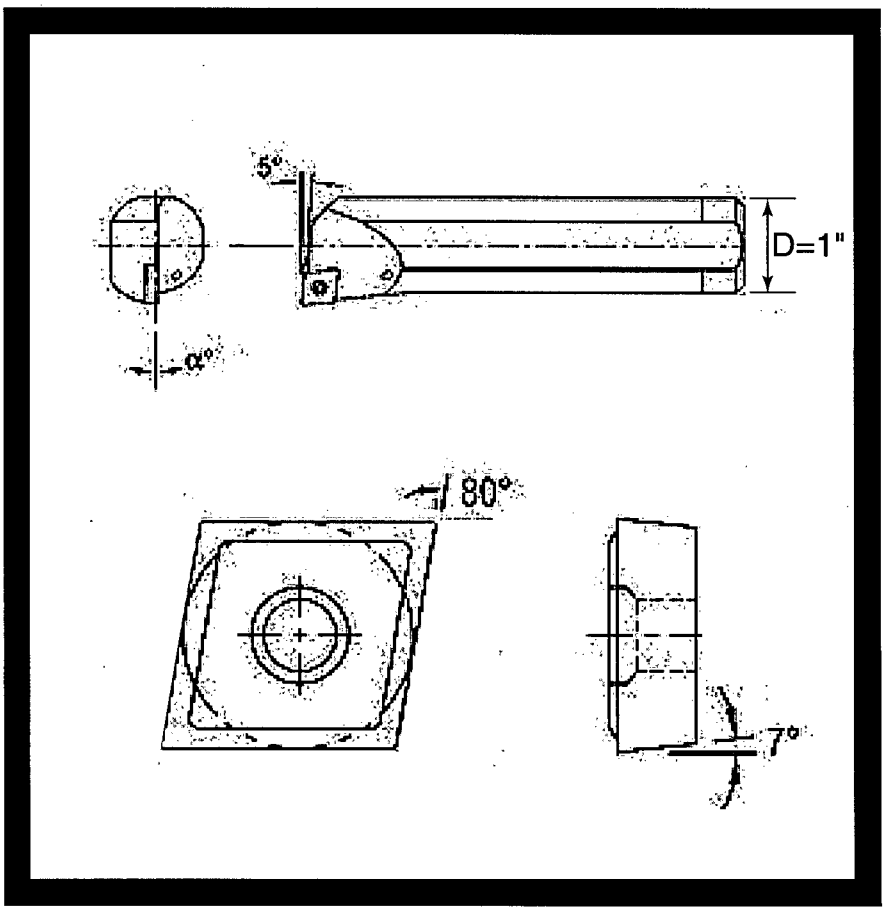

Figure 3.12 : Valenite CCGT432-FH 80° Carbide PVD coated diamond insert with A-SCLPR/L boring bar

3.3.1.3. Cutting Coefficient Identification

In this section, the development of the mechanistic force model is described in detail.

i-) Identification of the Edge Cutting Force Coefficients:

Tangential and friction cutting forces F_{tc}, F_{frc} are assumed to be proportional to the uncut chip area A [9].

$$F_{tc} = K_{tc}A \tag{3.11}$$

$$F_{frc} = K_{frc}A \tag{3.12}$$

This expression leads to the definition of the cutting force coefficients. Previous researchers reported that these coefficients vary with chip thickness h, cutting speed V, and geometrical properties of the tool, such as the side rake angle, the back rake angle and the relief angle [9, 16 and 17]. In this study, the previously proposed models have been modified such that cutting parameters, a, c, and V and the associated cutting edge contact length L_c, the uncut chip area A, and centroid of the uncut chip area geometry G, are used in the prediction of the cutting force coefficients and forces for the selected inserts (i.e. Kennametal CPMT-32.52 K720 and Valenite CCGT432-FH). In addition, the effective lead angle ϕ_L is predicted in order to find the direction of the friction force F_{fr}. Then, the radial and feed forces (F_r and F_f) are calculated as components of the predicted friction force.

Instead of chip thickness h, the depth of cut a and feed rate c are used in the model. This is because the cutting edge is an arc, due to the corner radius of the insert, rather than a straight line as in milling and orthogonal plunge turning. Hence, the chip thickness is not a constant but varies along the cutting edge contact length (Figure 3.13).

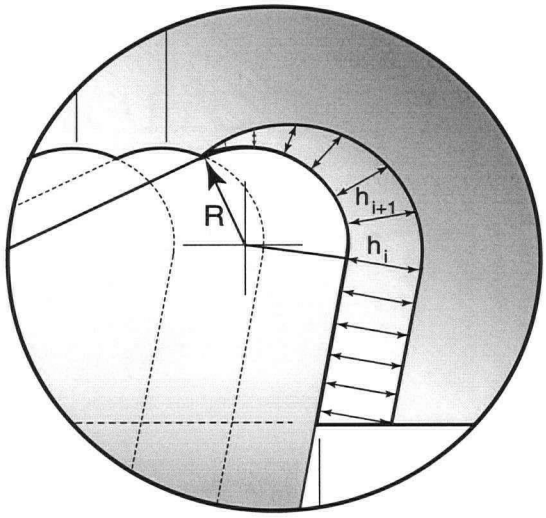

Figure 3.13 : Chip thickness variation along the corner radius of the tool

In the mechanistic modeling approach, the tangential cutting force coefficient K_{tc} is assumed to be a function of A $[mm^2]$ and V *[m/sec]*, whereas the friction cutting force coefficient K_{frc} is implemented as a function of the cutting edge contact length L_c and cutting speed V. It is proposed that the friction force is strongly dependent on the cutting edge contact length L_c, as the friction cutting force is generated by the friction on the cutting edge.

Cutting forces on the tool during machining consist of two components, which are the actual and the edge cutting forces [1] (Eq. 3.13). The actual cutting forces (F_{tc} and F_{frc}) are induced by shearing on the shear zone. The edge cutting forces (F_{te} and F_{fre}) are caused by rubbing and ploughing on the cutting edge and do not contribute to the cutting process. The edge cutting force components are functions of the cutting edge contact length L_c and the edge cutting force coefficients (K_{te} and K_{fre}) that represent the force for unit cutting edge contact length (i.e. 1[mm]).

$$F_t = F_{tc} + F_{te} = K_{tc}A + K_{te}L_c \tag{3.13}$$

$$F_{fr} = F_{frc_1} + F_{frc_2} + F_{fre} = K_{frc_1}A_1 + K_{frc_2}A_2 + K_{fre}L_c \tag{3.14}$$

where A_1 and A_2 are the uncut chip areas of Region 1 and Region 2 (Figure 3.14). F_{tc}, $F_{frc_{11}}$ and $F_{frc_{22}}$ are assumed to be proportional to the uncut chip area A. Unlike F_t, F_{fr} is considered as having two components acting in two separate regions of the uncut chip area, Region 1 and 2 (Figure 3.14) The reason for this separation is that for a small depth of cut the corner radius has a significant effect on the direction and magnitude of the friction force distribution. On the other hand, for large depths of cut, the straight edge of the insert, on which the magnitude and direction of the friction force distribution are constant, is predominant in the cutting operation. For comparatively large depths of cut, the direction of the total friction force ϕ_L tends to approach the side cutting edge angle γ_l of the insert. In such a case, the magnitude ratio of F_r/F_f decreases. For example, if the side cutting edge angle γ_l is zero, friction force F_{fr} does not contribute to F_r from Region 2, when a is selected larger than the nose radius R.

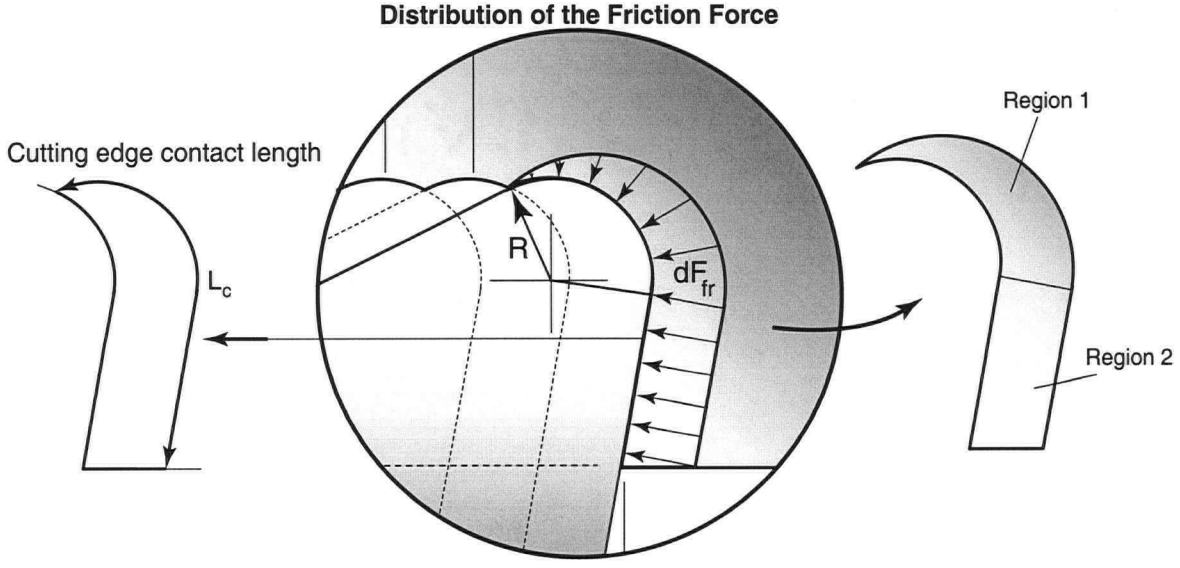

Figure 3.14 : Friction force distribution along the cutting edge

In order to determine the edge cutting force coefficients K_{te}, K_{re} and K_{fe}, 24 experiments have been conducted at constant *1.5[mm]* depth of cut and *150[m/min]* cutting speed but varying

feed rate c from *0.025* to *0.19 [mm/rev]*. Thereafter, linear regression was performed between the calibrated forces and the cutting edge contact length L_c. The following describes the method for predicting the edge cutting forces and their corresponding coefficients.

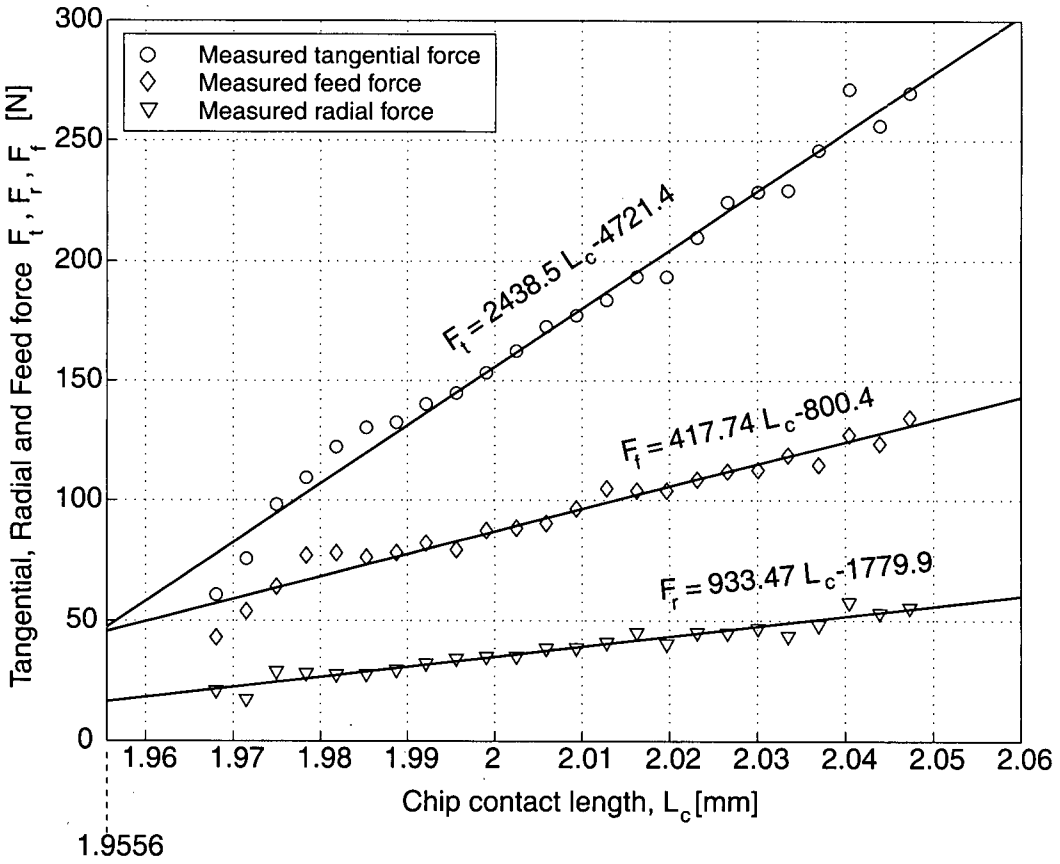

Figure 3.15 : Tangential, radial and feed force vs chip contact length

Performing linear regression leads to the following tangential force equation (Eq. 3.15). The first term on the right hand side corresponds to the actual tangential force component F_{tc}, and the second term is the tangential edge cutting force component F_{te}.

$$F_t = 2438.5L_c - 4721.4 \text{ [N]} \qquad L_c \geq 1.9556[mm] \tag{3.15}$$

where, L_c is the cutting edge contact length. This equation is valid only when L_c is equal to and greater than 1.9556 [mm], which corresponds to zero feed rate for a=1.5 [mm] depth of cut.

$c = 0$ *[mm/rev]* refers to the rubbing process on the cutting edge. Substitution of $L_c = 1.9556$ [mm] into the Eq. (3.15) gives F_{te} for the given a (1.5 [mm]) and zero feed rate.

$$F_{te} = F_t|_{L_c = 1.9556} = 47.41[N] \tag{3.16}$$

The tangential edge cutting coefficient K_{te} is determined dividing F_{te} by the total cutting edge contact length L_c.

$$K_{te} = \frac{F_{te}}{L_c} = 24.24\left[\frac{N}{mm}\right] \tag{3.17}$$

K_{te} represents the tangential rubbing force per unit cutting edge contact length L_c. Following the same procedure, the radial and feed edge cutting forces F_{re} and F_{fe} and corresponding edge cutting force coefficients K_{re} and K_{fe} are found as follows.

Table 3.1 : Edge cutting force coefficients for the Valenite CCGT432-FH insert

Expression	**Measured edge cutting forces** F_{te}, F_{re}, F_{fe} **[N]**	**Chip contact length,** L_c **[mm]**	**Edge cutting force coefficients** K_{te}, K_{re}, K_{fe} [N/mm]
$F_t = 2438.5L_c - 4721.4$	47.41	1.9556	24.24
$F_r = 417.74L_c - 800.40$	16.53	1.9556	8.45
$F_f = 933.47L_c - 1779.9$	45.58	1.9556	24.79

As the friction force F_{fr} is the compound of F_f and F_r, its edge cutting force and coefficient is calculated as follows.

$$F_{fre} = \sqrt{F_{re}^2 + F_{fe}^2} \tag{3.18}$$

$$K_{fre} = \sqrt{K_{fe}^2 + K_{re}^2} = 26.1928[N\backslash mm^2] \tag{3.19}$$

As can be noted that L_c does not change significantly with feed rate c, thus the effect of the c on edge cutting forces is negligible. The dependence of the edge cutting forces on the cutting speed V has also been investigated with a series of experiments. In these experiments, depth of cut was taken constant *1.0[mm]* but various feed rates, within the range of *0.015 to 0.14 [mm/*

rev], at three different cutting speeds V (75, 150 and 250 [m/min]), were employed. This investigation has been carried out with a *Kennametal* tool, and therefore, the edge cutting force coefficients cannot be compared with those presented above for the *Valenite* insert. The results are shown below in Figure 3.16. As noticed, the edge cutting forces at three different cutting speeds have almost the same magnitude and can be assumed to be independent of the cutting speed.

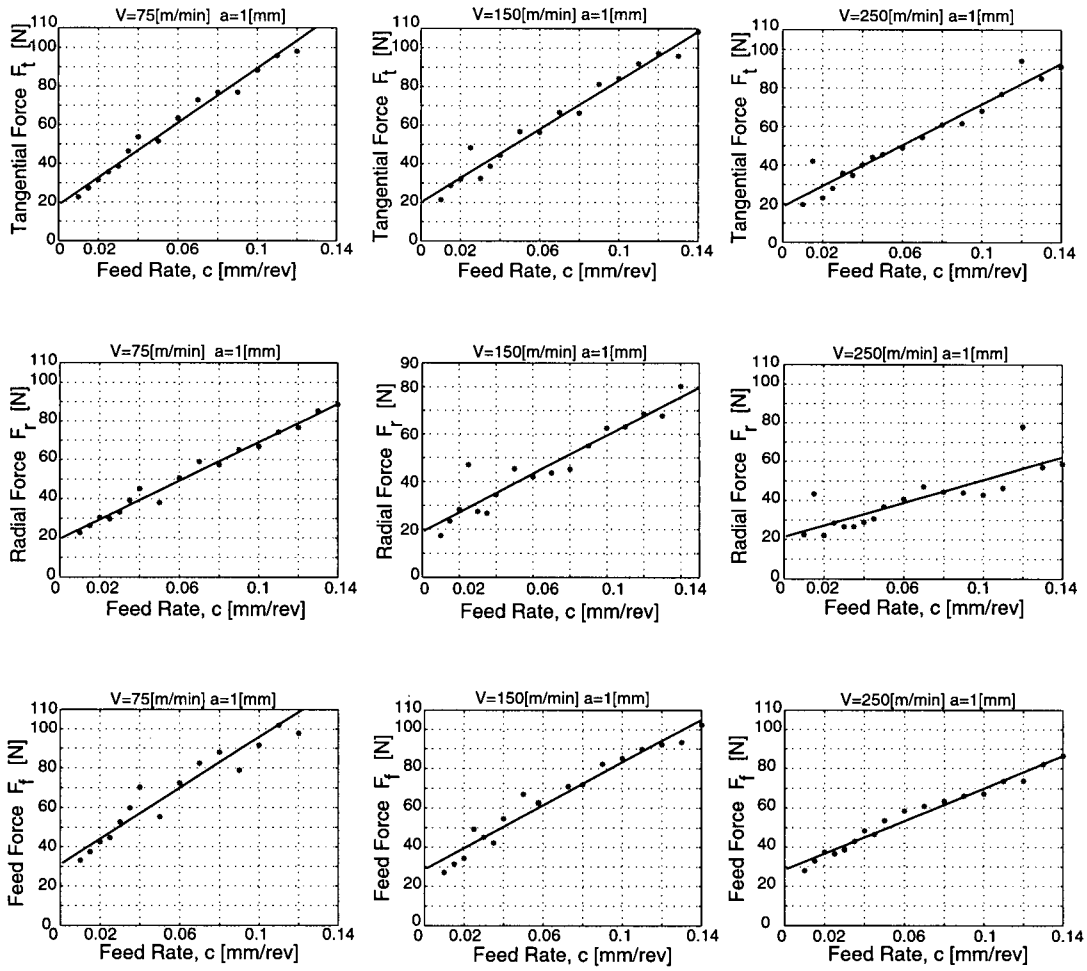

Figure 3.16 : Investigation of the dependence of the edge cutting forces on the cutting speed V; Material: Aliminum 6061-T6, Tool: Kennametal CPMT-32.52 K720 coated insert

ii-) Identification of the Cutting Force Coefficients for Valenite CCGT432-FH Insert

Experimental calibration tests showed that K_{tc} and K_{frc} change exponentially with uncut chip area A, cutting edge contact length L_c and cutting speed V. This variation can be represented with the following equations.

$$K_{tc} = e^{b_0} A^{b_1} V^{b_2} \tag{3.20}$$

$$K_{frc_1} = e^{m_0} L_{c_1}^{m_1} V^{m_2} \qquad K_{frc_2} = e^{n_0} L_{c_2}^{n_1} V^{n_2} \tag{3.21}$$

where, b_0, b_1, b_2, m_0, m_1, m_2, n_0, n_1 and n_2 are empricial constants, and estimated using the least squares method based on the experimental data (See Appendix C). For least squares estimates, cutting coefficients calculated from the experimental data were used. After processing the data, the following equations were obtained.

$$K_{tc} = e^{7.9477} A^{-0.0853} V^{-0.2750} \tag{3.22}$$

$$K_{frc_1} = e^{8.1965} L_{c_1}^{-0.6737} V^{-0.4210} \tag{3.23}$$

$$K_{frc_2} = e^{9.6152} L_{c_2}^{-0.0241} V^{-0.7597} \tag{3.24}$$

Once the friction cutting force coefficients K_{frc_1} and K_{frc_2}, the uncut chip area A and cutting edge contact length L_c are determined, the radial F_r and feed forces F_f are predicted as components of the friction force F_{fr}. However, this requires that the friction force direction, which is defined with the effective lead angle ϕ_L, to be known. The prediction of the effective lead angle consists of two steps. As mentioned above, the uncut chip area A is divided into two regions and the friction cutting force F_{frc} has been expressed separately (F_{frc_1} and F_{frc_2}), for each region for an accurate prediction.

In the above equations, the cutting force coefficients change inversely as functions of the uncut chip area A, cutting edge contact length L_c, and cutting speed V. The variations of the cutting force coefficients with uncut chip area and cutting edge contact length represent the effects of the tool geometry on the cutting forces. The relationship between the cutting force coefficients

and, the uncut chip area A and cutting edge contact length L_c is nonlinear, due to the corner radius of the tool and the chip breaking groove along the cutting edge. On the other hand, the decrease of the cutting force coefficients with cutting speed is induced by the reduction in the maximum shear strength of the material at high speeds. The material tends to soften and shear strength diminishes at high speeds, causing the cutting forces to lessen. As noted, the effect of each parameter in the equations of each cutting force coefficient is different. For the depths of cut which are larger than the corner radius R, the effect of the cutting edge contact length on the friction cutting force coefficient K_{frc_2} is not as significant as compared to the case in which the depth of cut is less than R. This may be because the straight side of the tool dominates the cutting process for the larger depths of cut. Thus, the friction cutting force coefficient K_{frc_2} does not change much with the depth of cut, due to the homogeneity of the friction force distribution on the straight side of the tool.

Since the friction force acts perpendicular to the cutting edge and is also proportional to the uncut chip area for each differential element along the cutting edge, it can be predicted by assuming that each component of the friction force passes through the gravity center of each related region (Figure 3.18). The friction force component of each region is added up vectorially, and the total friction force F_{fr} is obtained. It should be noted that these vectorial friction force components are presented with the notation $F^*_{fr_1}$, $F^*_{fr_2}$ (Figure 3.18) and are not identical to the ones in the Eq. (3.14). F_{fr_1} and F_{fr_2} in Eq. (3.14) are the components contributing from each region to the total friction force, and do not have vectorial meanings.

The determination of the centroid of the uncut chip area is shown in the following equation, as an example. The calculation is executed with respect to the origin of the corner radius C_2 for a given tool position (Figure 3.17).

$$\theta_G = \frac{\sum_{i=1}^{n} A_i \theta_i}{A_T} \tag{3.25}$$

where A_i, θ_i, and A_T are the area of a differential element, angular position of the differential element and the total area of the region, respectively.

Based on the definition of the friction force direction, the regional lead angle ϕ_{L_2} in Region 2 can be assumed to be equal to the side cutting edge angle γ_l of the tool along the straight line of the cutting edge. The total effective lead angle is determined from the sum of two friction force vectors (Figure 3.18).

After processing the data, analysis has shown that there were certain discrepancies between measured and predicted effective lead angles based on the above approach (Figure 3.14). This may be because the friction force F_{fr} is not really acting perpendicular to the cutting edge. This could be caused by the chip breakage groove along the cutting edge, or the assumption of the perpendicularity of the friction force to the cutting edge is not accurate. The difference between the measured and predicted effective lead angle ϕ_L has been investigated with two sets of 5 experiments, varying the cutting edge contact length L_c and cutting speed V (Figure 3.20). This investigation has revealed that the effective lead angle shows linear variation with V and L_c. Hence, it can be tuned in the calculation with a modification factor K_m that is also a linear function of L_c and V.

$$\phi_L = K_m \phi_L^* \tag{3.26}$$

where ϕ_L^* is the predicted effective lead angle based on the regular procedure described above and ϕ_L is the final modified-predicted effective lead angle. For the same five experimental conditions, the variation of the modification factor K_m depending on the cutting speed V and the

cutting edge contact length L_c is depicted in Figure 3.19. Graphical representation of the modified-predicted effective lead angle ϕ_L is shown in (Figure 3.21).

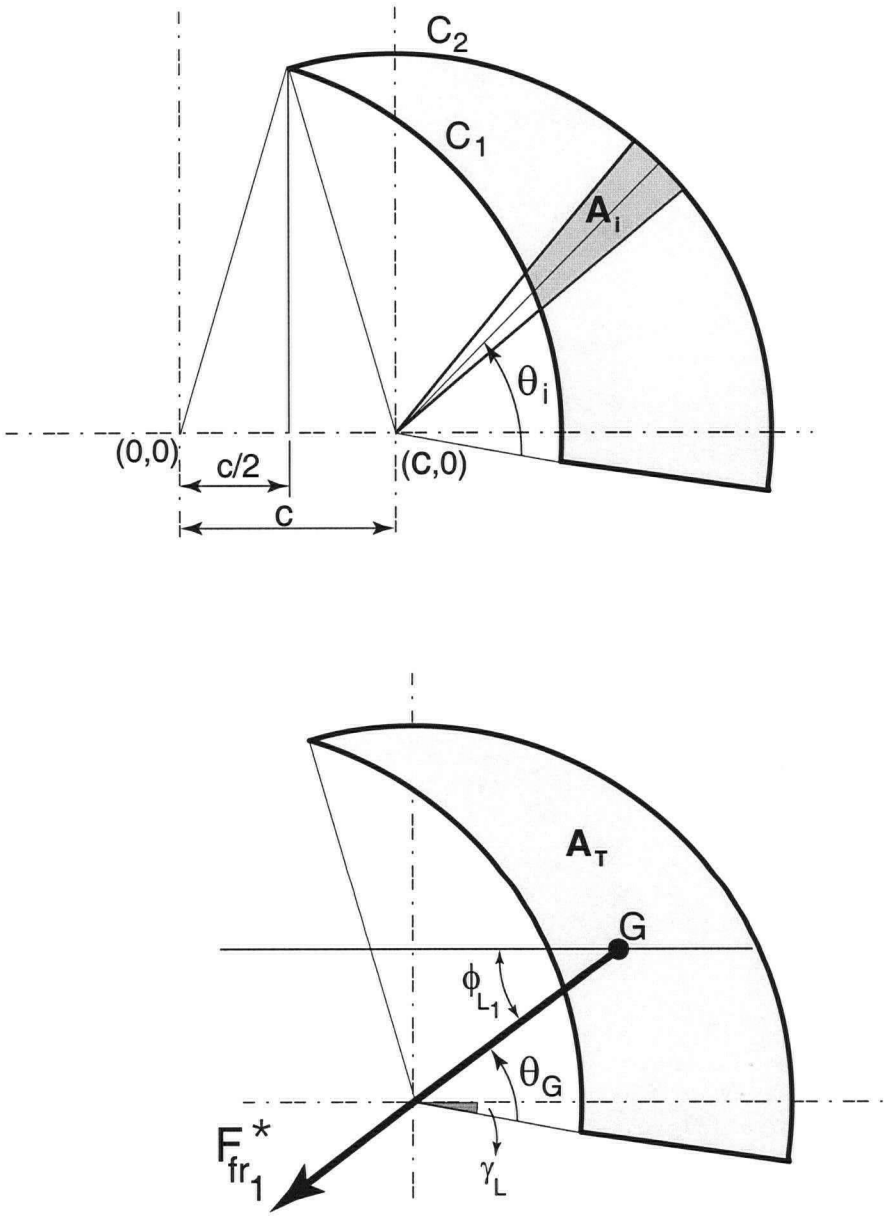

Figure 3.17 : Determination of the centroid of region 1

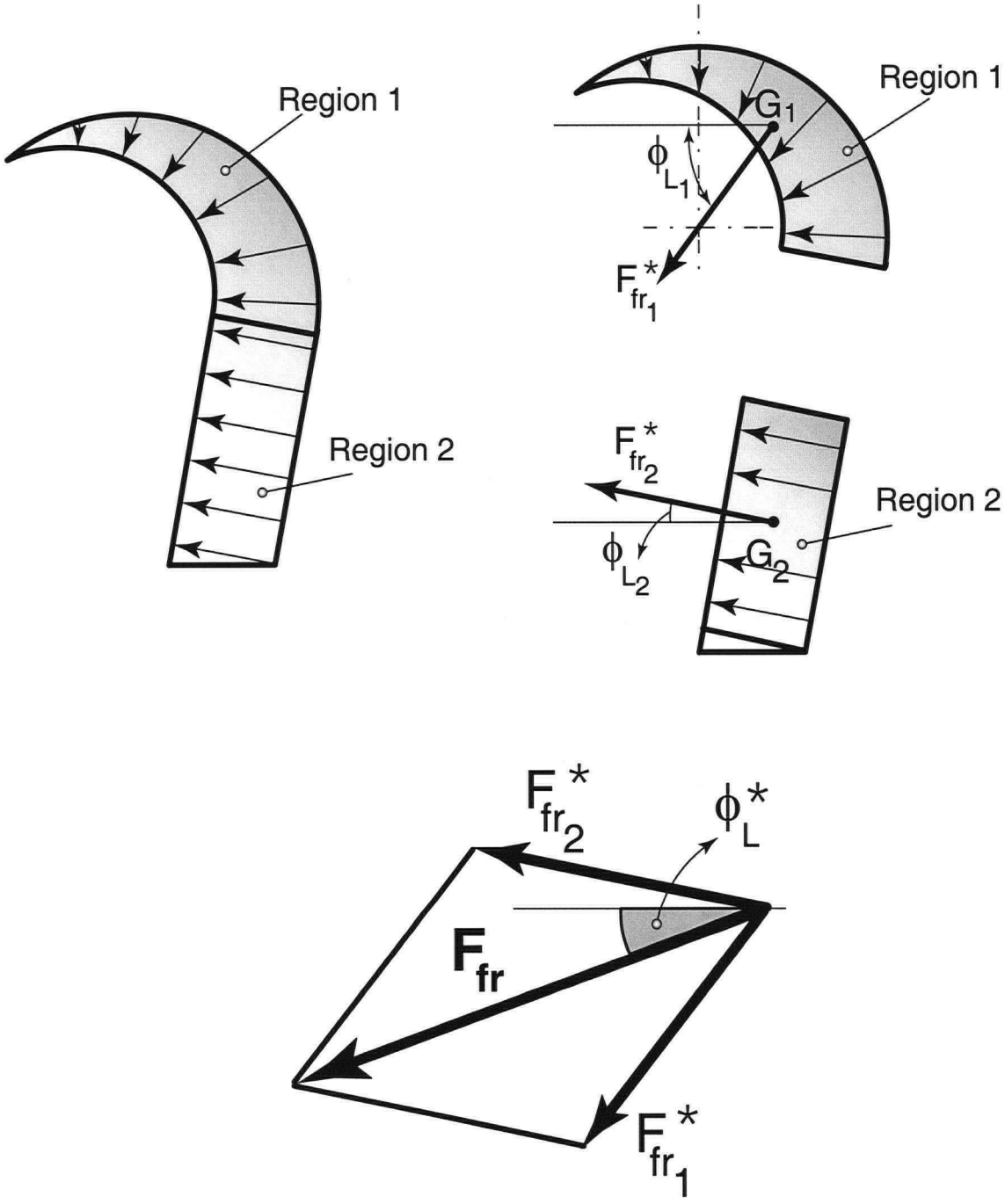

Figure 3.18 : The Effective lead angle ϕ_L prediction

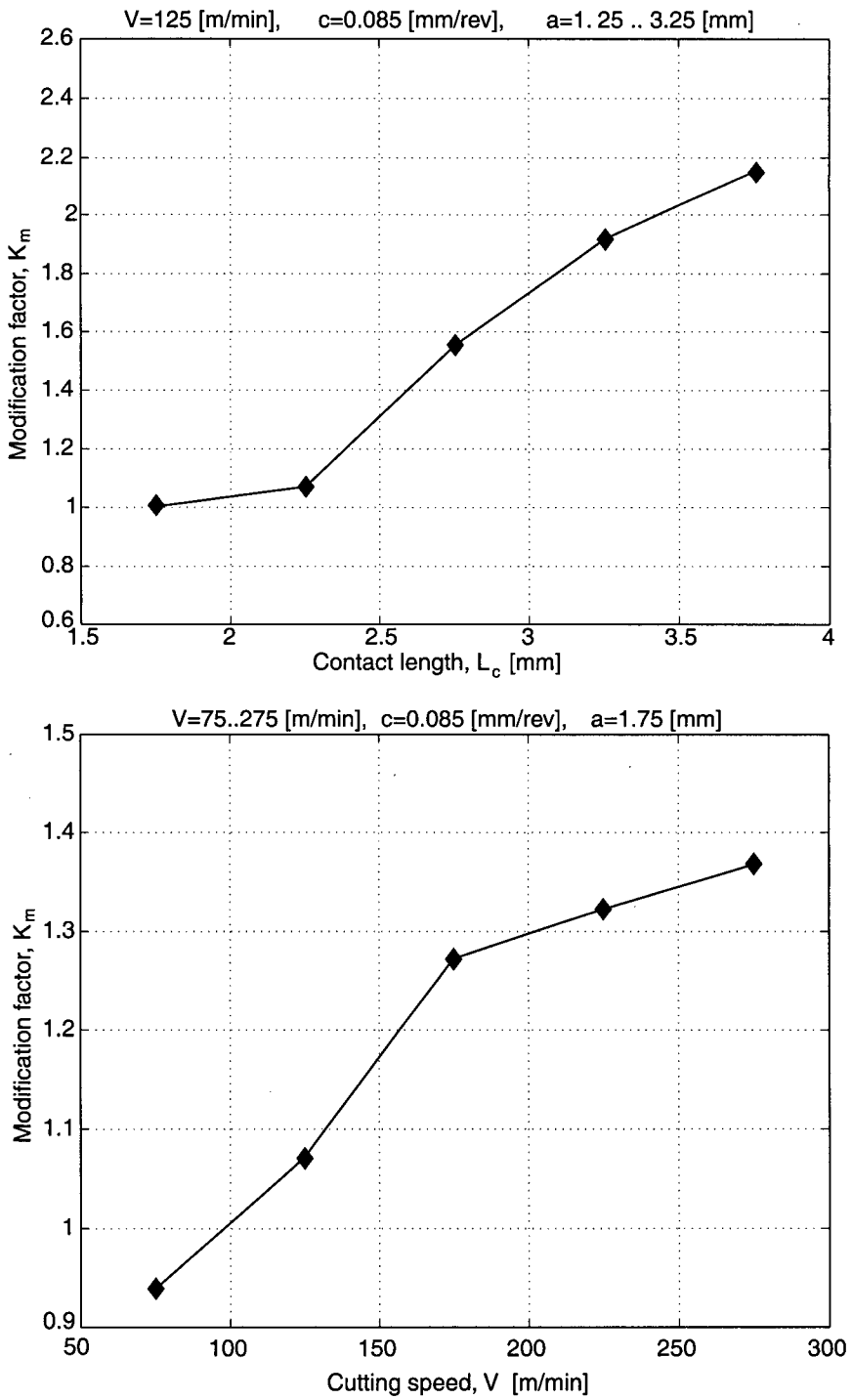

Figure 3.19 : Investigation of the variation of the effective lead angle modification factor K_m; K_m v.s V and L_c

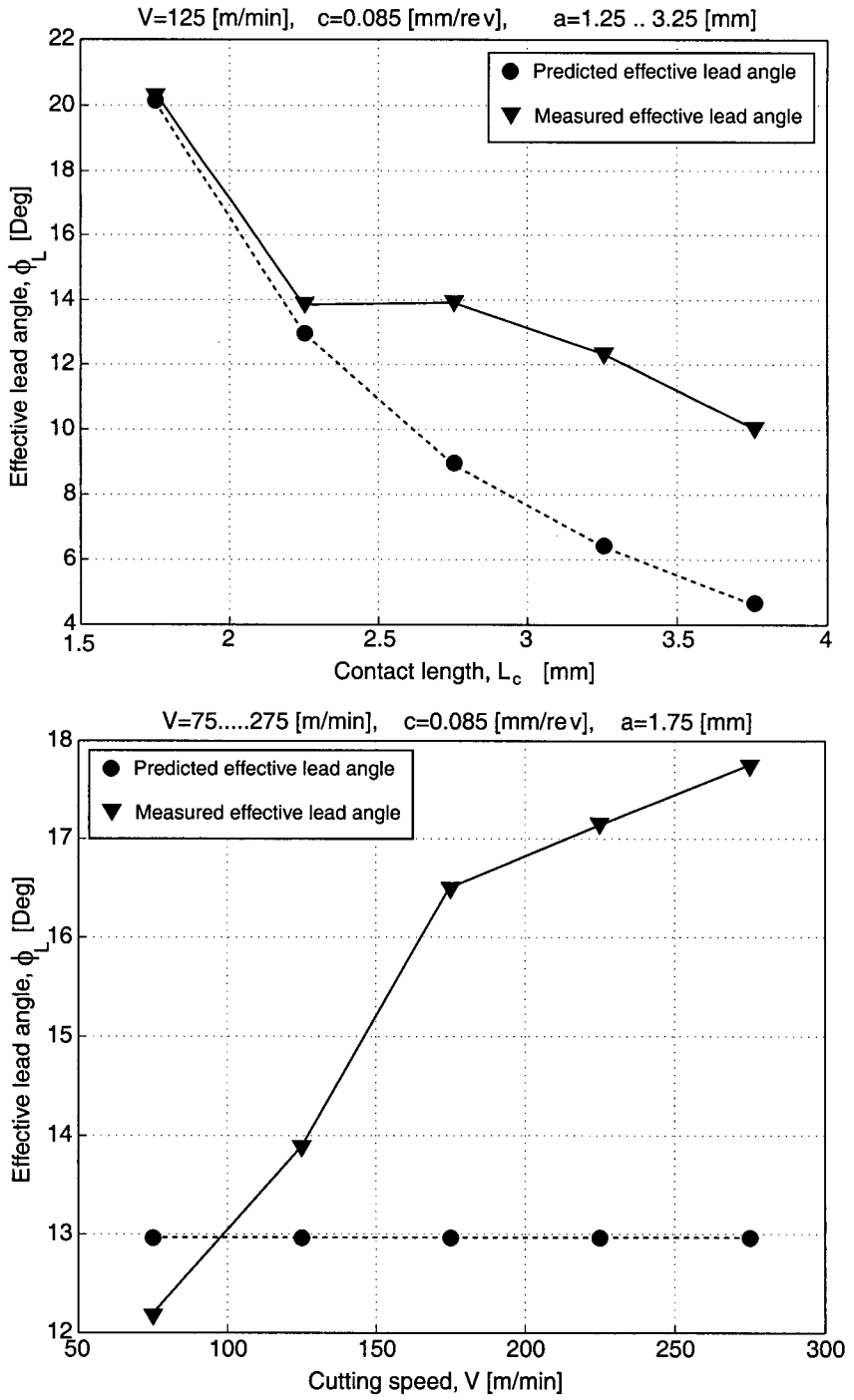

Figure 3.20 : Investigation of the Effective lead angle variation; ϕ_L v.s L_c and V

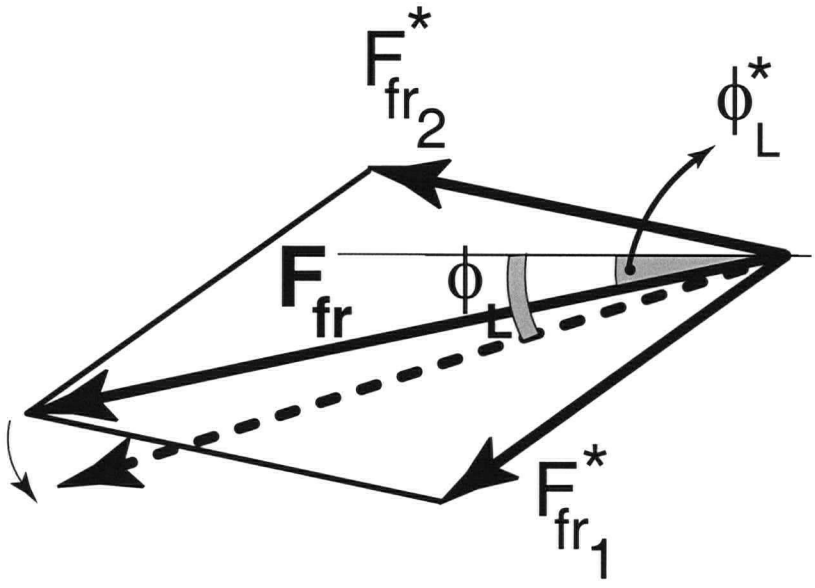

Figure 3.21 : Graphical representation of the predicted-modified effective lead angle

With the information obtained from the above investigation, the modification factor can be represented with the following expression.

$$K_m = q_0 + q_1 L_c + q_2 V \tag{3.27}$$

where q_0, q_1 and q_2 are the empirical constants and determined for the conditions $a < R$ and $a \geq R$ separately from the experimental data by performing the least squares method. This results in the following linear equations.

$$K_{m_1} = 1.0743 - 0.3567(10)^{-3} L_c + 0.9763(10)^{-4} V \text{ , for } a < R \tag{3.28}$$

$$K_{m_2} = -0.0163 + 0.6299 L_c + 0.0013 V \text{ , for } a \geq R \tag{3.29}$$

The above identified modification factors show that, for $a < R$, the effective lead angle ϕ_L has an almost constant deviation along the cutting edge contact length (i.e. the effects of L_c and V are negligible) (Eq. 3.28) . However, for $a \geq R$ the deviation has a strong dependence on L_c and V. This may arise from the nature of the chip flow. For $a < R$, the chip attempts to flow towards the center of the corner radius with an almost constant deviation. However, along the straight edge, the chip is forced to flow away, towards the outside of the contact in the radial direction and with a continuously diverging friction force, causing the chip to curl. The divergence of the chip exhibits a continuous increase along the cutting edge and reaches a maximum at the end of the contact length. A schematic representation of the directional variation of the friction force is shown in Figure 3.22. It should be noted that the cutting edge contact length in Eq. (3.29) is the total contact length including Region 1.

The variations of the modification factors K_{m_1} and K_{m_2} are presented in Figure 3.23 for 0.25...0.8 [mm] and 0.8..3.25 [mm] range of the depth of cuts a, 0.1[mm/rev] of constant feed rate c and 150[m/min] of constant cutting speed V. In these figures, the variation of the modification factors is examined changing cutting edge contact length L_c only. In the figures, the modification factor K_m for the condition $a < R$ decreases insignificantly with the cutting edge contact

length L_c. The effect of L_c on K_{m_1} is less than 1%, and is therefore negligible for the condition $a < R$. On the other hand, the modification factor K_{m_2} for the condition $a \geq R$ exhibits strong dependence on the cutting edge contact length L_c varying from 1.0 to 2.57 for 0.8... 3.25[mm] depth of cut range. The reason behind this has been explained in the previous paragraph.

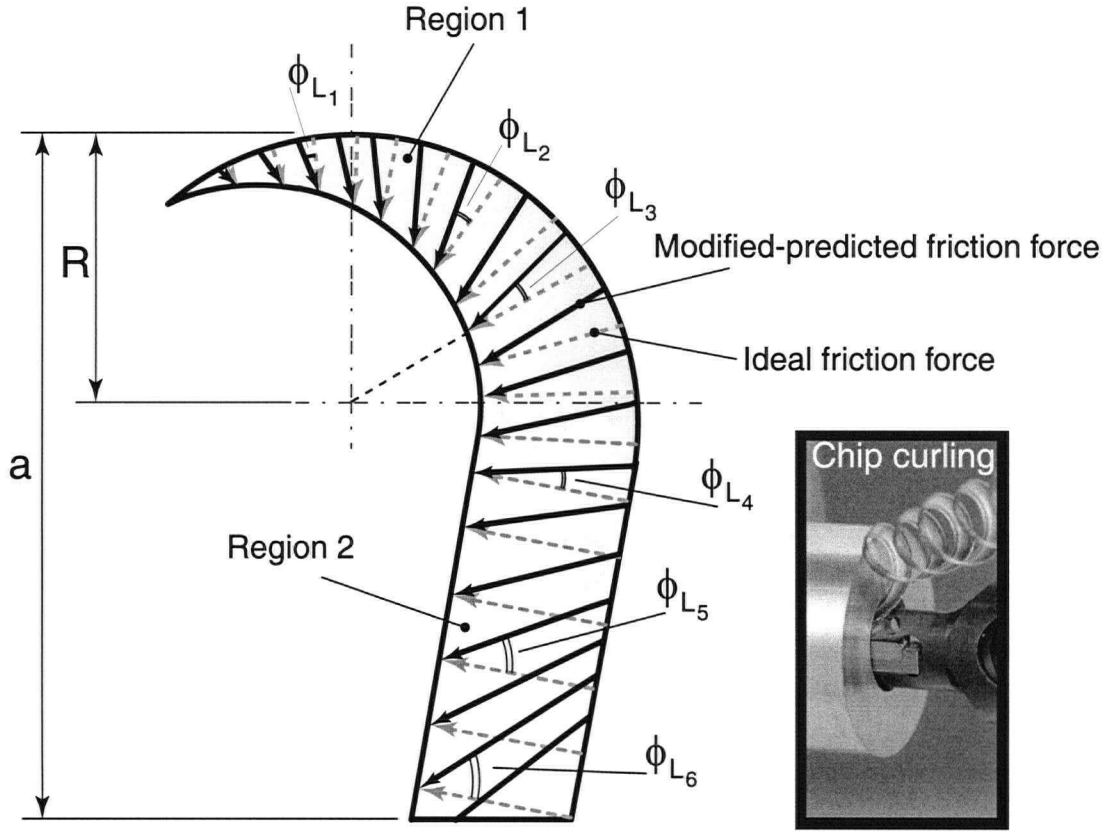

Figure 3.22 : Deviation of the effective lead angle ϕ_L along the cutting edge contact length

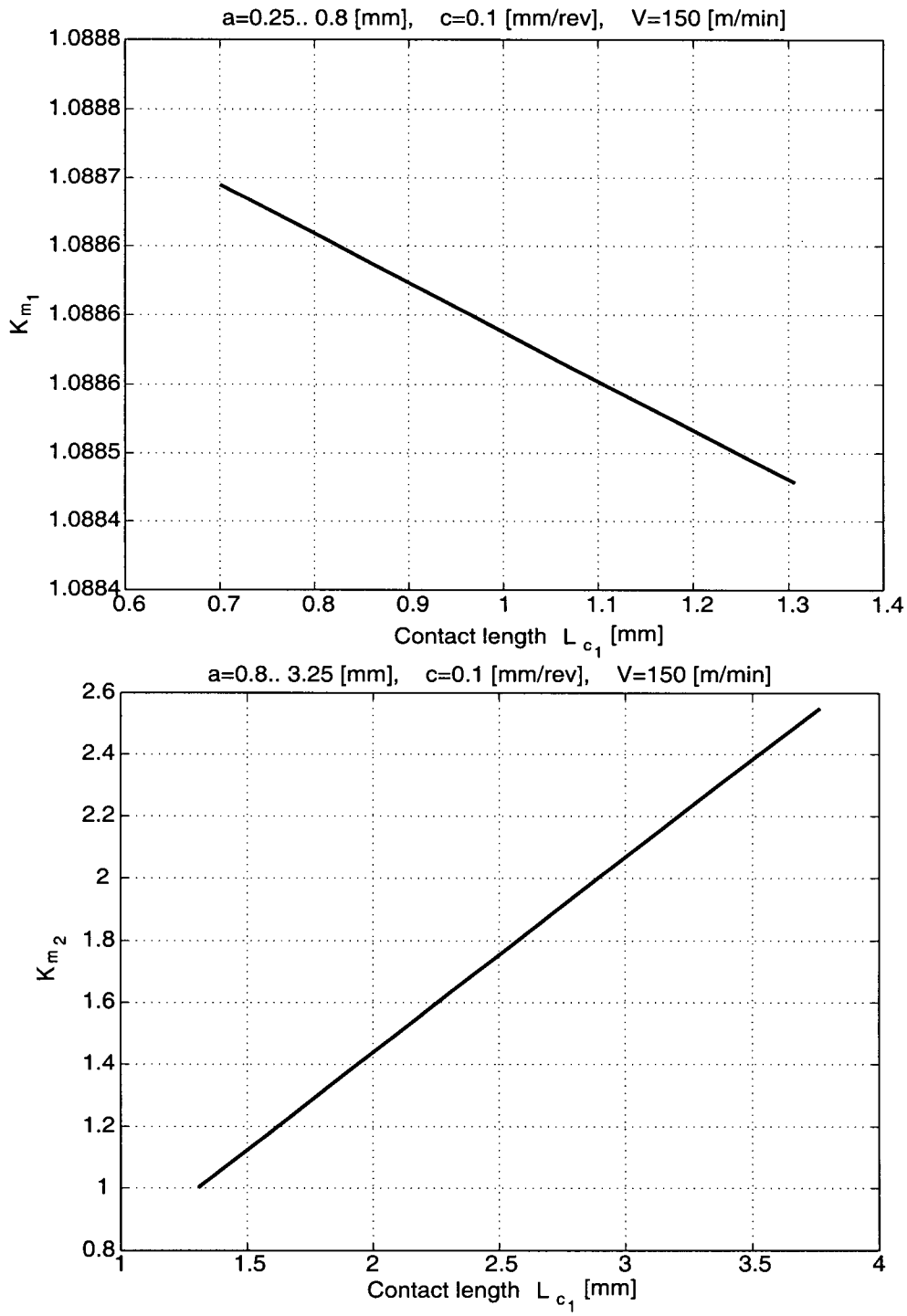

Figure 3.23 : Variation of the modification factor K_m with the cutting edge contact length for $a < R$ and $a \geq R$

It would also be possible to predict the effective lead angle through the direct use of cutting parameters, a, c and V. The goal of developing this approach is to find a generalized cutting force prediction model, so that the cutting forces can be predicted for both stable and unstable cutting conditions . Detail of this will be presented in chapter 5.

Once the above procedure has been completed, the radial and feed force predictions are made based on the predicted friction force F_{fr} and effective lead angle ϕ_L as follows.

$$\left.\begin{aligned} F_r &= F_{fr}\sin\phi_L \\ F_f &= F_{fr}\cos\phi_L \end{aligned}\right\} \tag{3.30}$$

Radial and feed actual cutting force components become,

$$F_{rc} = F_r - F_{re} \tag{3.31}$$

$$F_{fc} = F_f - F_{fe} \tag{3.32}$$

Corresponding cutting force coefficients are obtained as,

$$K_{rc} = \frac{F_{rc}}{A} \tag{3.33}$$

$$K_{fc} = \frac{F_{fc}}{A} \tag{3.34}$$

iii-) Cutting Force Coefficients of Kennametal CPMT-32.52 K720

Using the procedure presented above, the cutting force coefficients and effective lead angle modification factor for Kennametal CPMT-32.52 K720 insert have been obtained as follows.

$$K_{tc} = e^{8.0428} A^{-0.1696} V^{-0.2512} \tag{3.35}$$

$$K_{frc_1} = e^{7.7522} L_{c_1}{}^{-0.6093} V^{-0.2189} \tag{3.36}$$

$$K_{frc_2} = e^{9.3082} L_{c_2}{}^{0.0541} V^{-0.5470} \tag{3.37}$$

The effective lead angle modification factors,

$$K_{m_1} = 1.2963 + 0.0604L_c - 0.0006V, \quad a < R \tag{3.38}$$

$$K_{m_2} = -0.4138 + 0.7021L_c + 0.0025V, \quad a \geq R \tag{3.39}$$

Edge cutting force coefficients were determined by performing the linear regression method shown in Section 3.3.1.3.

$K_{te} = 13.777$ [N/mm], $K_{re} = 13.036$ [N/mm], $K_{fe} = 19.572$ [N/mm], $K_{fre} = 23.516$ [N/mm]

It can be noted that the trend of the variation of the cutting force coefficients and the effective lead angle modification factor depending on the parameters (i.e. cutting edge contact length L_c, cutting speed V, uncut chip area A) is similar to the ones for the Valenite insert, but only the empirical constants of these parameters are different. This is caused by the difference between the geometry of the two tools. The differences are;

- The Valenite tool has a $5°$ side cutting edge angle γ_l while the Kennametal insert's is $0°$.
- The Valenite tool has a $7°$ relief angle, while the Kennametal tool's is $11°$.
- The forms of the grooves on the two inserts are different.

All differences were considered in the determination of the empirical constants by performing the least-squares method.

3.3.1.4. Experimental Verification of the Mechanistic Model

In order to validate the mechanistic model, a different set of experiments was conducted under different cutting conditions from those used for the implementation of the mechanistic model expressions.

The presented model in the previous sections (3.3.1.1, ... 3.3.1.3) results in good force prediction with under 10% absolute average error, for both Valenite and Kennametal inserts. The tangential force F_t and friction forces for $a < R$ (F_{fr1}) and $a \geq R$ (F_{fr2}) are predicted with 99.5%, 93.5% and 98.4% correlations, respectively. The results of cutting force prediction for the Valen-

ite insert are presented in the following figures. Cutting conditions and prediction results are also shown in the tables in Appendix A.

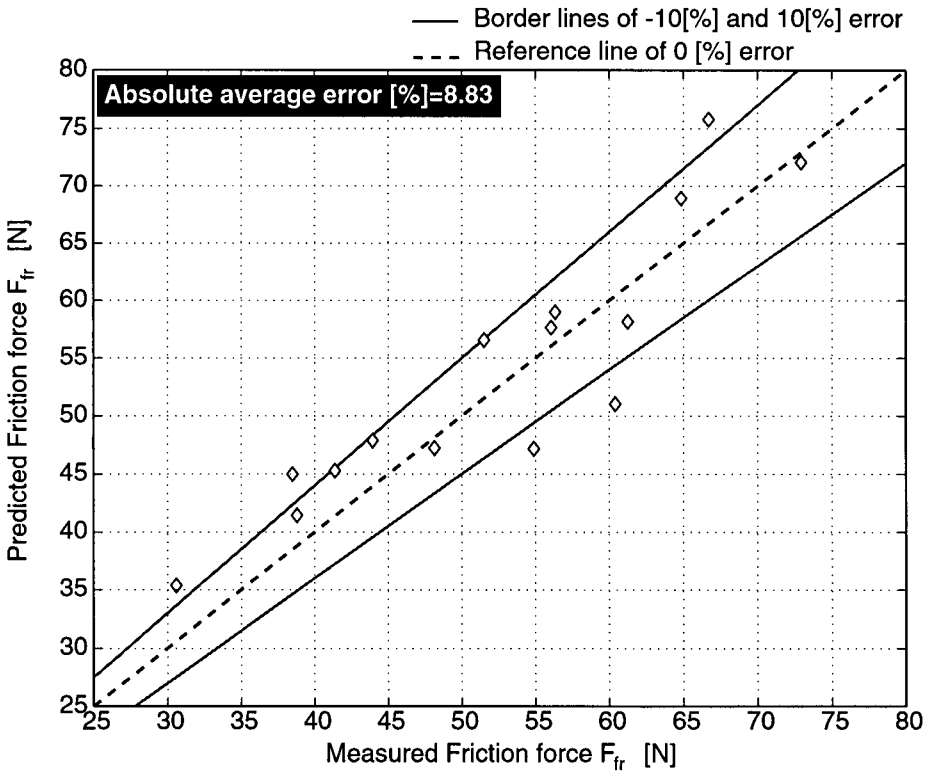

Figure 3.24 : Friction force verification for $a < R$

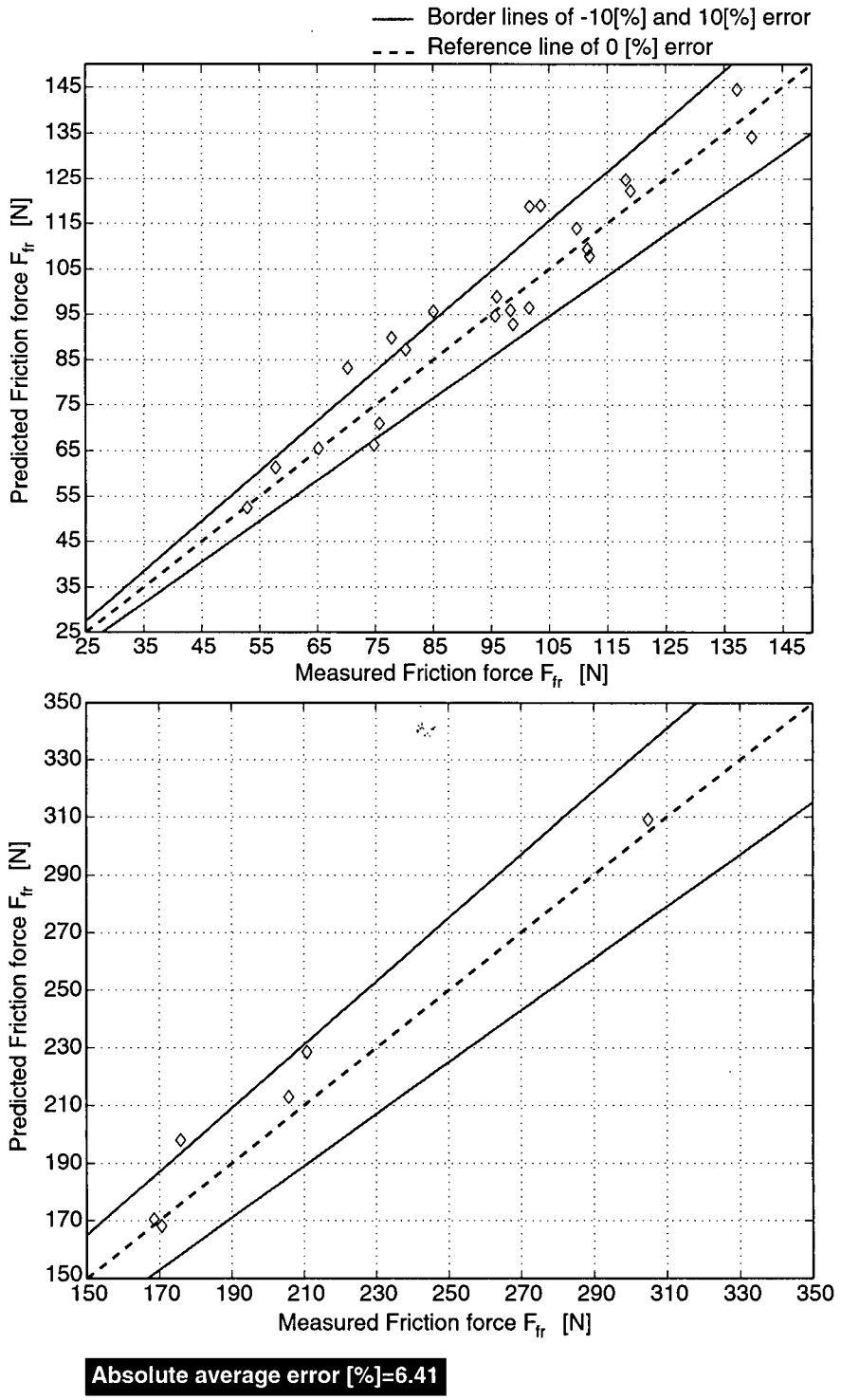

Figure 3.25 : Friction force verification for $a \geq R$

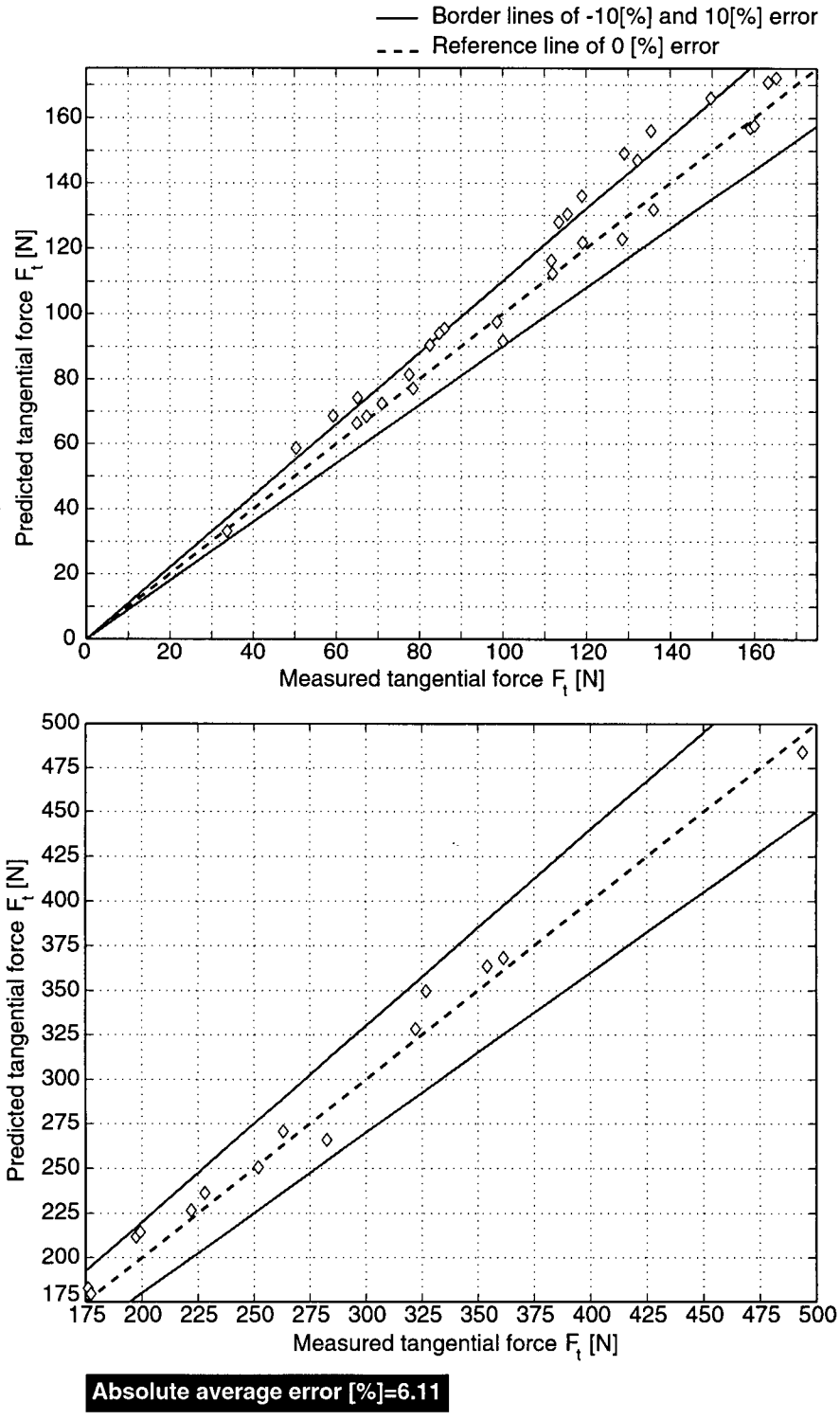

Figure 3.26 : Tangential force verification for a<R and $a \geq R$

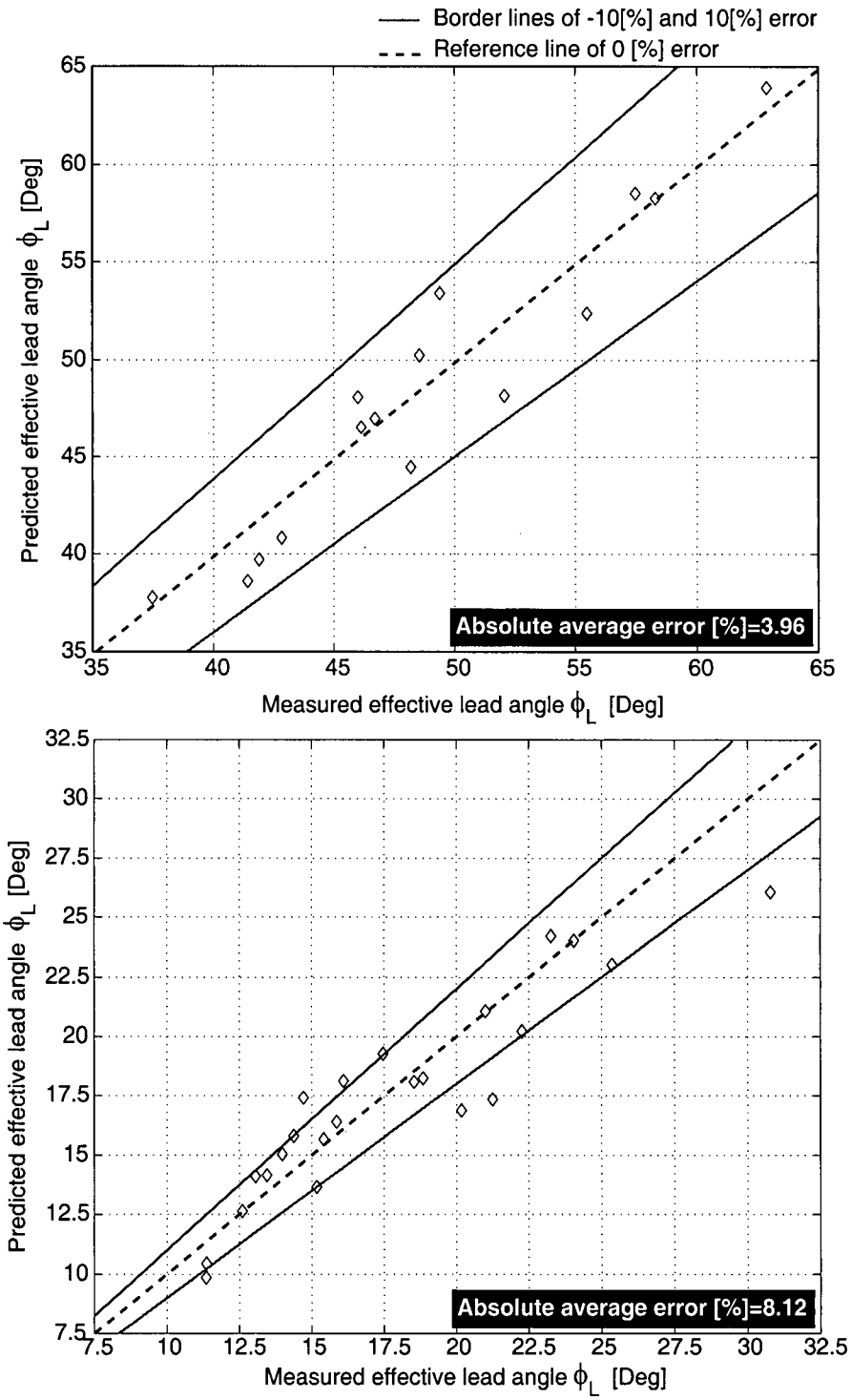

Figure 3.27 : Effective lead angle verification for a<R and $a \geq R$

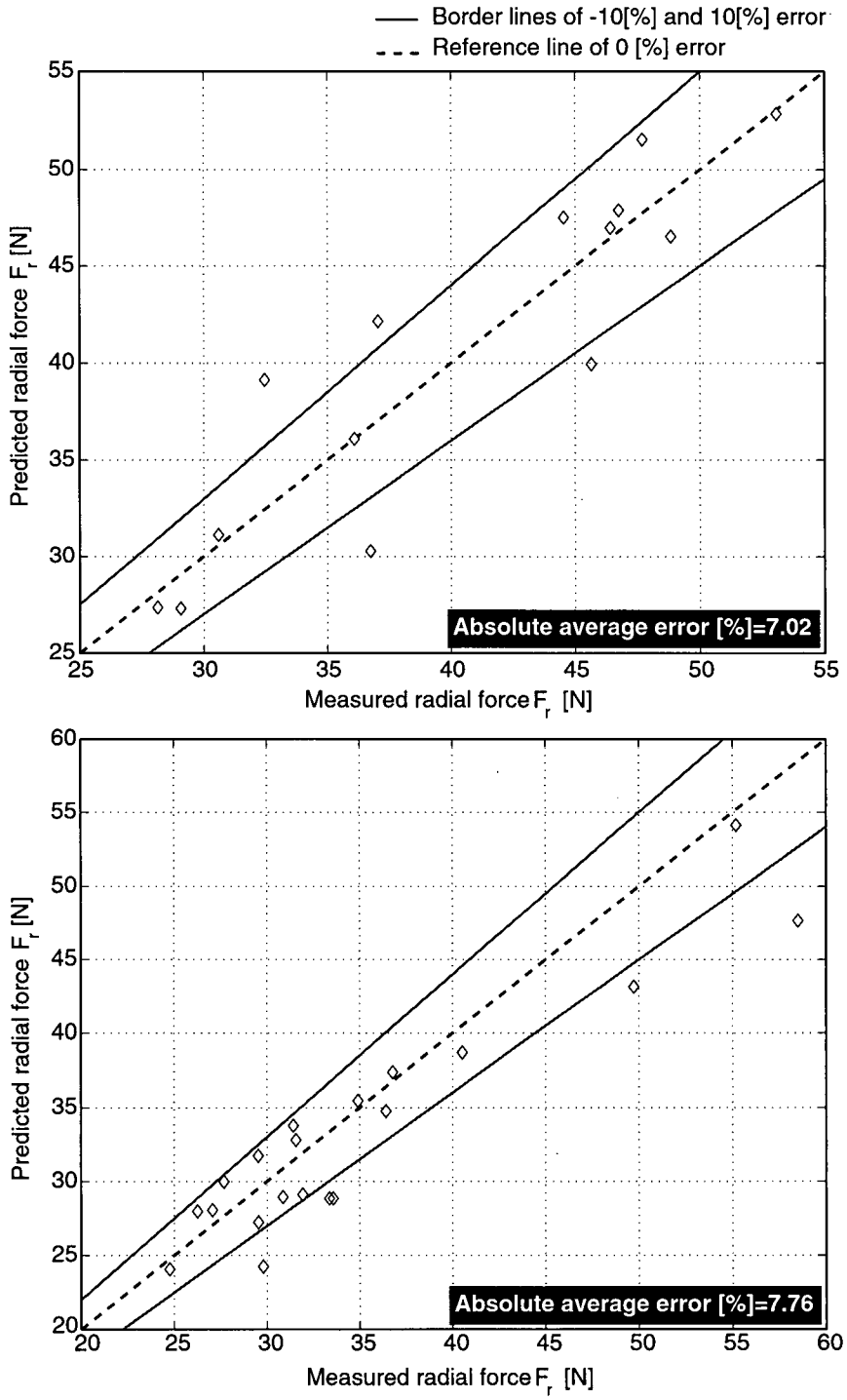

Figure 3.28 : Radial force verification for $a < R$ and $a \geq R$

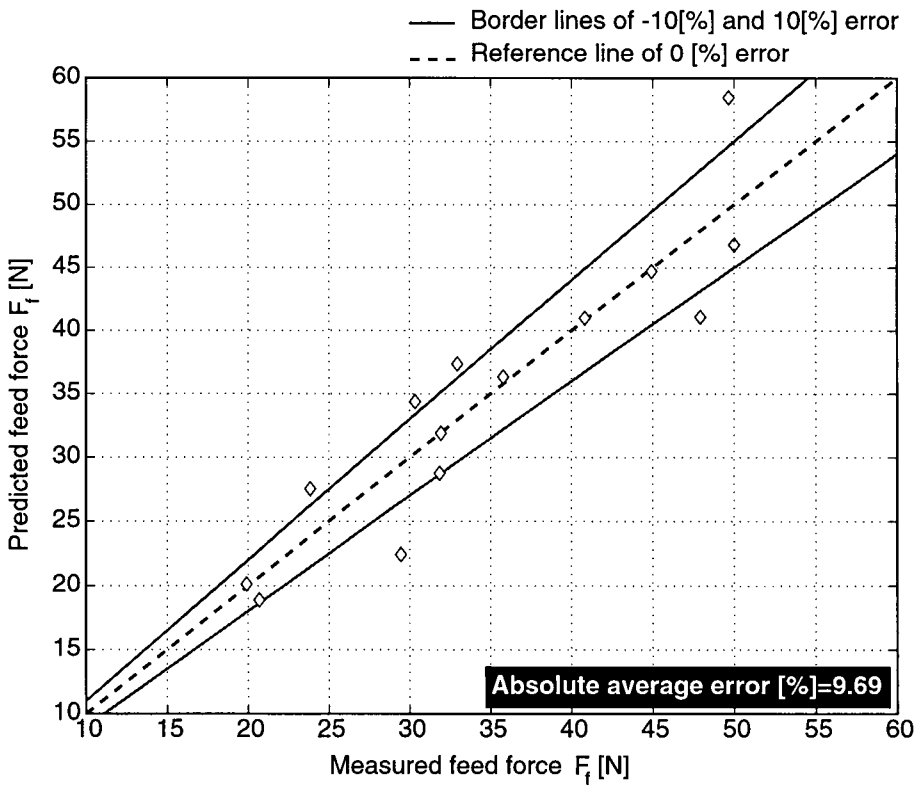

Figure 3.29 : Feed force verification for $a < R$

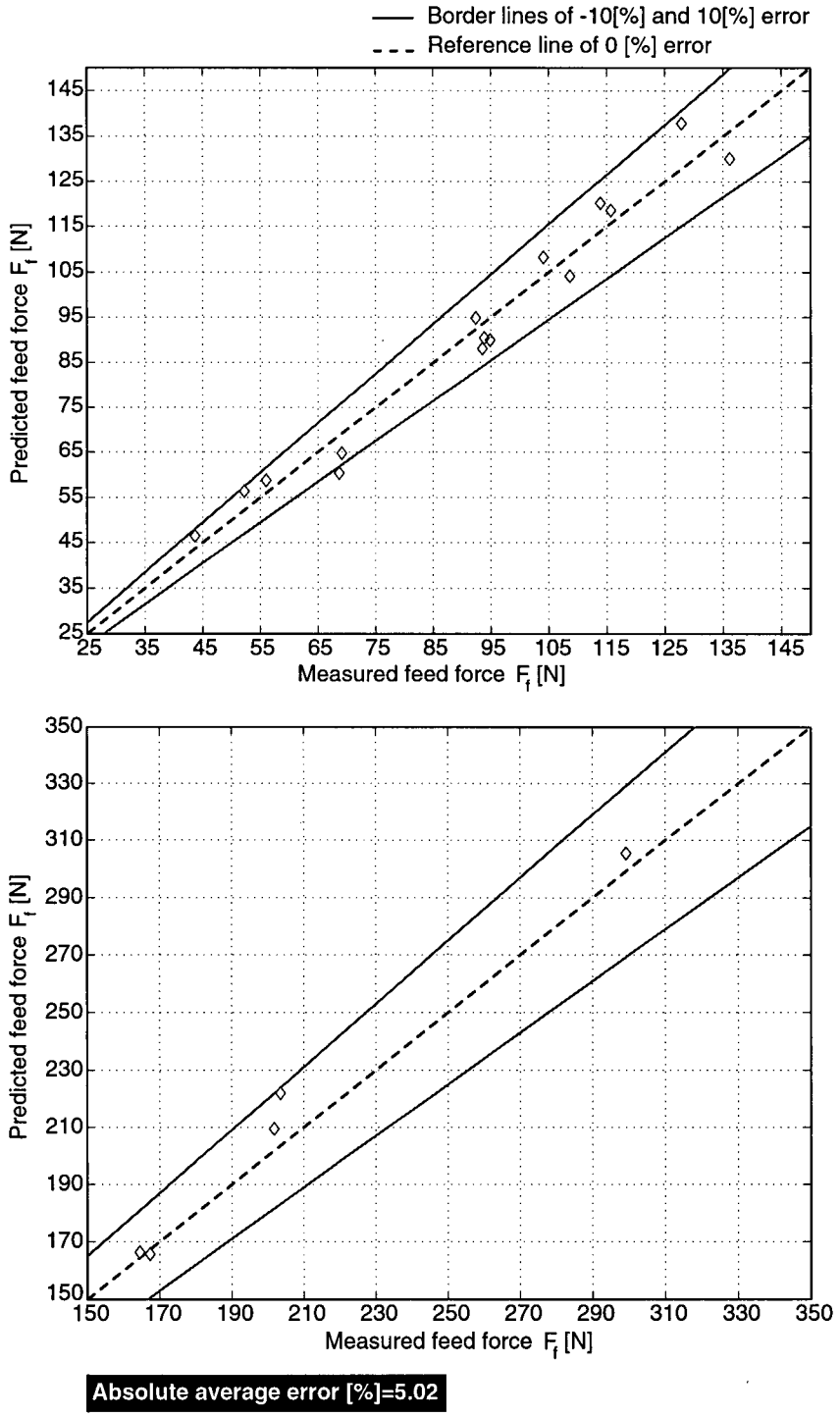

Figure 3.30 : Feed force verification for $a \geq R$

3.3.2. Orthogonal to Oblique Transformation Method

As mentioned in the earlier section, another method for predicting cutting force coefficients and forces in boring operations is to apply the *Orthogonal to Oblique Transformation Method,* as suggested in [1], [22] and [23]. The important parameters of the tool, which influence the force prediction and chip flow in the boring process, are the corner radius R, side cutting edge angle γ_l, end cutting edge angle γ_c, back rake angle α_p and side rake angle α_f (Figure 3.32). Among these parameters, rake angles have an important effect on controlling the direction of the chip flow and strength of the tool tip. Positive values of the rake angles reduce the cutting forces and temperature created on the tool. The corner radius of the tool causes oblique cutting parameters to change around the cutting edge. The effects of these parameters on the cutting forces can be examined with the *Orthogonal to Oblique Transformation Method.* The corner radius R also contributes to this process by making the tool tip stronger; It also has an effect on the surface finish quality. A larger corner radius results in a better surface finish, with less unwanted material left on the cut surface.

3.3.2.1. Orthogonal Cutting Test and Identification of Oblique Cutting Parameters

In the prediction of the cutting forces of a tool which has an oblique cutting geometry, the orthogonal cutting force coefficients K_{tc}, K_{te}, K_{fc}, K_{fe} and cutting parameters, such as chip ratio r_c, friction angle β_a, shear angle ϕ_c, shear stress τ_s, are identified for the specified workpiece-tool pair by performing orthogonal cutting tests. These parameters are then transfered to the oblique cutting geometry and cutting forces are predicted based on the method proposed in [1],[2], [22] and [23]. This is the fundamental concept of the *Orthogonal to Oblique Transformation Method.*

Orthogonal cutting tests are carried out with a tool which has specific rake and relief angles. In the tests, the workpiece rotates while the tool is fed linearly into the workpiece with the speed of the feed rate c [mm/rev]. The experimental setup is illustrated as in Figure 3.34. In orthogonal cutting tests, a tube material is utilized, instead of the shaft workpiece. It should also be noted that

the approach angle of the tool is supposed to be zero, in order for the process to be defined as orthogonal cutting. Tests are performed with varying feed rates c, at constant cutting speed V and width of cut b (corresponding to tube thickness). After the completion of the tests, linear regression is performed on the measured tangential and feed forces for the identification of the cutting and edge cutting force coefficients K_{tc}, K_{te}, K_{fc}, K_{fe}. This regression yields,

$$F_t = K_{tc}bh + K_{te}b \tag{3.40}$$

$$F_f = K_{fc}bh + K_{fe}b \tag{3.41}$$

where b and h are the width of cut and chip thickness, which is equal to the feed rate c. Later, the value of other parameters r_c, β_a, ϕ_c and τ_s for each orthogonal cutting test are determined with the following equations [2].

$$r_c = \frac{h}{h_c} \tag{3.42}$$

$$\beta_a = \alpha_r + \text{atan}\left(\frac{F_{fc}}{F_{tc}}\right) \tag{3.43}$$

$$\phi_c = \text{atan}\left(\frac{r_c\cos(\alpha_r)}{1 - r_c\sin(\alpha_r)}\right) \tag{3.44}$$

$$\tau_s = \frac{[F_{tc}\cos(\phi_c) - F_{fc}\sin(\phi_c)]\sin(\phi_c)}{bh} \tag{3.45}$$

where h_c and α_r are the cut chip thickness and the rake angle, respectively. Once the above parameters are obtained for each experimental condition, their calculated average values are used in the transformation method. These average values of the orthogonal cutting parameters developed at different cutting speeds V, rake α_f and relief angles ψ_r of the tool constitute the orthogonal cutting data base. For any tool whose cutting geometry can be defined as oblique cutting, this data base can be used for the force prediction without conducting any further calibration test.

Orthogonal cutting parameters, shear stress τ_s, friction angle β_a, and chip ratio r_c have already been identified by Ren [21] for carbide tools and P20 steel material as functions of feed rate c and cutting speed V. Correlations are given as follows.

$$\tau_s = 507.0 + 1398.76c + 0.327V \tag{3.46}$$

$$\beta_a = 33.69 - 12.16c - 0.022V \tag{3.47}$$

$$r_c = 0.227 + 2.71c + 0.00045V \tag{3.48}$$

where feed rate c, cutting speed V, shear stress τ_s and friction angle β_a are in the units of [mm/rev], [m/min], $\frac{N}{mm^2}$ and [Deg], respectively. Edge cutting coefficients K_{te}, K_{re} and K_{fe} have also been identified by Ren as presented in the following.

$$K_{te} = 0.1199(10)^{-3}V^2 - 0.1487V + 76.85 \tag{3.49}$$

$$K_{fe} = 0.1366(10)^{-3}V^2 - 0.2007V + 97.98 \tag{3.50}$$

$$K_{re} = K_{te}Sin(i) \tag{3.51}$$

where V and i are the cutting speed and oblique angle, respectively.

3.3.2.2. Prediction of the Oblique Cutting Forces

Once orthogonal cutting parameters are obtained, they are transferred to the oblique cutting geometry with the following assumptions [2].

1- The orthogonal shear angle is equal to the normal shear angle in oblique cutting $\phi_c \equiv \phi_n$

2- The normal rake angle in oblique cutting is equal to the rake angle in orthogonal cutting $\alpha_r \equiv \alpha_n$

3- The chip flow angle is equal to the oblique angle $\eta \equiv i$

4- The friction coefficient β_a and shear stress τ_s are the same in both orthogonal and oblique cutting for a given cutting condition.

Oblique tangential, radial, and feed cutting forces acting on the tool and cutting force coefficients are expressed in terms of cutting and geometrical parameters (i.e. width of cut b, chip

thickness h, oblique angle i, oblique shear angle ϕ_n, shear stress τ_s, friction angle β_n and normal rake angle α_n).

Cutting forces are expressed in the general form of,

$$F_t = K_{tc} bh + K_{te} b \tag{3.52}$$

$$F_r = K_{rc} bh + K_{re} b \tag{3.53}$$

$$F_f = K_{fc} bh + K_{fe} b \tag{3.54}$$

where oblique cutting force coefficients are defined as,

$$K_{tc} = \frac{\tau_s}{\sin\phi_n} \frac{\cos(\beta_n - \alpha_n) + \tan i \tan\eta \sin\beta_n}{\sqrt{\cos^2(\phi_n + \beta_n - \alpha_n) + \tan^2\eta \sin^2\beta_n}} \tag{3.55}$$

$$K_{fc} = \frac{\tau_s}{\sin\phi_n \cos i} \frac{\sin(\beta_n - \alpha_n)}{\sqrt{\cos^2(\phi_n + \beta_n - \alpha_n) + \tan^2\eta \sin^2\beta_n}} \tag{3.56}$$

$$K_{rc} = \frac{\tau_s}{\sin\phi_n} \frac{\cos(\beta_n - \alpha_n)\tan i - \tan\eta \sin\beta_n}{\sqrt{\cos^2(\phi_n + \beta_n - \alpha_n) + \tan^2\eta \sin^2\beta_n}} \tag{3.57}$$

In general, K_{te} and K_{fe} are determined in the evaluation of the orthogonal cutting test results. Because there is no radial force component measured in orthogonal cutting tests, K_{re} is not known. However, experimental investigations have shown that the radial cutting edge force F_{te} is very small and therefore negligible in the transfomation method.

3.3.2.3. Experimental Verification of the Method

Selecting an insert (Valenite CTPGPL-16-3C) with a nose radius, a sharp cutting edge, a flat rake face (Figure 3.33) , the *Orthogonal to Oblique Transformation Method* can be described for the boring process as follows. In this study the same uncut chip area configurations as in the mechanistic model has been considered, and a necessary force prediction program has been developed. Only the first configuration is presented in this section in order to demonstrate the procedure. The uncut chip area is divided into three regions (Region 1, 2 and 3, Figure 3.31). Region 1

then is discretized into equal angular segments θ_i in order for the transformation method to be applied. The reason for the discretization of the uncut chip area is that the oblique cutting geometry parameters vary in Region 1 along the cutting edge, due to the corner radius of the tool. However, in Region 2, the uncut chip area is uniform, and the oblique cutting parameters do not change with location. Thus, Region 2 is not discretized, but considered as one element in the evaluation. Similarly, Region 3 is considered as a whole element. For the selected *Valenite* tool, the back rake angle α_p and side cutting edge angle γ_l are zero, hence, the cutting in Region 2 and 3 cannot be characterized as an oblique cutting because there is no inclination angle between the cutting velocity vector and cutting edge of the tool. In such a case, the cutting process in Regions 2 and 3 is described as an orthogonal cutting , although the cutting in Region 1 is still oblique.

The uncut chip area and the oblique cutting geometry parameters for each discretized element are calculated with the following equations derived from the geometrical relations [2].

- REGION 1

- Uncut chip area, A_i Eq. (3.5)

- Approach angle $\psi_r = j\theta$, where j is the counter of differential elements and θ is the angular increment of each differential element.

- Orthogonal angle $\alpha_0 = \text{atan}(\tan\alpha_f \cos\psi_r + \tan\alpha_p \sin\psi_r)$, where α_f, α_p and ψ_r are the side rake angle, back rake angle and side relief angle respectively.

- Oblique angle $i = \text{atan}(\tan\alpha_p \cos\psi_r + \tan\alpha_f \sin\psi_r)$,

- Normal rake angle $\alpha_n = \text{atan}(\tan\alpha_0 \cos i)$, α_0 is orthogonal rake angle.

- Chip ratio Eq. (3.48)

- Normal shear angle $\phi_n = \text{atan}\dfrac{r_c \cos\alpha_n}{1 - r_c \sin\alpha_n}$, α_n is the normal rake angle.

- Friction angle Eq.(3.47)

- Normal friction angle $\beta_n = \text{atan}(\tan\beta_a \cos i)$

- Shear stress τ_s Eq. (3.46)

Substituting the necessary parameters into Equations (3.55), (3.56) and (3.57) tangential, radial, and feed cutting force coefficients, K_{tc}, K_{rc} and F_{fc} for each differential element are determined.

As can be noticed, the oblique cutting parameters change around Region 1 due to the variation of the approach angle ψ_r. Oblique radial and feed forces in Region 1 do not match the directions of the dynamometer (Y and Z) and need to be projected into dynamometer directions in order to obtain the total global forces in the three directions (Figure 3.35). For each differential element, oblique tangential, radial, and feed forces are expressed as,

$$\left.\begin{aligned} F_{t,i} &= K_{tc,i}A_{1,i} + K_{te}L_{c,i} \\ F_{r,i} &= K_{rc,i}A_{1,i} + K_{re}L_{c,i} \\ F_{f,i} &= K_{fc,i}A_{1,i} + K_{fe}L_{c,i} \end{aligned}\right\} \tag{3.58}$$

Then, the total forces in the dynamometer directions are calculated by adding together the forces acting on each differential element.

$$F_{x1} = \sum_{i=1}^{N} F_{t1,i} \tag{3.59}$$

$$F_{y1} = \sum_{i=1}^{N} [F_{f1,i}\sin(\theta_i) - F_{r1,i}\cos(\theta_i)] \tag{3.60}$$

$$F_{z1} = \sum_{i=1}^{N} [F_{f1,i}\cos(\theta_i) + F_{r1,i}\sin(\theta_i)] \tag{3.61}$$

-REGION 2

For Region 2 the same equations are used in the force prediction except the following.

- Uncut chip area Eq.(3.7)

- Approach angle $\psi_r = -\gamma_L$, γ_L is the side cutting edge angle of the tool.

Cutting forces in the dynamometer directions are found similarly.

$$F_{x2} = F_{t2} \tag{3.62}$$

$$F_{y2} = F_{f2}\sin(-\gamma_L) - F_{r2}\cos(-\gamma_L) \tag{3.63}$$

$$F_{z2} = F_{f2}\cos(-\gamma_L) + F_{r2}\sin(-\gamma_L) \tag{3.64}$$

-REGION 3

- Uncut chip area Eq. (3.8)
- Approach angle $\psi_r \cong -\frac{\gamma_L}{2}$

For this region the edge cutting force components are assumed to be zero due to the zero contact length. Cutting force components are obtained by using the same equations presented above.

$$\left.\begin{aligned} F_{t3} &= K_{te}A_3 \\ F_{r3} &= K_{re}A_3 \\ F_{f3} &= K_{fe}A_3 \end{aligned}\right\} \tag{3.65}$$

These oblique cutting forces contributed by region 3 are obtained as,

$$F_{x3} = F_{t3} \tag{3.66}$$

$$F_{y3} = F_{f3}\sin(-\gamma_L/2) - F_{r3}\cos((-\gamma_L)/2) \tag{3.67}$$

$$F_{z3} = F_{f3}\cos((-\gamma_L)/2) + F_{r3}\sin(-\gamma_L/2) \tag{3.68}$$

The total forces in dynamometer directions, X, Y and Z are found as,

$$F_X = F_{x1} + F_{x2} + F_{x3} \tag{3.69}$$

$$F_Y = F_{y1} + F_{y2} + F_{y3} \tag{3.70}$$

$$F_Z = F_{z1} + F_{z2} + F_{z3} \tag{3.71}$$

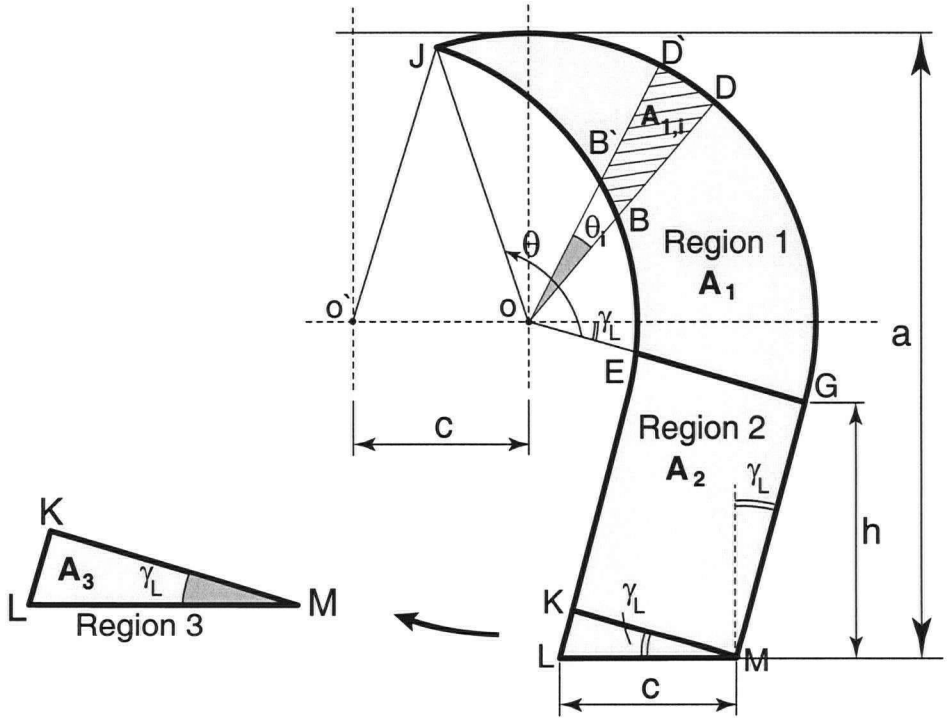

Figure 3.31 : Evaluation of the oblique cutting parameters for three regions of the uncut chip area

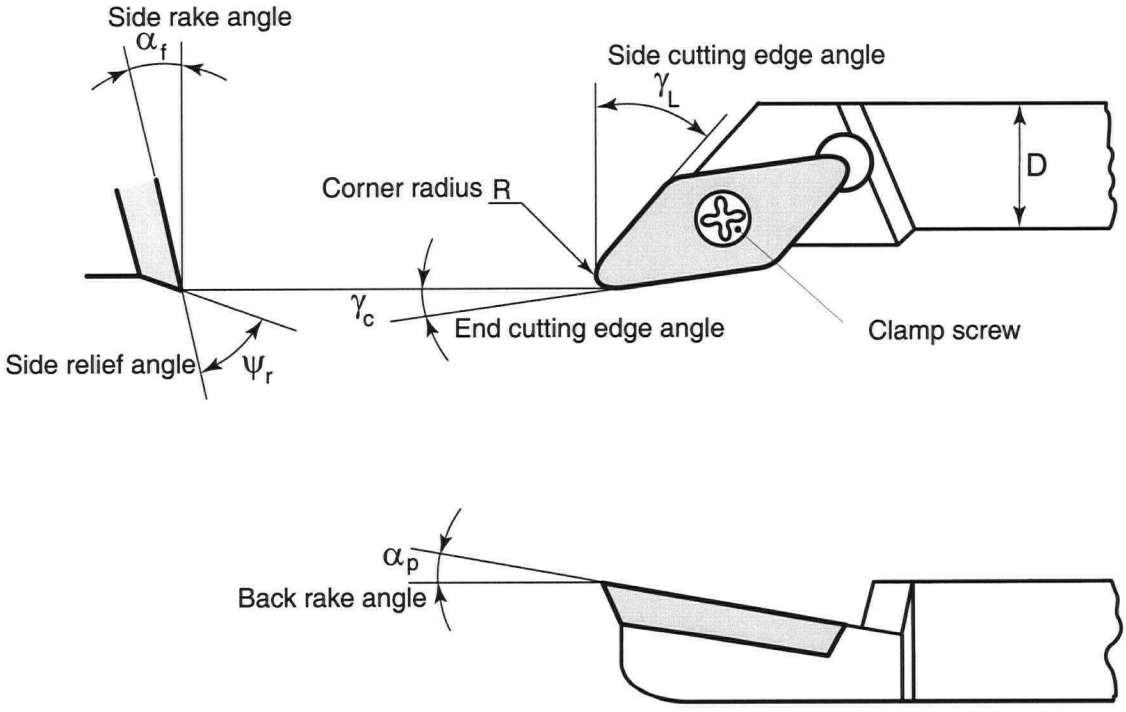

Figure 3.32 : Geometry of boring tool

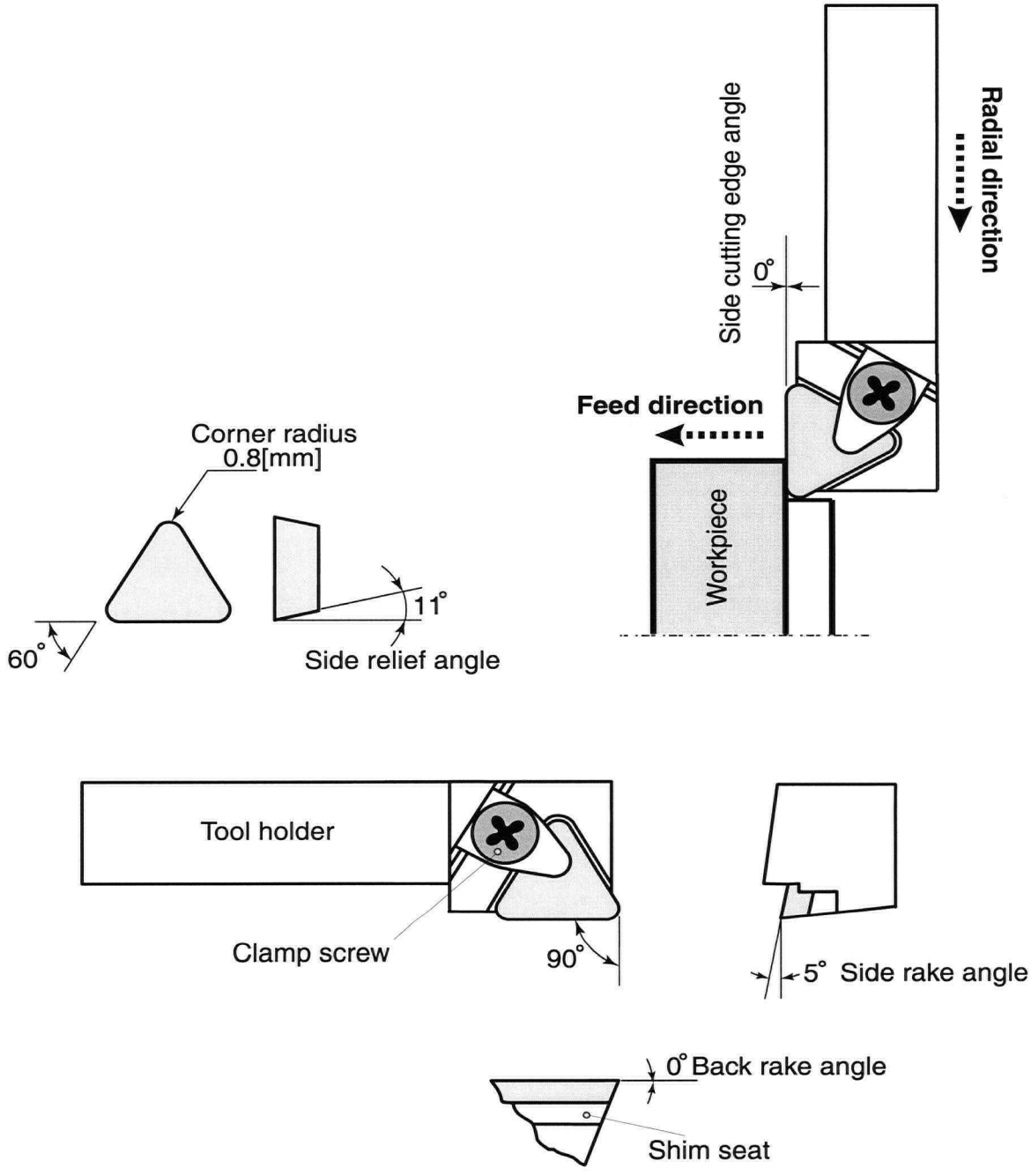

Figure 3.33 : Valenite CTPGPL-16-3C tool holder and TPC-322J-VC2 insert

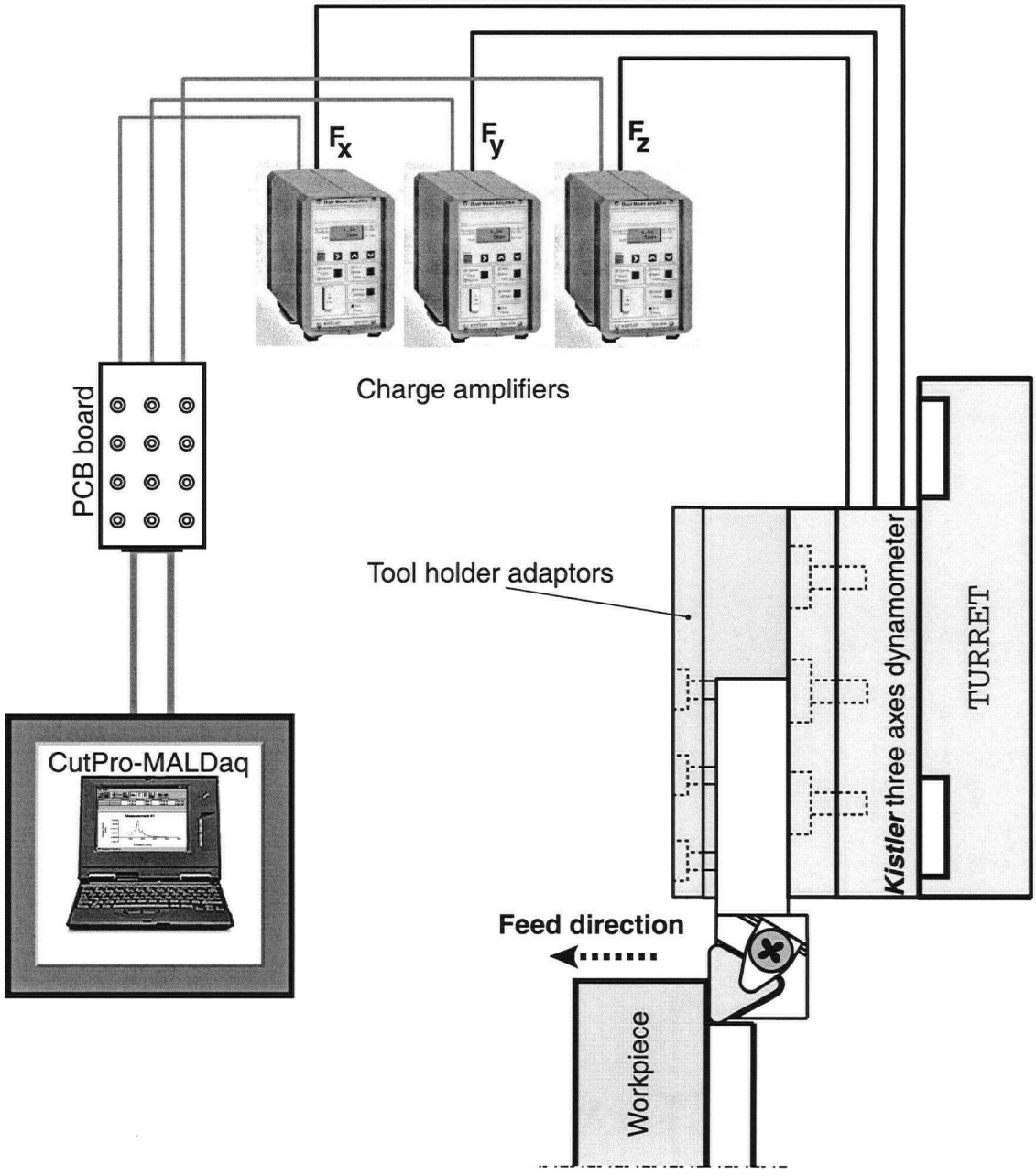

Figure 3.34 : Experimental setup for the verification of the Orthogonal to Oblique Transformation Method

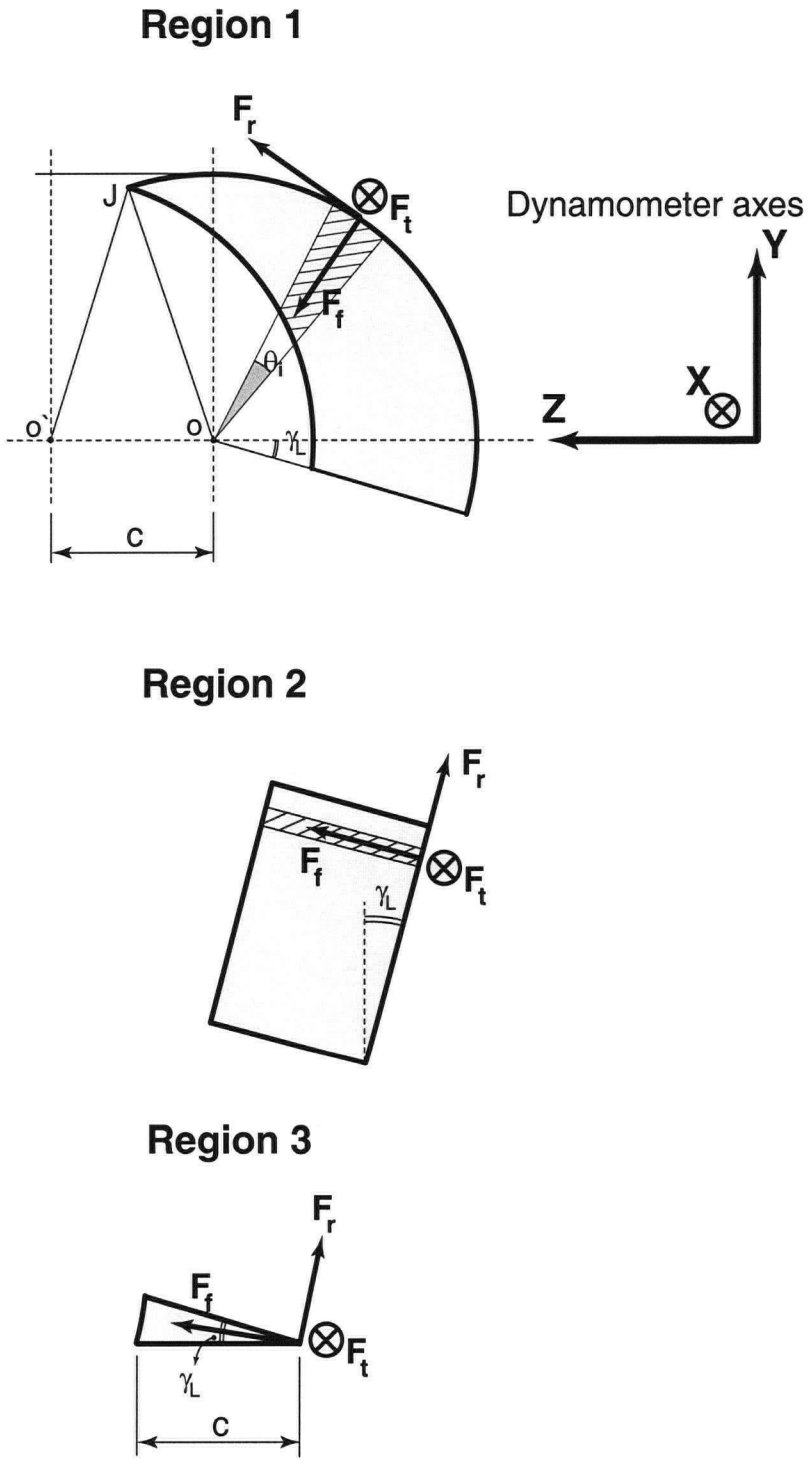

Figure 3.35 : Oblique tangential F_t, radial F_r and feed F_f force directions in each region and, dynamometer axes directions

3.3.2.4. Experimental Verification of Orthogonal to Oblique Transformation Method

For the verification of the method, 7 experiments were conducted with the material *P20 mold steel shaft* by using a *Valenite TPC 322J Uncoated VC2 grade CTPGL-16-3 C Left-hand tool holder* at different cutting speeds and depth of cuts, but with constant 0.05[mm/rev] feed rates. The specifications of the tool and tool holder are given in Figure 3.33. For the calibration, the experimental setup was the same as the one used in the development of the mechanistic model, except for the tool holder and workpiece. The experimental results are shown below in Figure 3.36 (The cutting conditions, the measured and the predicted forces are also presented in a table in Appendix B). Tangential force is predicted with under 10% average error; however, prediction error in radial and feed forces rises to 25% in some cases.

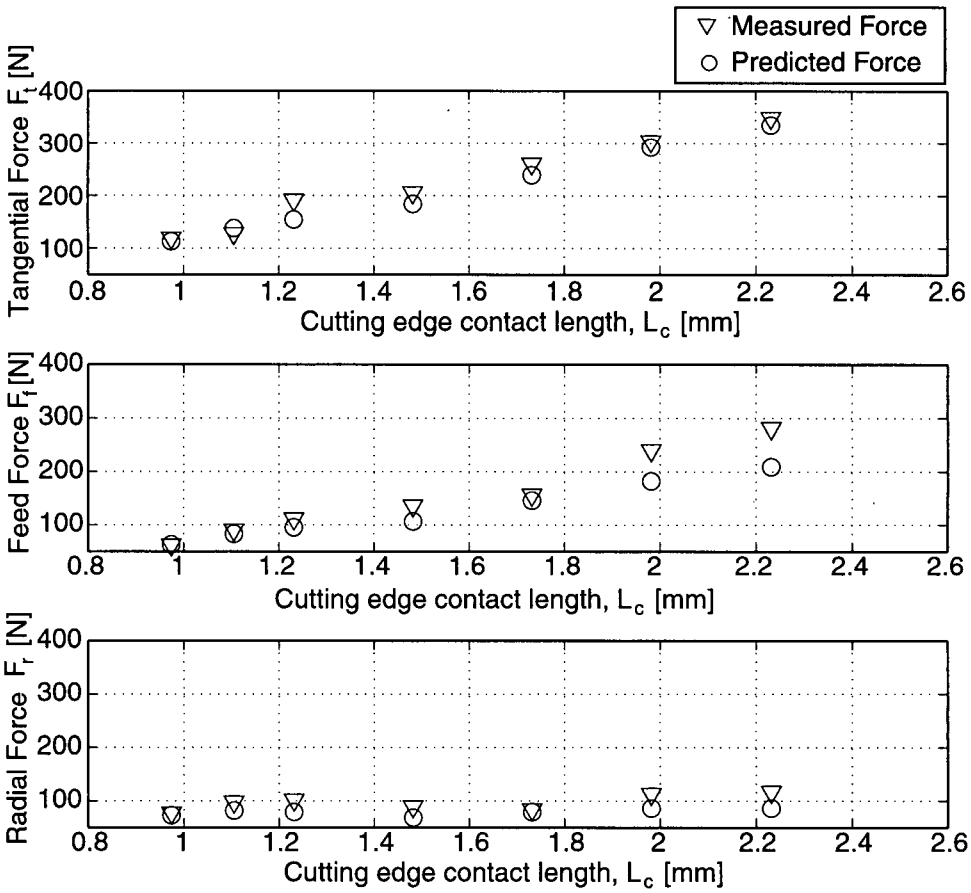

Figure 3.36 : Comparison between the measured and predicted tangential, radial and feed forces using the orthogonal to oblique transformation method

3.4. Summary

In this chapter, a mechanistic force prediction model has been developed for two inserts with a corner radius and grooves for chip breakage. This development allows for the force prediction of stable and unstable cutting conditions. The mechanistic model requires a vast amount of cutting data for each new cutter geometry, and, more importantly, the data cannot be generalized for application to other tools, as there is no explicit relationship between the tool geometry, cutting conditions, and the cutting force coefficients. The mechanistic model approach does not provide any physical insight into the process, such as shearing stress, or friction in the process. In the second part of the chapter, an orthogonal to oblique transformation method is utilized for the force prediction in the boring process. For the verification of this method, a previously developed orthogonal cutting database has been used. Once the orthogonal cutting data base is developed, this method does not require any further experiments for the force prediction. Both methods are experimentally verified with good accuracy.

Chapter 4

Process Faults in Boring

4.1. Introduction

Process faults are the most common problem associated with the use of multiple-inserted tools, causing the loss of accuracy in machining operations such as milling and boring. The main advantage of using a multiple-inserted boring bar is that the workpiece can be machined with a high feed rate, which is *the number of insert* times the d*esirable feed rate for one insert* ($N \times c$). High feed rates result in increased productivity in manufacturing. Because the inserts are arranged with symmetrical angular positions on the boring head, the forces on the inserts in the X and Y directions cancel each other, and the total force in these directions becomes zero. Hence, it is possible to obtain better tolerances with multiple-inserted bars with a large operational length-to-diameter ratio *(L/D)*.

Process faults in the multiple-inserted boring process are defined as any deviation of the boring head from the hole center, as well as insert runout. As mentioned in the previous chapter, the boring process is performed on an existing hole produced by preceding processes such as drilling and punching. In other words, boring is usually at least the second process applied to a workpiece. If the boring operation is not performed on the same machine as the one used for the previous operation, the center of the boring head and the hole should be aligned for an accurate process. In any case, if the boring head has a deviation, the depth of cut varies continuously around the rotational axis. Presumably, the cutting forces will also follow this depth of cut variation.

Although tool manufacturers produce very precise multiple inserted tool holders, the inserts may contain offsets in the radial and feed directions when they are secured through tightening of the insert screw. This is called *insert runout*. In this case, the insert having a radial offset rotates

with a larger radius with respect to the axis of the boring head, hence removing more material than the other inserts. Similarly, the insert having an offset in the feed direction moves into the workpiece ahead of the other ones and removes more material (Figure 4.1).

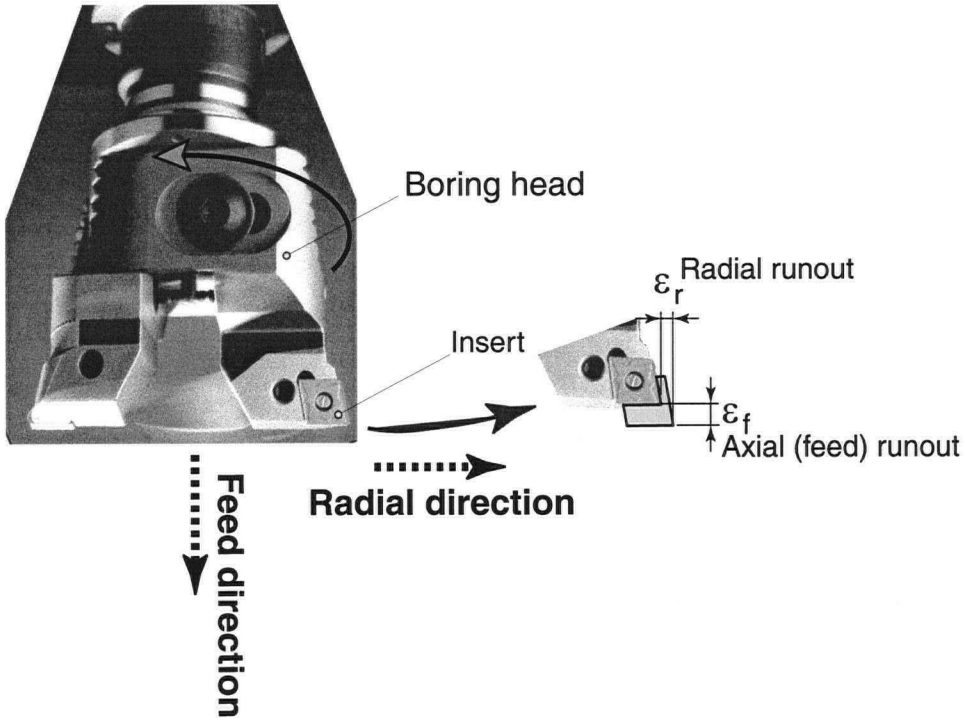

Figure 4.1 : Radial and axial (feed) runouts on a two-insert Valenite boring head

In this chapter, process faults in the boring process are investigated and cutting forces are predicted by employing the mechanistic model developed in Chapter 3. A *Valenite* boring head (Figure 4.1) with two inserts (the same insert as the one used in the implementation of the mechanistic model in Chapter 3) has been utilized in the experiments for the verification of the force prediction.

4.2. Mechanics of Multiple Inserted Boring Bar

In the multiple-inserted boring process, each insert has three cutting force components, tangential, radial, and feed forces (F_t, F_r and F_f). In the evaluation of the mechanics of multiple-inserted boring bars, the tangential and radial forces are combined to give a resulting force $F_{R,i}$ (i is the insert number). The direction of F_R for each insert changes with the rotation of the spindle and produces the total force in the X or Y directions. The total feed force acting on the bar is the summation of the feed forces on each insert.

Here, the equations of the total force in the X and Y directions are derived by considering a boring head with four inserts. They can later be generalized for any boring head that has a different number of inserts. Referring to Figure 4.2,

θ is an angle to define the direction of $F_{R,i}$,

$$\theta = 90 - \beta \tag{4.1}$$

where β is the rotation angle of the boring head in the clockwise direction. The direction of the resultant force $F_{R,i}$ for each insert is determined with the following equations (4.2) and (4.3).

$$\alpha_{1,3} = \theta + \text{atan}\left(\frac{F_{r_{1,3}}}{F_{t_{1,3}}}\right) \tag{4.2}$$

$$\alpha_{2,4} = \text{atan}\left(\frac{F_{r_{2,4}}}{F_{t_{2,4}}}\right) - \theta \tag{4.3}$$

where the indices *1, 2, 3* and *4* imply the insert numbers. The total forces in the *X* and *Y* directions are calculated as,

$$F_x = F_{R_1}\cos\alpha_1 + F_{R_2}\cos\alpha_2 - F_{R_3}\cos\alpha_3 - F_{R_4}\cos\alpha_4 \tag{4.4}$$

$$F_y = F_{R_1}\sin\alpha_1 - F_{R_2}\sin\alpha_2 - F_{R_3}\sin\alpha_3 + F_{R_4}\sin\alpha_4 \tag{4.5}$$

Ideally, F_x and F_y are expected to be zero for cutting conditions without any process faults, because the resulting forces $F_{R,i}$ on each insert should be equal and cancel each other for any

given cutting parameters. Process faults produce force differences on the inserts causing a periodic variation in the total force in the X and Y directions (F_x, F_y). The period of F_x and F_y is equal to the period of the spindle ($T = 60/n$), where n is the spindle speed in [rpm].

Cutting torque and power are obtained based on the tangential force F_t on each insert as,

$$T_c = \frac{D}{2} \sum_{i=1}^{N} F_{t,i} \tag{4.6}$$

$$P_c = \frac{\pi D n}{1000} \sum_{i=1}^{N} F_{t,i} \tag{4.7}$$

where D is the diameter of the hole in *[mm]*, N is the number of inserts on the boring bar, n is the spindle speed in *[rpm]* and $F_{t,i}$ is the tangential force on i th insert.

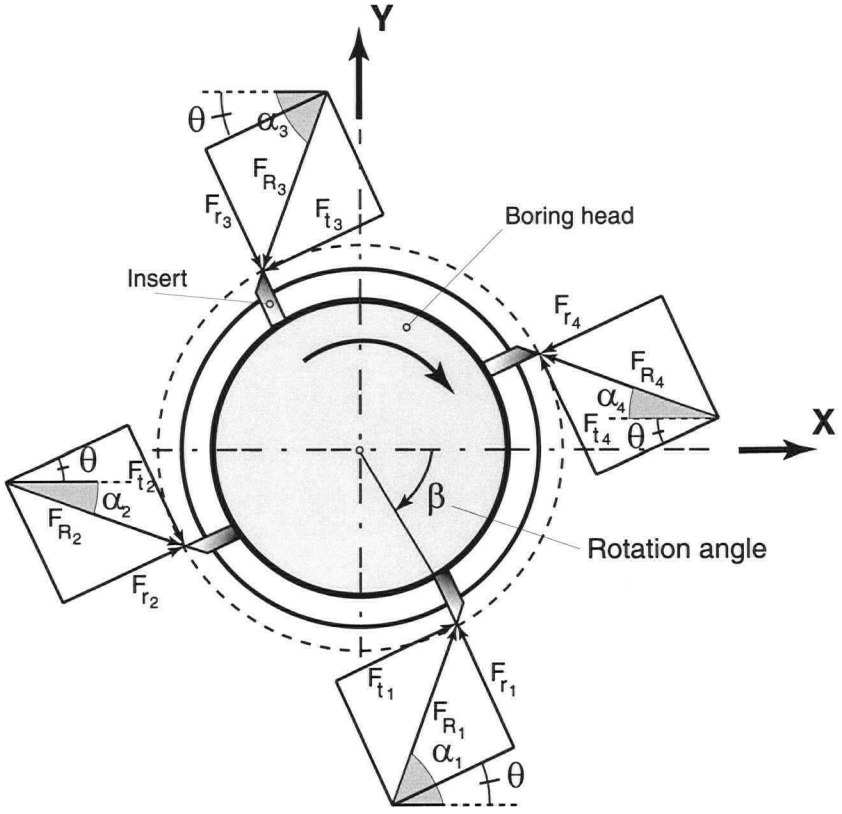

Figure 4.2 : Force diagram of a boring bar with four inserts

4.3. Insert Runout in the Radial and Feed (Axial) Directions

When the inserts on the boring head have runout in the radial or feed directions (or both), the amount of material being removed by each insert becomes different. This causes an unbalance in the total force in the X or Y direction. If there were no insert runout, the total force measured in the X or Y direction would be expected to be zero, as the tangential and radial cutting forces (F_t, F_r) acting on each insert are equal and in opposite directions, thus canceling each other (Figure 4.5).

For the *Valenite* boring head intended to be used in this study, there are more than 12 possible uncut chip area configurations to be considered, depending on which insert has the offset in the radial or feed directions. For example, one of the offsets may be on the first insert as the second one is on the second insert, or one insert may have both radial and feed offsets at the same time. In this study, only two configurations, which are defined in detail below, are considered. The conditions of these configurations are as follows.

Configuration 1: Runout in the feed direction is on the first insert and greater than the desired feed rate for one insert $\varepsilon_f \geq c$, where c is in the unit of [(mm/rev)/insert]), and runout in the radial direction is greater than zero, $\varepsilon_r > 0$, and is on the second insert (Figure 4.3).

Configuration 2: Runout in the feed direction of the first insert is less than the desired feed rate for one insert, $\varepsilon_f < c$, where c is in the unit of [(mm/rev)/insert]), and runout in the radial direction of the second insert is greater than zero, $\varepsilon_r > 0$ (Figure 4.4).

The corresponding uncut chip areas are illustrated in Figures 4.3 and 4.4. These uncut chip areas also represent the amount of material removed by each insert. As can be seen from these figures, the uncut chip area has rather an irregular shape due to the runouts (ε_r and ε_f). The uncut chip area A and cutting edge contact length L_c for each insert are calculated in a similar fashion as performed in Chapter 3, Section 3.3.1.1 in order to predict the forces.

In the process faults model, the depth of cut a is defined with the depth of cut of the insert that has the radial runout ε_r. The phase difference between the inserts is T/N in time and $2\pi/N$

in angular position, where N is the number of inserts on the boring head and T is the period of one revolution. If a *Valenite* boring head with two inserts is considered, the phase becomes $T/2$ and π in time and angular position, respectively.

When there are more than 2 inserts on the boring head, the number and complexity of the uncut chip area configurations increase depending on the distribution of the runout among the inserts. In such a case, for an accurate force prediction model to be achieved, each single uncut chip area configuration needs to be defined based on the inserts' runouts and their corresponding directions.

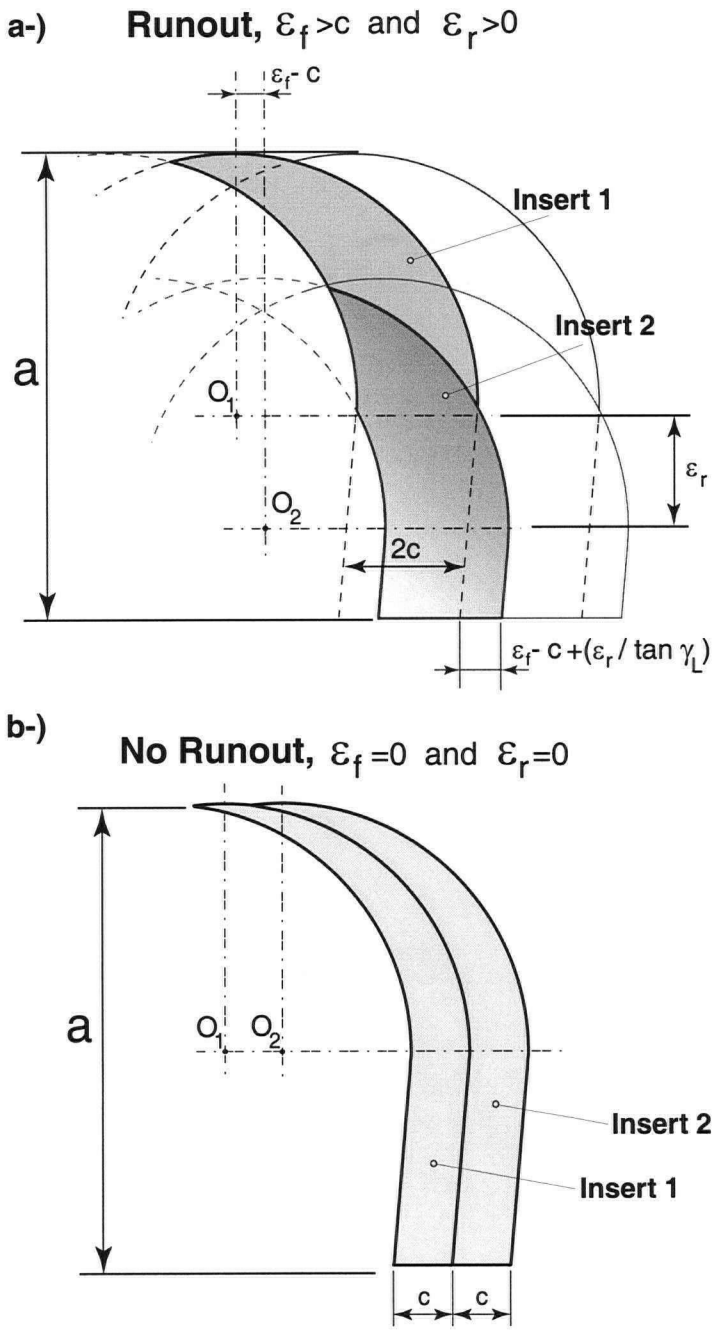

Figure 4.3 : **a-) Configuration 1:** The amount of material removed from the workpiece when the radial runout of insert 1 is greater than 0 ($\varepsilon_r > 0$) and feed runout of insert 2 is greater than feed rate ($\varepsilon_f > c$), **b-)** Uniform uncut chip area for the condition without any insert runouts.

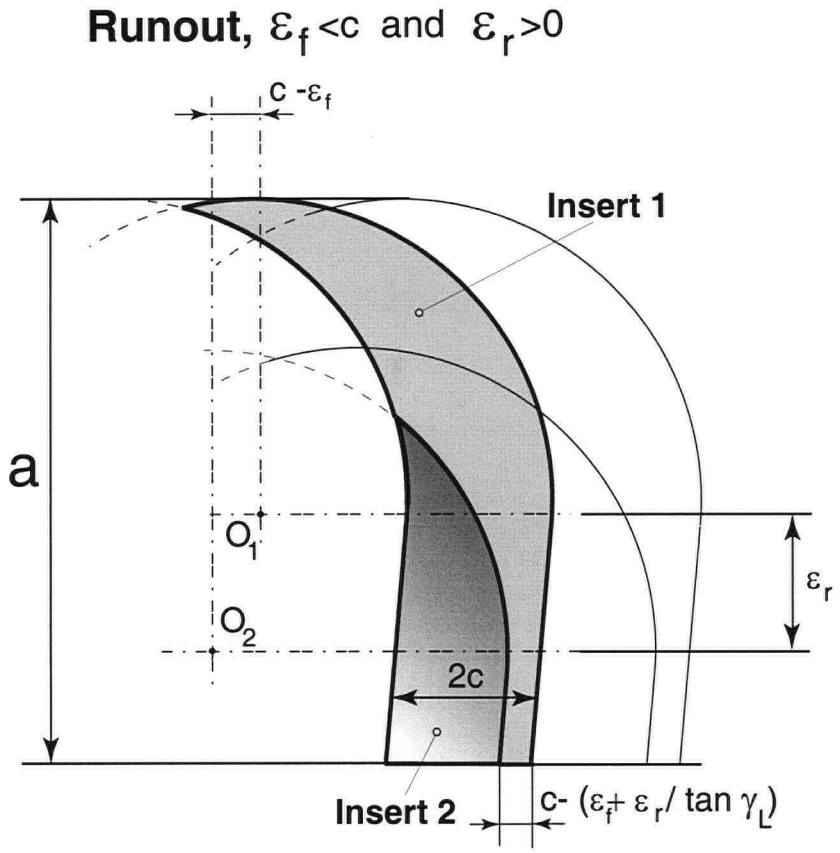

Figure 4.4 : **Configuration 2:** The amount of material removed from the workpiece when the radial runout of insert 1 is greater than 0 ($\varepsilon_r > 0$) and feed runout of insert 2 is less than feed rate ($\varepsilon_f < c$)

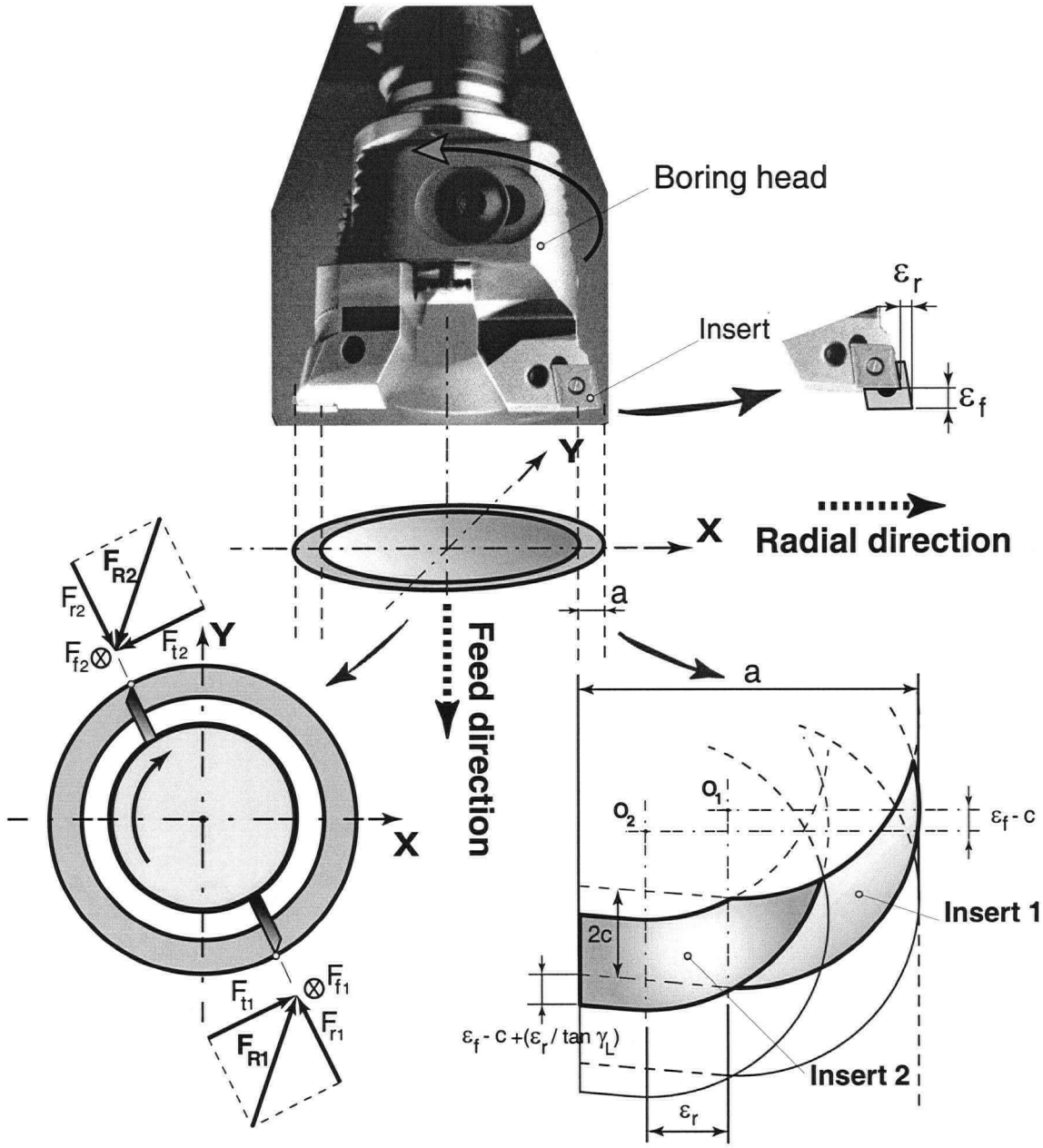

Figure 4.5 : *Valenite* boring head with twin cutter; Runout in radial and feed (axial) directions; The amount of material removed by each insert is shown by the shaded area in the bottom right part of the figures

4.4. Deviation of the Boring Head from the Hole Center

As explained in the introduction, the boring operation is performed in conjuction with other processes. Consequently, the centers of the boring head and the hole, which is produced in the preceding operation, need to be aligned for an accurate process. When the center of the boring head has a deviation with respect to the hole center, the depth of cut varies around the rotational axis of the boring head. The uncut chip area A and the cutting forces (F_t, F_r and F_f) follow the same variation in the relationships formulated in Chapter 3 (Eq. (3.13), (3.14), (3.22), (3.23) and (3.24)). The depth of cut reaches a maximum when the tool reaches the clockwise rotational position of,

$$\beta = \beta_i - \pi \tag{4.8}$$

where β_i is the angle where the depth of cut a is the minimum and calculated as,

$$\beta_i = \text{atan}\left(\frac{\Delta y}{\Delta x}\right) \tag{4.9}$$

where Δx and Δy are the deviations in X and Y directions. The depth of cut variation caused by these deviations occurs only in the first pass of the boring process, after which the centers of the boring head and hole align. The depth of cut for each insert is different at each angular location around the spindle axis because of misalignment and insert runouts (Figure 4.6). Depending on the magnitude of the misalignment, the configuration of the uncut chip areas of each insert may not be constant, and may jump to another configuration during the revolution. In other words, the configurations of the uncut chip areas could be different at rotational increments in the simulation. Once this happens, the simulation process must be able to select the corresponding configuration so that the uncut chip area A, effective lead angle ϕ_L, cutting force coefficients (K_{tc}, K_{frc}, K_{rc} and K_{fc}) and forces (F_t, F_r and F_f), can be calculated accurately.

As previously mentioned, the deviation of the boring head affects the force variation only during the first pass. If the deviation is large compared to the intended depth of cut a, the force variation caused by the runouts and the deviation may cause the system to forced vibrations.

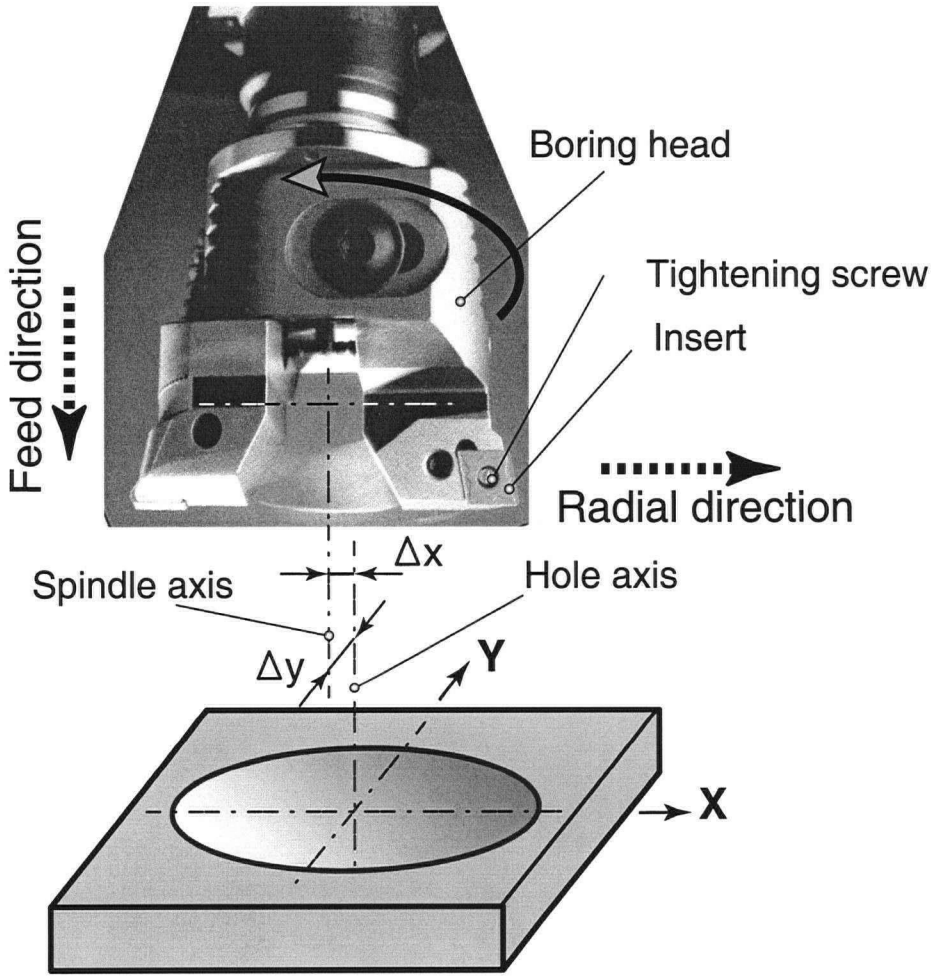

Figure 4.6 : Schematic illustration of the deviations Δx, Δy of the boring head from the hole center

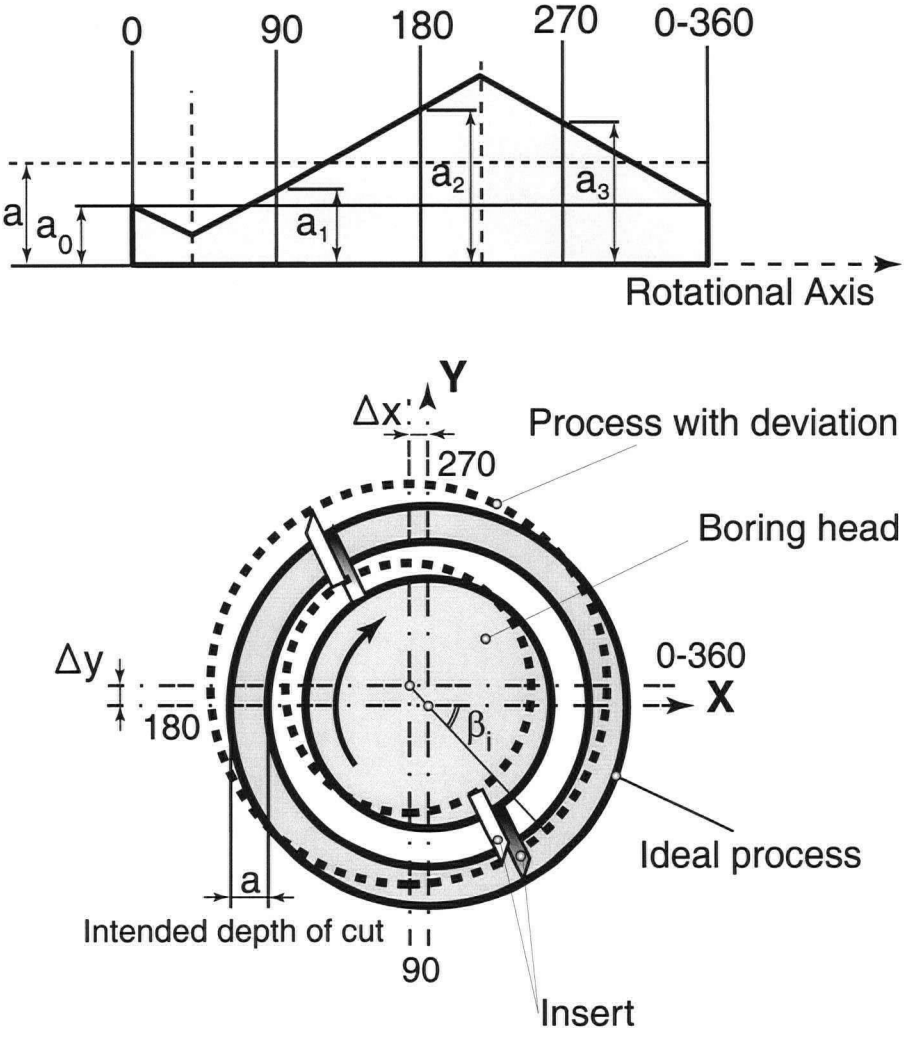

Figure 4.7 : The depth of cut variation caused by deviations Δx, Δy (a is the intended depth of cut)

4.5. Experimental Setup

The experimental setup used for the force calibration consists of components similar to those used for data collection in the mechanistic model development in Chapter 3. The same insert (i.e.*Valenite* CCGT432-FH 80° Carbide PVD coated diamond insert) for which the mechanistic model was developed has been used in the experiments for the verification of the force prediction in the presence of runouts in the radial and feed directions. Two *Valenite* CCGT432-FH inserts were attached to a *Valenite* boring head (Figure 4.1). The experiments were conducted on a *FADAL* VMC-2216 machining center (Figure 4.8). A *Kistler* 9255B-605027 3 axis dynamometer, *Kistler* charge amplifiers, and *CutPro-MalDAQ* data acquisition software, were used to generate, amplify, and digitize the force signals. The total resulting and feed forces were measured in the X, Y and Z directions, respectively.

In the preparation of the experiments, the dynamometer and vise were first mounted on the table of the *FADAL* machining center. Then the hollow cylindrical workpiece, which is the same as the one used in the development of the mechanistic model in Chapter 3 (See Figure 3.7), was held on the vise. The runouts of the boring head were measured using the dial gauge with 0.01[mm] precision. During the experiments, the workpiece is stationary but the boring head rotates and moves into the workpiece at the speed of feed rate, c *[(mm/rev)/insert]*. The signals produced by the dynamometer were amplified by charge amplifiers and sent to the data acquisition software .

Figure 4.8 : Fadal VMC-2216 Machining Center

4.6. Mechanistic Model Verification

Force variation has been simulated around the rotational axis and experimentally verified for the case in which the boring head has only runouts in the radial and feed directions (ε_r and ε_f). However, the case in which runouts and deviation are considered together was only simulated, not validated.

The cutting forces were predicted as a function of the uncut chip area A, cutting edge contact length L_c, and cutting speed V, in the mechanistic model developed in Chapter 3. As stated earlier, the mechanistic model also has the ability to predict the cutting forces for the case in which the uncut chip area does not have a uniform but rather an irregular and complex shape. The shapes of the uncut chip area become irregular with the incorporation of insert runouts (i.e. ε_r and ε_f) and deviation of the boring head from the hole center (Δx and Δy). The uncut chip area A and cutting edge contact length L_c need to be calculated for the force prediction. Force prediction considering the runouts of the inserts is executed in the following order.

- Angular increments for one full revolution are set for the force simulation.

- The uncut chip areas (A_1 and A_2) are calculated separately for each insert (insert 1 and insert 2). This calculation is performed in the same way as in the development of the mechanistic model.

- Centers of gravity of the uncut chip areas corresponding to each insert , G_1 and G_2, are determined in the way presented in Chapter 3, Eq.(3.25).

- The modification factor K_m is predicted using Eq. (3.28) and (3.29).

- Effective lead angles ϕ_L for each insert are predicted based on the calculated G_1 , G_2 and K_m Eq. (3.26).

- Cutting edge contact lengths of each insert (L_{c_1} and L_{c_2}) are calculated using the method in Chapter 3, Section 3.3.1.1.

- Tangential cutting force coefficient K_{tc} and tangential force F_t are predicted (Eq.(3.13) and (3.22)).

- Friction cutting force coefficients K_{frc_1}, K_{frc_2} and friction force F_{fr} are predicted (Eq. (3.14), (3.23), (3.24)).

- Radial and feed forces, F_r and F_f, are calculated with Eq. (3.26) and (3.30).

- Total resulting cutting forces in the X and Y directions, F_x and F_y, at each angular increments are predicted with Eq. (4.4) and (4.5).

Due to the rotation of the spindle, the amplitude of the resulting forces varies with the same period of the spindle, T.

4.7. Experimental Verification of the Mechanistic Model for Process Faults

For the verification of the mechanistic model, experiments were conducted with different insert runouts in both radial and feed directions. The cutting conditions were selected so that the uncut chip area of the inserts stays in the two configurations mentioned in section 4.3. In these selections, the radial and feed runouts were distributed separately (i.e. radial runout was on the first insert while the feed runout was on the second insert or vice versa). Four experiments were conducted under the conditions specified in section 4.3.

Figure 4.13 shows the simulated total force F_x in the X direction when the boring head has both runouts in the radial and feed directions ε_r and ε_f, and deviations defined by Δx and Δy. Note that when the deviation increases the peaks of F_x shift to the right and the left. This can be explained as follows: the uncut chip area for each insert has an irregular shape, due to the radial and feed runouts. When the deviation of the boring head is also included, the variation of the depth of cut of each insert is affected, and the engagement of the inserts with the workpiece vary in the depth of cut direction as shown in Figure 4.7. The uncut chip areas of each insert have similar irregular shapes. Since there is no linear relationship between the cutting force and depth of cut variation, the effect of the deviation may reflect the force variation as positive and negative shifts as shown in Figure 4.13 (i.e.the maximum peak of the force diagram shifts to right-hand side while the minimum peak moves to the left, with an increase of the boring bar deviation). When deviations in both directions are zero ($\Delta x = 0$ and $\Delta y = 0$), the total force in the X direc-

tion F_x makes its minimum at the rotational position of 64° while it has its maximum value at 244° angular position. Note that there is a 180° phase shift between the two peaks for this condition. When both Δx and Δy are set to 0.05[mm], F_x has its maximum and minimum at the positions of 60°, and 250°. The angular phase shift is 190° in this case. Similarly, for the deviations of Δx = 0.10 [mm] and Δy = 0.10 [mm], the maximum and minimum forces are on angular positions of 57° and 256°, increasing the phase shift to 199°. This investigation states that, the deviation of the boring head changes the amplitude of the total force in the X direction (F_x) as the phase shift between the maximum and minimum forces increases.

The conditions in which the experiments were performed for the verification of the force prediction are shown in the following Table 4.1. The results of this investigation are presented in Figures 4.9, 4.10, 4.11 and 4.12. As seen, for the first three tests, the forces were predicted with a good accuracy of under 10% error. However, in the last test the error is over 10%. This may be due to a mistake made at the stage of the measurement of runouts. As a result of this experimental verification, it can be stated that the mechanistic model can be used for the force prediction of a cutting condition that generates an irregular and complicated uncut chip area shape.

Table 4.1 : Experiments with runout in both feed and radial directions; a_1 and a_2 are the radial depth of cuts of insert 1 and insert 2.

Exp. #	V [m/min]	c [mm/rev-insert]	ε_f [mm]	ε_r [mm]	a_1 [mm]	a_2 [mm]
1	150	0.0600	0.09(insert 2)	0.20	1.485	1.285
2	100	0.0700	0.12(insert 2)	0.10	1.830	1.730
3	175	0.0550	0.14(insert 2)	0.18	1.100	0.920
4	225	0.0900	0.055(insert 1)	0.25	0.870	1.120

where a_1 and a_2 are the depth of cuts of the insert 1 and 2, respectively. As stated earlier, in the model, the intended depth of cut and radial runout are considered with respect to the insert that has the largest depth of cut. In other words, if the depth of cut of the insert 2 is greater than the

depth of cut of the insert 1, i.e. $a_2 > a_1$, the intended depth of cut is assumed to be a_2 and radial runout ε_r, which is calculated as $\varepsilon_r = a_2 - a_1$, is on the insert 2, or vice versa. It should be also noted that the radial and feed (axial) runouts are on different inserts in the above experimental conditions.

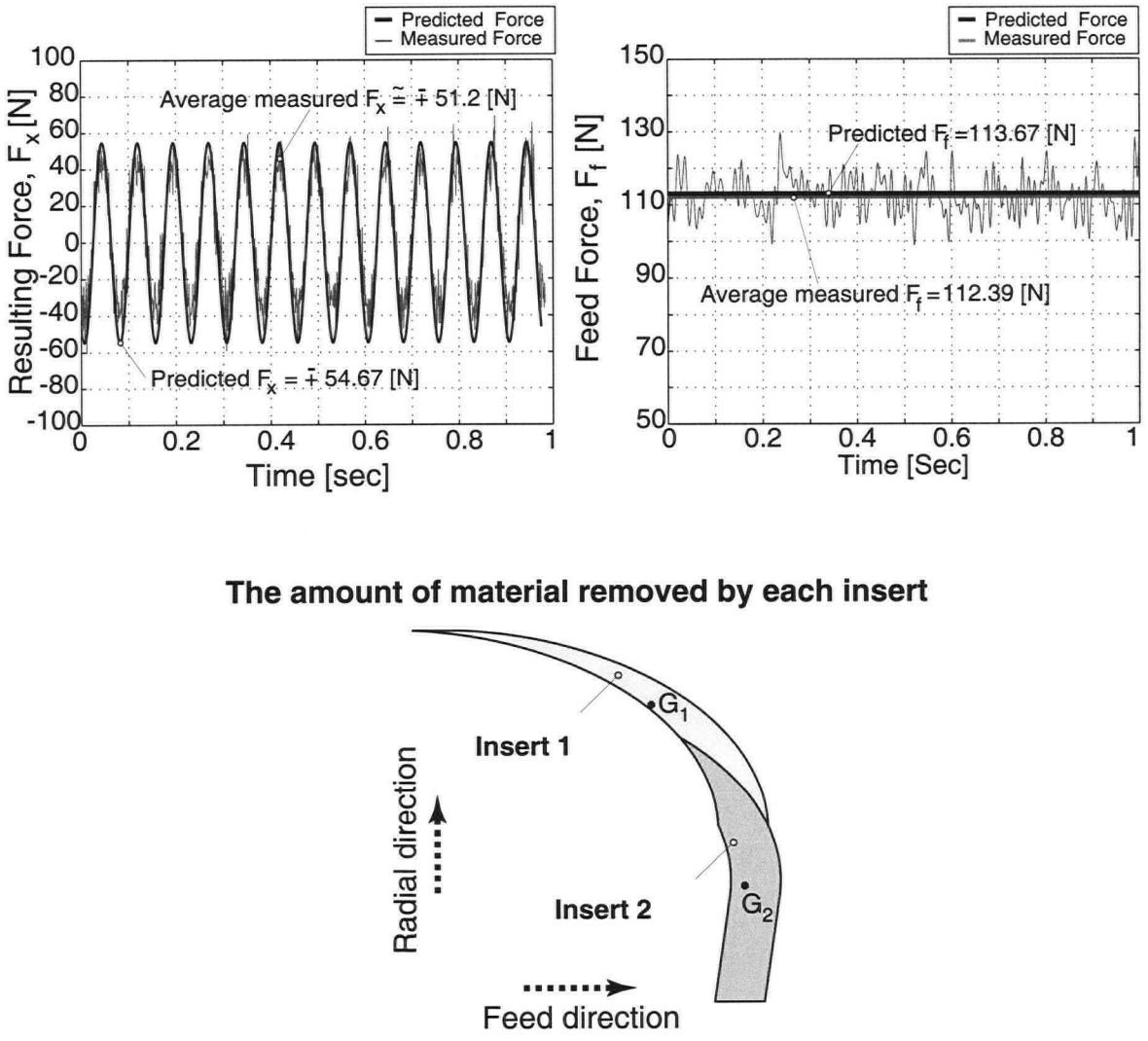

Figure 4.9 : Resulting force in X direction F_x and Feed force F_f prediction for the condition of $a_1 = 1.485[mm]$, $a_2 = 1.285mm]$, $\varepsilon_r = 0.20[mm]$, $\varepsilon_f = 0.09[mm]$, $c = 0.06[mm]$, $V = 150[m/min]$

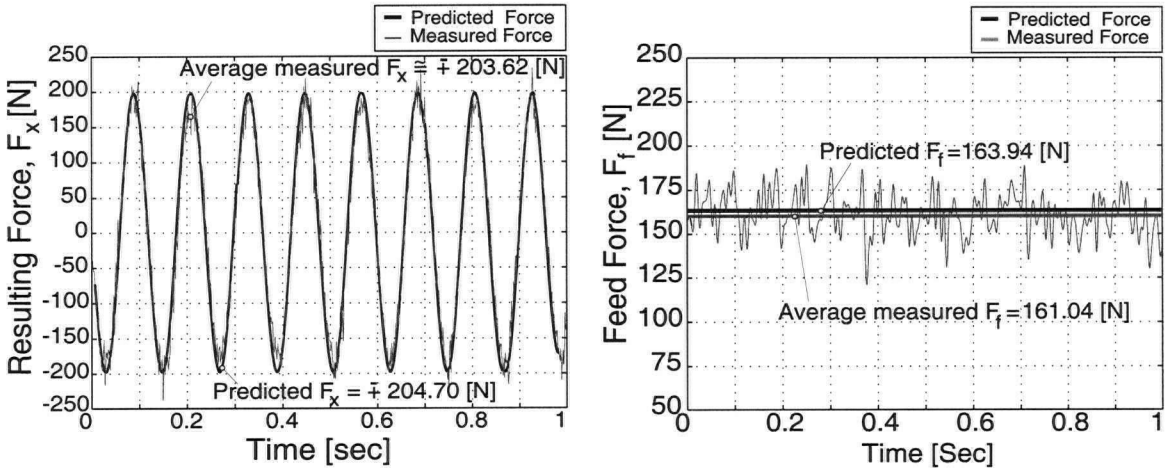

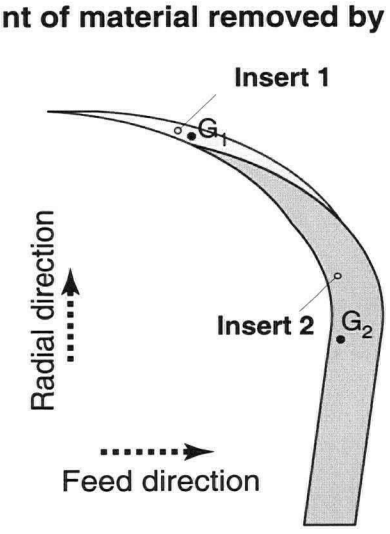

Figure 4.10 : Resulting force in X direction F_x and Feed force F_f prediction for the condition of $a_1 = 1.830[mm]$, $a_2 = 1.730mm]$, $\varepsilon_r = 0.10[mm]$, $\varepsilon_f = 0.12[mm]$, $c = 0.07[mm]$, $V = 100[m/min]$

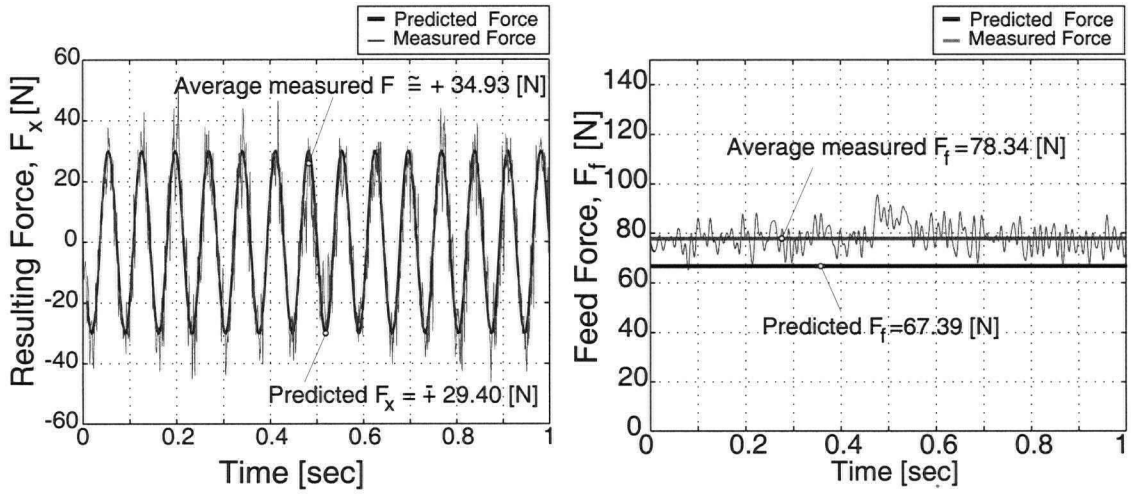

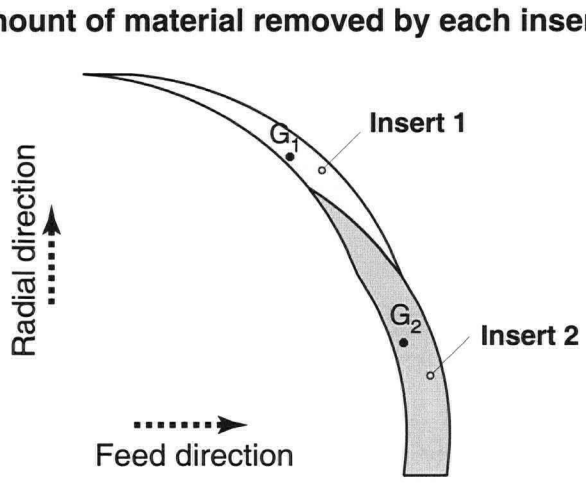

Figure 4.11 : Resulting force in X direction F_x and Feed force F_f prediction for the condition of $a_1 = 1.1[mm]$, $a_2 = 0.92[mm]$, $\varepsilon_r = 0.18[mm]$, $\varepsilon_f = 0.14[mm]$, $c = 0.055[mm]$, $V = 175[m/min]$

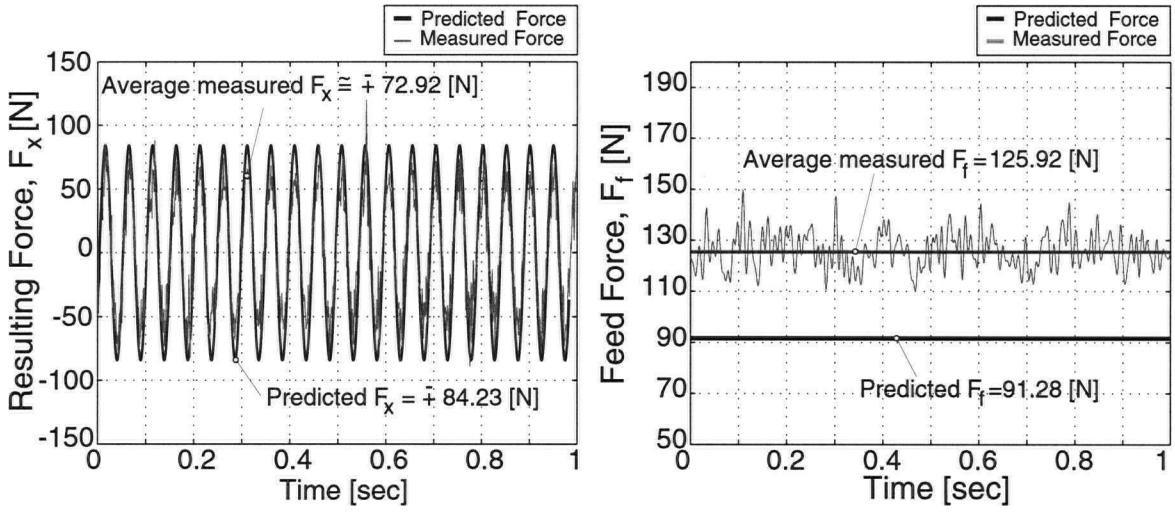

The amount of material removed by each insert

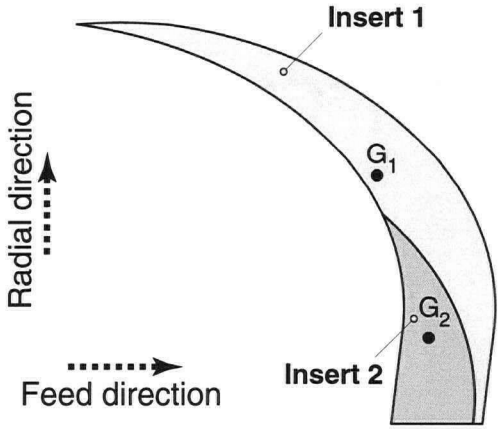

Figure 4.12 : Resulting force in X direction F_x and Feed force F_f prediction for the condition of $a_1 = 0.870[mm]$, $a_2 = 1.12mm]$, $\varepsilon_r = 0.25[mm]$, $\varepsilon_f = 0.055[mm]$, $c = 0.09[mm]$, $V = 225[m/min]$

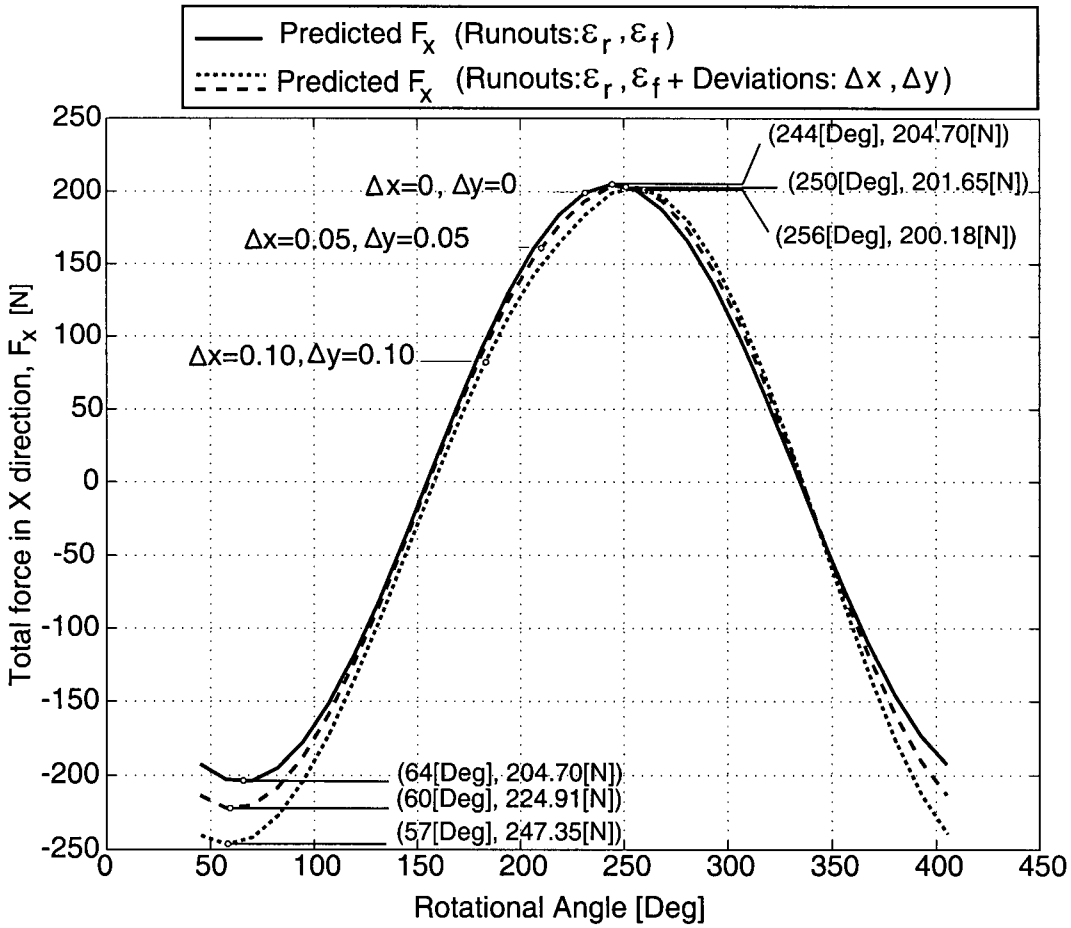

Figure 4.13 : The variation of the total force in X direction when considered the process has insert runouts in radial and axial directions, and deviation in both X and Y directions. ε_r = 0.1 [mm], ε_f = 0.12 [mm], V = 100 [m/min], a = 1.83 [mm], c = 0.07 [(mm/rev)/Insert], Δx_1 = 0 [mm], Δx_2 = 0.05 [mm], Δx_3 = 0.10 [mm], Δy_1 = 0 [mm], Δy_2 = 0.05 [mm] and Δy_3 = 0.10 [mm]

4.8. Summary

In this chapter, the effects of process faults on cutting forces have been investigated. Using the mechanistic model developed in Chapter 3, the cutting forces have been predicted for the verification of only two uncut chip area configurations. This validation also shows that, in the mechanistic model, relating the cutting forces not only to cutting parameters, but also to the geometry of the uncut chip area allows the prediction of cutting forces for a cutting condition that causes the material to be removed with an irregular uncut chip area shape.

Chapter 5

Dynamic Modeling of Boring and Chatter Stability

5.1. Introduction

Chatter vibrations are an undesirable phenomenon in machining operations. If uncontrolled, they result in poor surface finish and dimensional accuracy, may damage machine tool components, cause early tool wear, chipping and failure of the cutting tool and generate undesirable noise. Various factors cause vibrations in machining. Vibrations are categorized as *forced* or *self-excited.*

Forced vibrations can be generated by unbalanced rotating components of the machine tool, and backlash in the transmission gear. Chatter vibrations are self-excited vibrations induced by the regenerative effect, which can be explained with a simple orthogonal cutting process such as plunge turning (Figure 5.1). In this process, the tool moves into the rotating workpiece mounted between the chuck and the tail stock, with the feed rate of c which is also equal to the intended chip thickness h_0. The workpiece tends to oscillate under the feed force F_f, due to its flexibility in the feed direction. The relative vibrations between the tool and the workpiece generate waves on the cut surface. In the following pass, the tool encounters a wavy surface and removes a chip with time-varying thickness, h . Since the feed force is proportional to the uncut chip area, it (the feed force) follows the same periodic variation and excites the structure, causing *chatter vibrations.*

The regenerative effect is caused by the phase difference ε between two successive revolutions. If the phase difference is zero, as encountered when the frequency of the spindle speed n [rev/sec] and the chatter frequency have an integer ratio, self-excited force and chatter vibra-

tions may not be generated. The relationship between the spindle speed n and chatter frequency ω_c is expressed with the following equation.

$$\frac{60\omega_c}{n} = N + \frac{\varepsilon}{2\pi} \tag{5.1}$$

where the chatter frequency ω_c is in [Hz] and the spindle speed n is in [rev/min]. N is the integer number of waves and $\varepsilon/2\pi$ is the fraction of a wave. When the phase angle ε is zero, the chip thickness does not vary even though there are still vibrations taking place. The most drastic variation in chip thickness occurs when the phase angle becomes 180° (Figure 5.1).

In the model, the feed force F_f is expressed as a linear function of the width of cut b, chip thickness h, and the feed force cutting coefficient K_f, assuming that the cutting coefficient does not vary significantly for the selected range of the cutting parameters and is constant. In reality, the cutting force coefficient is not constant, but a function of the instantaneous chip thickness and cutting speed [9]. This approach has been modified in Chapter 3, and cutting coefficients have been established as exponential functions of the uncut chip area A, cutting speed V, cutting edge contact length L_c and centroid of the uncut chip area. At high speeds, the material being cut tends to soften due to excessive heat, and the shear stress decreases causing the forces to lessen. However, for the low speed range, the variation of the cutting force with the cutting speed and the chip thickness may be negligible, as considered in Equation (5.2). This approach simplifies force prediction modeling and system stability analysis.

The dynamic variable of the orthogonal cutting system is the chip thickness $h(t)$ that incorporates the vibrations of the tool at current and previous revolutions, $y(t)$ and $y(t-T)$ Eq(5.4).

$$F_f(t) = K_f A(t) \tag{5.2}$$

$$A(t) = ah(t) \tag{5.3}$$

$$h(t) = h_0 - y(t) + y(t-T) \tag{5.4}$$

where a, h_0 and A are the depth of cut, the intended chip thickness and the uncut chip area, respectively.

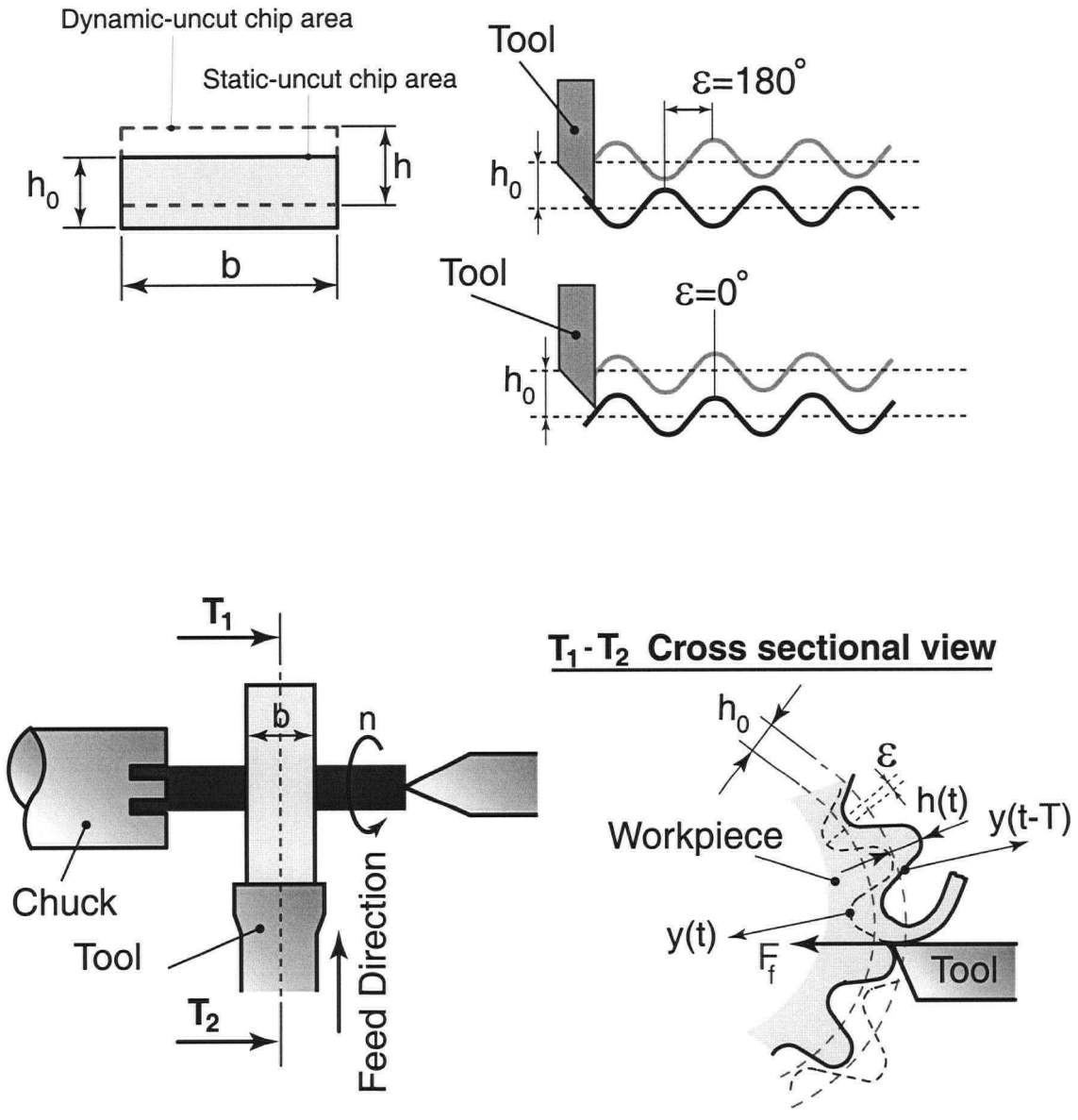

Figure 5.1 : Orthogonal plunge turning with regenerative chatter vibrations

Figure 5.2 shows a block diagram representation of the chatter vibrations, in which all the dynamic parameters of the system are presented in the Laplace domain. In the model, the input of the system is the intended chip thickness h_0 and the output is the current vibration $y(s)$. The vibration of the tool during the previous revolution is represented with a delay term, $e^{-sT}y(s) = Ly(t-T)$, where T is the period for one full revolution. The stability is analyzed based on the frequency response method. The mathematical derivations yield the following equation, (5.5) [4].

$$a_{lim} = \frac{-1}{2K_f G(\omega_c)} \tag{5.5}$$

where a_{lim} is the maximum allowable critical depth of cut for the stable cutting condition, and $G(\omega_c)$ is the real part of the transfer function of the structure $\Phi(s)$. As it is difficult to model the nonlinearities of the system, such as process damping, the tool jumping out from the workpiece, dependency of the cutting force coefficients on cutting parameters, and multiple regeneration, the chatter stability is examined based on the linear stability theory introduced by Tobias[30], Tlusty[4] and Merrit[7]. Nonlinearities of the process can only be taken into account when a time domain simulation method is used. One of the disadvantages of the time domain solution method is that the process is considered with small time increments, and therefore requires a long time to compute a result. On the other hand, analytical modeling is considerably faster and is preferred in practice.

In the past decades, extensive research has been devoted to the chatter problem in machining, but detailed work on chatter stability in boring has been rare. This may be because the tool used in the boring process is a single point cutting tool with a corner radius, such that the cutting geometry in the boring operation is more complicated compared to other machining operations.

In this chapter, the dynamic characteristics and the regenerative effect in the boring process are presented in detail. The stability solution of the boring process in both frequency and time

domains is discussed from all perspectives, based on the information introduced in the following sections.

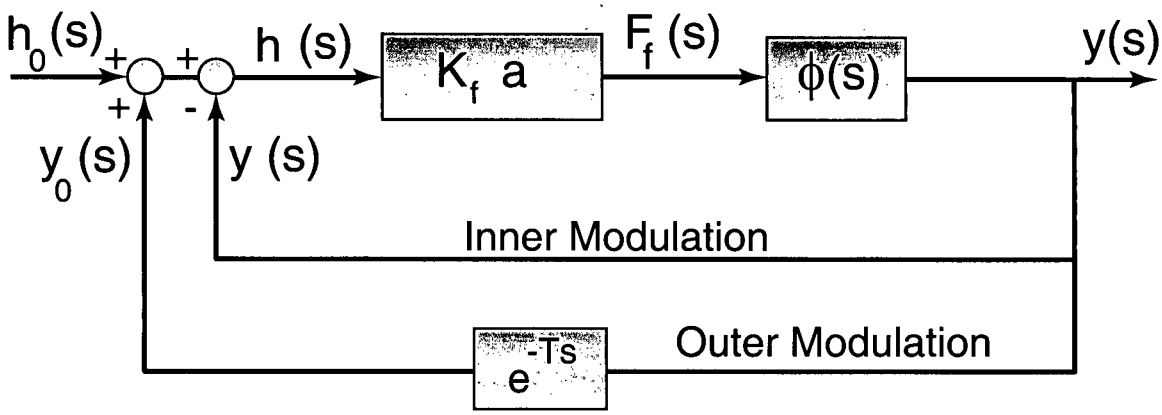

Figure 5.2 : Block diagram of the regenerative chatter vibrations in orthogonal cutting

5.2. Dynamic Characteristics of the Boring Process

5.2.1. Regenerative Effect in Boring

The regenerative effect in the boring process is different from the one in milling and turning processes. The boring bar structure is significantly stiffer in the feed direction, which aligns with the boring bar axis. Chatter vibrations are therefore caused mainly by flexibility in the radial and tangential directions (Figure 5.4). For the purpose of conceptual evaluation, the boring bar structure can be modeled by two orthogonal single degree of freedom systems in the radial and tangential directions. A schematic illustration of the boring bar structure is shown in Figure 5.5.

The position of the tool in the boring operation is defined with only the current instantaneous vibration $y(s)$ in the radial direction.

$$a(s) = a_0 + y(s) \tag{5.6}$$

where $a(s)$ and a_0 are the instantaneous dynamic and intended radial depths of cut. The next position of the tool in the feed direction will be ahead of the previous position by the amount of the feed rate c. Due to the phase angle, only the periodic uncut chip area interactions, which depend on the tool positions in the successive revolutions, produce the regenerative effect. The regenerative effect in boring can be explained with Figure 5.6. The figure depicts the simulated tool positions by assuming sinusoidal chatter vibrations with 0.1[mm] amplitude. In the simulation, only one period of sinusoidal path, which also implies the generation of one wave, is considered. The parameters for the simulation have been selected from experiments conducted under the conditions defined in Table 5.1.

Table 5.1 : Simulation parameters selected from the conducted chatter tests

Depth of Cut, a [mm]	Feed Rate, c[mm /rev]	Cutting Speed, V [m/min]
0.8[mm]	0.10	225
Spindle Speed, n [rpm]	Measured Chatter Freq. [Hz]	Measured Phase Angle, ε [Deg]
2228	771	274.7

Figure 5.6 shows 6 full and a fraction of the 7th revolutions. As it can be noticed that the depth of cut a and the uncut chip area A have different but periodic variations at each revolution, due to the phase angle ε between two successive revolutions. The difference in depth of cut variation at each revolution continues until *the number of revolutions* times *phase angle* adds up to $360°$; when the subtotal of the fractions of the waves $\varepsilon/2\pi$ becomes one full wave (one period, 2π). The depth of cut variation for each revolution is then repeated in the same fashion. This second periodic repetition is illusrated in Figure 5.7, with the surface roughness measurement of a workpiece on which the chatter test was performed with another specified cutting condition (depth of cut a=0.75[mm], feed rate c=0.12[mm/rev], cutting speed V=184[m/min], spindle speed n=1650[rpm]). In this test, the chatter frequency is measured as ω_c= 849.7[Hz] and the phase angle is obtained as $\varepsilon \cong 324°$ using Equation (5.1). The surface roughness measurement is performed with a surface roughness analyzer. It should be noted that the measurement has been carried out on a linear reference path in the feed direction (or on the same angular position of the hole circumference). In other words, the tool positions shown in the figure are taken on this line. In this test, the process is expected to have a different depth of cut variation in each period of the first 10 revolutions, due to a $324°$ phase angle. After 10 revolutions, the phase angle completes itself to $360°$ (or $0°$), and the same depth of cut variations seen in the first 10 revolutions will be repeated. The determination of the number of the revolution N (corresponds to 10 in the above example) when the phase angle ε becomes zero, and the corresponding phase angles at each revolution, are shown in the following algorithm (Figure 5.3). This algorithm determines wave generation characteristics based on spindle speed n [rpm], and measured chatter frequency ω_c. It is therefore assumed that the test has been conducted under specific cutting conditions, and the chatter frequency ω_c has been determined from FFT of the measured force (or acceleration) data. Using Eq.(5.1), the phase angle ε, which is assumed to be the initial phase angle at the 1st revolu-

tion of the process with chatter vibrations, is first calculated. Then, the phase angle ε at each revolution is found. This regeneration process keeps repeating itself until the end of cutting.

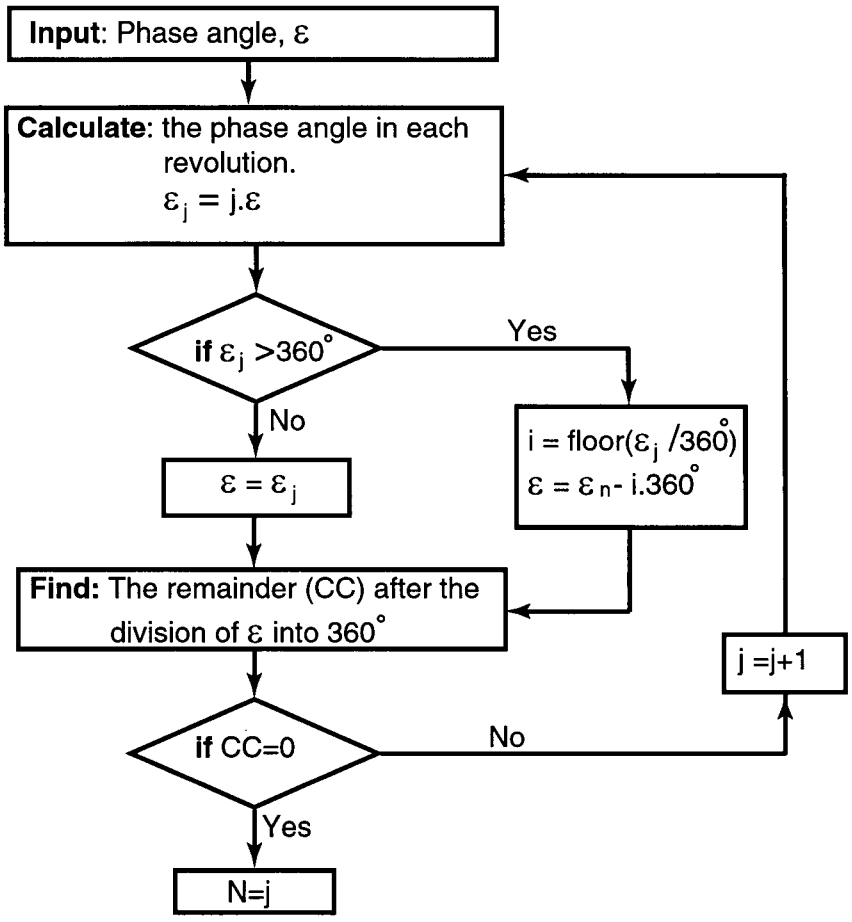

This algorithm finds the total number of revolution N for the completion of the phase angle to 360 [Deg] (i.e. after N revolutions the tool will start the (N+1)th revolution in the phase angle of 1st revolution. After N+1)th revolution, the same depth of cut (or uncut chip area) variation perceived in the first N revolutions will be repeated upto 2N th revolution.

Figure 5.3 : Algorithm for the determination of the phase angle for each revolution

At each instantaneous position of the tool, the uncut chip area may have an irregular and complex form, due to the corner radius of the tool. For example, if the tool is frozen at each revolution when it reaches a reference line, the corresponding uncut chip area takes the forms shown in Figure 5.6. The amount of material removed by the tool at each revolution differs, and may have a complicated form in some cases.

So far, the significant differences between regeneration of the waviness in boring and, turning and milling have been highlighted. The following question ensues: Do the vibrations in the tangential direction influence the regeneration of the waviness in addition to those in the radial direction? As it can be recognized from the transfer function measurement (Figure 5.4), the boring bar in the tangential direction is as flexible as in the radial direction. However, its contribution to the depth of cut variation is comparatively smaller than that in the radial direction. Consequently, the influence of vibrations in the tangential direction can be assumed to be negligible in the evaluation of the regenerative effect in boring.

The influence of the tangential displacements can be examined with Figure 5.8. Considering the boring bar with the tangential and radial vibrations (Δx and Δy), the total depth of cut variation is found to be,

$$a_d = a + \Delta y + \Delta a_t \tag{5.7}$$

The portion of the tangential displacement in depth of cut variation is,

$$\Delta a_t = R - \sqrt{R^2 - \Delta x^2} \tag{5.8}$$

where a, a_d, Δy, Δx, R and Δa_t are the intended depth of cut [mm], dynamic depth of cut [mm], the displacement of the tool in radial direction [mm], the displacement of the tool in tangential direction [mm], the radius of the hole [mm] and the variation of the depth of cut caused by the displacement of the tool in tangential direction, respectively.

The influence of the displacements in the tangential direction on the depth of cut variation can be examined with an example. $\Delta x = 0.1$ [mm] displacement in the tangential direction, when the radius of the hole is 40 [mm], leads to 1.25×10^{-4} [mm] depth of cut variation, Δa_t. However, the same displacement in the radial direction has a direct effect on the depth of cut variation with the same magnitude. Therefore, it is reasonable to neglect Δa_t in order to simplify the problem.

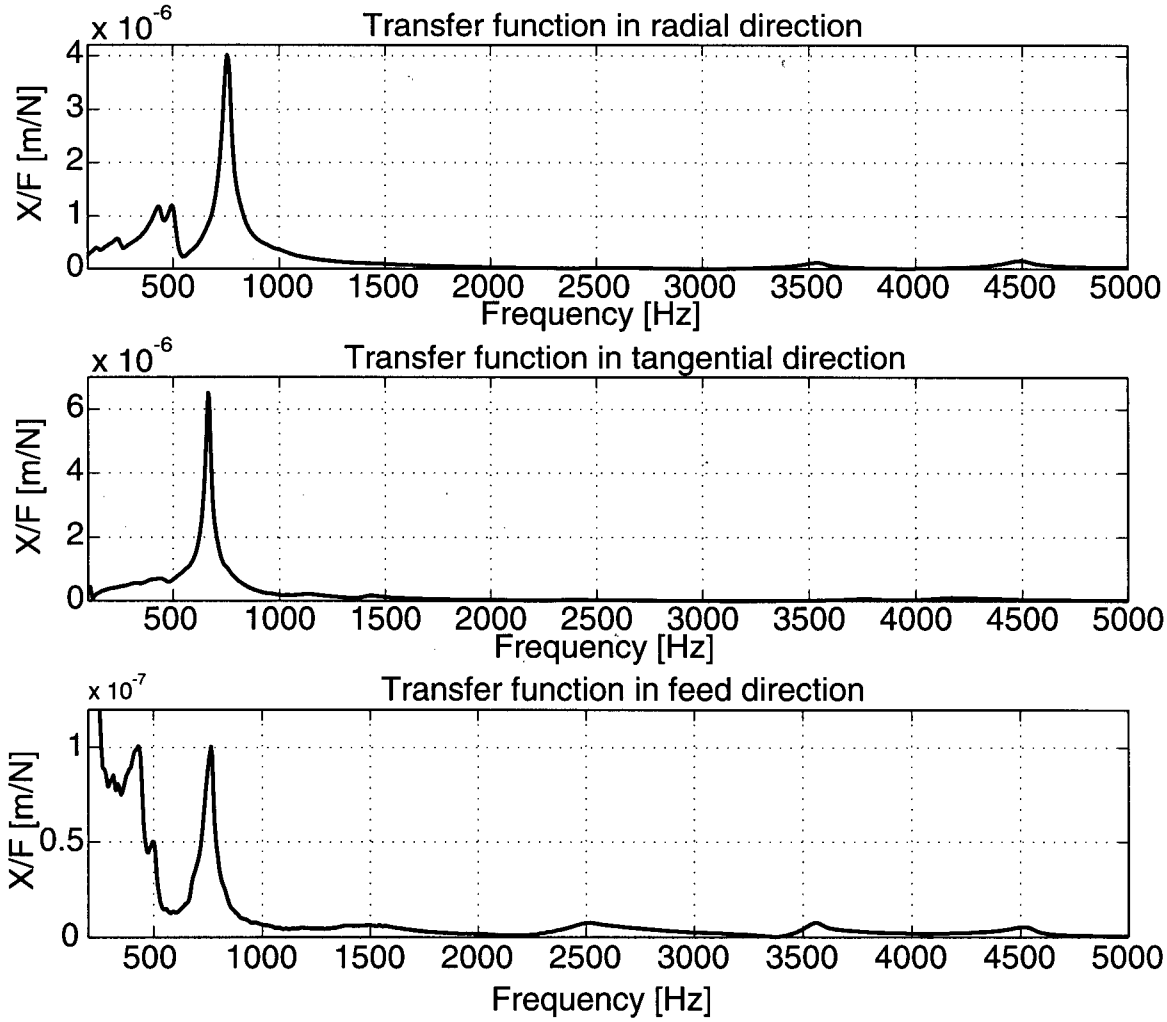

Figure 5.4 : Transfer function of the boring bar in tangential, radial and feed direction

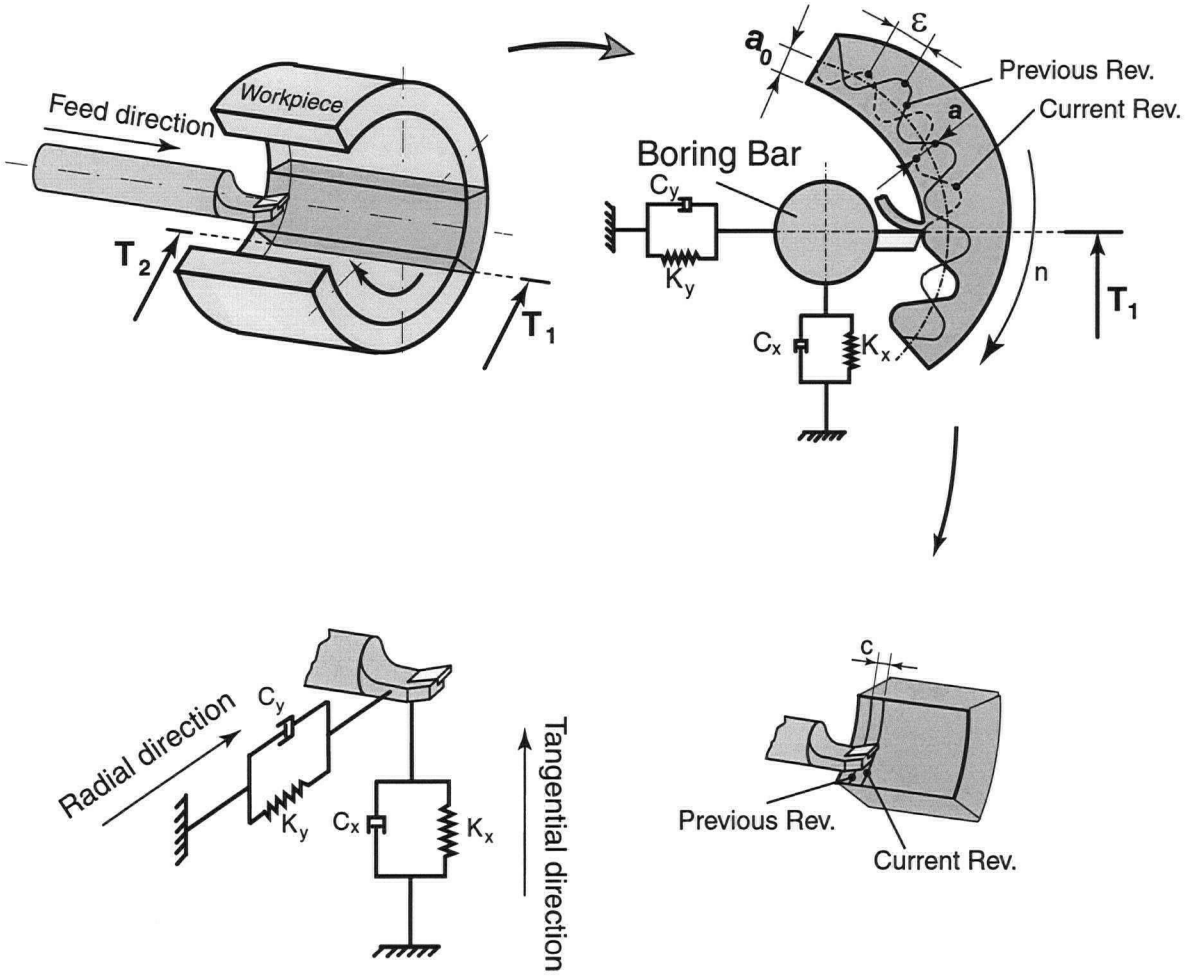

Figure 5.5 : Boring bar structure with two spring-mass and damping models of a single degree of freedom system

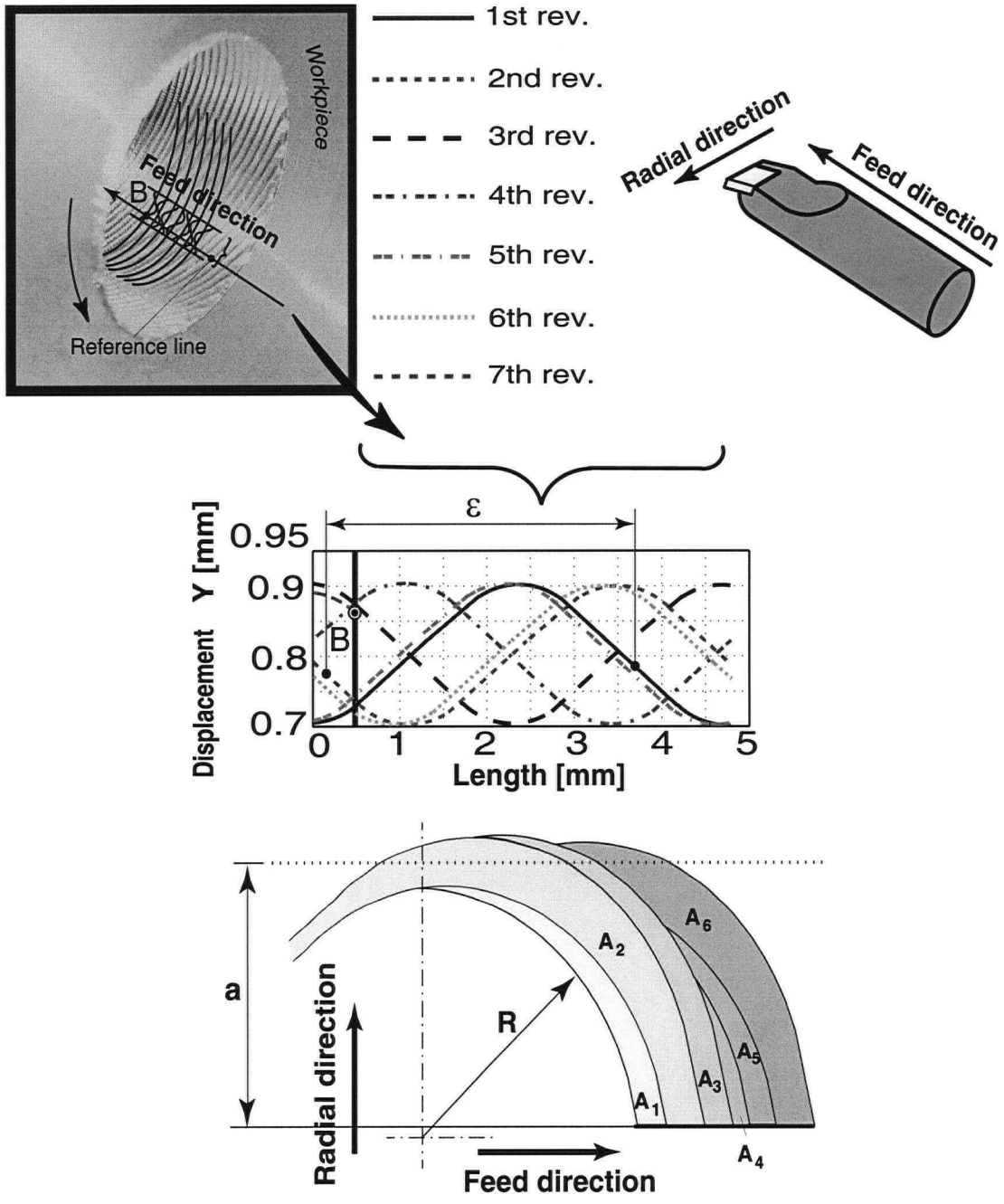

Figure 5.6 : Regeneration of the waviness in boring process

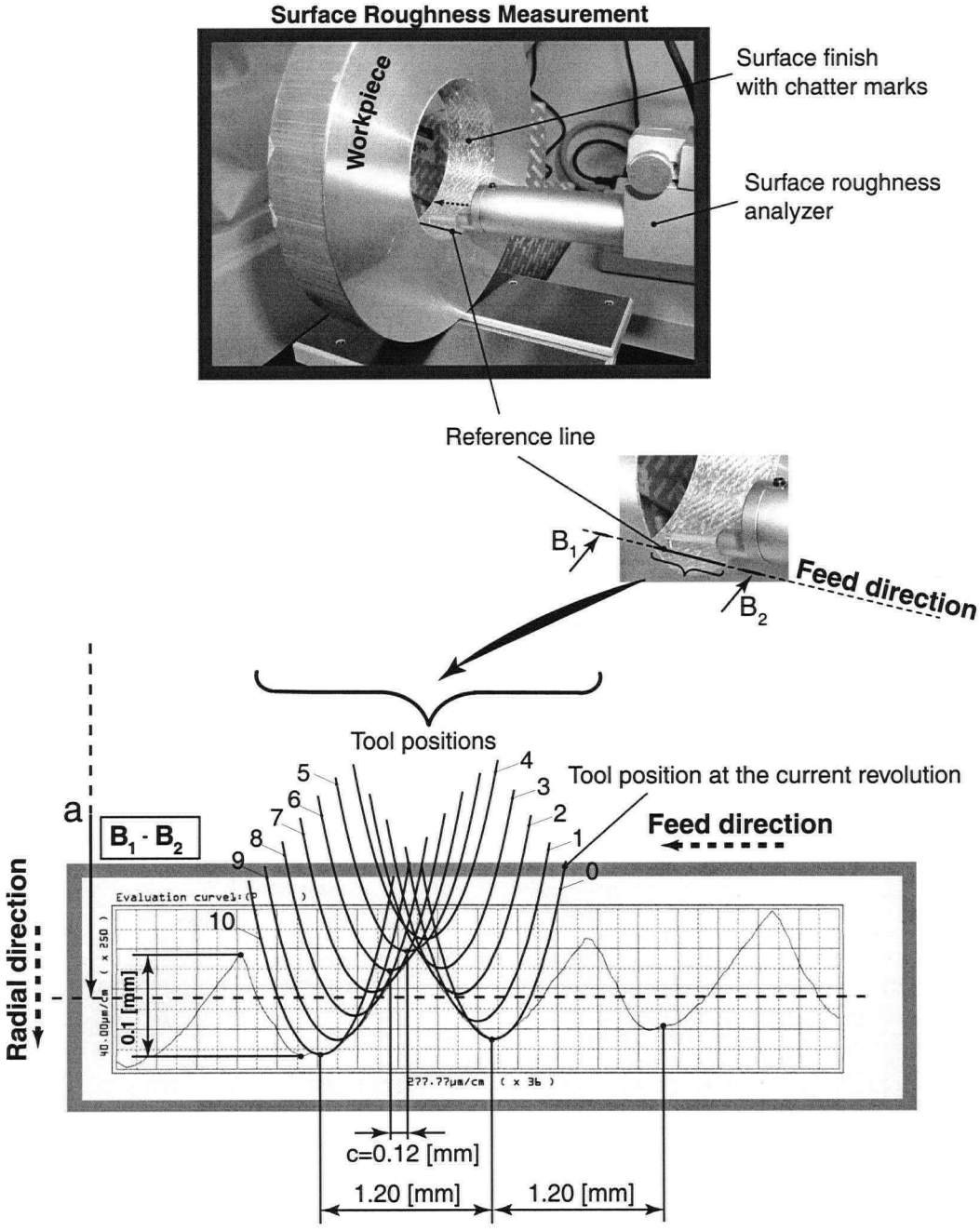

Figure 5.7 : Surface rougness measurement of the workpiece, a=0.75 [mm], c=0.12[mm/rev], V=184[m/min], n=1650[rpm], $\omega_c \cong 849.7$ [Hz], $\varepsilon \cong 324$ [Deg

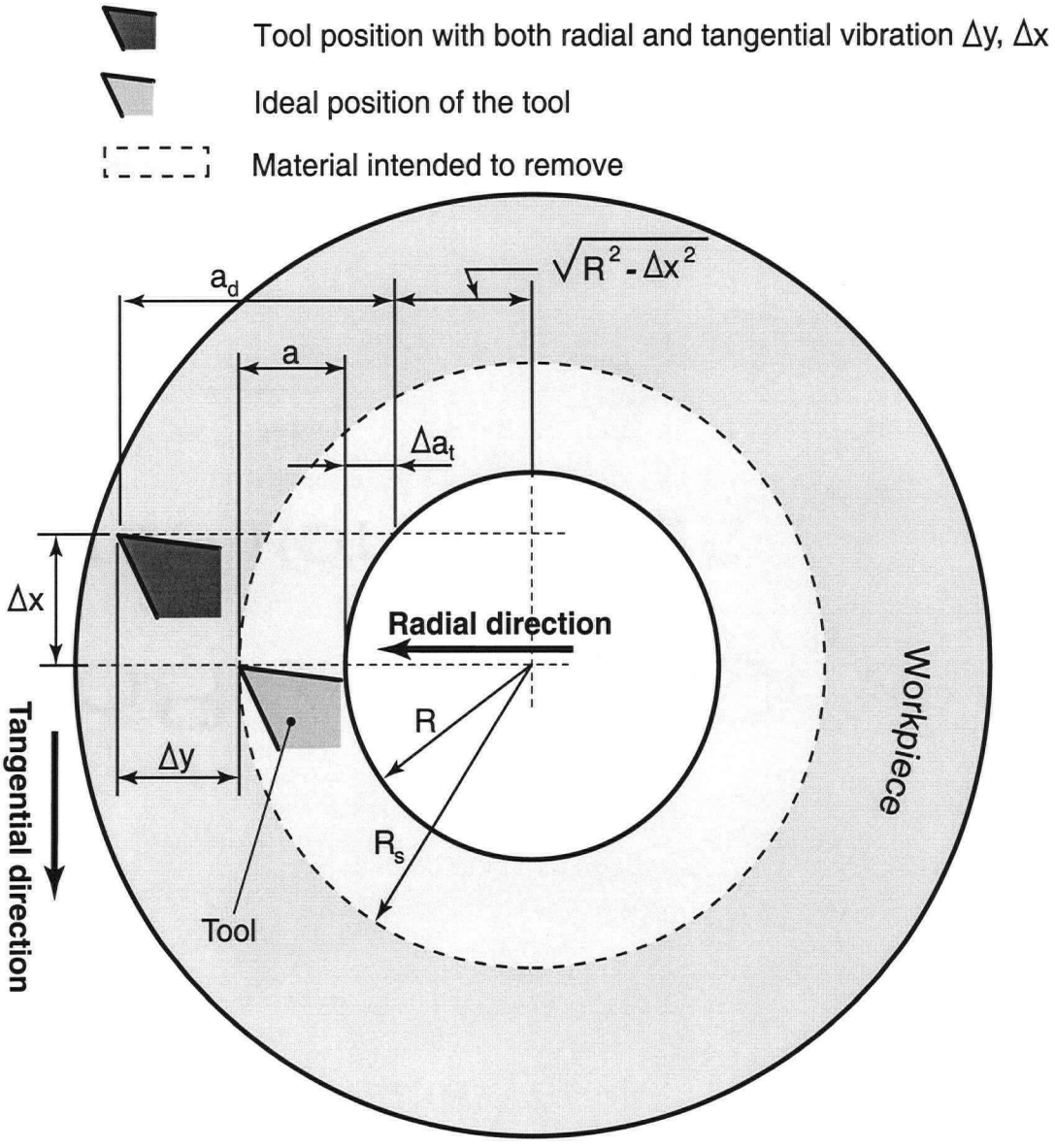

Figure 5.8 : The effect of the tangential vibrations in the regeneration of the waviness

5.2.2. Dynamic Cutting Force Prediction

The uncut chip area has a uniform shape during rigid cutting conditions. However, it varies drastically and may have an irregular and complicated form when the tool begins to vibrate (Figure 5.9). In some cases, more than three revolutions before the current one may need to be taken into consideration for the uncut chip area calculation and radial force prediction. Chapter 3 described the calculation of the uncut chip area, considering its exact geometry for cutting conditions with free chatter vibrations. The radial force was obtained as an exponential function of the cutting parameters Eq. (5.9). The prediction of the radial force requires the uncut chip area to be separated into two regions for more accurate results (Figure 3.15). Regions 1 and 2 are defined on the corner radius and the straight side of the tool, respectively. Based on the equations derived in Chapter 3, the radial force is determined as a component of the friction force.

$$F_r = F_{fr} Sin(\phi_L)$$

$$F_r = [K_{frc_1} A_1 + K_{frc_2} A_2 + K_{fre}(L_{c_1} + L_{c_2})] Sin(\phi_L)$$

$$F_r = [(e^{8.1965} L_{c_1}^{-0.6737} V^{-0.4210}) A_1 + (e^{9.6152} L_{c_2}^{-0.0241} V^{-0.7597}) A_2 + K_{fre}(L_{c_1} + L_{c_2})] \sin(\phi_L) \quad (5.9)$$

The radial cutting force is found as,

$$F_{rc} = F_r - K_{re} L_c \quad (5.10)$$

Then, the radial cutting force coefficient is obtained by dividing F_{rc} into A.

$$K_{rc} = \frac{F_{rc}}{A} \quad (5.11)$$

Variations in the depth of cut for stable and unstable cutting conditions are not equivalent in terms of the uncut chip area and force variation, due to the nonlinearities of the process caused by the corner radius of the insert R. As explained in the previous section, cutting force variations are completely dependent on the instant interaction between the current and previous tool positions at the same angular position of the hole circumference. Using the mechanistic model presented in

Chapter 3, the friction force is predicted based on the uncut chip area geometry, rather than by using the cutting parameters directly. This consideration was achieved by taking the contact length L_c of the tool with the workpiece into the derivation, and assuming that the total friction force passes through the centroid of each related region (Region 1 and 2). This approach adequately covers the complication of the uncut chip area geometry encountered in unstable cutting conditions, and enables the prediction of the cutting forces with good accuracy.

In Figure 5.9, the graphical representation of the dynamic friction force distribution along the cutting edge contact length L_c and uncut chip area variation are shown in comparison to those in the regular static case. The friction force is distributed proportionally to the uncut chip area of each differential element along the cutting edge contact length. The figures at the bottom (5.9-b1 and b2) show how much error could occur between the direct use of the cutting parameters (static base) and use of the uncut chip area geometry (dynamic base) for the same depth of cut variation in the prediction of the effective lead angle ϕ_L.

In the figure, indices *s* and *d* represent static and dynamic instances. Figure 5.9a shows a regular static uncut chip area form, in which the current and previous tool positions are the same. In this case, the chip thickness is reduced towards the tip of the tool, while its elemental effective lead angle increases with respect to the center of the corner radius. The friction force distribution conforms to the chip thickness reduction, which varies proportionally to the uncut chip area of each differential element along the cutting edge contact length. The friction force has the same magnitude at each differential element, and the elemental effective lead angle is the same on the straight side of the uncut chip area. Aditionally, the interaction of two positions that represent the dynamic variation of the depth of cut generates the uncut chip area 3 (Figure 5.9b). For this case, if the static model is considered, the effective lead angle and the total friction force, ϕ_{L-s}, F_{fr-s} will be over-predicted (Figure 5.9-b1). Consequently, the radial and feed forces (F_{r-s} and F_{f-s}) will be over-predicted as well. Figure 5.9-b2 shows the actual friction force distribution and the total friction force F_{fr-d} with corresponding effective lead angle ϕ_{L-d}. Presumably, the error

varies depending on the current interaction of the tool positions. Another schematic comparison is illustrated in Figure 5.9-c, in which the current tool position interacts with the tool position of the second revolution before the current one. This interaction produces the uncut chip area 4. Similar to this last case, when the current depth of cut becomes greater than the previous one, the total friction force F_{fr} and effective lead angle ϕ_L are under-predicted when the static-based model is considered.

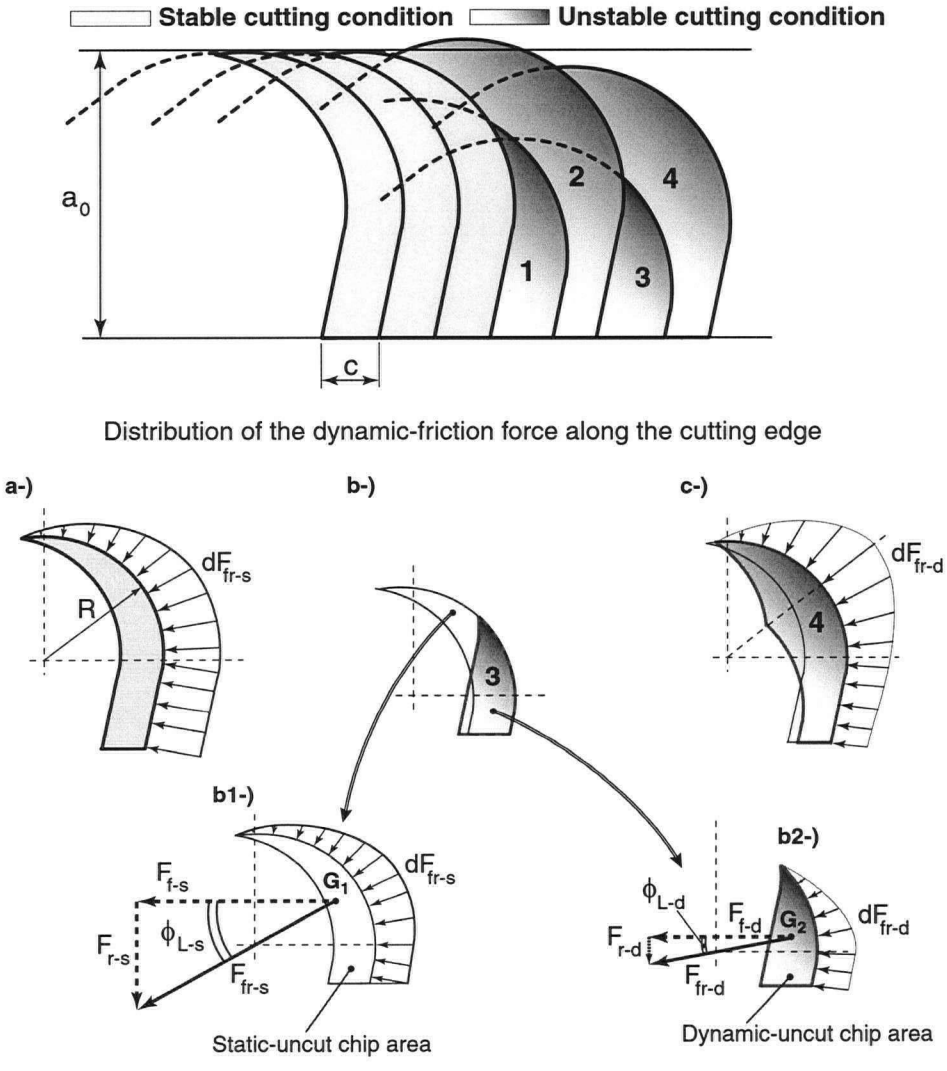

Figure 5.9 : The uncut chip area variation for unstable cutting condition; s and d imply the static and dynamic cutting conditions.

5.2.3. Wave Generation on the Surface

The number of waves left on the cut surface between subsequent revolutions is simply calculated with Eq. (5.1).

$$N = \frac{60\omega_c}{n} - \frac{\varepsilon}{2\pi}$$

In the boring process, the surface waviness shows different characteristics depending on the phase angle ε and the chatter frequency ω_c. The number of waves left on the cut surface should be equal to $N + \frac{\varepsilon}{2\pi}$ after a cutting operation. However, when counted, it was found to be different than expected. This can be explained as follows.

Depending on the interactions of the tool positions that are functions of the phase angle ε, different undulated patterns are created on the cut surface. This is explained in Figure 5.11, which shows the simulated surface finish for a wave period of 12 successive revolutions with the following system parameters: n=1650 [rpm], D=31.5 [mm] (Diameter of the hole), $a = 0.7[mm]$, $\varepsilon = 275°$, $\omega_c = 770\ [Hz]$

The period and length of a wave are calculated as,

$$T = \frac{1}{\omega_c} \qquad L_T = \frac{n}{60} 2\pi RT \tag{5.12}$$

where R is the radius of the circular hole and n is the spindle speed in [rpm].

In the first revolution, the tool reaches maximum depth at point-1 on its sinuosidal route (Figure 5.11 and 5.12). Having completed one full revolution, the tool moves inside the workpiece with the feed rate and reaches the maximum depth again, which is L_p [mm] ahead of the previous depth, at point 2 in the same period. L_p is the distance between two successive depths (in rotational direction) and defined as,

$$\begin{aligned} \varepsilon < \pi &\Rightarrow L_p = \varepsilon RT \\ \varepsilon \geq \pi &\Rightarrow L_p = (2\pi - \varepsilon)RT \end{aligned} \tag{5.13}$$

Other geometrical identification parameters may be c_i, L_i, α_1 and α_2, which identify the exact positions of the depths, and the inclination of the wave pattern created on the surface finish (Figure 5.12). These identification parameters can be determined with the algorithm illustrated with the flow charts (Figure 5.13 and 5.14). In these algorithms, the exact phase angle for each revolution is defined with respect to the phase angle in the first revolution. The tool makes the maximum depth when the period angle reaches to $\frac{2\pi}{3}$ for each revolution. Based on this definition, the angle θ, which indicates the distance of the tool depth L_n from the beginning of the period, is introduced, where n implies the number of revolutions. The positions of the tool depths in the feed direction are calculated with the following equation (5.14).

$$c_n = (n-1)c + \frac{L_n}{2\pi R}c \tag{5.14}$$

where R is the radius of the hole. Once, L_n and c_n are calculated, the depths are grouped and installed as a row of a matrix (as vectors) so that the inclination angles of the wave grooves can be obtained by using the specific elements of the vectors (Figure 5.12). Two inclination angles on the surface finish that describe the route of the tool with respect to the edge of the workpiece are defined as,

$$\alpha_1 = \text{atan}\left(\frac{L_{i,q+1} - L_{i,q}}{c_{i,q+1} - c_{i,q}}\right) \tag{5.15}$$

$$\alpha_2 = -\text{atan}\left(\frac{L_{i-1,q} - L_{i,q}}{c_{i-1,q} - c_{i,q}}\right) \tag{5.16}$$

where i is the group number, q is the element number of each vector. Hence, L_{q+1}, L_q and c_{q+1}, c_q are the second and first elements of any position vector defined by a group matrix.

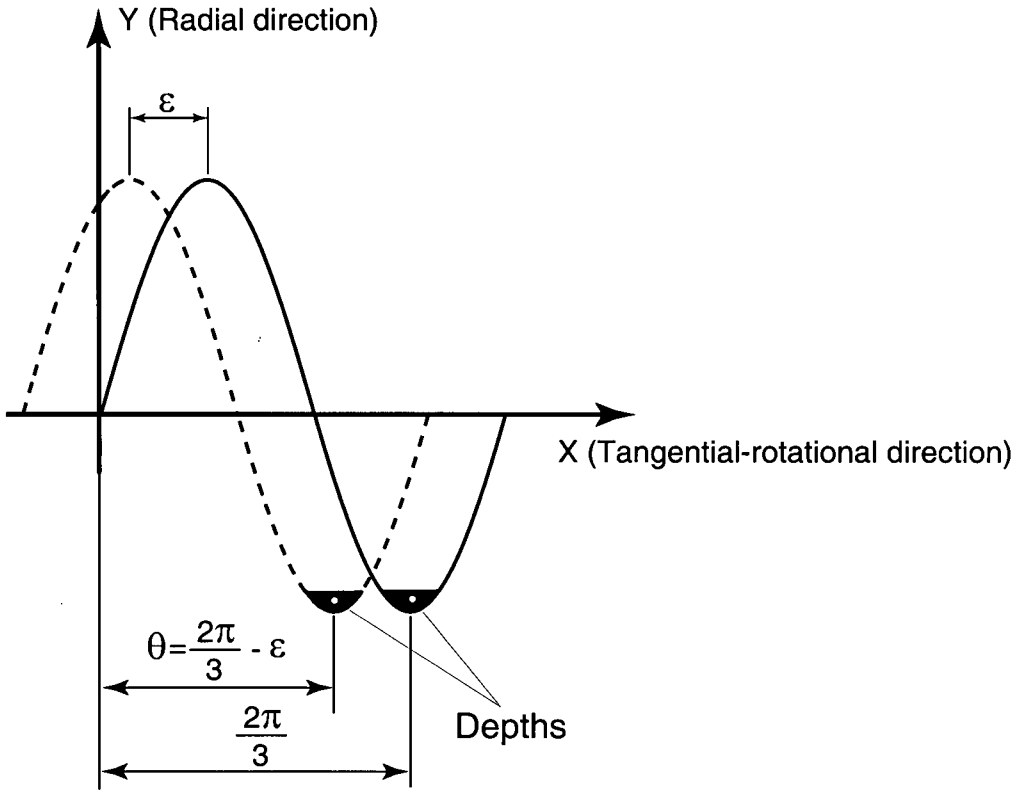

Figure 5.10 : Definition of the depth positions with θ

The process continues as formulated and produces the illustrated patterns for the given parameters. When counted, the number of waves is usually higher than expected because the tool depths are arranged in grooves, which are seen as waves.

In addition to the first one, two more examples exposing different patterns can be depicted for different parameters (Figure 5.15 and 5.16).

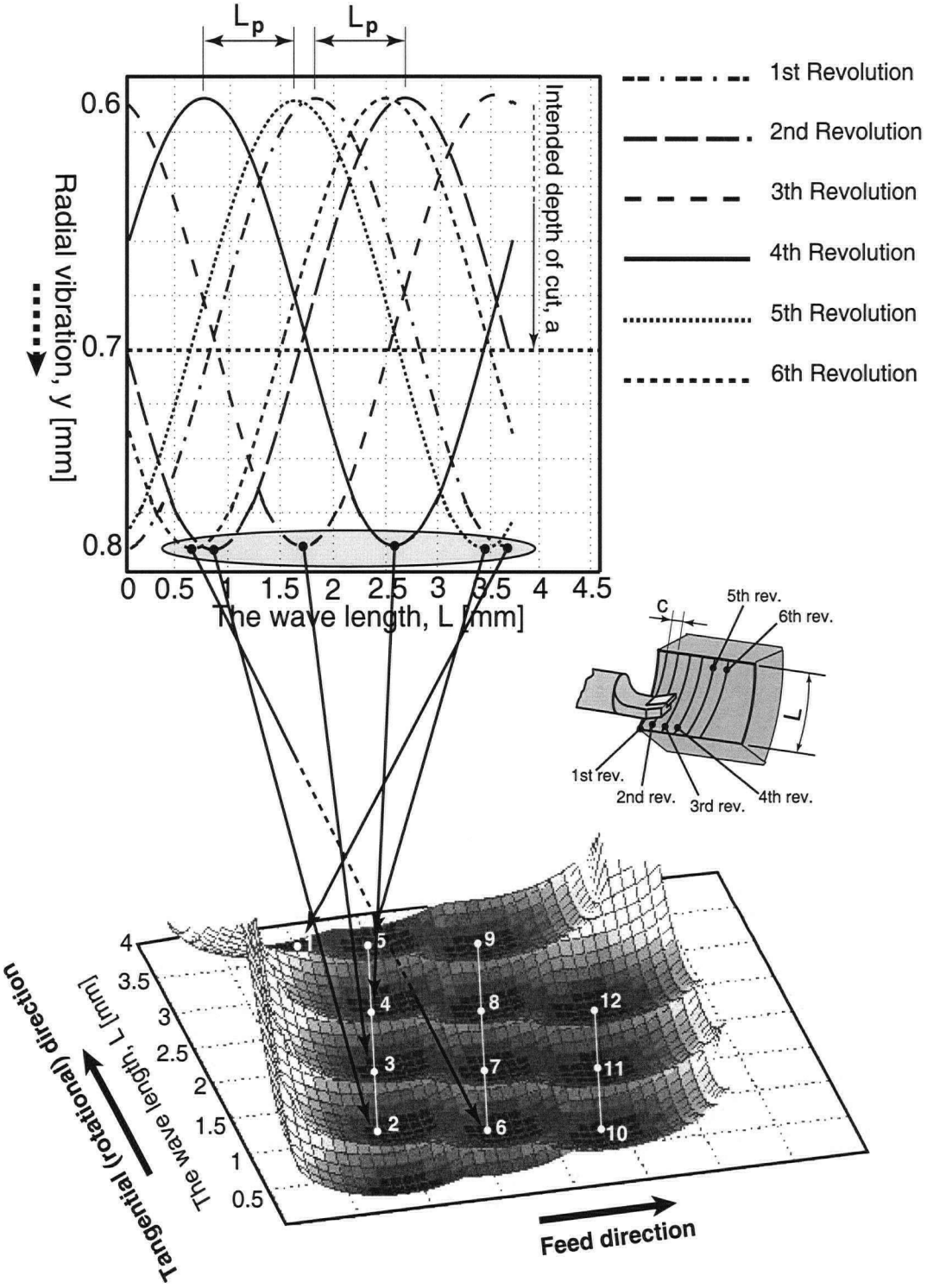

Figure 5.11 : Wave generation, phase angle $\varepsilon = 275°$, chatter frequency $\omega_c = 770$ [Hz], black and white dots show the depths the tool make in the first 6 revolutions

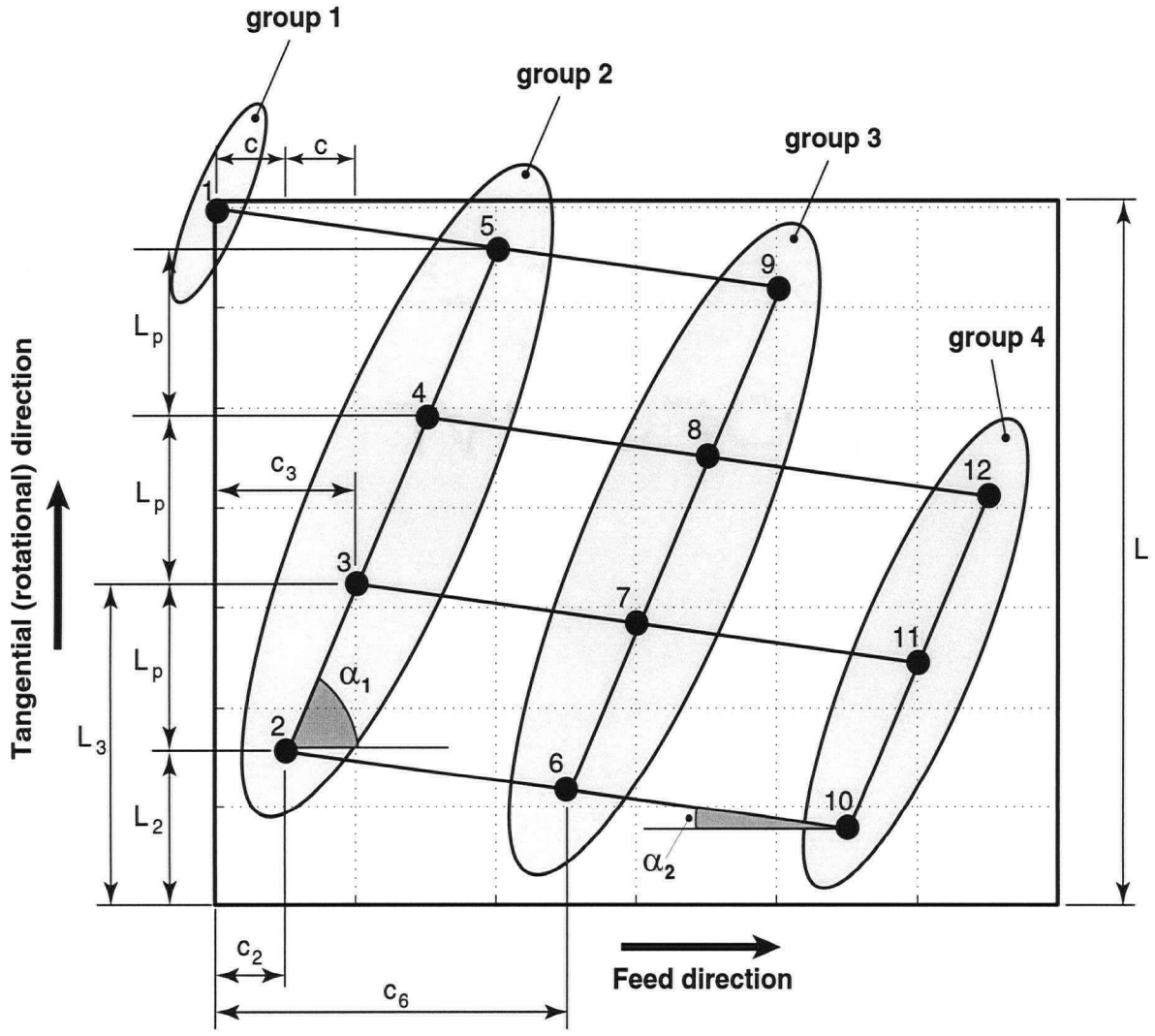

Figure 5.12 : Identification of the surface finish geometrical parameters. Black dots show the depths created by the tool in its sinusoidal vibration; $n = 1650[rpm]$, $D = 31.5[mm]$, $\varepsilon = 275°$, $\omega_c = 770[Hz]$

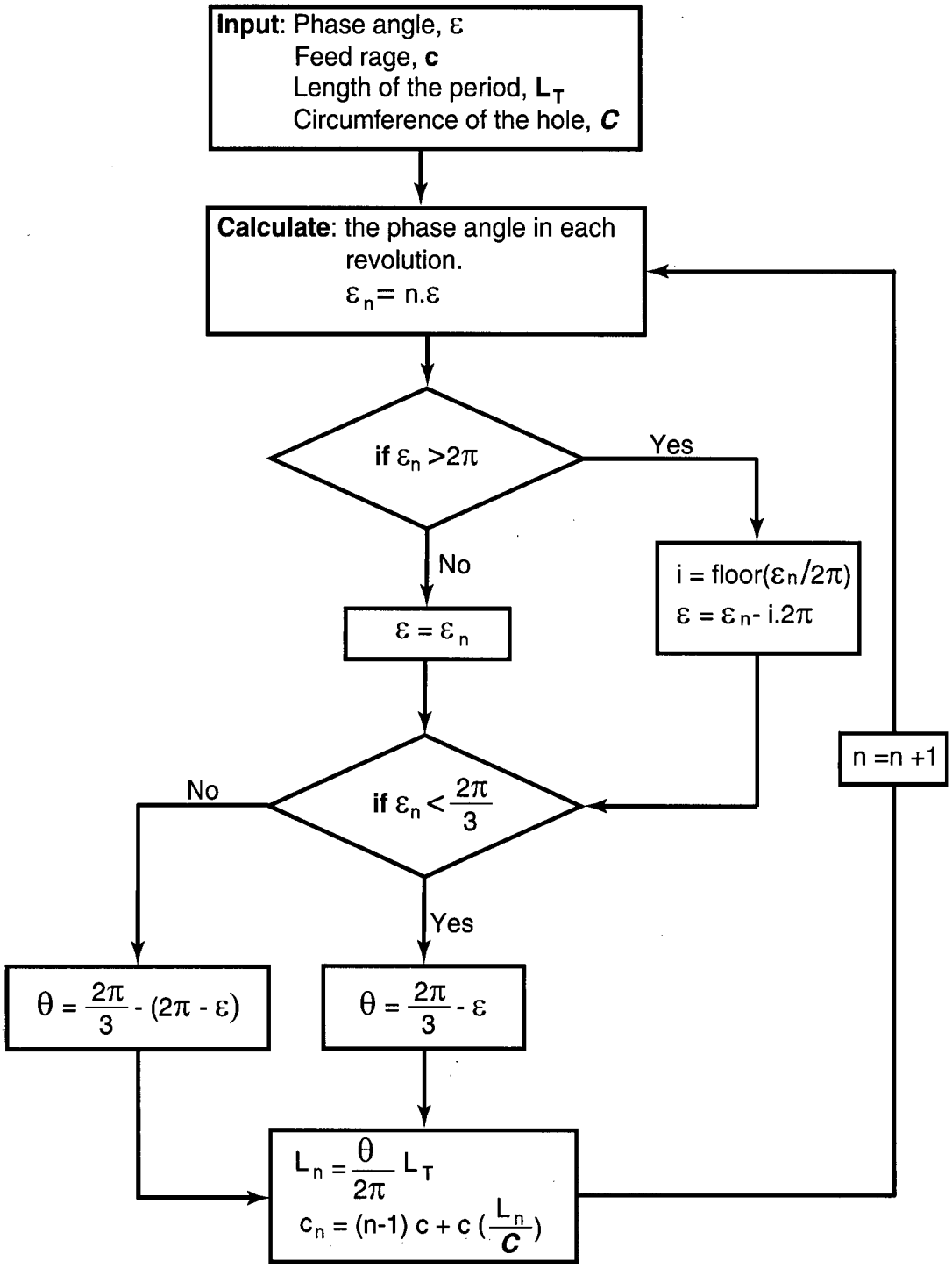

Figure 5.13 : Depth position determination algorithm in each wave period

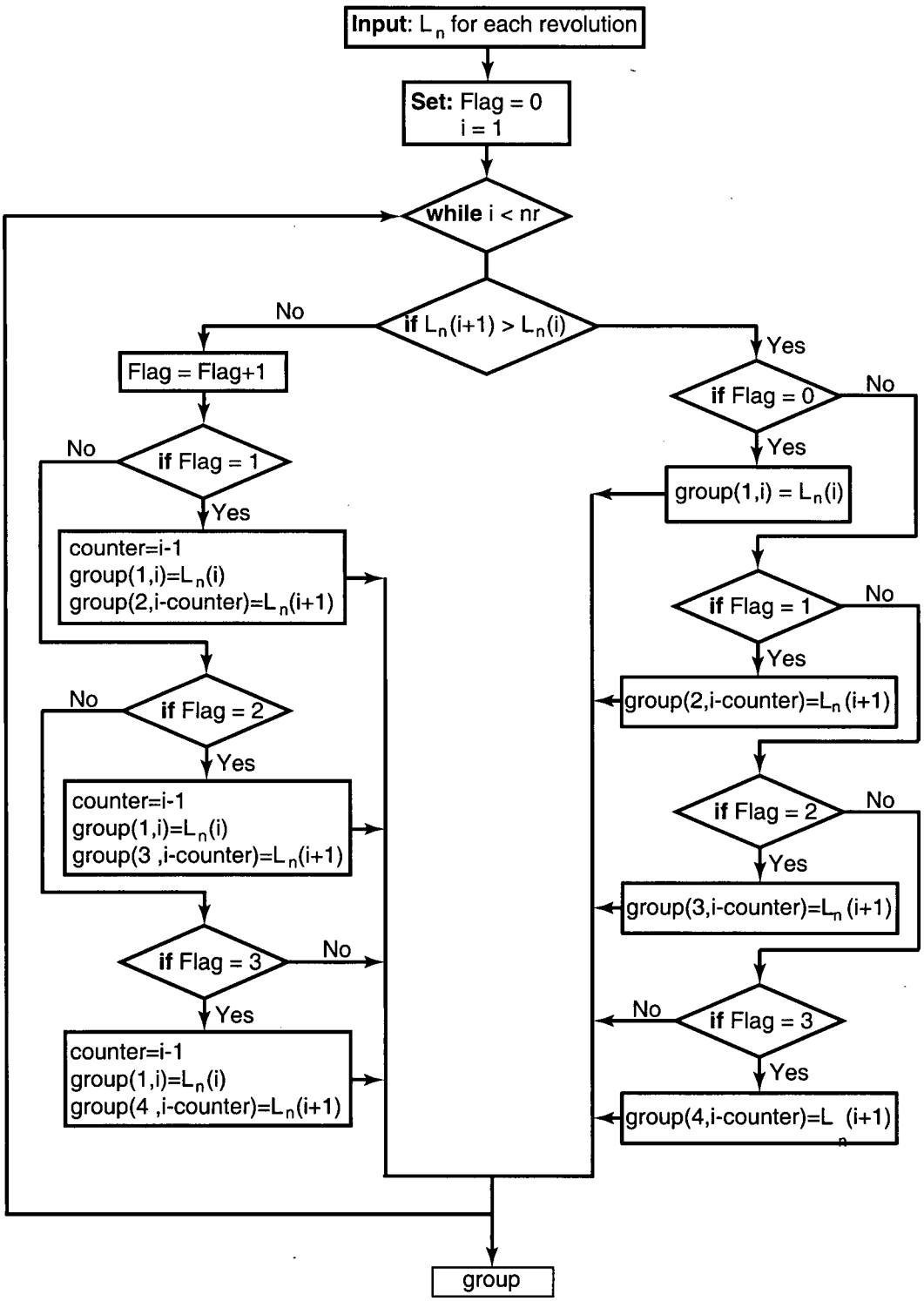

Figure 5.14 : Flow chart to group the deeps for the identification of the inclination angles α_1 and α_2.

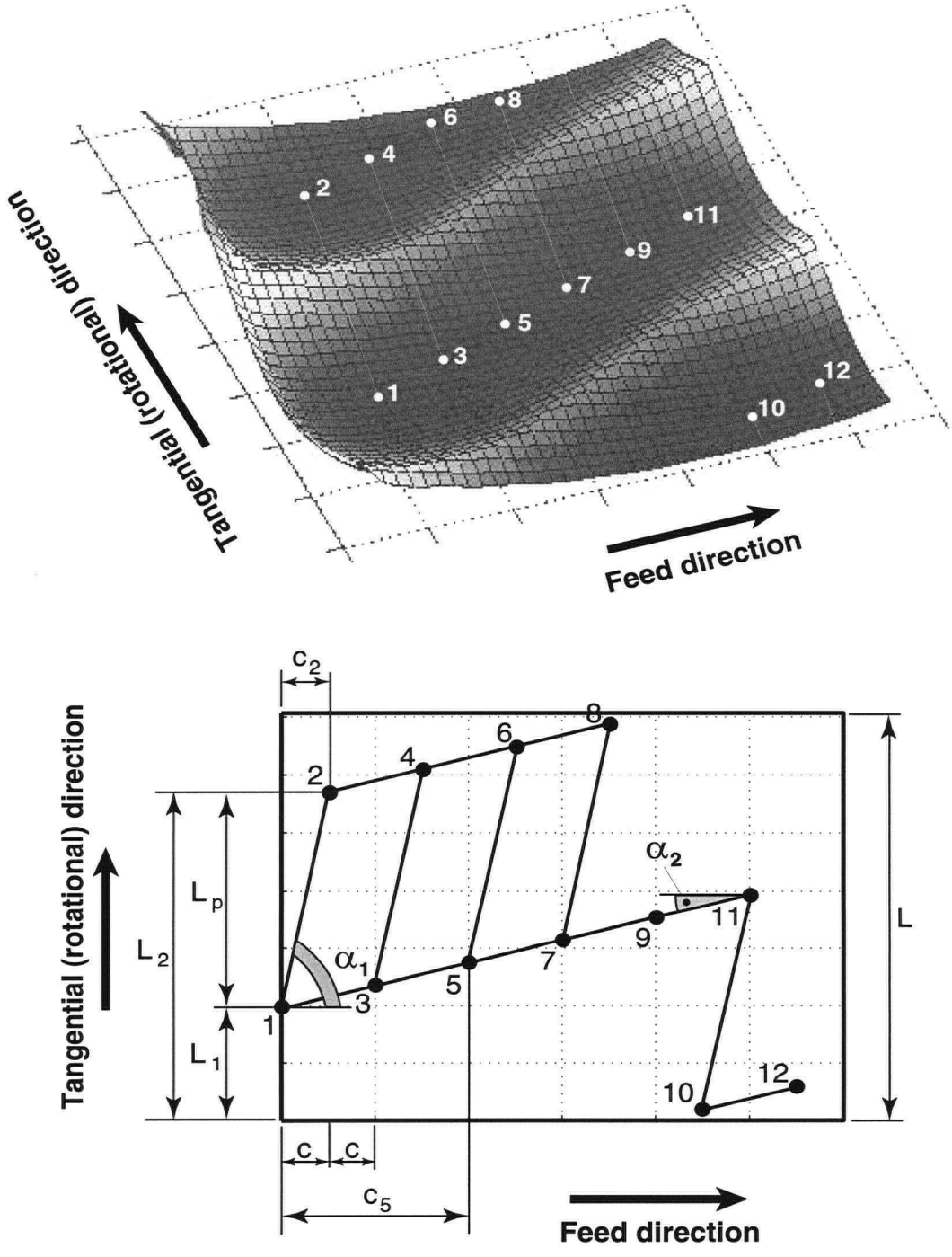

Figure 5.15 : Simulated wave generation on the surface finish under the contidion of phase angle $\varepsilon = 170°$, chatter frequency $\omega_c = 770$ [Hz]; Black dots show the depths.

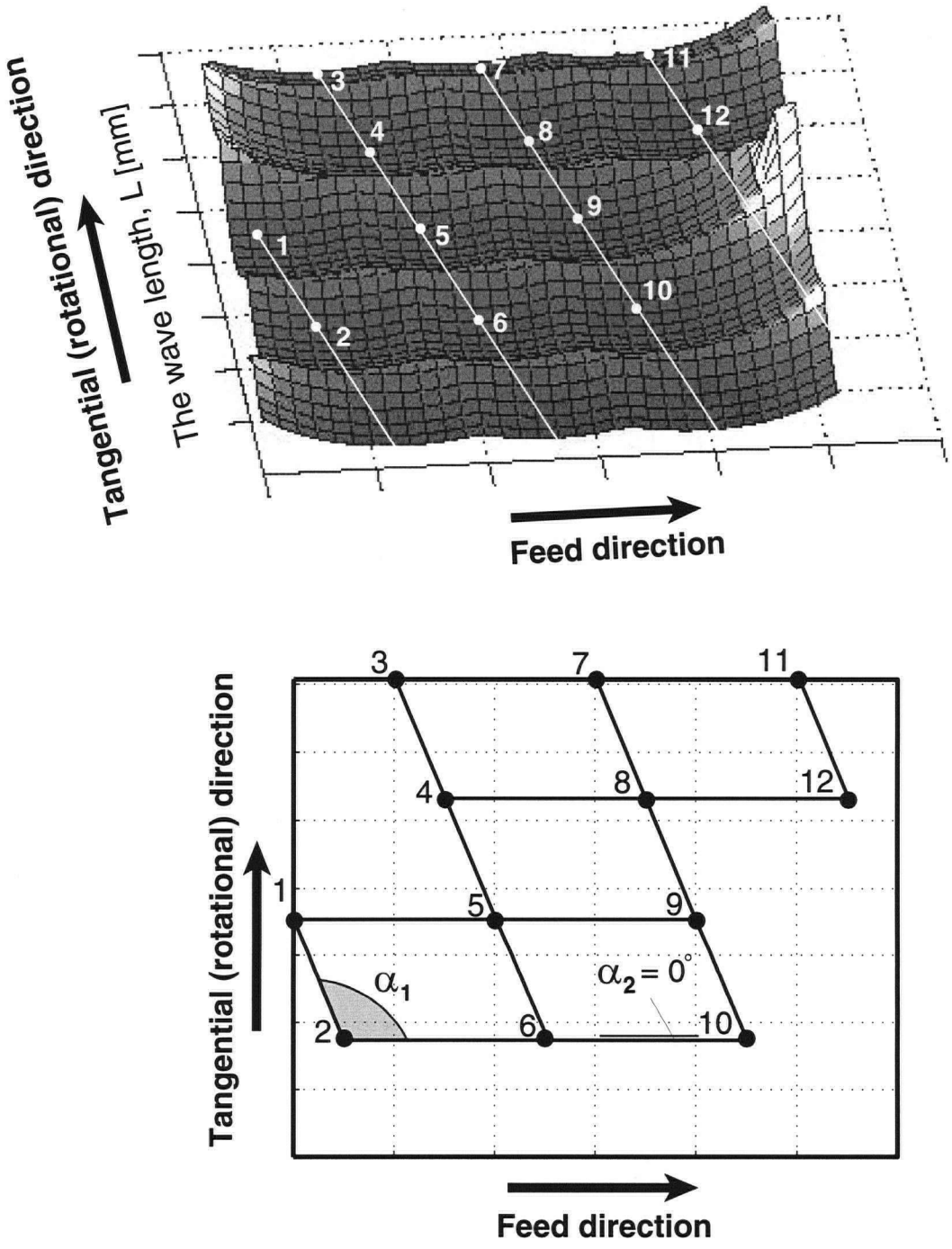

Figure 5.16 : Simulated wave generation on the surface finish under the contidion of phase angle $\varepsilon = 90°$, chatter frequency $\omega_c = 770$ [Hz]

5.3. Chatter Stability

5.3.1. Analytical Approach for Stability Solution

This section presents an analytical approach for the dynamic boring process, in which the regenerative effect is modeled considering only the vibrations in the radial direction.

As detailed in the preceding sections, the geometry and dynamics of the regenerative effect in boring are different. Nonlinear variation of the radial force with the instantaneous radial vibration, and the preceding vibration history of more than one revolution, makes the modeling of chatter in the boring process more difficult than other existing models, such as milling and turning. The main consideration in the analytical solution is how the nonlinear dynamic characteristic parameters, namely radial cutting force coefficient K_{rc}, and uncut chip area A, are involved in the dynamic boring model. The first stage has been to make certain assumptions that will facilitate the analysis, and linearize the relation between the parameters K_{rc}, A, and L_c, which are employed in the radial force prediction and the vibration of the boring bar y. The following assumptions are made to simplify the process.

- The amplitude of the chatter vibrations is assumed to be within a range of %10 of the intended depth of cut a.

- The radial cutting force coefficient K_{rc} is determined with Equation (5.11) and is assumed not to change and remain constant for the given range of the vibration amplitude. Only the influence of the uncut chip area variation is considered in the radial force variation.

- The uncut chip area calculation is simplified with the following linear equation, [10]

$$A = ca \tag{5.17}$$

where c and a are the feed rate and depth of cut. Based on the assumptions made above, the chatter vibrations in the boring process can be represented with the following block diagram, in which three gain factors, K_1, K_2, and K_3, are used to linearize the dynamic uncut chip area variation (Figure 5.17). The input of the system is the intended radial depth of cut a_0. y_1, y_2 and y_3

are the vibrations measured on the same angular position of the hole circumference, in the current, previous, and the second revolution before the current one, respectively. The dynamic depth of cut a_1 is obtained by adding the current vibration y_1 to the intended depth of cut a_0 (Eq.(5.6)). In this case, the vibration direction into the workpiece is taken as positive. The effect of the previous vibrations (y_2 and y_3) on the uncut chip area variation are considered with the linear relation presented in Equation (5.18). In the model, gain factors K_1, K_2, and K_3 are supposed to be tuned throughout the depth of cut range with small segments. For each segment, 20 different combinations of the tool vibrations within the vibration amplitude range (10% of the depth of cut) are considered, and the corresponding uncut chip areas are calculated. Based on the calculated uncut chip areas and the expression (5.18), linear regression has been performed for the identification of the gain factors.

$$A = c[K_1(a_0 - y_1) + K_2(a_0 - y_2) + K_3(a_0 - y_3)] \tag{5.18}$$

$$A = K_1A_1 + K_2A_2 + K_3A_3 \tag{5.19}$$

In this evaluation, the dynamic uncut chip area A is determined based on the vibration history of two preceding revolutions considered by the gain factors K_1, K_2, K_3, and the aspect of the static behaviour of the process, in which the uncut chip area is approximately calculated with Equation (5.17). The geometrical representation of the evaluation is indicated in Figure 5.17. It should be noted that A_1, A_2, and A_3 are the corresponding static uncut chip areas for the depth of cuts a_1, a_2, and a_3.

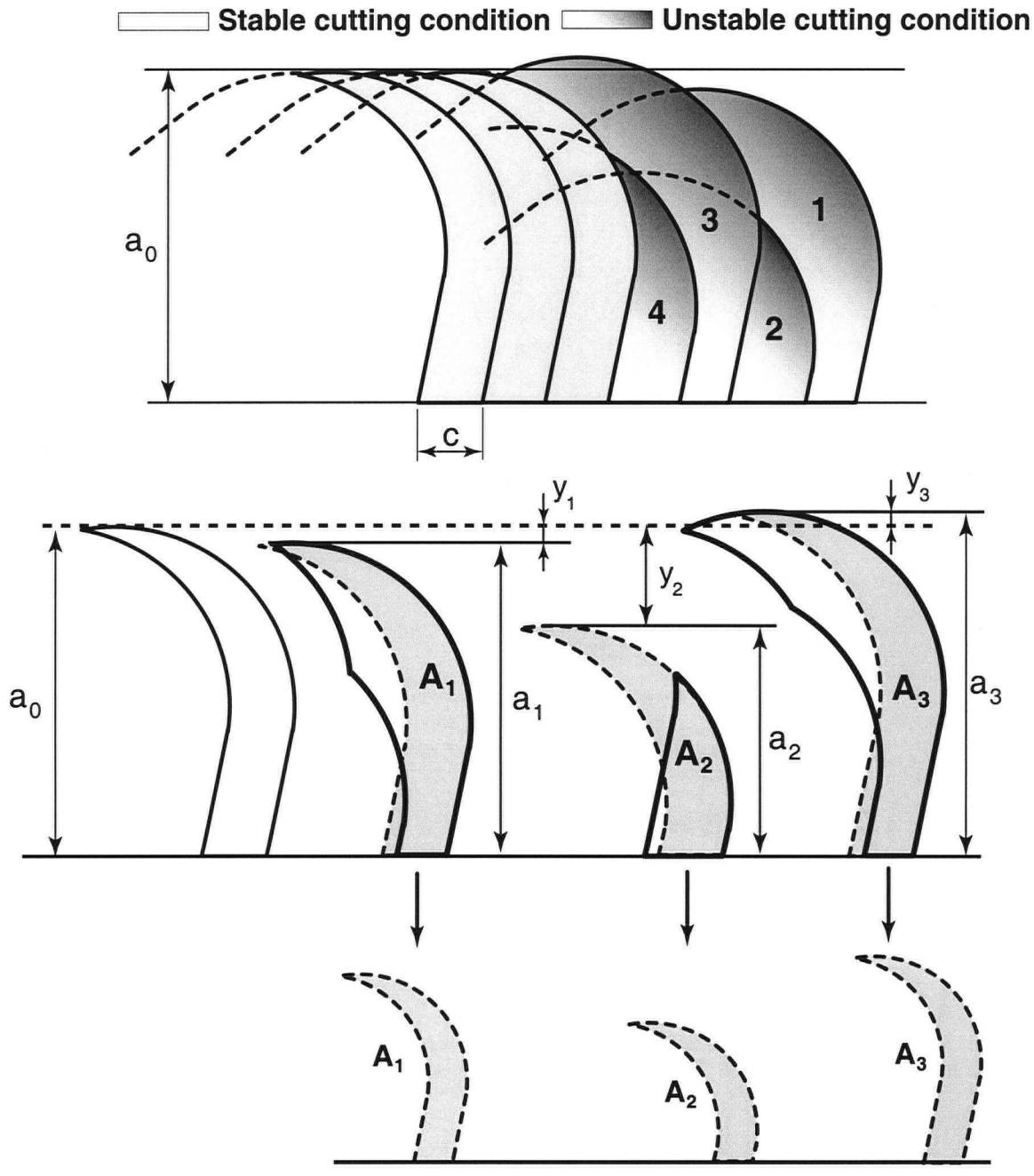

Figure 5.17 : Illustration of the uncut chip areas in Eq. (5.18)

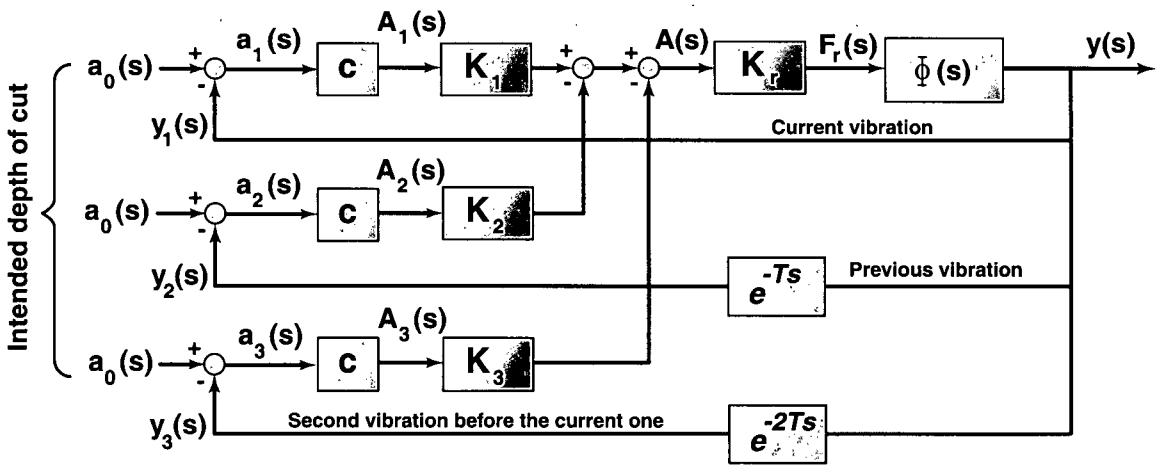

Figure 5.18 : Block diagram representation of the boring process

The dynamic chip area can be written in Laplace domain as follows.

$$A(s) = c\{K_1[a_0(s) - y_1(s)] - K_2[a_0(s) - y_2(s)] - K_3[a_0(s) - y_3(s)]\} \tag{5.20}$$

The dynamic uncut chip area produces the dynamic radial cutting force with the following expression.

$$F_{rc}(s) = K_{rc}A(s) \tag{5.21}$$

The radial cutting force induces vibration on the boring bar,

$$y(s) = F_{rc}(s)\Phi(s) \tag{5.22}$$

where $\Phi(s)$ is the transfer function of the system, which is implemented based on the dynamic characteristics of the boring bar structure obtained by performing impact hammer tests (Figure 5.19). For the conceptual evaluation, the structure with a single mode can be considered with the following transfer function (Eq. (5.23)). The implementation of the transfer function is explained in detail in the next section.

$$\Phi(s) = \frac{y(s)}{F_{rc}(s)} = \frac{1/m}{s^2 + 2\zeta\omega_n s + \omega_n^2} \tag{5.23}$$

Substitution of $A(s)$ and $F_{rc}(s)$ into Equations (5.21) and (5.22) yields,

$$y(s) = \left[a_0(s)\left[K_1 - K_2 - K_3\right] - y(s)\left[K_1 - K_2 e^{-sT} - K_3 e^{-2sT}\right]\right] cK_r\Phi(s) \tag{5.24}$$

The previous vibrations, y_2 and y_3, are defined with delay terms in the model. The resulting transfer function between the vibration of the structure $y(s)$ and intended depth of cut a_o can be obtained as follows.

$$\frac{y(s)}{a_0(s)} = \frac{\left[K_1 - K_2 - K_3\right] cK_{rc}\Phi(s)}{1 + \left[K_1 - K_2 e^{-sT} - K_3 e^{-2sT}\right] cK_{rc}\Phi(s)} \tag{5.25}$$

The characteristic equation of the above transfer function is,

$$1 + \left[K_1 - K_2 e^{-sT} - K_3 e^{-2sT}\right] cK_r \Phi(s) = 0 \tag{5.26}$$

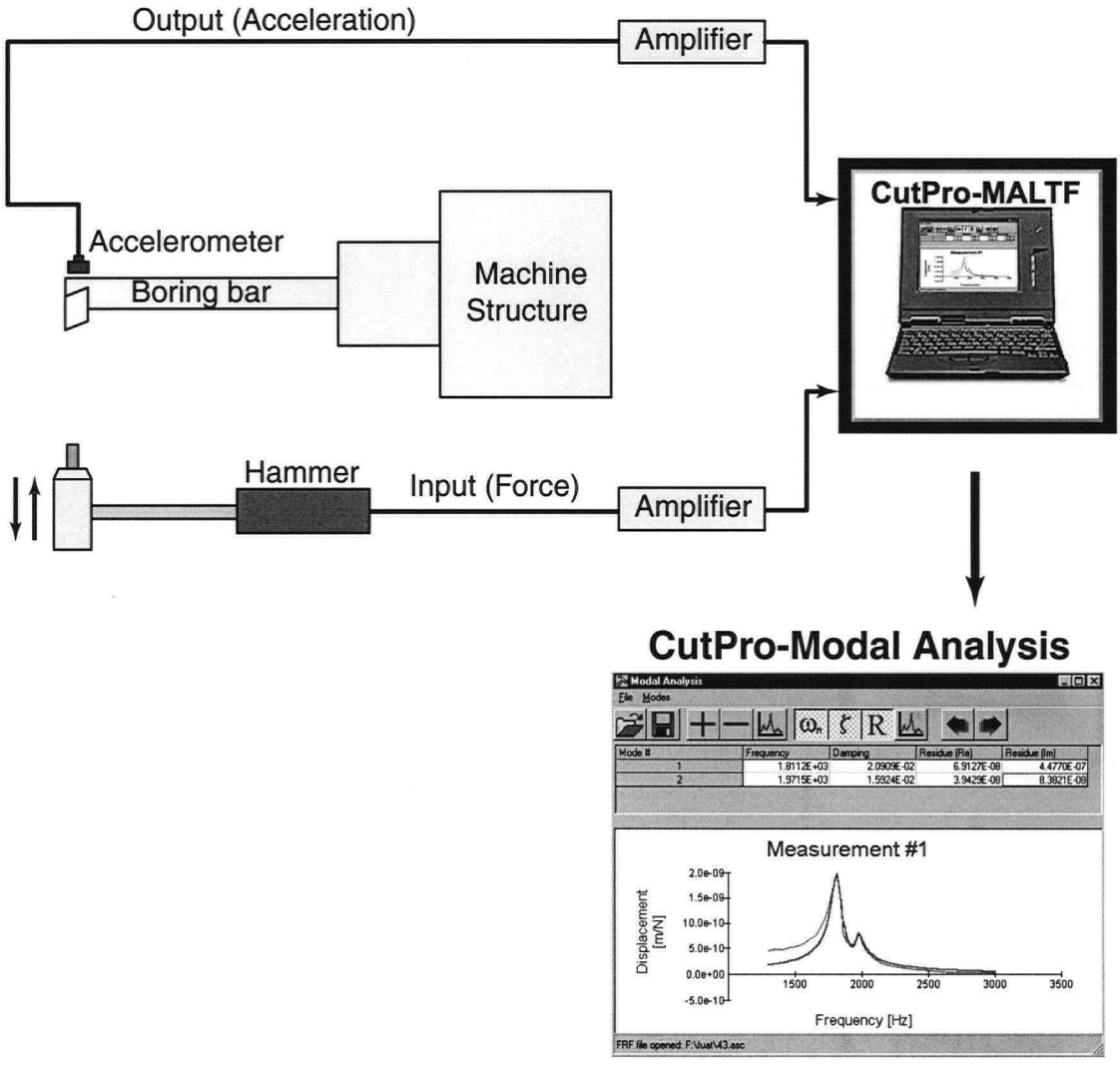

Figure 5.19 : Transfer function measurement using the impact hammer test

After the linearization of the system, the stability of the process can be examined with the frequency response method, which is performed by replacing s with $j\omega$ in the transfer function of the system. The magnitude and phase angle of the transfer function ($\phi(j\omega)$) can be illustrated by graphical plots that provide significant insight.

The block diagram representation of Eq. (5.22) is shown in Figure 5.20. The input of the system is sinusoidal radial force $F_r(s)$, and the resulting output is the radial displacement of the structure $y(s)$, which differs from the input waveform only in amplitude and phase angle .

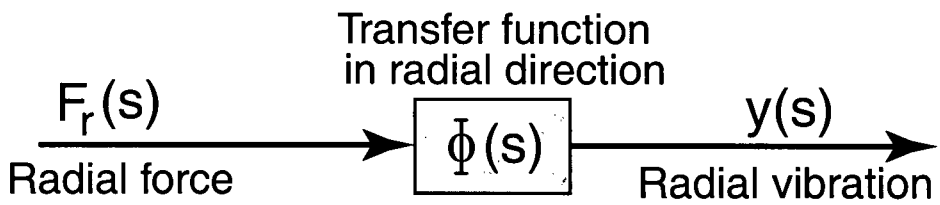

Figure 5.20 : Block diagram representation of Equation (4.23)

The transfer function is described in the frequency domain as,

$$\Phi(j\omega) = G + jH \tag{5.27}$$

where G is the real and jH the imaginary part of the transfer function. From the characteristic equation of the transfer function (Eq. 5.26) the critical borderline of feed rate value is obtained as,

$$c_{lim} = \frac{-1}{K_r[G(K_1 - K_2 cos(\omega_c T) - K_3 cos(2\omega_c T)) - H(K_2 sin(\omega_c T) + K_3 sin(2\omega_c T))]} \tag{5.28}$$

c_{lim} is the maximum allowable critical feed rate for a cutting condition with free chatter vibration.

Phase angle of the structure ψ is,

$$\tan\psi = \frac{H(\omega_c)}{G(\omega_c)} = \frac{\sin(\omega_c T)(K_2 + 2K_3\cos(\omega_c T))}{[-K_1 + K_2\cos(\omega_c T) + K_3\cos(2\omega_c T)]} \tag{5.29}$$

Equation (5.1) is expressed in the form of,

$$\omega_c T = 2\pi N + \varepsilon \tag{5.30}$$

where ω_c and T are the chatter frequency in [rad/sec] and period of the one full revolution. Substituting Eq. (5.30) into Eq. (5.29) yields,

$$\psi = \text{atan}\left[\frac{\sin(\varepsilon)[K_2 + 2K_3\cos(\varepsilon)]}{[-K_1 + K_2\cos(\varepsilon) + K_3\cos(2\varepsilon)]}\right] \tag{5.31}$$

Equation (5.31) is a nonlinear and requires an iterative solution to find the phase angle ε.

The variation in the radial cutting force coefficient in the presence of chatter vibrations is investigated with the following parameters: depth of cut, $a = 0.7[mm]$, feed rate, $c = 0.1[mm/rev]$ and cutting speed, $V = 150[m/min]$.

The displacements of the tool for five successive revolutions were considered to be in the range of %10 of the depth of cut, a, (i.e. ∓ 0.07 [mm]). a_1, a_2, a_3, a_4, and a_5 are the instant depth of cuts of the current, previous, third, fourth, and fifth revolutions at the selected 8 positions of a wave period as shown in Figure 5.21. The corresponding vibrations are shown with the same indices with the notation of y. For the selected tool positions, calculated uncut chip areas A, cutting edge contact lengths L_c, predicted radial cutting forces F_{rc} and its coefficients K_{rc}, are shown in Table 5.2. Figures 5.22 and 5.23 depict the corresponding uncut chip area shapes, (i.e. the amount of material removed by the tool) at the selected 8 positions of the 5th revolution of the simulated process. As can be noticed, the uncut chip area A varies drastically at these particular positions of 5 sucessive revolutions during each revolution.

Figures 5.24, 5.25 and 5.26 show the actual values of the parameters determined, based on the mechanistic model and their average values calculated by considering only the static nature of the process (second assumption). These average values are determined for the test conditions given above. As can be seen in the figures, the error between the predicted dynamic radial cutting force coefficients K_{rc} and average values may go up to 20[%] in some cases.

Table 5.2 : Prediction of the radial force considering the specified vibration history

	POINT-1	POINT-2	POINT-3	POINT-4	POINT-5	POINT-6	POINT-7	POINT-8
a_1 [mm]	0.6345	0.6673	0.7264	0.7577	0.77	0.7322	0.6641	0.63
a_2 [mm]	0.7211	0.7601	0.7661	0.7427	0.7018	0.6396	0.6381	0.6953
a_3 [mm]	0.7678	0.739	0.6805	0.6468	0.6302	0.6615	0.7295	0.7695
a_4 [mm]	0.686	0.644	0.6318	0.6518	0.6909	0.7563	0.765	0.7119
a_5 [mm]	0.6308	0.6552	0.7123	0.7481	0.7688	0.7444	0.6773	0.6317
L_c [mm]	0.5852	0.5932	0.9344	1.3840	1.4312	1.2760	0.9728	0.6823
A [mm^2]	0.0251	0.0266	0.0489	0.0878	0.1338	0.1317	0.0710	0.0303
Predicted K_{rc} [N/mm^2]	394.31	343.27	331.95	381.49	391.63	385.43	410.59	413.55
Predicted F_{rc} [N]	9.88	9.14	16.25	33.51	52.39	50.77	29.16	12.52
Predicted F_r [N]	14.83	14.15	24.15	45.21	64.49	61.55	37.38	18.29
Predicted ϕ_L [Deg]	29.27	26.82	31.88	43.76	52.10	49.60	41.91	32.37
Predicted K_{frc} [N/mm^2]	631.44	625.71	460.68	353.57	345.68	373.46	448.37	569.38
Predicted F_{frc} [N]	15.82	16.65	22.55	31.06	46.25	49.19	31.84	17.24
Predicted F_{fr} [N]	30.33	31.36	45.72	65.37	81.73	80.82	55.96	34.15

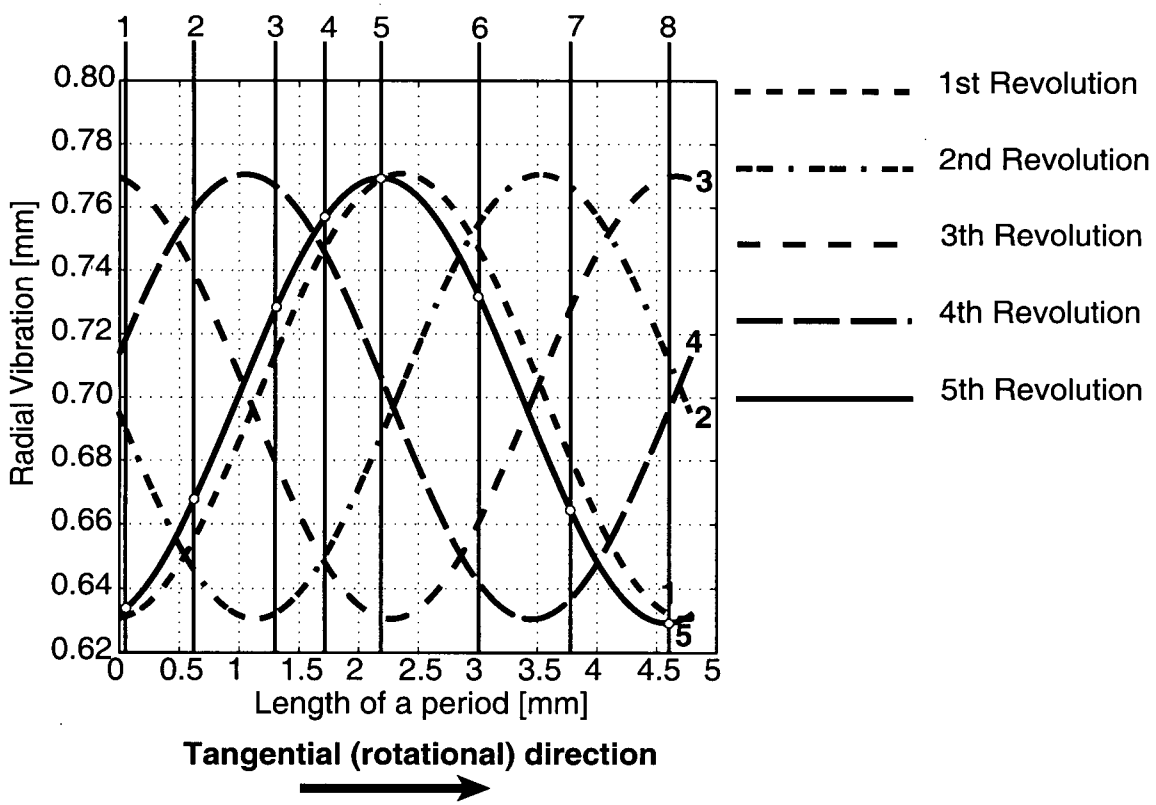

Figure 5.21 : Dynamic radial force simulation, a=0.7 [mm], amplitude of the vibration=0.07[mm]

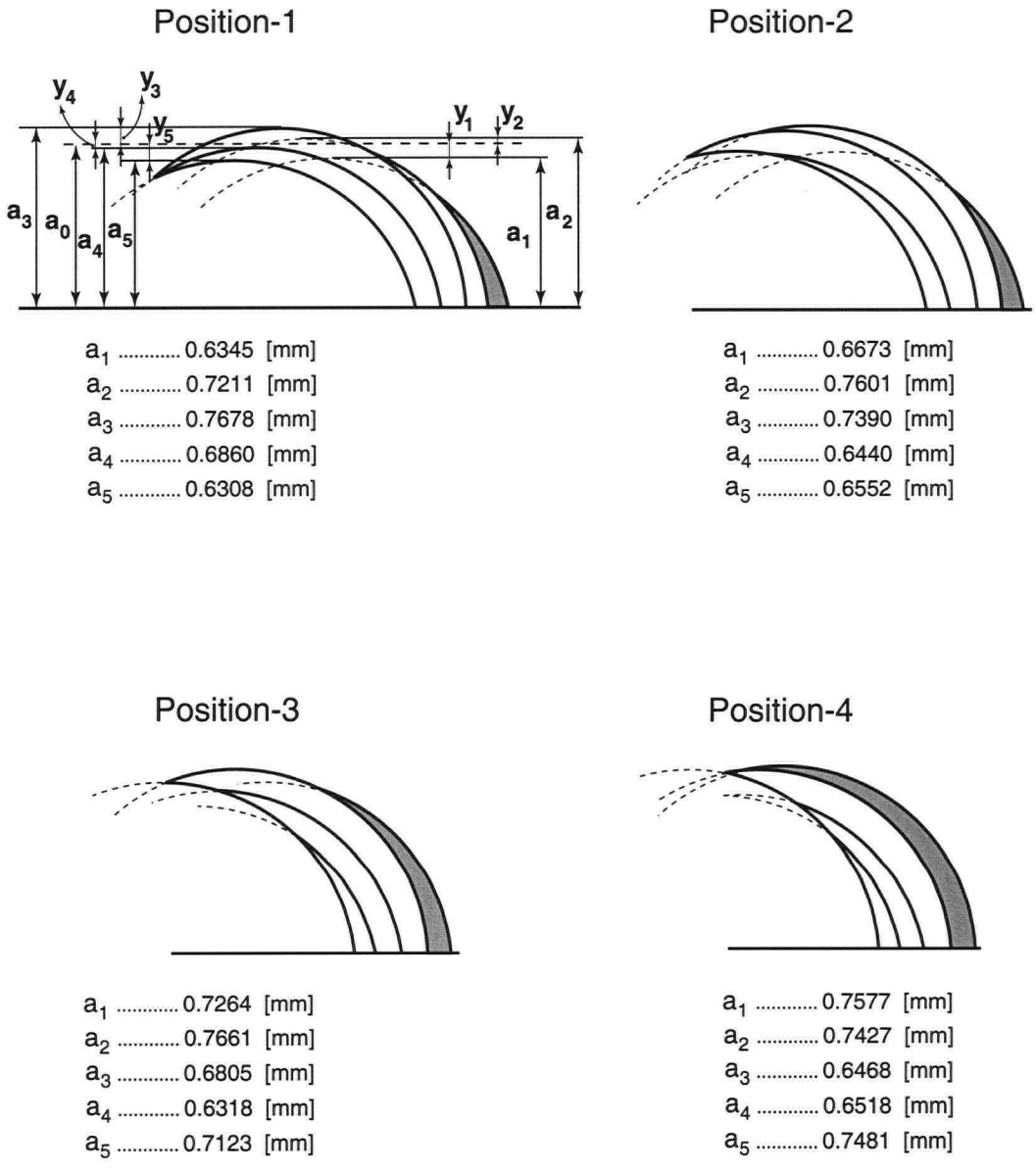

Figure 5.22 : The uncut chip area variations at the positions 1, 2, 3 and 4

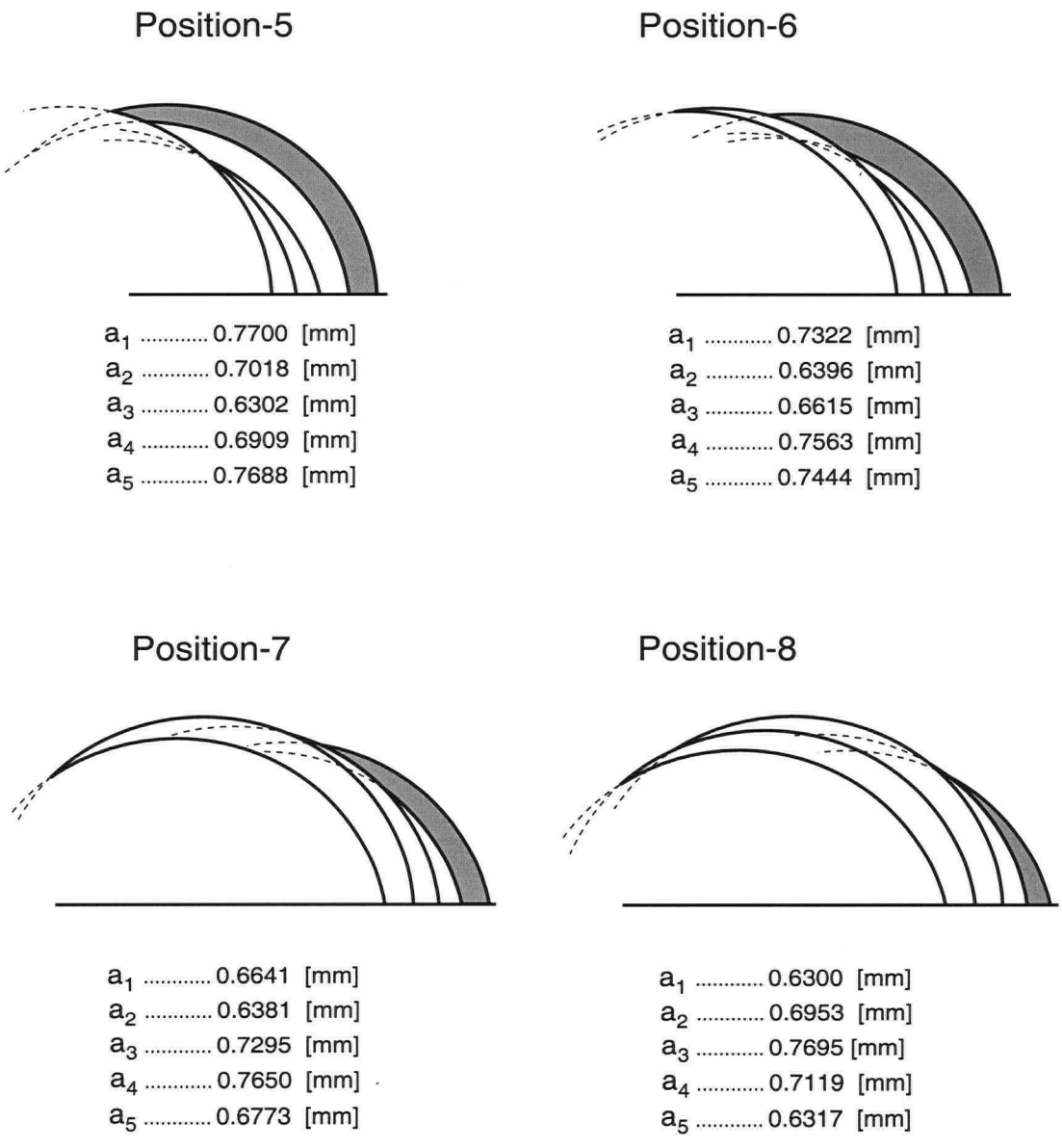

Figure 5.23 : The uncut chip area variations at the positions 5, 6, 7 and 8

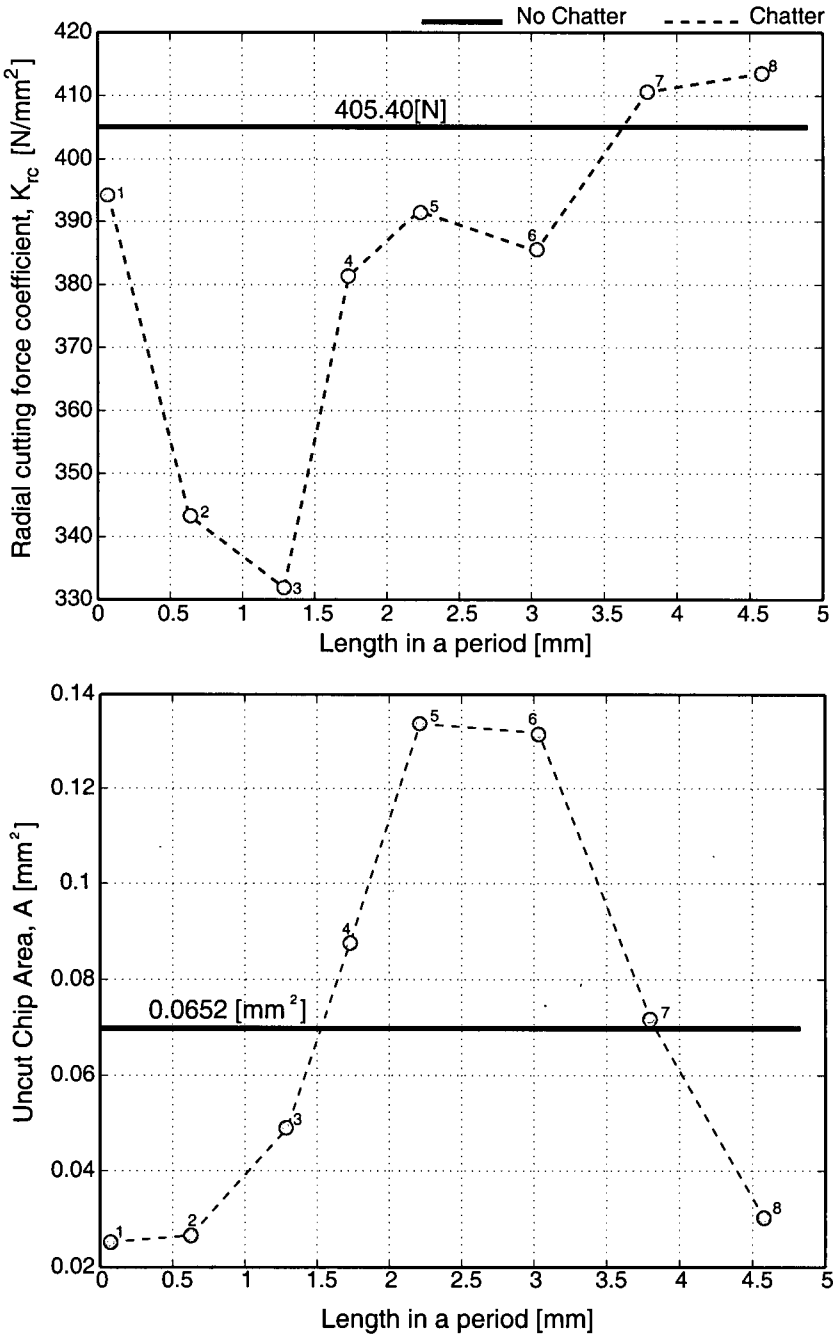

Figure 5.24 : The Variation of the radial cutting force coefficient and uncut chip area for the specified vibration history (Table 5.2)

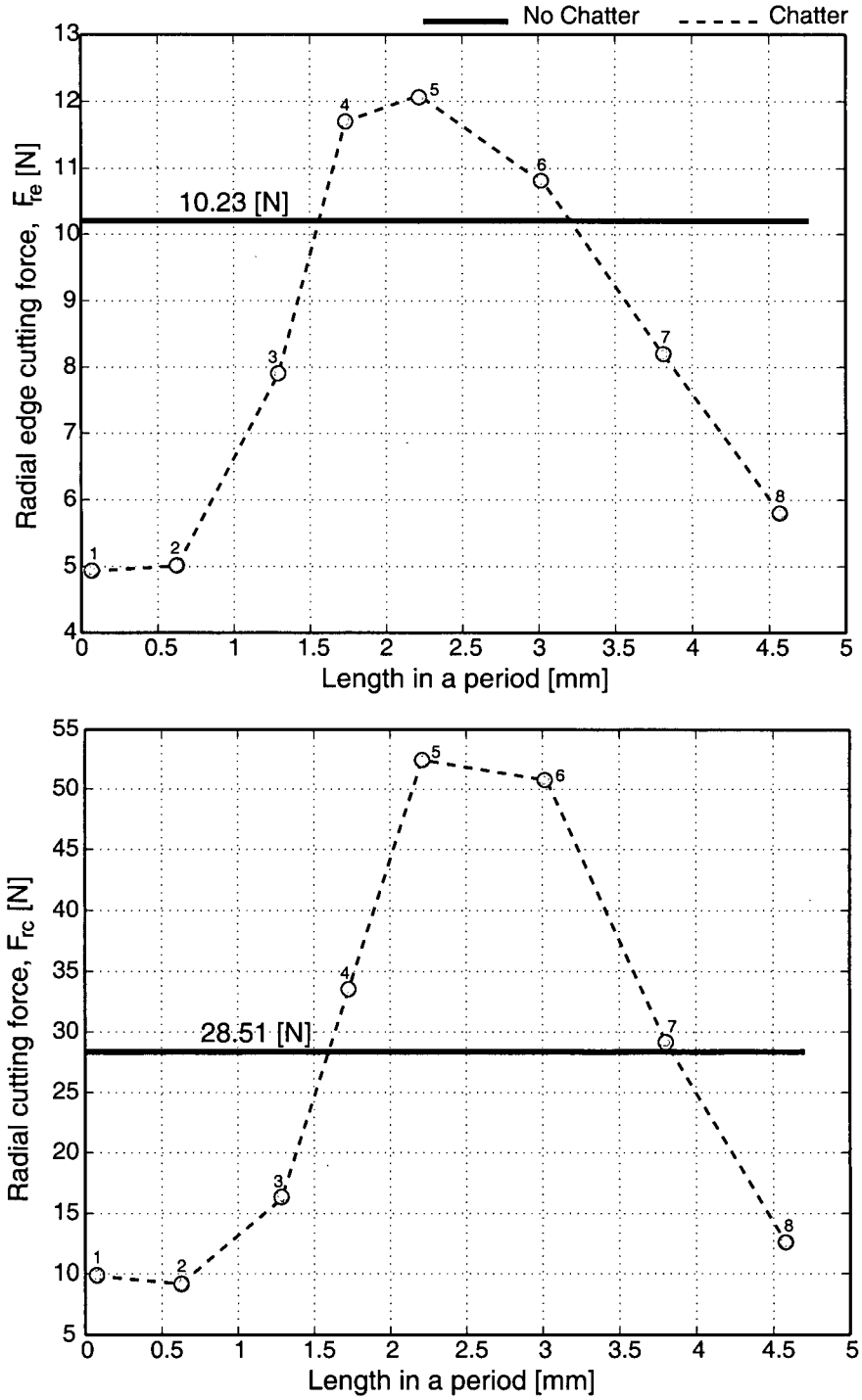

Figure 5.25 : The variation of the radial cutting and edge cutting coefficients for the given vibration history in Table 5.2

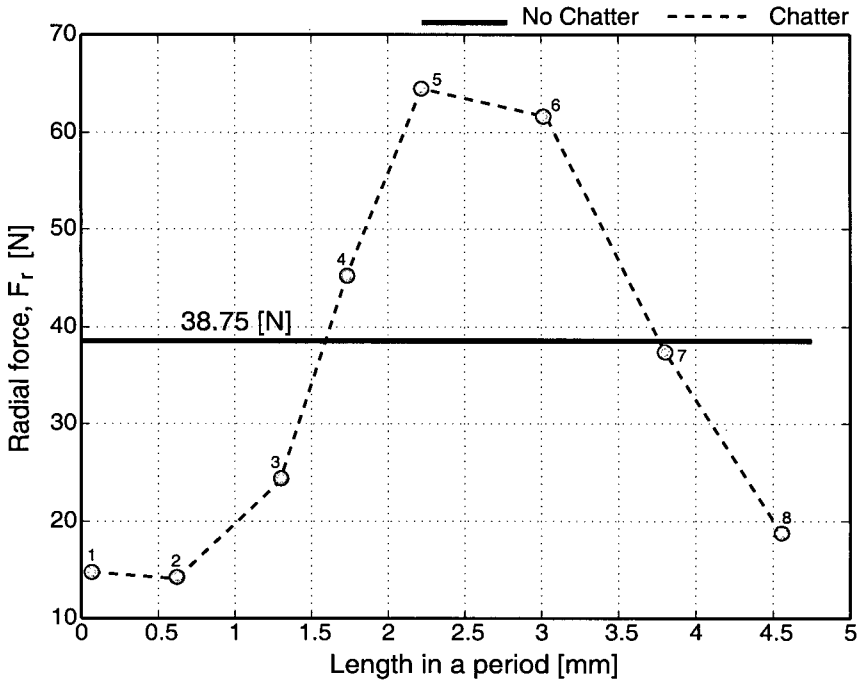

Figure 5.26 : The Variation of the total radial force for the vibration history in (Table 5.2)

5.3.2. Chatter Stability Prediction in Time Domain

This section presents the development of the digital simulation method for the boring process which is to predict the occurrence of chatter vibrations. The time domain model enables us to understand aspects of the regenerative effect and chatter, with a good insight into the dynamic behaviour of the boring bar structure. It is also possible to consider the nonlinearities of the process in chatter vibrations. One of the nonlinearities is the tool jumping out of the cut, due to vibrations with large amplitude. In this case the cutting forces become zero for a short period. The second nonlinearity is caused by the nature of the cutting geometry of the boring process. As explained in detail in the preceding sections, when the tool vibrates, the uncut chip area varies drastically due to the corner radius of the tool, and more than three revolutions may be involved in the evaluation of the parameters necessary for the force prediction. All possible nonlinear interactions of the tool positions are considered in the time domain solution.

The block diagram of the time domain solution model is shown in Figure 5.27. The model consists of 3 sub-models, namely a chip load geometry model, a tool dynamics model in radial direction, and a force model. The inputs of the model for simulation are: the radial depth of cut a, feed rate c, and cutting speed V. Based on these inputs, the uncut chip area A, cutting edge contact length L_c, and effective lead angle ϕ_c, which are the necessary parameters for the radial force prediction, are determined. From these parameters, the friction cutting force F_{frc} and edge cutting force components F_{fre} are first predicted. Radial force is then calculated from the total predicted friction force F_{fr}, and the effective lead angle ϕ_L. Eventually, the radial force generates vibrations, changing the radial position of the tool (depth of cut). This process continues with the specified order.

The steps of the time domain solution can be summarized as follows.

- The workpiece is considered to be rolled out, like a rectangular block, and discretized with small elements. In this discretization, the elements are selected small enough relative to the corner radius of the insert.

- Based on the exact kinematics of the boring process, the position of the insert and corresponding coordinates defining the cutting edge are calculated and subtracted from the coordinates of the workpiece surface profile.

- The simulation starts with the above evaluation for the inputs, which are, depth of cut, feed rate, and cutting speed. Depending on these inputs, the uncut chip area, cutting edge contact length, and effective lead angle, which are necessary for the prediction of the radial force, are determined by utilizing the mechanistic model presented in Chapter 3.

- The predicted radial force excites the structure and generates vibrations, and these vibrations are calculated.

- For each time-increment, the position of the tool (the current depth of cut), the uncut chip area A, the cutting edge contact length L_c, and the effective lead angle ϕ_L, are updated, based on the calculated vibration and current interaction between the insert and workpiece surface profile.

Figure 5.29 illustrates a scheme of the simulation, showing the amount of material being removed from the workpiece for an instant of time. As can be noticed in the figure, the fourth revolution before the current one is being taken into account for the determination of the simulation parameters and the radial force prediction.

- The workpiece surface profile is updated after the evaluation of the tool displacement at each time-increment.

- The process continues in the specified course for each increment of the workpiece rotation.

The detailed algorithm steps of the time domain simulation is illustrated in Figure 5.28.

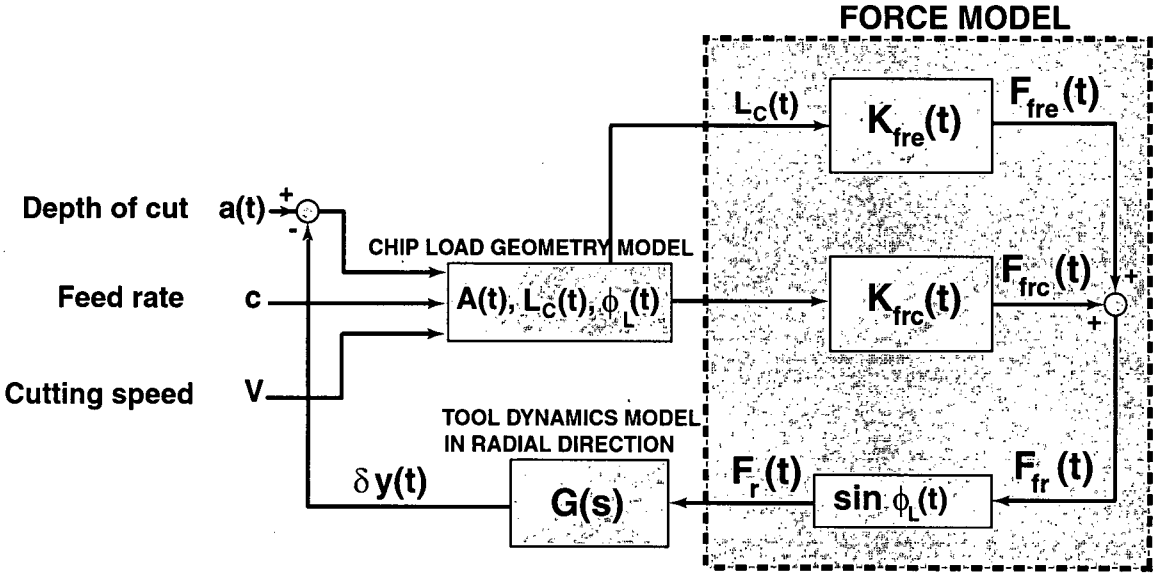

Figure 5.27 : Block diagram of time domain simulation model

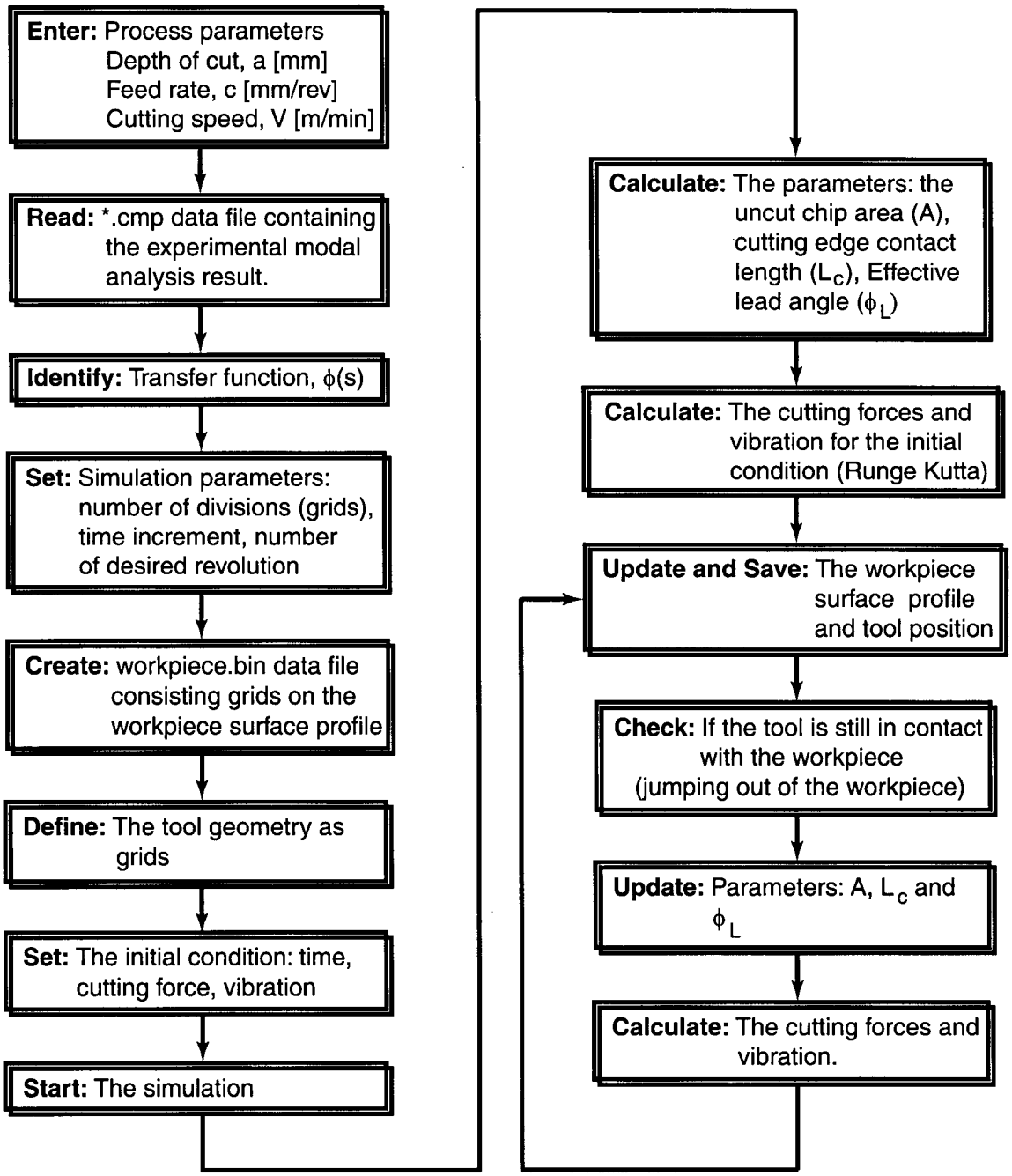

Figure 5.28 : Algorithm of the time domain solution model

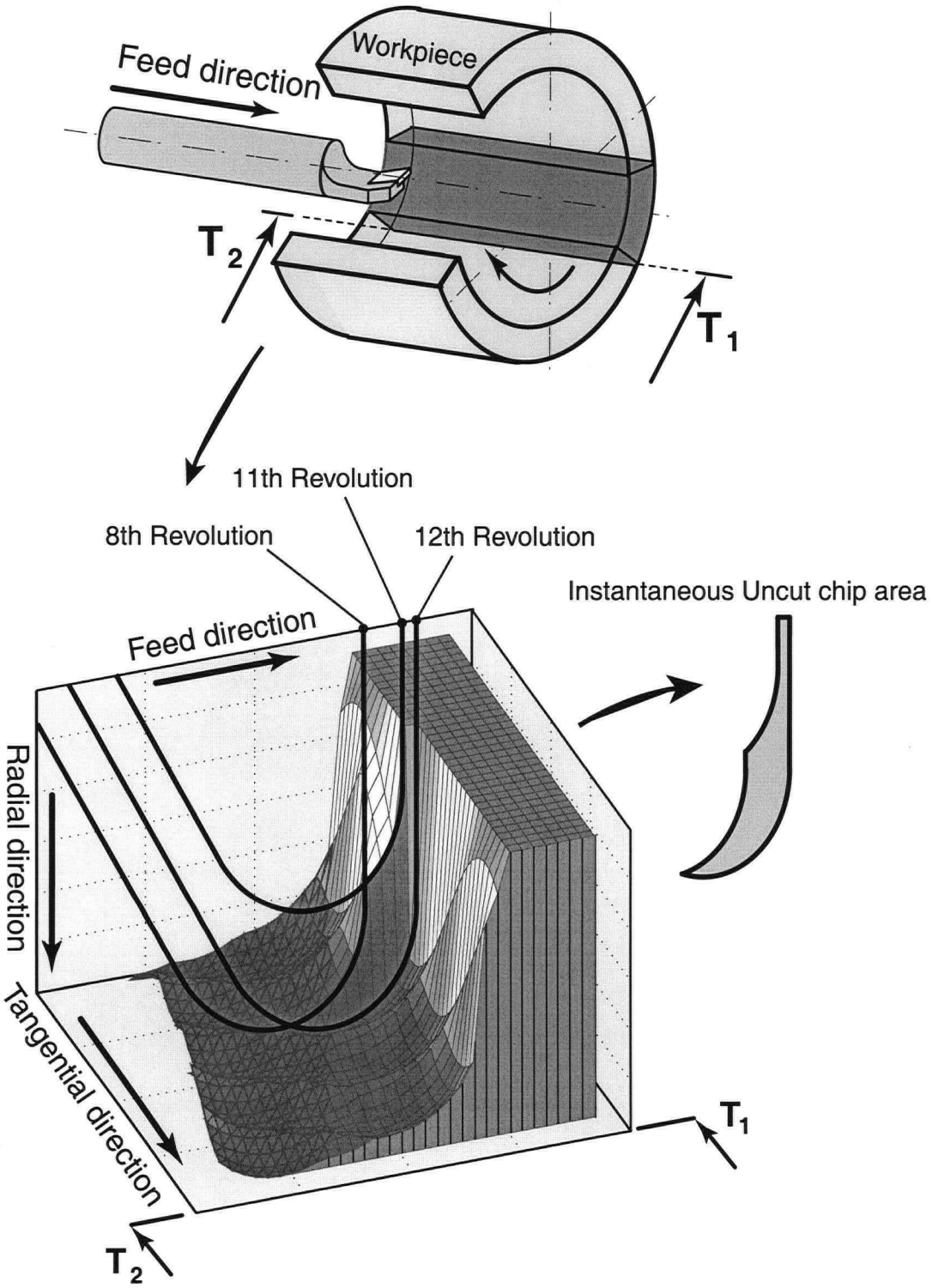

Figure 5.29 : Illustration of the tool position for an instant of time in time domain simulation

5.3.2.1. Tool Dynamics Model

Using the experimental modal analysis method [2], the transfer function of the structure is obtained in the following form.

$$\phi(s) = \frac{Y(s)}{F(s)} = \sum_{k=1}^{n} \frac{\alpha_k + \beta_k s}{s^2 + 2\zeta_k \omega_{n,k} s + \omega_{n,k}} \tag{5.32}$$

where n is the total number of modes in the system and k represents each of these modes. α and β are the parameters derived based on the following equation.

A second order system is represented in Laplace domain as,

$$\phi(s) = \frac{X(s)}{F(s)} = \frac{1/m}{s^2 + 2\zeta\omega_n s + \omega_n^2}$$

The partial fraction expansion of the transfer function can be written in the following order.

$$\phi(s) = \frac{r}{s - s_1} + \frac{r^*}{s - s_1^*} = \frac{\alpha + \beta s}{s^2 + 2\zeta\omega_n s + \omega_n^2} \tag{5.33}$$

where the residues are,

$$r = \sigma + j\nu \qquad r^* = \sigma - j\nu$$

and s_1 and s_2 are the complex conjugate roots of the characteristic equation of the transfer function.

$$s_1 = -\zeta\omega_n + j\omega_d \qquad s_2 = -\zeta\omega_n - j\omega_d$$

The parameters, α and β are expressed as,

$$\alpha = 2(\zeta\omega_n\sigma - \omega_d\nu) \qquad \beta = 2\sigma \tag{5.34}$$

Having performed the impact hammer test, the measured data is processed in *CutPro* (modal analysis software) for the determination of the dynamic characteristics of the boring bar system structure. The outputs of this process are: the damping ratio ζ, natural frequencies ω_n, equivalent stiffness k and mass m of each mode of the structure, and the residue values (r and r^*) shown

above. Using these parameters, the transfer function of the structure is built based on the Eq. (5.32).

To obtain the time domain solution, the nested programing method is conducted and the transfer function of the structure in radial direction Eq. (5.32) is modified into the state space representation with the observable canonical form [8]. The displacement in the radial direction can then be expressed as,

$$Y(s) = \frac{1}{s}[\beta F_r(s) - 2\zeta\omega_n Y(s)] + \frac{1}{s^2}[\alpha F_r(s) - \omega_n^2 Y(s)] \tag{5.35}$$

State variables are defined as follows,

$$X_1(s) = \frac{1}{s}[\alpha F_r(s) - \omega_n^2 Y(s)] \tag{5.36}$$

$$X_2(s) = \frac{1}{s}[\beta F_r(s) - 2\zeta\omega_n Y(s) + X_1(s)] \tag{5.37}$$

The Eq.(5.35) can be written as,

$$Y(s) = X_2(s) \tag{5.38}$$

Substituting Eq. (5.38) into Eq.(5.36) and (5.37) leads to the state and output equations in a vector-matrix form as follows.

$$\begin{bmatrix} \dot{x}_1 \\ \dot{x}_2 \end{bmatrix} = \begin{bmatrix} 0 & -\omega_n^2 \\ 1 & -2\zeta\omega_n \end{bmatrix} \begin{bmatrix} x_1 \\ x_2 \end{bmatrix} + \begin{bmatrix} \beta \\ \alpha \end{bmatrix} \tag{5.39}$$

$$Y = X_2 \tag{5.40}$$

Fourth order Runge Kutta equation is used in the numerical integration of the process [20]. The general equation of Runge Kutta is presented as,

$$X_{k+1} = X_k + \frac{1}{6}(k_1 + 2k_2 + 2k_3 + k_4) \tag{5.41}$$

The slopes of each state variable equation are defined as follows.

$$k_{1,1} = h(-\omega_n^2 X_2 + \alpha F_r)$$

$$k_{2,1} = h\left(-\omega_n^2\left(X_2 + \frac{1}{2}k_{1,1}\right) + \alpha F_r\right)$$

$$k_{3,1} = h\left(-\omega_n^2\left(X_2 + \frac{1}{2}k_{2,1}\right) + \alpha F_r\right)$$

$$k_{4,1} = h(-\omega_n^2(X_2 + k_{3,1}) + \alpha F_r)$$

where h is the time interval. The first value of the state variable is obtained as,.

$$X_{1_{i+1}} = X_{1_i} + \frac{1}{6}(k_{1,1} + 2k_{2,1} + 2k_{3,1} + k_{4,1}) \tag{5.42}$$

Similarly, the slopes for the second state variable X_2,

$$k_{1,2} = h(X_1 - 2\zeta\omega_n X_2 + \beta F_r)$$

$$k_{2,2} = h\left(\left(X_1 + \frac{1}{2}k_{1,1}\right) - 2\zeta\omega_n\left(X_2 + \frac{1}{2}k_{1,2}\right) + \beta F_r\right)$$

$$k_{3,2} = h\left(\left(X_1 + \frac{1}{2}k_{2,1}\right) + \left(-2\zeta\omega_n\left(X_2 + \frac{1}{2}k_{2,2}\right)\right) + \beta F_r\right)$$

$$k_{4,2} = h((X_1 + k_{3,1}) - 2\zeta\omega_n(X_2 + k_{3,2}) + \beta F_r)$$

Finally, the second state variable that is also equal to the radial vibration (Eq. 5.40)) is accomplished with the following equation.

$$Y = X_{2_{i+1}} = X_{2_i} + \frac{1}{6}(k_{1,2} + 2k_{2,2} + 2k_{3,2} + k_{4,2}) \tag{5.43}$$

5.3.3. Simulation and Experimental Results

In order to investigate the stability's dependence on the cutting parameters, and verify the time domain solution model, two series of experiments were performed. For each test, the initial surface of the workpiece was cleaned and the diameter set to the desired specification. Chatter

vibrations during the test were detected by means of accelerometers (*PCB 353B11 SN 65847, SN 68836 and Kistler SN C128797*) and a microphone attached to the boring bar and to the turret of the lathe. Acceleration signals were amplified by charge amplifiers (*Kistler-Type 5114*), and later digitized by data acquisition software *CutPro-MalDAQ*.

In these experiments, the boring bar was first mounted on the turret with a critical length, in order to catch a critical border between the stable and unstable cutting conditions within the specified cutting parameter ranges. If the boring bar is held on the turret with a short length, the system may be stable for all cutting conditions; if it is mounted with a long length, only unstable cutting conditions would be observed.

In the first set of experiments, workpieces with 32.14 [mm] hole diameter were employed, the depth of cut was selected less than corner radius of the tool ($a < 0.8$ [mm]), and the feed rate was kept constant for all conditions with the value of 0.1 [mm/rev]. At the beginning, a high cutting speed was chosen, and gradually reduced by varying the depth of cut until the critical border of cutting speed was observed. As seen in Table 5.6, there is a certain chatter vibration stability border between the cutting speeds 112.5 and 125 [m/min]. The effect of the depth of cut in this critical border seems to be insignificant. However, it has a notable effect on the system stability for cutting conditions with larger depth of cut ranges. In the second set of experiments, both the depth of cut and the feed rate were changed, and the system stability showed dependency not only on the depth of cut, but also on the feed rate (Table 5.10).

Linearizing assumptions expect system stability to remain independent of the radial depth of cut, which is the input of the system. However, results of the experiments conducted so far have contradicted this expectation, showing dependence of the system stability on radial depth of cut.

In the experiments, in order to have the identical analysis for the system stability, the hole diameter of the workpiece was kept the same. Different hole diameters may affect the stability as regards process damping, even though the cutting parameters (depth of cut, a, feed rate c and cutting speed V) are the same. The process tends to damp due to the friction associated with the

tool flank face and workpiece interference as a result of the short waves left on the cut surface (Figure 5.30). For a different hole diameter D, but the same cutting speed V, spindle speed n *[rpm]* will be different. At each revolution, the phase angle ε (for the same chatter frequency ω_c and cutting speed V) varies. Hence, due to the different phase angle for the same cutting condition (i.e. the same depth of cut, a, feed rate c and cutting speed V), the depth of cut variation will not be the same. Consequently, the experiments performed with a different hole diameter may not be identical. The relation between the integer number of waves, spindle speed, chatter frequency, and phase angle, is expressed with the Eq. (5.1)

Figures 5.34 and 5.35 show time domain simulation results for experiments 1 and 17 in the first series of experiments (Table 5.6). Both simulation results exhibit unstable cutting conditions, even though no chatter is expected for the condition of experiment 1. Note that the radial vibrations in experiment 1 are even more severe. This may be explained as follows. The radial cutting force changes inversely with the cutting speed V, based on the mechanistic model expression presented in Chapter 3. Thus, the lesser cutting speed V produces more cutting force, which causes large displacement on the boring bar structure. On the other hand, friction on the rake face of the tool increases with low cutting speed. This additional friction causes extra damping in the process and prevents chatter vibrations. Furthermore, if the process tends to vibrate, the length of the wave becomes short at low speeds, and rubbing between the flank face of the tool and wavy surface also contributes to damping of system (Figure 5.30).

The wave length becomes shorter at low cutting speeds. The flank face of the tool is then in continuous contact with the material surface, adding an extra positive damping (known as process damping) effect to the system. As can be seen in Figure 5.30, with short waves the relief angle of the tool may be zero, whereas with long waves it is greater than zero, and has no significant effect on the damping of the system. Modeling process damping is difficult, and is therefore not included in the time domain simulation model.

The results of the second set of experiments are presented in Table 5.10 and Figure 5.33. These experiments were conducted at various cutting speeds (from 75 to 175[m/min]), depths of cut (from 0.25 to 2.5[mm]), and two feed rates (0.075 and 0.125[mm/rev]). As can be noticed, there is a certain stability border of depth of cut at 100[m/min] of cutting speed. After reaching 100[m/min] cutting speed, the system exhibits unstable cutting conditions regardless of the depth of cut and feed rate. The effect of the feed rate is also seen in the figures. For a feed rate value of 0.075[mm/rev] feed rate the system has no chatter vibrations until the depth of cut reaches 1.25[mm]. However, the maximum allowable depth of cut is 0.65[mm] when the feed rate is set to 0.125[mm/rev]. These series of experiments show that the system stability of a boring process depends on both depth of cut and feed rate..

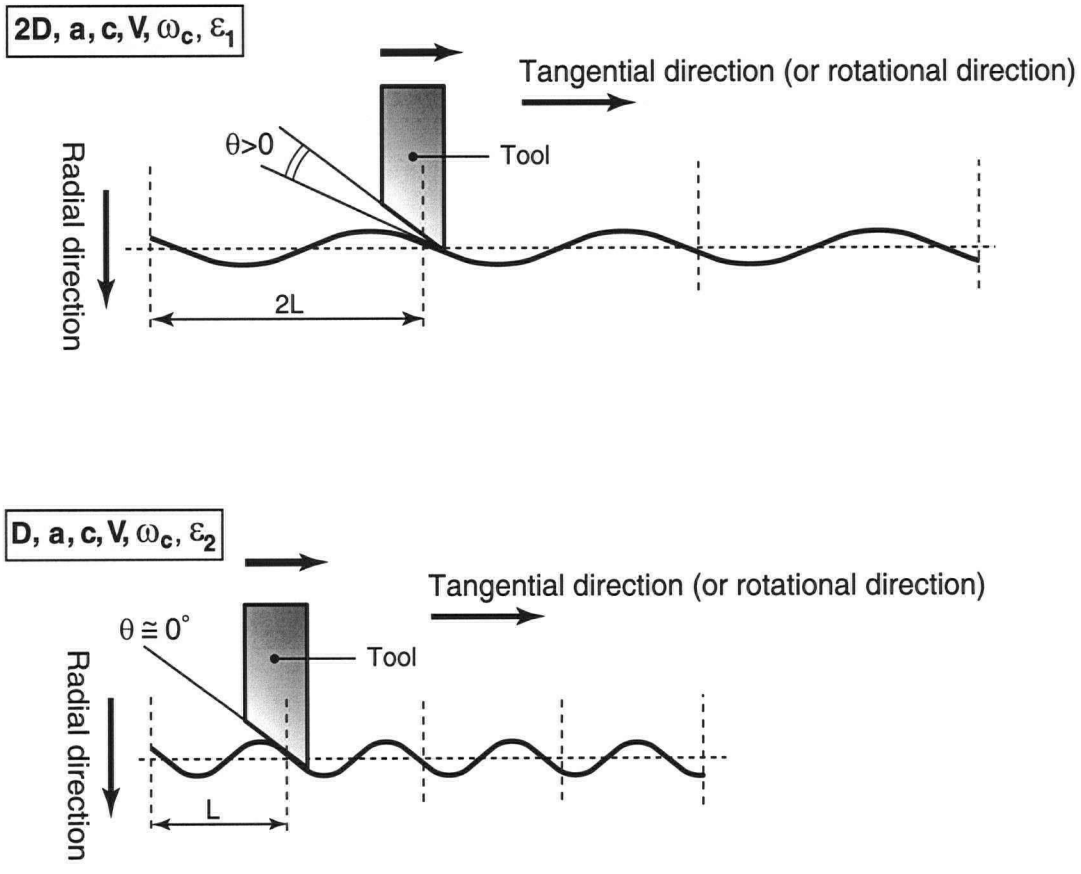

Figure 5.30 : The relation between the length of generated waves and process damping

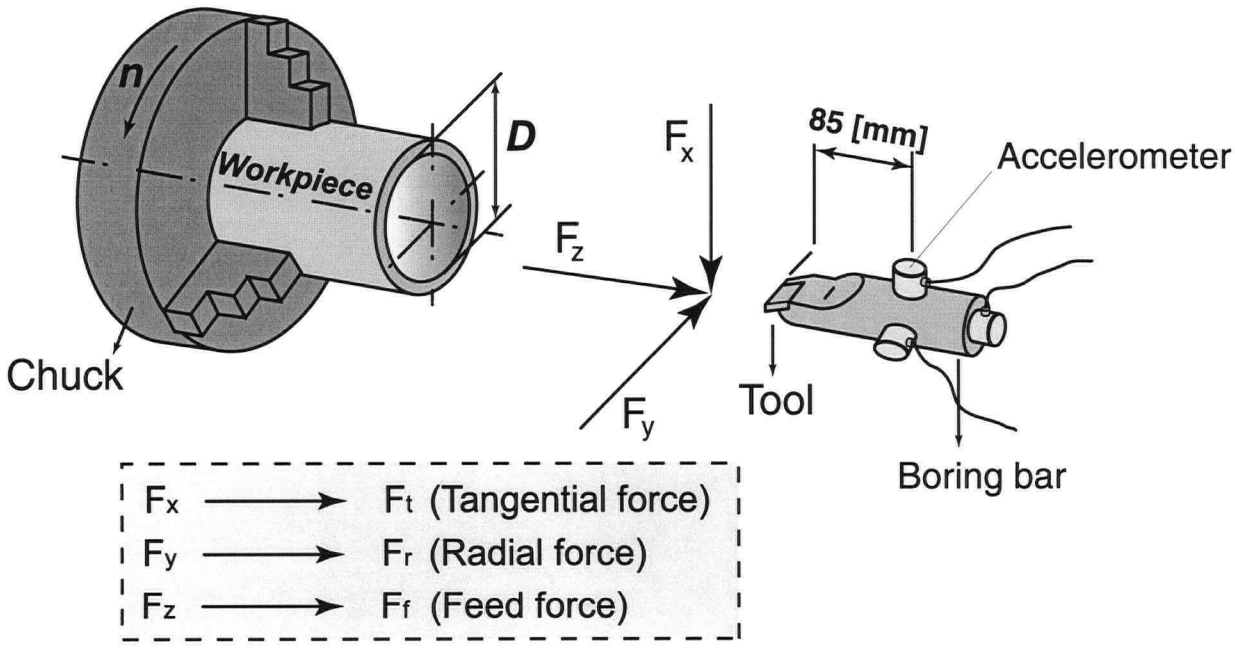

Figure 5.31 : Experimental setup-Chatter tests

5.3.3.1. Experimental Results:

- Modal Parameters of the Boring Bar Structure for the First Set of Experiments

Table 5.3 : Modal parameters in radial direction

Mode#	Freq. [Hz]	Damping Ratio [%]	Residue (Real)	Residue (Im)	Stiffness [N/m]	Mass [kg]
1	483.02	9.33	1.026623E-05	-2.784654E-04	5.473229E+06	0.5942
2	753.03	2.62	3.041659E-05	-4.995113E-04	4.737671E+06	0.2116

Table 5.4 : Modal parameters in tangential direction

Mode#	Freq. [Hz]	Damping Ratio [%]	Residue (Real)	Residue (Im)	Stiffness [N/m]	Mass [kg]
1	665.67	2.26	7.90253E-06	-5.778915E-04	3.62E+06	0.2069

Table 5.5 : Modal parameters in feed direction

Mode#	Freq. [Hz]	Damping Ratio[%]	Residue [Real]	Residue [Im]	Stiffness [N/m]	Mass [kg]
1	432.82	10.59	1.082661E-05	-4.111103E-05	3.326233E+07	4.497
2	754.56	2.49	5.757860E-06	-1.490884E-05	1.590511E+08	7.076

Table 5.6 : Experimental results of the first set

Exp.#	V [m/min]	n [rpm]	c [mm/rev]	a [mm]	D [mm]	Result	ε [Deg]	ω_c [H]
1	75	743	0.10	0.75	32.14	Nochatter		
2	100	990	0.10	0.30	32.14	Nochatter		
3	100	990	0.10	0.60	32.14	Nochatter		
4	75	743	0.10	0.30	32.14	Nochatter		
5	87.5	867	0.10	0.60	32.14	Nochatter		
6	87.5	867	0.10	0.30	32.14	Nochatter		
7	112.5	1114	0.10	0.30	32.14	Nochatter		
8	112.5	1114	0.10	0.60	32.14	Nochatter		
11	125	1238	0.10	0.30	32.14	Nochatter		
9	225	2228	0.10	0.75	32.14	Chatter	273.5	771
10	125	1238	0.10	0.50	32.14	Chatter	243.3	798
12	175	1733	0.10	0.60	32.14	Chatter	261.2	772
13	175	1733	0.10	0.30	32.14	Chatter	223.8	769
14	150	1486	0.10	0.60	32.14	Chatter	239.2	784
15	150	1486	0.10	0.30	32.14	Chatter	239.2	784
16	225	2228	0.10	0.30	32.14	Chatter	225.0	766
17	250	2476	0.10	0.60	32.14	Chatter	263.5	773
18	275	2724	0.10	0.60	32.14	Chatter	282.3	762

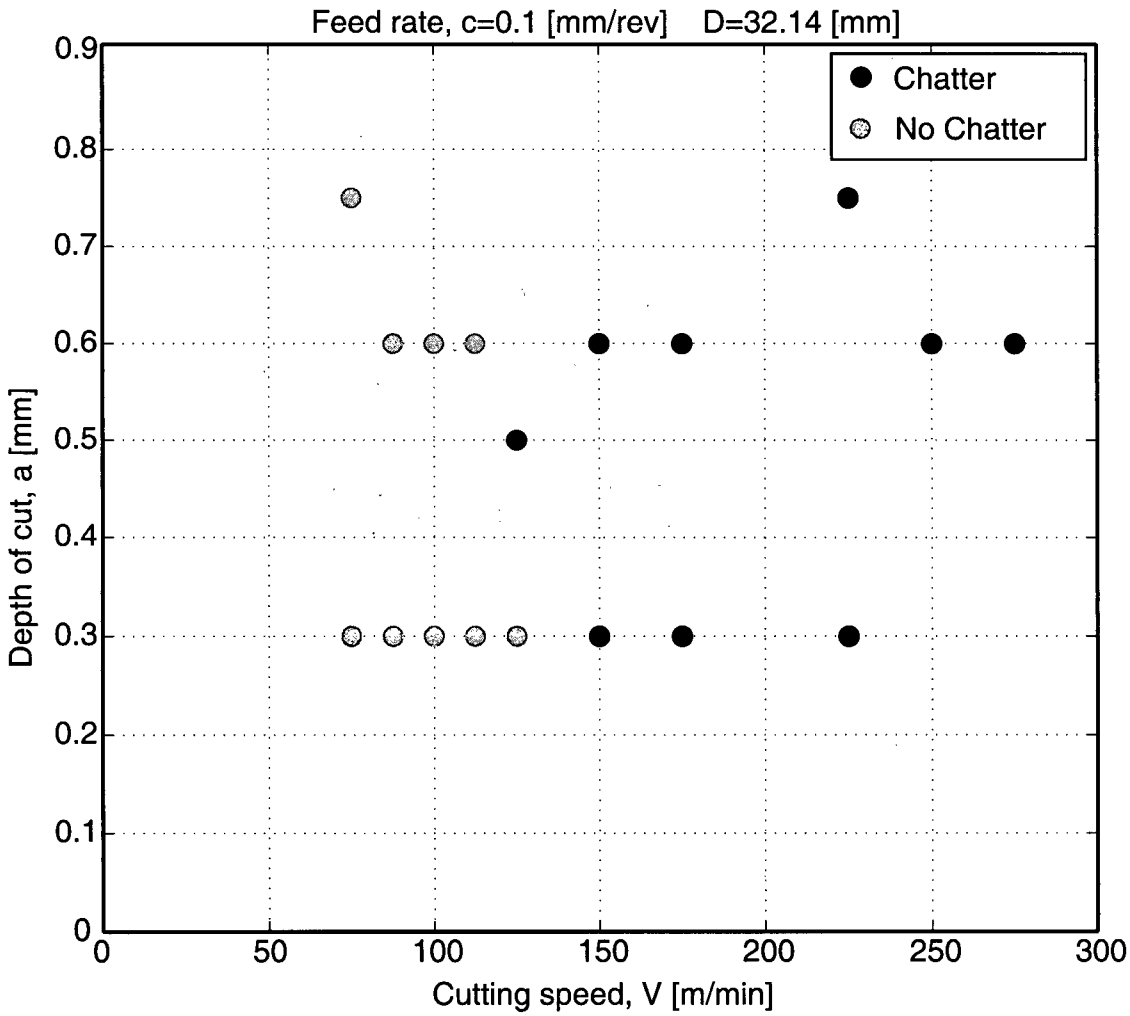

Figure 5.32 : The results of the first set of experiments

- Modal Parameters of the Boring Bar Structure for the Second Set of Experiments

Table 5.7 : Modal parameters in radial direction

Mode#	Freq. [Hz]	Damping Ratio [%]	Residue (Real)	Residue (Im)	Stiffness [N/m]	Mass [kg]
1	764.53	2.40	-9.42390E-07	-1.264124E-04	1.900543E+07	0.8236

Table 5.8 : Modal parameters in tangential direction

Mode#	Freq. [Hz]	Damping Ratb [%]	Residue (Real)	Residue (Im)	Stiffness [N/m]	Mass [kg]
1	764.51	3.43	-6.59550E-06	-1.574528E-04	1.526302E+07	0.6615

Table 5.9 : Modal parameters in feed direction

Mode#	Freq. [Hz]	Damping Ratio[%]	Residue (Real)	Residue (Im)	Stiffness [N/m]	Mass [kg]
1	281.23	9.52	-1.16473E-07	-1.266268E-07	7.009194E+09	2244.8153
2	1369.57	7.84	3.06011E-07	-1.73772E-06	2483663312	33.5402908

Table 5.10 : The results of the second set of experiments

Exp.#	V [m/min]	n [rpm]	c [mm/rev]	a [mm]	Result	ε [Deg]	ω_c [Hz]
1	175	754	0.075	0.6	Chatter	212.9	774
2	175	1869	0.125	0.75	Chatter	247.3	769
3	175	775	0.075	0.9	Chatter	220.6	770
4	175	1763	0.125	1.5	Chatter	196.4	780
5	150	700	0.075	0.5	Chatter	185.1	776
6	150	687	0.075	1	Chatter	215.4	774
7	150	665	0.075	1.5	Chatter	203.0	771
8	150	491	0.125	0.25	Chatter	209.7	774
9	150	497	0.125	0.5	Chatter	115.2	773
10	150	487	0.125	1	Chatter	134.5	766
11	125	596	0.075	0.5	Chatter	294.8	773
12	125	585	0.075	0.75	Chatter	175.4	775
13	125	571	0.075	1	Chatter	290.0	769
14	125	1160	0.075	1.5	Chatter	260.7	768
15	125	641	0.125	0.75	Chatter	252.2	766
16	125	557	0.125	1	Chatter	223.6	767
17	125	623	0.125	1.5	Chatter	173.9	763
18	112.5	527	0.075	0.5	Chatter	280.8	771
19	112.5	517	0.075	0.75	Chatter	323.1	766
20	112.5	504	0.075	1	Chatter	214.3	761
21	112.5	489	0.075	1.25	Chatter	267.2	764
22	112.5	471	0.075	1.5	Chatter	293.5	760
23	112.5	399	0.125	0.5	Chatter	121.8	767
24	112.5	394	0.125	0.75	Chatter	179.1	765
25	112.5	386	0.125	1	Chatter	216.4	763
26	112.5	377	0.125	1.5	Chatter	41.1	761
27	100	866	0.075	0.45	No Chatter		
28	100	840	0.075	0.55	No Chatter		

Exp.#	V [m/min]	n [rpm]	c [mm/rev]	a [mm]	Result	ε [Deg]	ω_c [Hz]
29	100	813	0.075	0.65	No Chatter		
30	100	783	0.075	0.8	No Chatter		
31	100	748	0.075	1	No Chatter		
32	100	711	0.075	1.25	No Chatter		
33	100	669	0.075	1.65	Chatter	122.7	762
34	100	776	0.125	0.4	No Chatter		
35	100	802	0.125	0.55	No Chatter		
36	100	767	0.125	0.65	No Chatter		
37	100	740	0.125	1	Chatter	311.4	763
38	100	703	0.125	1.25	Chatter	311.4	760
39	100	662	0.125	1.65	Chatter	154.4	755
40	100	569	0.125	2.5	Chatter	201.2	745
41	87.5	464	0.075	0.5	No Chatter		
42	87.5	455	0.075	0.75	No Chatter		
43	87.5	443	0.075	1	No Chatter		
44	87.5	429	0.075	1.5	Chatter	156.1	761
45	87.5	341	0.125	0.5	NoChatter		
46	87.5	336	0.125	0.75	No Chatter		
47	87.5	329	0.125	1	No Chatter		
48	87.5	321	0.125	1.5	No Chatter		
49	87.5	295	0.125	1.75	Chatter	48.8	748
50	75	498	0.075	0.5	No Chatter		
51	75	488	0.075	0.75	No Chatter		
52	75	472	0.075	1	No Chatter		
53	75	365	0.075	1.25	Chatter	29.6	767
54	75	453	0.075	1.5	Chatter	143.0	758
55	75	324	0.125	0.5	No Chatter		
56	75	320	0.125	0.75	No Chatter		

Exp.#	V [m/min]	n [rpm]	c [mm/rev]	a [mm]	Result	ε [Deg]	ω_c [Hz]
57	75	312	0.125	1	Chatter	332.3	764
58	75	295	0.125	1.5	Chatter	268.5	751
59	75	256	0.125	1.25	Chatter	236.3	758

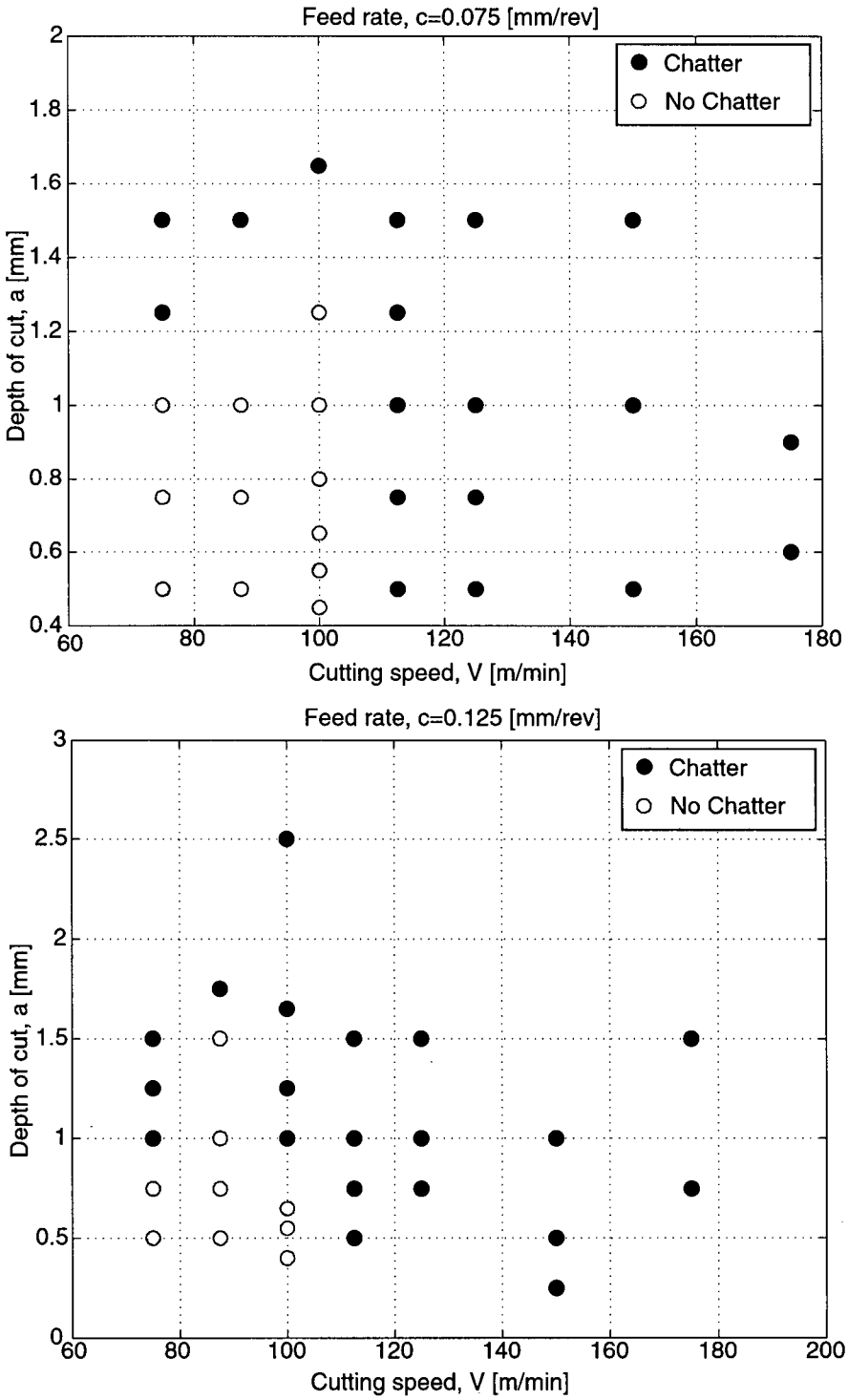

Figure 5.33 : Results of the second set of experiments

5.3.3.2. Time Domain Simulation Results:

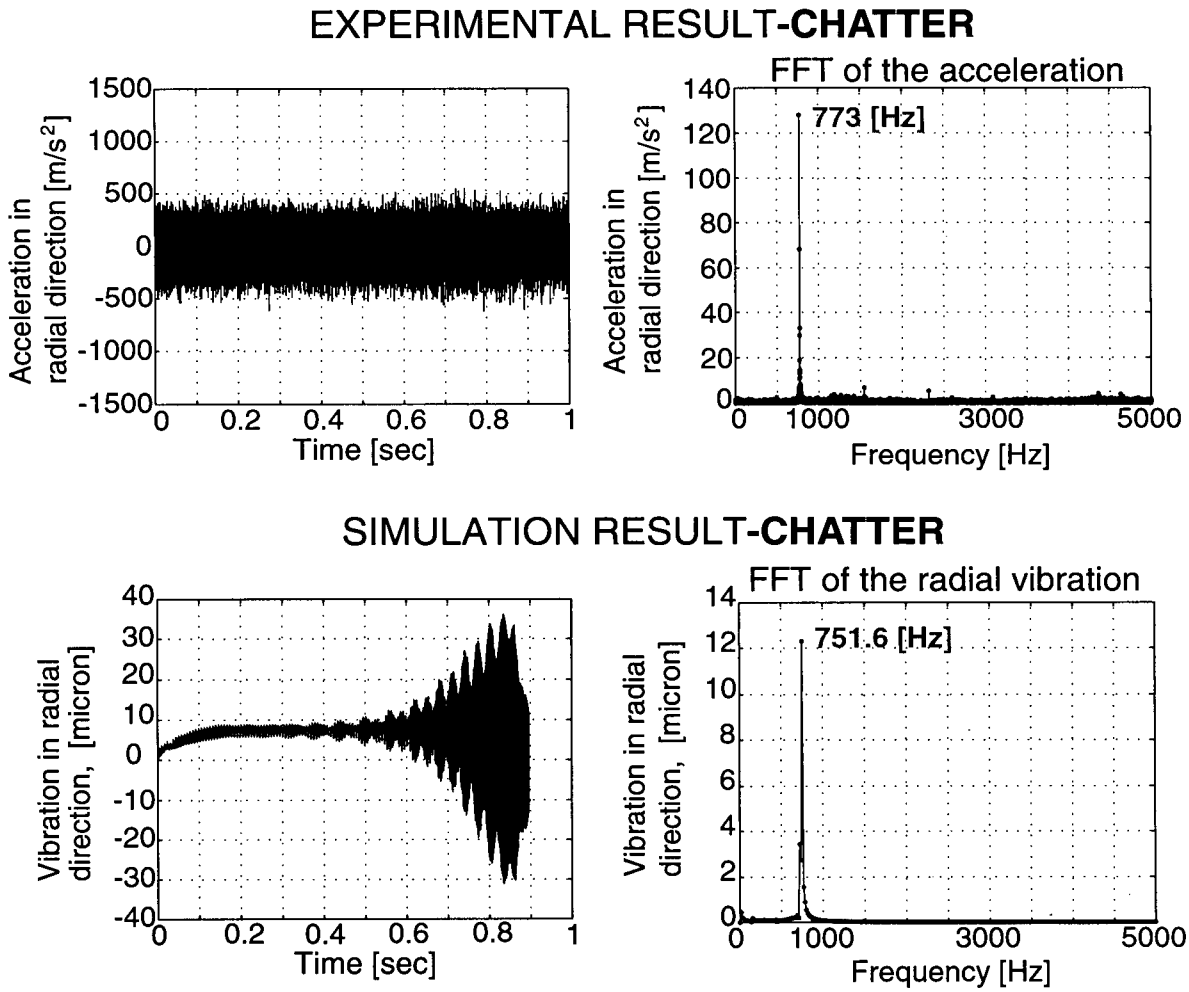

Figure 5.34 : Time domain simulation result, Set-1, Test#17, a=0.6[mm], V=250[m/min], c=0.1[mm/rev], n=2476[rpm]

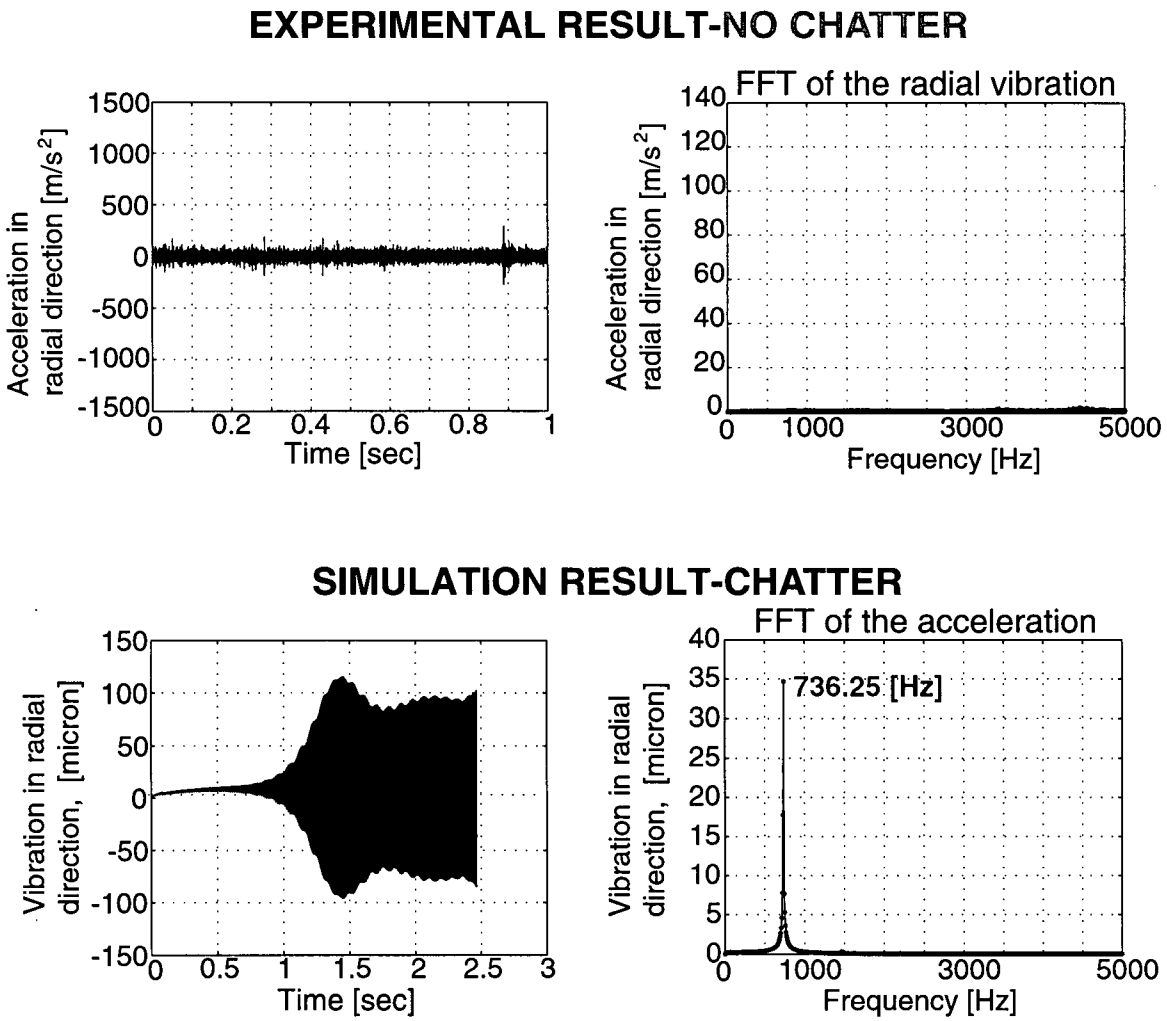

Figure 5.35 : Time domain simulation result, Set-1, Test#1, a=0.75[mm], V=75[m/min], c=0.1[mm/rev], n=743[rpm]

5.4. Summary

This chapter described the self-excited chatter vibrations originating from the regenerative effect and the dynamic characteristics of the boring process in detail. The mechanism of wave regeneration in the boring process differs from other models and has a nonlinear nature, due to the dynamic characteristics of the boring process. In this chapter, an approach for the analytical solution of the chatter stability was presented, but not experimentally validated. A time domain solution model was also implemented to predict cutting forces and chatter stability limits. Only radial vibrations were taken into account in the time domain solution, since vibrations in the tangential direction do not have a significant effect in wave regeneration. A time domain simulation model was experimentally examined, and some discrepancies were noticed between predicted and experimentally observed cutting conditions, which were most likely due to the effects of process damping. The time domain solution model is capable of considering the nonlinearity of the process, such as the loss of tool contact caused by chatter vibrations during machining. On the other hand, the time domain simulation model can be used for the static process force prediction, if the vibrations are neglected.

Chapter 6

Conclusions

This thesis investigates the dynamics of boring operations. The mechanics of boring operation deal with the prediction of cutting forces as a function of tool geometry, work material properties and cutting conditions such as feed rate, radial depth of cut, and cutting speed. The dynamics of the process involve the modeling of interactions between the structural dynamics of a long, slender boring bar with boring process mechanics. Evaluation of forces allows the prediction of static deflection errors, torque and the power required from the machine tool. Evaluation of dynamic stability of the process allows the prediction of chatter vibration free feed rate, spindle speed, radial depth of cut, and tool geometry.

The thesis shows that boring forces strongly depend on tool nose geometry, side cutting edge angle, radial depth of cut, feed rate and cutting speed. The chip thickness distribution along the curved edge of the tool is rather complex. The chip is thin close to the nose, and becomes thicker along the curved edge as the radial depth of cut increases. The chip thickness distribution is also affected by the feed rate.

The mechanics of boring are investigated. The shape of the chip is modeled as a function of tool nose radius, side cutting edge angle, radial depth of cut, and feed rate. The chip area is divided into regions. One of the regions is the nose radius area where the chip starts with zero thickness and increases as a function of nose radius and feed. Along the straight inclined edge, the chip thickness is constant and the chip area is defined by a rectangle. The area of each region and its center of gravity is evaluated. The cutting pressure along the edge of the tool is identified, using either orthogonal to oblique cutting transformation, or mechanistically calibrated force coefficients. Oblique transformation uses the shear stress, shear angle and friction coefficient of

the material identified from orthogonal machining tests. They are mapped to oblique or curved cutting edge at digitized regions. The differential cutting pressures are summed up along the cutting edge, which leads to total cutting forces in each region. Alternatively, the cutting forces at each region are evaluated using mechanistically identified cutting coefficients which relate the chip area or contact length to the cutting force magnitudes. The cutting forces in all regions are summed up to find resultant friction and tangential cutting forces. Using an equivalent friction or lead angle, the friction force is projected in the radial and feed directions. The model allows the prediction of cutting forces in all three Cartesian directions.

When the boring bar with multiple inserts is used, the chip load distribution to all inserts is modeled. The radial and axial setting errors of the inserts are integrated with the process mechanics model.

A significant number of experiments have been conducted in the boring of Aluminum 6061 alloy. It is shown that the predicted and measured cutting forces are in good agreement with the predictions provided by the proposed mechanics models. The predictions are shown to have errors varying between 2% to 15%. The proposed model contributes to the improved prediction of boring mechanics.

The fundamental mechanism behind chatter vibrations in boring is also investigated. It is shown that the cutting coefficients, i.e. process gain, and directional factors, are dependent on the feed rate, radial depth of cut, tool geometry, and cutting speed. While the tool geometry and speed may be kept constant, vibrations modulate radial depth of cut, leading to time-varying process input parameter. The vibrations of the tool in the radial direction change the effective radial depth of cut. The tool travels over the previously machined surface marked by the vibrations generated during the previous revolutions. The changes in the chip area become very abrupt and significant, difficult to track even in the time domain. The changes in the chip area affect cutting force coefficients (e.g. process gains) and directional factors (e.g. strength of modal parameters in each direction). This is the fundamental non-linearity in the process, which differs from milling

operations. The author presents the block diagram model of the process in the frequency domain, and illustrates the nonlinear influence of process changes. In addition, the process is simulated in the time domain. However, it is shown that even the time domain modeling suffers, mainly due to the digital integration of a significant number of tool deflection waves left on the boring surface.

Future work should focus on the development of an improved time domain solution for chatter in the boring process. If a more simple tool geometry is used, it may be possible to minimize the drastic nonlinear changes in the cutting coefficients and directional factors, which may lead to the approximate solution of chatter stability in the frequency domain.

Appendix A: Experimental Results of The Mechanistic Model Verification

Friction force verification for $a < R$

Exp#	c [mm/rev]	a [mm]	V [m/min]	Measure F_{fr} [N]	Predicted F_{fr} [N]	Error [%]
1	0.0600	0.7750	112.5	51.02	60.40	-15.52
2	0.1700	0.6500	155.0	72.06	72.92	-1.17
3	0.1800	0.4500	180.0	57.65	56.06	2.82
4	0.1000	0.5500	190.0	47.24	48.14	-1.86
5	0.1650	0.5500	220.0	58.99	56.34	4.70
6	0.0650	0.4750	230.0	35.37	30.59	15.61
7	0.1850	0.6750	250.0	68.92	64.85	6.28
8	0.0725	0.7750	270.0	47.88	43.94	8.97
9	0.1350	0.4250	235.0	44.99	38.49	16.89
10	0.0675	0.7250	252.5	45.29	41.37	9.47
11	0.1375	0.3250	97.5	47.19	54.88	-14.01
12	0.0580	0.5600	114.0	41.43	38.79	6.81
13	0.1110	0.6660	152.0	58.15	61.24	-5.05
14	0.1400	0.7770	123.0	75.79	66.71	13.62
15	0.1200	0.6000	156.0	56.57	51.51	9.81

The absolute average error [%]=8.83

Friction force verification for $a \geq R$

Exp#	c [mm/rev]	a [mm]	V [m/min]	Measured F_{fr} [N]	Predicted F_{fr} [N]	Error [%]
1	0.0400	2.3750	85.0	103.60	118.94	14.80
2	0.1300	1.5650	100.0	137.20	144.48	5.30
3	0.1450	0.8650	120.0	80.30	87.28	8.70
4	0.0700	3.1000	130.0	170.67	168.15	-1.47
5	0.0750	1.8750	135.0	111.63	109.40	-2.00
6	0.1600	1.6500	145.0	156.34	144.73	-7.43
7	0.0550	0.9500	165.0	52.86	52.43	-0.82
8	0.0900	1.0000	170.0	65.20	65.49	0.44
9	0.1100	2.2500	200.0	139.74	134.17	-3.98
10	0.0375	3.1000	205.0	101.66	118.71	16.78
11	0.0550	2.1500	210.0	85.08	95.63	12.41
12	0.0775	1.2500	240.0	74.78	66.25	-11.42
13	0.0925	1.9500	137.5	118.18	124.79	5.60
14	0.0575	2.1500	142.5	111.97	107.88	-3.65
15	0.1275	2.7750	127.5	205.79	212.94	3.47
16	0.0465	1.3500	217.5	57.78	61.33	6.14
17	0.1150	1.4500	195.0	95.72	94.64	-1.14
18	0.1500	3.0000	87.5	304.90	309.10	1.37
19	0.0825	2.3000	187.5	118.98	122.25	2.75
20	0.0950	1.2750	262.5	75.72	70.91	-6.35
21	0.1085	3.1000	152.5	175.90	198.08	12.61
22	0.0666	1.7350	172.5	77.85	89.83	15.39
23	0.1475	2.3750	185.0	168.54	170.48	1.15
24	0.0825	1.4750	125.0	98.38	95.88	-2.54
25	0.1330	1.3330	188.0	101.58	96.46	-5.04
26	0.1440	1.6660	222.0	109.78	113.91	3.76
27	0.0444	1.8880	177.0	70.27	83.27	18.50
28	0.1666	2.0000	88.0	210.86	228.58	8.40
29	0.0888	1.8300	266.0	98.81	92.81	-6.08
30	0.0600	2.0000	181.0	96.03	98.87	2.96

The absolute average error [%]=6.41

Tangential force verification for $a < R$ and $a \geq R$

Exp#	c [mm/rev]	a [mm]	V [m/min]	Measured F_t [N]	Predicted F_t [N]	Error [%]
1	0.0400	2.3750	85	149.72	166.00	10.87
2	0.1300	1.5650	100	228.07	236.29	3.60
3	0.0600	0.7750	112.5	78.51	77.12	-1.78
4	0.1450	0.8650	120	132.24	147.12	11.25
5	0.0700	3.1000	130	263.07	270.56	2.85
6	0.0750	1.8750	135	177.37	179.47	1.18
7	0.1600	1.6500	145	282.52	265.75	-5.94
8	0.1700	0.6500	155	128.63	122.83	-4.51
9	0.0550	0.9500	165	77.56	81.38	4.91
10	0.0900	1.0000	170	111.99	112.46	0.41
11	0.1800	0.4500	180	100.07	91.64	-8.43
12	0.1000	0.5500	190	70.97	72.46	2.11
13	0.1100	2.2500	200	251.90	250.66	-0.49
14	0.0550	2.1500	210	135.49	156.12	15.23
15	0.1650	0.5500	220	98.67	97.54	-1.15
16	0.0775	1.2500	240	111.71	116.34	4.14
17	0.1850	0.6750	250	119.20	121.77	2.16
18	0.0450	0.3500	260	33.74	33.11	-1.87
19	0.0725	0.7750	270	65.12	74.22	13.96
20	0.0925	1.9500	137.5	197.48	211.93	7.32
21	0.0575	2.1500	142.5	163.38	170.79	4.54
22	0.1275	2.7750	127.5	361.39	368.23	1.89
23	0.0465	1.3500	217.5	86.06	95.50	10.97
24	0.1150	1.4500	195	169.18	176.44	4.30
25	0.1500	3.0000	87.5	493.83	484.04	-1.98
26	0.0825	2.3000	187.5	199.28	214.51	7.64
27	0.1350	0.4250	235	59.25	68.62	15.82
28	0.0675	0.7250	252.5	67.30	68.48	1.76
29	0.0950	1.2750	262.5	136.10	131.73	-3.21
30	0.1085	3.1000	152.5	326.84	349.67	6.98

Exp#	c [mm/rev]	a [mm]	V [m/min]	Measured F_t [N]	Predicted F_t [N]	Error [%]
31	0.0666	1.7350	172.5	129.12	149.25	15.59
32	0.1475	2.3750	185	322.18	328.29	1.90
33	0.1375	0.3250	97.5	64.95	66.38	2.20
34	0.0825	1.4750	125	159.11	156.98	-1.34
35	0.0444	1.8350	102.5	119.03	136.00	14.26
36	0.0580	0.5600	114	50.33	58.63	16.48
37	0.1110	0.6660	152	84.80	94.00	10.85
38	0.1330	1.3330	188	176.11	182.59	3.68
39	0.1440	1.6660	222	221.96	226.59	2.09
40	0.0444	1.8880	177	113.50	127.96	12.73
41	0.1666	2.0000	88	354.18	363.62	2.67
42	0.0888	1.8300	266	165.30	172.09	4.11
43	0.1400	0.7770	123	115.55	130.40	12.85
44	0.1200	0.6000	156	82.54	90.44	9.57
45	0.0600	2.0000	181	160.09	157.68	-1.51

The absolute average error [%]=6.11

Effective lead angle prediction for $a < R$

Exp#	c[mm /rev]	a[mm]	V[m/min]	Measured ϕ_L [Deg]	Modified-Predicted ϕ_L [Deg]	Error[%]
1	0.0600	0.7750	112.5	37.47	37.78	0.81
2	0.1700	0.6500	155.0	46.70	46.98	0.58
3	0.1800	0.4500	180.0	58.30	58.23	-0.12
4	0.1000	0.5500	190.0	48.55	50.25	3.49
5	0.1650	0.5500	220.0	55.48	52.37	-5.61
6	0.0650	0.4750	230.0	49.40	53.40	8.09
7	0.1850	0.6750	250.0	46.13	46.52	0.85
8	0.0725	0.7750	270.0	41.42	38.62	-6.76
9	0.1350	0.4250	235.0	57.48	58.49	1.75
10	0.0675	0.7250	252.5	42.83	40.82	-4.71
11	0.1375	0.3250	97.5	62.87	63.92	1.67
12	0.0580	0.5600	114.0	52.07	48.16	-7.49
13	0.1110	0.6660	152.0	48.19	44.48	-7.70
14	0.1400	0.7770	123.0	41.89	39.71	-5.22
15	0.1200	0.6000	156.0	46.00	48.09	4.55

The absolute average error [%]=3.96

Verification of the effective lead angle for $a \geq R$

Exp#	c [mm/rev]	a [mm]	V [m/min]	Measured ϕ_L [Deg]	Modified-Predicted ϕ_L [Deg]	Error[%]
1	0.1300	1.5650	100.0	21.25	17.34	-18.41
2	0.0700	3.1000	130.0	11.35	9.85	-13.15
3	0.1600	1.6500	145.0	20.18	16.88	-16.38
4	0.0900	1.0000	170.0	30.79	26.07	-15.33
5	0.1100	2.2500	200.0	13.05	14.11	8.11
6	0.0550	2.1500	210.0	14.38	15.81	9.91
7	0.0775	1.2500	240.0	23.26	24.21	4.08
8	0.0925	1.9500	137.5	15.42	15.66	1.57
9	0.0575	2.1500	142.5	13.99	15.04	7.52
10	0.1275	2.7750	127.5	11.36	10.44	-8.08
11	0.0465	1.3500	217.5	25.36	23.03	-9.18
12	0.1150	1.4500	195.0	22.27	20.23	-9.16
13	0.0825	2.3000	187.5	13.45	14.16	5.23
14	0.0950	1.2750	262.5	24.05	24.03	-0.11
15	0.0666	1.7350	172.5	16.10	18.12	12.53
16	0.1475	2.3750	185.0	12.60	12.63	0.23
17	0.0825	1.4750	125.0	17.47	19.28	10.34
18	0.1330	1.3330	188.0	21.01	21.06	0.27
19	0.1440	1.6660	222.0	18.54	18.09	-2.44
20	0.0444	1.8880	177.0	14.72	17.41	18.31
21	0.1666	2.0000	88.0	15.17	13.66	-9.96
22	0.0888	1.8300	266.0	18.85	18.24	-3.24
23	0.0600	2.0000	181.0	15.86	16.40	3.36

The absolute average error [%]=8.12

:

Radial force verfication for $a < R$

Exp#	c [mm/rev]	a [mm]	V [m/min]	Measured F_r [N]	Predicted F_r [N]	Error [%]
1	0.0600	0.7750	112.5	36.74	30.29	-17.57
2	0.1700	0.6500	155.0	53.07	52.86	-0.39
3	0.1800	0.4500	180.0	47.70	51.55	8.07
4	0.1000	0.5500	190.0	36.09	36.09	0.01
5	0.1650	0.5500	220.0	46.42	46.94	1.13
6	0.1850	0.6750	250.0	46.75	47.85	2.35
7	0.0725	0.7750	270.0	29.07	27.29	-6.11
8	0.1350	0.4250	235.0	32.46	39.14	20.59
9	0.0675	0.7250	252.5	28.13	27.34	-2.79
10	0.1375	0.3250	97.5	48.84	46.49	-4.81
11	0.0580	0.5600	114.0	30.59	31.13	1.75
12	0.1110	0.6660	152.0	45.65	39.94	-12.52
13	0.1400	0.7770	123.0	44.54	47.47	6.56
14	0.1200	0.6000	156.0	37.05	42.14	13.71

The absolute average error [%]=7.02

Radial force verfication for $a \geq R$

Exp#	c[mm /rev]	a[mm]	V[m/min]	Measured F_r [N]	Predicted F_r [N]	Error[%]
1	0.1300	1.5650	100.0	49.73	43.17	-13.19
2	0.0700	3.1000	130.0	33.57	28.85	-14.06
3	0.0550	0.9500	165.0	29.79	24.24	-18.63
4	0.0900	1.0000	170.0	33.37	28.85	-13.56
5	0.1100	2.2500	200.0	31.56	32.80	3.93
6	0.0775	1.2500	240.0	29.54	27.24	-7.79
7	0.0925	1.9500	137.5	31.42	33.78	7.49
8	0.0575	2.1500	142.5	27.06	28.07	3.71
9	0.1275	2.7750	127.5	40.53	38.69	-4.54
10	0.0465	1.3500	217.5	24.75	24.06	-2.80
11	0.1500	3.0000	87.5	58.49	47.66	-18.52
12	0.0825	2.3000	187.5	27.68	29.98	8.30
13	0.0950	1.2750	262.5	30.86	28.95	-6.21
14	0.1475	2.3750	185.0	36.78	37.38	1.64
15	0.0825	1.4750	125.0	29.53	31.73	7.44
16	0.1330	1.3330	188.0	36.42	34.76	-4.56
17	0.1440	1.6660	222.0	34.91	35.46	1.58
18	0.1666	2.0000	88.0	55.19	54.13	-1.92
19	0.0888	1.8300	266.0	31.93	29.12	-8.79
20	0.0600	2.0000	181.0	26.25	27.98	6.60

The absolute average error [%]=7.76

Feed force verfication for $a < R$

Exp#	c [mm/rev]	a [mm]	V [m/min]	Measured F_f [N]	Predicted F_f [N]	Error [%]
1	0.0600	0.7750	112.5	47.94	41.08	-14.31
2	0.1700	0.6500	155.0	50.01	46.81	-6.39
3	0.1800	0.4500	180.0	29.46	22.44	-23.81
4	0.1000	0.5500	190.0	31.86	28.76	-9.75
5	0.1650	0.5500	220.0	31.93	31.90	-0.08
6	0.0650	0.4750	230.0	19.91	20.13	1.11
7	0.1850	0.6750	250.0	44.94	44.72	-0.48
8	0.0725	0.7750	270.0	32.95	37.35	13.36
9	0.1350	0.4250	235.0	20.69	18.88	-8.76
10	0.0770	0.3000	242.5	12.27	9.96	-18.82
11	0.0675	0.7250	252.5	30.34	34.39	13.35
12	0.0580	0.5600	114.0	23.85	27.53	15.45
13	0.1110	0.6660	152.0	40.83	41.00	0.43
14	0.1400	0.7770	123.0	49.66	58.45	17.72
15	0.1200	0.6000	156.0	35.79	36.34	1.55

The absolute average error [%]=9.69

Feed force verification for $a \geq R$

Exp#	c [mm/rev]	a [mm]	V [m/min]	Measured F_f [N]	Predicted F_f [N]	Error [%]
1	0.1300	1.5650	100.0	127.87	137.88	7.83
2	0.0700	3.1000	130.0	167.33	165.66	-1.00
3	0.0550	0.9500	165.0	43.66	46.49	6.46
4	0.0900	1.0000	170.0	56.01	58.79	4.96
5	0.1100	2.2500	200.0	136.13	130.10	-4.43
6	0.0775	1.2500	240.0	68.70	60.39	-12.11
7	0.0925	1.9500	137.5	113.92	120.14	5.46
8	0.0575	2.1500	142.5	108.65	104.17	-4.12
9	0.1275	2.7750	127.5	201.76	209.40	3.78
10	0.0465	1.3500	217.5	52.21	56.42	8.05
11	0.1500	3.0000	87.5	299.24	305.40	2.06
12	0.0825	2.3000	187.5	115.71	118.52	2.42
13	0.0950	1.2750	262.5	69.15	64.74	-6.38
14	0.1475	2.3750	185.0	164.48	166.33	1.12
15	0.0825	1.4750	125.0	93.84	90.47	-3.59
16	0.1330	1.3330	188.0	94.83	89.98	-5.12
17	0.1440	1.6660	222.0	104.08	108.25	4.00
18	0.1666	2.0000	88.0	203.51	222.08	9.12
19	0.0888	1.8300	266.0	93.51	88.12	-5.77
20	0.0600	2.0000	181.0	92.37	94.83	2.66

The absolute average error [%]=5.022

Appendix B: Experimental Results of The Orthogonal to Oblique Transformation Method

Orthogonal to oblique transformation method tangential, radial and feed force verifications

Tangential force verification

Exp. #	V [m/min]	c [mm/rev]	a [mm]	Measured F_t [N]	Predicted F_t [N]	Error [%]
1	240	0.050	1.000	203.626	184.106	-9.586
2	150	0.050	0.500	106.207	112.656	6.072
3	150	0.050	0.750	152.219	154.959	1.800
4	150	0.050	1.250	224.270	238.594	6.387
5	100	0.050	1.500	301.647	291.984	-3.203
6	100	0.050	1.750	346.888	335.193	-3.372
7	115	0.050	0.625	126.027	138.553	9.940

Radial force verification

Exp. #	V [m/min]	c [mm/rev]	a [mm]	Measured F_r [N]	Predicted F_r [N]	Error [%]
1	240	0.050	1.000	87.825	68.770	-21.696
2	150	0.050	0.500	75.737	73.340	-3.165
3	150	0.050	0.750	99.956	79.238	-20.727
4	150	0.050	1.250	82.262	79.230	-3.686
5	100	0.050	1.500	111.172	85.900	-22.732
6	100	0.050	1.750	115.137	85.900	-25.393
7	115	0.050	0.625	96.351	82.090	-14.801

Feed force verification

Exp. #	V [m/min]	c [mm/rev]	a [mm]	Measured F_f [N]	Predicted F_f [N]	Error [%]
1	240	0.050	1.000	134.309	107.200	-20.184
2	150	0.050	0.500	60.718	62.944	3.666
3	150	0.050	0.750	109.580	95.680	-12.685
4	150	0.050	1.250	154.594	145.700	-5.753
5	100	0.050	1.500	238.613	183.000	-23.307
6	100	0.050	1.750	279.764	209.000	-25.294
7	115	0.050	0.625	88.636	83.380	-5.930

Appendix C

-Determination of the Emprical Contants in Mechanistic Model

Least squares method:

$$K_{tc} = e^{b_0} A^{b_1} V^{b_2} \tag{6.1}$$

$$\log(K_{tc}) = \log(e^{b_0}) + b_1 \log(A) + b_2 \log(V) \tag{6.2}$$

The terms are redefined as follows.

$$K = \log(K_{tc}) \qquad C = \log(A) \qquad D = \log(V), \tag{6.3}$$

$$K = b_0 + b_1 C + b_2 D \tag{6.4}$$

b_0, b_1 and b_2 in Eq. (6.4) should be selected such that the square of distances between the predicted curve and measured data are minimized. The deviation between the points and curve is,

$$d_i = K_i - (b_0 + b_1 C_i + b_2 D_i) \qquad 1 \le i \le n \tag{6.5}$$

Hence, $\sum_{i=1}^{n} d^2{}_i$ is minimized.

$$f(b_0, b_1, b_2) = d_1^2 + d_2^2 + d_3^2 + \ldots\ldots\ldots\ldots\ldots + d_n^2 = \sum_{i=1}^{n} [K_i - (b_0 + b_1 C_i + b_2 D_i)]^2 \tag{6.6}$$

The numbers K_i, C_i and D_i are all constants. The partial derivatives of the f are,

$$\frac{\partial f}{\partial b_0} = -2 \sum_{i=1}^{n} [K_i - (b_0 + b_1 C_i + b_2 D_i)] \tag{6.7}$$

$$\frac{\partial f}{\partial b_1} = -2 \sum_{i=1}^{n} C_i [K_i - (b_0 + b_1 C_i + b_2 D_i)] \tag{6.8}$$

$$\frac{\partial f}{\partial b_2} = -2\sum_{i=1}^{n} D_i[K_i - (b_0 + b_1 C_i + b_2 D_i)] \tag{6.9}$$

When both partial derivatives are set to zero, the following linear equations are obtained.

$$\frac{\partial f}{\partial b_0} = 0 \qquad \Rightarrow \sum_{i=1}^{n} K_i = \sum_{i=1}^{n} (b_0 + b_1 C_i + b_2 D_i) \tag{6.10}$$

$$\frac{\partial f}{\partial b_1} = 0 \qquad \Rightarrow \sum_{i=1}^{n} K_i C_i = \sum_{i=1}^{n} (b_0 C_i + b_1 C_i^2 + b_2 C_i D_i) \tag{6.11}$$

$$\frac{\partial f}{\partial b_2} = 0 \qquad \Rightarrow \sum_{i=1}^{n} K_i D_i = \sum_{i=1}^{n} (b_0 D_i + b_1 C_i D_i + b_2 D_i^2) \tag{6.12}$$

We can solve these three equations for b_0, b_1 and b_2. The resulting curve $K_{tc} = e^{b_0} A^{b_1} V^{b_2}$ always minimizes the sum of the squares of the deviations.

The equations can be expressed in matrix form.

$$\sum_{i=1}^{n} \begin{bmatrix} K_i \\ K_i C_i \\ K_i D_i \end{bmatrix} = \sum_{i=1}^{n} \begin{bmatrix} 1 & C_i & D_i \\ C_i & C_i^2 & C_i D_i \\ D_i & C_i D_i & D_i^2 \end{bmatrix} \begin{bmatrix} b_0 \\ b_1 \\ b_2 \end{bmatrix} \tag{6.13}$$

$$T = \sum_{i=1}^{n} \begin{bmatrix} K_i \\ K_i C_i \\ K_i D_i \end{bmatrix}, \quad Z = \sum_{i=1}^{n} \begin{bmatrix} 1 & C_i & D_i \\ C_i & C_i^2 & C_i D_i \\ D_i & C_i D_i & D_i^2 \end{bmatrix}, \quad W = \begin{bmatrix} b_0 \\ b_1 \\ b_2 \end{bmatrix} \tag{6.14}$$

$$W = Z^{-1} T \tag{6.15}$$

The resulting curve $K_{tc} = e^{b_0} A^{b_1} V^{b_2}$ always minimizes the sum of the squares of the deviations.

Bibliography

[1] E. Budak, Y. Altintas, E. J. A Armarego, 1996, Prediction of Milling Force Coefficients From Orthogonal Cutting Data, ASME Vol. 118, pp. 216-224

[2] Y. Altintas, 2000, Course Book, Manufacturing Automation, Metal Cutting Mechanics, Machine Tool Vibrations, and CNC Design, Cambridge, ISBN 0521659736

[3] Merchant, M.E., Basics Mechanics of the Metal Cutting Process, Journal of Applied Mechanics ASME, pp A-168 to A-175, 1944

[4] J. Tlusty and M. Polacek, The Stability of Machine Tools Against Self Excited Vibrations in Machining, International Research in Production Engineering, ASME, pages 465-474, 1963

[5] Kronenberg M. Machining Science and Application, Pergamon Press Inc., 1966 pp 209-225

[6] R. A. Hallam and R. S. Allsopp, The Design, Development and Testing of a Prototype Boring Dynamometer, Int. J. Mach. Tool Des. Res. Vol. 24, No. 1, 1962, pp. 241-266

[7] H.E. Merrit. Theory of Self-Excited Machine Tool Chatter. Trans. ASME Journal of Engineering for Industry, 87:447-454, 1965

[8] K. Ogata, Modern Control Engineering, Prentice Hall, 1990

[9] Sabberwal, A.J.P, Chip Section and Cutting Force During the Milling Operation, Annals of the CIRP, 1960, pp, 197-203

[10] O.Burak Ozdogonlar W.J. Endres An Analytical, Non-Dimensional Representation of Chip Area for Corner-Radiused Tools Under Depth of Cut and Feed Variations, ASME 1998 Manufacturing Science and Engineering Division, Vol. 8. pp251-258

[11] J. Tlusty Machine Dynamics, McMaster University,

[12] F. Kuster; IWF, ETH Zurich, Cutting Dynamics and Stability of Boring Bars, Annals of the CIRP Vol. 39 pp361-366, January 15, 1990

[13] Kline, W. A., R.E.Devor, and J.R. Linberg, The Prediction of Cutting Force in End Milling with Application to Cornering Cuts, Int. Jour. Mach. Tool Des. and Res. Vol. 22 No.1 1982, pp 7-22

[14] Sutherland, J.W, and R.E.Devor, and S.G.Kapoor, A Mechanistic Model for the Prediction of the Force and Surface Error Prediction in Flexible End Milling Systems, ASME Journal of Engineering for Industry, Vol.108, pp, 269-279, 1986

[15] .Fu, H.J., R.W.Devor, and S.G. Kapoor, A Mechanistic Model for the Prediction of the Force System in Face Milling Operations, Journal of Engineering fo Industry, Transaction ASME, Vol. 106, pp,81-88 1984

[16] Subramani, G., R. Suvada, S.G. Kapoor, R. W. Devor, and W. Meingast, A Model for the Prediction of Force System for Cyclinder Boring Process, Proc. XV North American Manufacturing Research Conference, pp, 449-446, 1987

[17] J.W. Sutherland, G.Subramani, M.J.Kuhl, R.E.Devor, S.G.Kapoor, An Investigation into the Effect of Tool and Cut Geometry on Cutting Force System Prediction Models, Proc. of XVI North American Manufacturing Research Conference, 1990, pp 264-272

[18] Ph.D Thesis By Zhang G., Dynamic Modeling and Dynamic Analysis of the Boring Machining System, University of Illinois at Urbana-Champain, 1986

[19] G.M. Zhang, S.G. Kapoor Dynamic Modeling and Analysis of the Boring Machining System, Journal of Engineering for Industry, Vol. 109 pp219-226 1987

[20] Frank R. Giordano and Maurice D. Weir, Differential Equations (A Modeling Approach), Addison Wesley Publishing, 1994

[21] Ren H., Mechanics of Machining with Chamfered Tools, Master thesis, University of British Columbia, Vancouver, Canada, 1998

[22] E. J. A. Armarego, and Uthaichaya, M., Mechanics of Cutting Approach for Force Prediction in Turning Operations, Journal of Engineering Preduction, Vol. 1, No.1, pp. 1-18, 1977

[23] E.J.A. Armarego. Material Removal Processes-An intermadiate Course, The University of Melbourn, 1993

[24] Sanjiv G. Tewani, Keith E. Rouch, and Bruce L. Walcott, Cutting Process Stability of a Boring Bar with Active Dynamic Absorber, Vibration Analysis-Analytical and Computational ASME 1991, Vol. 37 pp 205-213

[25] D. R. Browning, I. Golioto, N. B. Thompson, Active Chatter Control System for Long-Overhang Boring Bars, Proceedings of SPIE The International Society for Optical Engineering, 1997, Vol. 3044, pp 270-280

[26] S. G. Tewani, T. C. Switzer, B. L. Walcott, K. E. Rouch, T. R. Massa, Active Control of Machine Tool Chatter for a Boring Bar: Experimental Results, Vibration and Control of Mechanical Systems, ASME 1993, Vol. 61 pp103-115

[27] S. Jayaram, M. Iyer, An Alalytical Model for Prediction of Chatter Stability in Boring, Transactions of NAMRI/SME, Volume XXVIII, 2000, pp. 203-208

[28] E. W. Parker, Dynamic Stability of a Cantilever Boring Bar With Machined Flats Under Regenerative Cutting Conditions, Journal Mechanical Engineering Science Vol. 12 No 2 1970, pp.104-115

[29] S.A. Tobias and W. Fishwick A Theory of Regenerative Chatter, The Engineer-London, 1958

[30] S.A. Tobias, Machine Tool Vibration, Blackie, 1965

[31] J. Tlusty and F. Ismail, Basic Nonlinearity in Machining Chatter, Annals of the CIRP, 30:21-25, 1981

[32] J. Tlusty, Analysis of the State of Research in Cutting Dynamics, Annals of the CIRP, 27: 583-589, 1978

[33] J. Tlusty, High-Speed Machining, Annals of the CIRP, 42:733-738, 1993

[34] D. Montgomery, Milling of Flexible Structures, Master's Thesis, University of British Columbia, 1990

[35] J. Tlusty, A Method of Analysis of Machine Tool Stability, Proceedings of the 6th Machine Tool Design and Research Conference, pp5-14, 1965

[36] E.I.Rivin, H. Kang, Enhancement of Dynamic Stability of Cantilever Tooling Structures, Int. J. Mach. Tools Manufact. Vol. 32 pp539-561, 1992

[37] S. Ema, E. Marui, Supression of Chatter Vibration of Boring Tools Using Impact Dampers, International Journal of Machine Tools& Manufacture, Vol. 40 pp1141-1156, 2000